ORNL-4600
UC-25 – Metals, Ceramics, and Materials

Cy 1

FUELS AND MATERIALS DEVELOPMENT PROGRAM

QUARTERLY PROGRESS REPORT

FOR PERIOD ENDING JUNE 30, 1970

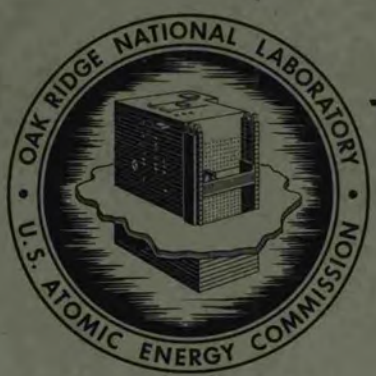

OAK RIDGE NATIONAL LABORATORY
operated by
UNION CARBIDE CORPORATION
for the
U.S. ATOMIC ENERGY COMMISSION

Printed in the United States of America. Available from
National Technical Information Service
U.S. Department of Commerce, Springfield, Virginia 22151
Price: Printed Copy $3.00; Microfiche $0.65

ORNL-4600

Contract No. W-7405-eng-26

METALS AND CERAMICS DIVISION

FUELS AND MATERIALS DEVELOPMENT PROGRAM QUARTERLY PROGRESS REPORT FOR PERIOD ENDING JUNE 30, 1970

Compiled by

P. Patriarca

Edited by

D. J. Rucker

NOVEMBER 1970

OAK RIDGE NATIONAL LABORATORY
Oak Ridge, Tennessee
operated by
UNION CARBIDE CORPORATION
for the
U.S. ATOMIC ENERGY COMMISSION

FOREWORD

This quarterly progress report describes research and development on nuclear fuels and materials performed at the Oak Ridge National Laboratory for the U.S. Atomic Energy Commission. This work is either sponsored by or of particular interest to the Fuels and Materials Branch of the Division of Reactor Development and Technology.

Progress on these programs is reported for the three major divisions of the work — Fast Reactor Technology, Space Power Technology, and General Reactor Technology — under the appropriate AEC activity titles listed below.

AEC Activity Title	AEC Activity Number
PART I. FAST REACTOR TECHNOLOGY	
FUELS	
DEVELOPMENT OF LMFBR OXIDE FUELS	04 40 02 01 1
DEVELOPMENT OF HIGH-PERFORMANCE LMFBR FUELS	04 40 02 01 1
EFFECT OF POWER CYCLING ON LMFBR FUEL-CLADDING BEHAVIOR	04 40 02 01 1
LMFBR FUEL ELEMENT DESIGN AND MODEL DEVELOPMENT	04 40 02 01 1
CLADDING AND OTHER STRUCTURAL MATERIALS	
MECHANICAL PROPERTIES OF ALLOYS IN REACTOR ENVIRONMENTS	04 40 02 03 1
DEVELOPMENT OF LMFBR CLADDING AND STRUCTURAL MATERIALS	04 40 02 01 1
FABRICATION DEVELOPMENT FOR LMFBR STAINLESS STEEL TUBING	04 01 61 01 5
WELDING DEVELOPMENT FOR LMFBR VESSELS AND COMPONENTS	04 40 02 04 1
SHIELDED METAL-ARC WELDING FOR LMFBR COMPONENTS	04 01 61 01 5
PROPERTIES OF FERRITIC STEEL WELDS	04 40 02 05 1
NONDESTRUCTIVE TESTING TECHNIQUES FOR LMFBR	04 40 02 04 1
SODIUM CORROSION STUDIES	04 40 02 02 1
DEVELOPMENT OF FAST-REACTOR NEUTRON-ABSORBER MATERIALS	04 40 02 02 1

*Research sponsored by Division of Space Nuclear Systems.

CONTENTS

PART II. SPACE POWER TECHNOLOGY

FUELS

CLADDING AND OTHER STRUCTURAL MATERIALS

PART III. GENERAL REACTOR TECHNOLOGY

FUELS

CLADDING AND OTHER STRUCTURAL MATERIALS

SUMMARY

PART I. FAST REACTOR TECHNOLOGY

FUELS

1. DEVELOPMENT OF FAST-REACTOR OXIDE FUELS

A total of 1.2 kg of Pu sol and 4.5 kg of 93% enriched U sol was prepared to meet the requirements of the oxide fuels program. About 1 kg of dense $(^{235}U_{0.8},Pu_{0.2})O_2$ microspheres was also prepared. About 1.5 kg of $(^{235}U_{0.75},Pu_{0.25})O_2$ microspheres 350 to 595 μm in diameter and about 0.2 kg of additional microspheres less than 44 μm in diameter were prepared for fuel development studies at Argonne National Laboratory. All of the fuel has been prepared for the fuel pins for the 37-pin subassembly for the series II irradiation tests in the Experimental Breeder Reactor-II (EBR-II). Nine of these fuel pins were loaded with Sphere-Pac microspheres and two were loaded with pellets. Nine of these fuel pins were tagged with Xe.

A great effort was made to statistically characterize analytical data on $(U,Pu)O_2$ fuel before irradiation, including methods for determining Pu content of $(U,Pu)O_2$ microspheres by γ-ray spectroscopy and α-ray autoradiography and variations in analyses for the ratio of O:metal in $(U,Pu)O_2$. In addition to this effort both light and replica electron microscopy and α-ray autoradiography were used to characterize the microstructure of sol-gel $(U_{0.8},Pu_{0.2})O_2$ fabricated for the instrumented tests in the Engineering Test Reactor (ETR). All of these show the fuel to be of excellent and consistent quality.

A sol-gel Sphere-Pac capsule that contains $(U,Pu)O_2$ attained a calculated burnup of 9.7 fissions per initial actinide metal atom (FIMA) in the ETR, and the irradiation of the capsules is continuing at a peak heat rate of 15 kw/ft to a burnup of 10 at. %. The postirradiation examination of two capsules that contain UO_2 and $(U,Pu)O_2$ Sphere-Pac fuels that have been irradiated to a peak burnup of 6.5% FIMA was completed during the quarter. The third instrumented capsule irradiated

in the Oak Ridge Research Reactor (ORR), which contains one Sphere-Pac fuel pin and one sol-gel pellet fuel pin of the same composition and smear density, was removed from the reactor after operating successfully. This experiment, which provided direct comparison of pellet and Sphere-Pac fuels to central fuel temperatures near 2000°C, indicated, again, that Sphere-Pac and pellet fuels have essentially the same effective thermal conductance during irradiation at low burnup.

Two instrumented capsules were constructed to investigate fuel swelling and chemical interaction of fuel and cladding and to compare Sphere-Pac and pellet fuels under peak conditions for a liquid-metal-cooled fast breeder reactor (LMFBR). These capsules were inserted into the ETR in May 1970.

We continued destructive examination of six fuel pins that contain Sphere-Pac and pellet fuels that were subjected to power transients in the Transient Reactor Test Facility (TREAT). Metallography indicates extensive restructuring of the fuel and the presence of large gas bubbles formed from the release of adsorbed gases from the molten fuel during the power transient.

Encapsulated Sphere-Pac $(U,Pu)O_2$ fuel pins were removed from EBR-II subassembly X050 after having attained the calculated peak burnup of 6.2% FIMA. Two of these pins are to be returned to ORNL after neutron radiographs have been made, and three others have been scheduled to be reinserted in a new subassembly for continued irradiation to a peak burnup of 11.8% FIMA. This additional burnup has been approved so that the three encapsulated pins can serve as lead experiments for the unencapsulated tests for the series II irradiation tests.

2. DEVELOPMENT OF ADVANCED LMFBR FUELS

Ten fuel pins consisting of cold-pressed-and-sintered (U,Pu)N pellets clad with type 316 stainless steel were fabricated for irradiation testing in the Engineering Test Reactor. These pins have a 0.010-in. radial gap filled with NaK-19 (Na–19% K) between the fuel and cladding to simulate Na bonding.

Arc-melted, nominally U–20% Pu alloy, fully enriched in ^{235}U, that was ordered from WADCO will be shipped October 21, 1970. The Pu content was lowered to about 18% to reduce pyrophoricity which we believe is due to the presence of the ζ phase.

The use of phosphoric acid to dissolve UN before quantitative analysis for N_2 improved precision and eliminated the loss of N_2 that occurred previously. This method is now to be applied to the analysis of mixed nitrides.

The lattice constants of (U,Pu)N solid solutions were found to deviate significantly from Vegard's law.

3. EFFECT OF POWER CYCLING ON LMFBR FUEL-CLADDING BEHAVIOR

This program investigates the effect of power cycling on fuel behavior and the mechanical interaction of fuel and cladding for a liquid-metal-cooled fast breeder reactor (LMFBR). The initial objectives of the study are to compare the mechanical interaction of mixed oxide fuel and cladding during thermal cycling conditions typical of those to be expected in an LMFBR. The first two capsules for power cycling in-reactor will be designed as prototype fuel pins for the Fast-Flux Test Facility Reactor and will operate in the poolside facility of the Oak Ridge Research Reactor in such a fashion as to measure in-reactor the axial extension of the fuel column and cladding and the internal gas pressure of the fuel pin during operation. The design effort on the first capsule (MINT-1) is progressing satisfactorily. The capsule design is now being detailed, and we expect that the capsule will be inserted in September or November 1970.

4. LMFBR FUEL ELEMENT DESIGN AND MODEL DEVELOPMENT

We determined the variation of grain size with radial position for a Sphere-Pac $(U,Pu)O_2$ fuel pin after thermal-reactor irradiation at a linear heat rate of 10.5 kw/ft to a burnup of 0.5% fissions per initial actinide metal atom (FIMA). We determined that the activation energy for grain growth in the irradiated $(U,Pu)O_2$ was only one-fifth of that determined for out-of-reactor grain growth in UO_2 and ThO_2. Electron

microprobe analysis was used to determine the distribution of Pu across a transverse section of a Sphere-Pac $(U,Pu)O_2$ pin irradiated in the Engineering Test Reactor at a linear heat rate of 13.6 kw/ft to a burnup of 0.7% FIMA. A radial scan made simultaneously for Pu and U in the region of columnar grains adjacent to the central void showed that the Pu content decreased and the U content increased with decreasing fuel temperatures. Observations of high Pu content near the central void and low Pu content in vapor-deposited fuel tend to confirm the theory of transport down the temperature gradient of a gas phase rich in U.

The computer subroutine used in the FMØDEL computer code for mechanical analysis of cladding was separated from that code and extensively modified so that it can handle power-cycling conditions and calculate ratchetting of plastic strains during power cycling. A simple problem formulated to test the code confirmed that the subroutine functions properly. We are now altering the integrated model for cladding performance to convert it for use with power cycling. We continued our compilation of available data on the physical and tensile properties of type 316 stainless steel and our discrete-element analysis of the creep of stainless steel tubing for use in liquid-metal-cooled fast breeder reactors.

CLADDING AND OTHER STRUCTURAL MATERIALS

5. MECHANICAL PROPERTIES OF ALLOYS IN REACTOR ENVIRONMENTS AND DEVELOPMENT OF LMFBR CLADDING AND STRUCTURAL MATERIALS

Specimens of type 304 stainless steel were irradiated at 370 to 600°C to fast-neutron fluences of 2 to 6.7×10^{22} neutrons/cm^2. After irradiation at 370 to 470°C, their microstructures consisted of voids and faulted interstitial dislocation loops. The void concentration increased with increasing fluence at constant temperature. Specimens irradiated at 600°C contained a dislocation network, a few unfaulted dislocation loops, and voids. These changes in microstructure brought about large changes in the creep properties at 600°C. The fracture strain was reduced by all exposures.

Nickel 270 was irradiated at 370 to 525°C to fast-neutron fluences up to 1.4×10^{20} neutrons/cm^2. A comparison with other studies showed that the void configuration was very dependent upon the source and condition of the material but that the macroscopic swelling was independent of such variables. These findings and observed inhomogeneous void distributions lead us to propose that the voids are nucleated by preexisting gas bubbles or He produced during irradiation.

Specimens of Mo, Mo—0.5% Ti, and Mo—50% Re were irradiated at 425°C to a fast-neutron fluence of 1.5 to 3.5×10^{22} neutrons/cm^2. Tensile tests after irradiation showed that the ductility was reduced drastically for all alloys at test temperatures of 400 to 800°C.

We observed in previous irradiation experiments that Incoloy 800 had lower fracture strains when irradiated at 500°C than at higher temperatures. The possibility of a thermal instability was checked further by aging material that had been solution annealed and material that had received a further treatment at 800°C to agglomerate carbides. Creep tests at 650°C showed that aging strengthened both materials and that the ductility of the sample that had been solution annealed was reduced whereas that of the material annealed to agglomerate carbides was unaffected.

6. FABRICATION DEVELOPMENT FOR LMFBR STAINLESS STEEL TUBING

Our investigation of the use of artificial defects to simulate natural defects in tubing is continuing. Additional specimens have been prepared for testing mechanical properties at elevated temperatures.

Modifications to the planetary swager were completed. By combining the more conventional process of mandrel drawing with planetary swaging, we are examining the possibility of improved quality and properties for type 316 stainless steel tubing. It appears that tubes manufactured by this combined process are about 10% stronger but less ductile than tubes produced by mandrel drawing alone. Increasing the rotational speed of the swager head and bench speed increased the strengths with no significant changes in ductility.

7. WELDING DEVELOPMENT FOR LMFBR VESSELS AND COMPONENTS

Submerged-arc weldments were prepared in 1-in.-thick type 304 stainless steel with a variety of commercial fluxes and a range of energy input conditions. Tests of mechanical properties showed these welds to be consistently weaker but much more ductile than similar shielded metal-arc welds. Composite (fusion-line) specimens showed lower strength in the base metal but ruptured in the stronger weld metal due to the early initiation and short duration of third-stage creep in the weld metal. Welds made with various energy inputs showed more substantial variations in mechanical properties after longer test times.

Corrosion studies by means of the Strauss Test on heat-treated weldment specimens are being performed at Combustion Engineering, Inc., at Chattanooga, Tennessee, in conjunction with extensive metallographic heat-treatment studies at ORNL.

An irradiation program involving 226 weldment specimens was designed; all specimens were machined, and installation into the irradiation assembly was begun.

Metallographic studies have continued, emphasizing the effect of the amount and morphology of the delta-ferrite phase on subsequent metallurgical reactions and mechanical properties at elevated temperatures.

8. SHIELDED METAL-ARC WELDING FOR LMFBR COMPONENTS

Prior investigations indicated that perhaps the decreasing ductility with increasing time to rupture at 650°C (1200°F) exhibited by the standard lime-TiO_2-coated electrode was due primarily to formation of sigma phase at the phase boundaries. However, new creep-rupture tests at 593°C (1100°F) indicate that the loss in ductility is still severe after 1000 hr at the testing temperature. This may imply that precipitation of carbides causes some of the phase-boundary instability.

Three experimental batches of lime-coated electrodes were added to the program. These new batches contain additions of ferro-titanium, ferro-titanium plus B, and ferro-titanium plus B and P. These additions significantly increase rupture life and rupture ductility.

Further tests at 650°C (1200°F) indicate that additions of C increase the strength somewhat while only slightly improving the ductility. However, additions of B and P, as indicated above, tend to increase the rupture time and ductility more than C.

9. PROPERTIES OF FERRITIC STEEL WELDS

This is a new program in which we compare the weldabilities of four types of ferritic steel for liquid-metal-cooled steam generators: plain-C steels (for background data); 2.25% Cr–1% Mo low-alloy steel; low-C (0.02% C) 2.25% Cr–1% Mo steel; and stabilized 2.25% Cr–1% Mo steel. The overall weldability of these materials will be assessed by use of such weldability tests as the VARESTRAINT, Lehigh restraint, TIGAMAJIG, and Duffer's Gleeble tests.

A thorough search into the weldability of these steels has included correspondence and discussion with various domestic and foreign organizations and firms. To date, we have received conflicting reports concerning the weldability of the stabilized 2.25% Cr–1% Mo steels. We are now procuring research quantities of these materials. Specimens for Lehigh restraint tests were machined from the standard 2.25% Cr–1% Mo steel plate and were ordered from SAE 1010 steel plate. A Jominy test was run on the stabilized material, and specimens for Duffer's Gleeble and TIGAMAJIG weldability tests were also made from this material. Great care was taken to assure identical microstructures in the as-received material and the prepared specimens.

10. NONDESTRUCTIVE TESTING TECHNIQUES FOR LMFBR

We are developing new methods, techniques, and equipment for nondestructively evaluating materials for liquid-metal-cooled fast breeder reactors (LMFBR) with emphasis on measuring cold work in stainless steel tubing.

We are developing an eddy-current instrument to measure both size and depth of defects and have constructed new modular circuits for the instrument. Ultrasonic schlieren techniques are being compared with

both delta and conventional ultrasonic techniques for the examination of flaws in welds of both Al and stainless steel.

Construction and assembly of components is continuing on the high-sensitivity impedance bridge to be used in the measurement of changes in magnetic permeability related to cold work in stainless steel tubing. We began studies with the electron microscope on samples that contain various degrees of cold work to relate microstructural changes to the results of nondestructive tests.

11. SODIUM CORROSION STUDIES

The partitioning of O between V alloys and Na at 600°C was investigated. The addition of Mo to V lowered the concentration of O entering into solid solution during equilibration with Na. Vanadium alloys that contained Zr additions were internally oxidized by O in Na. The effect of N contamination on the creep properties of unalloyed V was determined at 600°C. Interaction of N with V at N_2 pressures to 3.4×10^{-6} torr lowers the creep strength; however, on the basis of time required to produce a given strain, V was strongest at a N_2 pressure of 1.5×10^{-6} torr.

A bimetallic thermal-convection loop composed of V and type 321 stainless steel was examined following operation with Na for 3000 hr at a maximum temperature of 700°C. Insert specimens of V increased in C, N, and O; however, the amount picked up at 700°C was less than that for an earlier loop with type 304 stainless steel rather than type 321 stainless steel. The tensile properties of the hottest V inserts were not noticeably changed by the test exposure.

The effect of Na leakage on the oxidation of type 304L stainless steel was studied in a N_2 + 1% O_2 mixture that contained 100 ppm H_2O. Sodium was passed through a defect in a stainless steel tube at 760°C and into a contiguous thermal insulation layer which also was at 760°C. Unlike earlier tests in which we had heated the tube but not the insulation, there was no plugging of Na in the defect; the Na was quickly absorbed by the insulation with negligible oxidation of the stainless steel.

12. DEVELOPMENT OF FAST-REACTOR NEUTRON-ABSORBER MATERIALS

Transmission electron microscopy techniques were developed for B_4C with the use of an ion-bombardment milling machine. Transmission electron photomicrographs indicate that B_4C is capable of twinning and also show the crystallographic orientation of the voids within the grains.

Additional specimens are undergoing thermal irradiation at 500°C and will be removed at an estimated 3.1×10^{21} depletions/cm^3 (15% burnup of ^{10}B).

Fabrication of Ta disks containing B_4C as a dispersoid was unsuccessful because of extensive reaction between the materials at the fabrication temperatures.

Powder samples of commercial-grade TaB and TaB_2 are now being characterized. X-ray diffraction indicates that TaB_2 is single phase whereas TaB contains Ta_3B_2 and Ta in addition to TaB.

PART II. SPACE POWER TECHNOLOGY

FUELS

13. DEVELOPMENT OF URANIUM MONONITRIDE FUELS

Postirradiation examination of the bottom pin of capsule UN-3 revealed incipient failure of the T-111 cladding. This pin was a duplicate of the middle pin in the same capsule that failed after 5800 hr at peak temperatures above 1400°C.

CLADDING AND OTHER STRUCTURAL MATERIALS

14. CLADDING MATERIALS FOR SPACE ISOTOPIC HEAT SOURCES

We continued our efforts to develop alloys with optimum strength and resistance to oxidation for use as cladding materials for space isotopic heat sources. Partial replacement of Cr with Ti in the ordered Pt_3Cr alloy increased hardness and critical temperature for ordering.

Additions of Hf to form ordered Pt_3Hf in Pt-Mo and Pt-W solid-solution alloys are also being investigated to improve strength and retard grain growth at high temperatures.

The weight losses of alloys Pt_3Cr and Pt—0.6% W—1% Hf in air oxidation tests at 1000°C approximated that of pure Pt while $Pt_3(Cr_{0.84},W_{0.16})$ gained weight at the same low rate.

15. PHYSICAL AND MECHANICAL METALLURGY OF REFRACTORY ALLOYS

The existence of a stable miscibility gap in the Ta-Zr system was confirmed by x-ray studies of a Ta—43.5 wt % Zr alloy. The diamond pyramid hardness (DPH) of this alloy decreases from about 500 to about 300 DPH after aging for 4×10^3 min at 850°C. The precipitation of uniform Hf-rich particles in Ta-Hf alloys is attributed to the possible existence of a metastable miscibility gap with a critical temperature of about 1400°C. The oxidation rate of Ta—65 wt % Hf at 1000°C in air is comparable to the rates of the complex Hf-Ta base alloys developed by the Illinois Institute of Technology Research Institute, Chicago. Crack-free zones observed at the surfaces of ruptured creep specimens of alloy C-129Y are attributed to interstitial contamination. Measurements of the width of these zones agree with the diffusion rates of interstitials in Nb. The compatibility of Ta and Pt with various metals at 1200°C was studied to find a suitable transition barrier between tubular welds of these metals. The thermal conductivity of Ta, estimated from experimentally derived low-temperature phonon conductivity and Lorenz function values, is within 3% of the recommended values to 3000 K.

16. TUNGSTEN METALLURGY

In our development of chemical vapor deposition we produced large sheet deposits of W with a low F impurity content by cooling the deposition chamber. Preliminary experiments were performed on the deposition of W with a {110} orientation from WCl_6. A study of the effect of gas composition on formation of nodules and porosity in W—5% Re deposits showed that the best deposits are produced at a stoichiometric mixture

of H_2, WF_6, and ReF_6. Bend tests of chemically vapor deposited W specimens joined by gas W-arc welding showed that 0.050-in.-thick material had a ductile-to-brittle transition temperature greater than 550°C whereas 0.030-in.-thick material bent at 450°C.

Data on the secondary creep rate at 1200 to 2200°C for arc-melted W, W–5% Re, W–26% Re, W–25% Re–30% Mo and chemically vapor deposited W are presented. We obtained excellent agreement of our data for arc-melted W with data from three other sources. The creep rate varied with the hyperbolic sine of the stress. The creep strength of W–25% Re in an atmosphere of 10^{-6} torr O_2 was greater than in a vacuum of 10^{-8} torr. This effect is opposite to that observed in unalloyed W.

17. FAST-NEUTRON IRRADIATION EFFECTS ON ELECTRICAL INSULATORS

Advanced materials (sapphire Al_2O_3, single-crystal MgO, and transparent, polycrystalline Y_2O_3) were irradiated at low temperature (below 150°C) in the Engineering Test Reactor (ETR) to fast fluences up to 2×10^{21} neutrons/cm^2 (> 1 Mev). Metallographic examinations revealed no microfracturing. One MgO specimen and one Y_2O_3 specimen broke during irradiation, but all sapphire specimens survived without fracturing.

Polycrystalline alumina expanded more in volume and sustained greater microstructural damage in irradiations in the Experimental Breeder Reactor-II (EBR-II) than in the ETR for comparable fast fluences with energies above 1 Mev. This is explained on the basis of differences in the neutron-energy spectra of the two reactors.

18. ALKALI-METAL CORROSION STUDIES

We completed testing a forced-circulation loop of T-111 with Li at high temperature. The loop operated for 3000 hr at a maximum temperature of 1370°C. A vent line that failed after 1735 hr was successfully repaired. Additional thermocouples were attached to the loop during this repair, and we obtained a very accurate measurement of the temperature distribution and Li flow rate during subsequent operation. Our analysis of the failed vent line indicated that the failure was not

produced by any effect of the Li. Rather, it appears to have been caused by traces of Ni that had contaminated the failed area before or during fabrication of the loop.

PART III. GENERAL REACTOR TECHNOLOGY

FUELS

19. FISSION-GAS RELEASE AND PHYSICAL PROPERTIES OF FUEL MATERIALS DURING IRRADIATION

The preliminary evaluation of data shows the thermal diffusivity to be a function of fission-rate density. The mathematical process of evaluating data is working well, and the method of measuring thermal diffusivity during irradiation by perturbation techniques has been established. The evaluation of the physical condition of mixed oxide fuel specimens by analysis of fission gas was confirmed by analysis after irradiation.

20. DEVELOPMENT OF FUEL ELEMENT FABRICATION

Fabrication of the irradiation experiment to be inserted into the High Flux Isotope Reactor (HFIR) for the purpose of establishing the irradiation performance of Advanced Test Reactor (ATR) types of fuel at high burnup is continuing.

Postirradiation examination of the HFIR fuel element 49-I is in progress with no evidence of any blisters of the fuel core. The use of Al_2O_3 particles in the filler side of the shaped HFIR core was successful in reducing fabrication blisters in a proof test run by the manufacturer of the fuel elements.

Good correlation was obtained between the void volume generated in plates fabricated at ORNL and at Texas Instruments, Inc.

Deformation behavior of shaped cores to be used for UAl_x cores is being studied.

21. TECHNICAL ASSISTANCE IN PROCUREMENT OF FUEL ELEMENTS

Various possibilities are being examined to explain why some fuel plates have small holes or cracks in the cladding that expose the fuel composite to the reactor coolant.

CLADDING AND OTHER STRUCTURAL MATERIALS

22. BEHAVIOR OF REFRACTORY MATERIALS UNDER IRRADIATION

The status of the work under this program, which was terminated on June 30, 1970, is summarized.

23. JOINING RESEARCH ON NUCLEAR MATERIALS

Elevated-temperature (650°C) tensile data obtained for welds on Incoloy 800 base metal showed that the Inconel 82T commercial filler metal has the best strength and ductility properties. The welds made from filler metals prepared from an electroslag-remelted commercial heat of Incoloy 800 and the experimental heat that contained P had strengths comparable to that of the Inconel 82T welds. The ductility of the Inconel 82T filler metal at 650°C was considerably better than that of either of the other two filler metals.

We began studies of the ductility of Inconel 600 at intermediate temperatures. Preliminary data indicate that this alloy will lose ductility in the 600°C temperature range. A ternary composition, Ni–15.5% Cr–8% Fe, had not recovered its ductility at 900°C.

The quantitative television microscope is being used to determine the correlation between the Magne-gage readings currently being used to measure qualitatively the amount of ferrite in the microstructure of the experimental stainless steel alloys.

The investigation of the interrelationship between ferrite and martensite on the properties of stainless steel weldments is continuing. Martensite was produced by cold rolling. Its presence is verified by the Magne gage. Metallographic studies by means of bright-field optical

microscopy did not satisfactorily differentiate the martensite and slip and mechanical twins. Some success was obtained with phase-contrast microscopy. We are now investigating the use of a magnetic-particle etching technique that appears to permit the identification of the martensite.

24. NONDESTRUCTIVE TESTING

A matrix method using Green's functions was developed; it improves methods of calculating solutions to problems of electromagnetic induction. Computer programs were used to design an eddy-current coil with superior accuracy for the measurement of electrical conductivity.

Our studies of frequency analysis of ultrasonic signals emphasized characterization of hidden flaws. Analytical expressions that we developed were confirmed experimentally for the determination of both angular orientation and diameter of reflectors using analysis of the frequency spectrum.

Fluorescent x rays excited in U by radiation from a Pm source were used to measure changes in Al thickness placed on the U. We began preliminary development of techniques for using a closed-circuit television system as part of a high-speed, high-resolution densitometer.

25. IMPROVEMENT OF HASTELLOY N AND RELATED COMPOSITIONS

The mechanical properties of several heats of modified Hastelloy N were evaluated after irradiation at 760°C to a thermal fluence of 3×10^{22} neutrons/cm^2. We studied alloys containing additions of Ti, Hf, and Nb, both singly and in combination; those containing at least 0.5% Hf seemed to have the highest ductilities. These additions had very little effect on the creep strength except that one alloy that contained 3% Ti was very strong but had low ductility. Some small commercial heats of these alloys were procured for study. Transmission electron microscopy revealed several differences in the microstructures of the commercial alloys and those of our laboratory melts.

26. ADVANCED MATERIALS FOR STEAM GENERATORS

A comparison of the general corrosion at 650°C of our weldments of alloys for steam generators with results for unwelded specimens exposed at 620°C by the General Electric Company, Vallecitos, showed that, in spite of the temperature difference, our materials were corroded only 1/2 to 2/3 as much as theirs. Although the steam used by General Electric contained 20 ppm O and 2.5 ppm H, compared to undetectable levels in our work, we attribute the lower corrosion of our specimens to differences in surface condition.

Studies designed to show differences in corrosion at 595 and 650°C of root passes (the ones exposed to the steam side of heat exchangers) of weldments as a function of differing composition and surface condition revealed large differences in amounts of corrosion. At the extremes, the corrosion rates of type 304 stainless steel welded with type 308 stainless steel and Incoloy 800 welded with Inconel 82 with the as-welded finish were two orders of magnitude higher than those of Hastelloy X joined to Incoloy 800 with Inconel 82 with the as-welded, ground, sandblasted, and electropolished finishes.

PART I

FAST REACTOR TECHNOLOGY

FUELS

1. DEVELOPMENT OF FAST-REACTOR OXIDE FUELS

P. Patriarca A. L. Lotts

The objective of this program is to obtain an economically optimized $(U,Pu)O_2$ fuel cycle for a liquid-metal fast breeder reactor (LMFBR) by extending the performance capability and advancing the fabrication technology of oxide fuels. These fuels have the most advanced technology and greatest potential for reliable operation in first-generation LMFBR's. They have been tested in fast-flux environments but as yet have not been exposed under actual prototypic conditions. Currently, the burnup and heat rate are limited to about 50,000 Mwd/metric ton and 16 kw/ft, respectively, based on irradiation experiments with fuels that are not necessarily optimized for thermal, chemical, and mechanical performance.

The capability of oxide fuels can possibly be improved by adjusting structures or void distribution in the fuels. We emphasize irradiating fuels derived from the sol-gel process with thoroughly characterized structures and void distributions different from those of the oxide fuels irradiated heretofore. These include fuels fabricated by Sphere-Pac, vibratory compaction, extrusion, and pelletization. We compare the performance of these with the performance of reference fuels such as pellets derived from mechanically blended powders and coprecipitated material. The development of computer programs to assist in the analysis of test results and the development of a mathematical model to predict the performance of a fuel pin are integrated with the test program.

Preparation of $(U,Pu)O_2$ Fuel Materials

W. T. McDuffee[1]

Preparation of PuO_2 Sol

We prepared eight standard PuO_2 sols (150 g each). All were blended with enriched UO_2 sol prepared from 93% enriched $UO_2(NO_3)_2$. The mixed

sol was then converted into dense microspheres. Six of the sols were blended to obtain a ratio of Pu:(U+Pu) of 0.25. From the blended sol, Sphere-Pac fuel is being prepared for fuel development studies in progress at Argonne National Laboratory (ANL). The remaining two sols were blended to obtain a ratio of Pu:(U+Pu) of 0.2. From this blended sol, dense microspheres were formed to obtain material for development studies at ORNL on fuel fabrication and fuel dissolution.

Preparation of Enriched UO_2 Sol

We prepared a total of fifteen lots of UO_2 sol (about 300 g U) from 93% enriched U as $UO_2(NO_3)_2$ for use in studies of fuel fabrication.

Preparation of $(U,Pu)O_2$ Microspheres

Dense $(^{235}U_{0.8},Pu_{0.2})O_2$ Microspheres. — We prepared about 1 kg of dense $(^{235}U_{0.8},Pu_{0.2})O_2$ microspheres (420 to 595 μm in diameter). This material, which is of high quality (lustrous, high density, and very uniform in appearance and texture) is to be used in reprocessing studies at ORNL. Before it can be used in irradiation specimens, however, the ratio of O:metal will have to be adjusted from the present level (2.05 to 2.15) to less than 2.0.

Dense $(^{235}U_{0.75},Pu_{0.25})O_2$ Microspheres. — We are preparing 2.5 kg of Sphere-Pac fuel for development studies at ANL. A mixed $(U,Pu)O_2$ sol (a total of about 3.5 kg of heavy metal) was blended in lots that contained a total of about 100 to 200 g of heavy metal to obtain a ratio of Pu:(U+Pu) of 0.25; the mixed sols were then converted into dense microspheres. About 65% of the microspheres are to be 350 to 595 μm in diameter; the remainder are to be less than 44 μm in diameter. We have now prepared 1.5 kg of the larger size fraction and 0.5 kg of the smaller size fraction that meet all specifications of homogeneity, uniform texture, and density, and about 0.2 kg of the smaller size fraction has been prepared, but has not yet been fired. All of the material has yet to be blended and have the ratio of O:metal adjusted.

Development of Fabrication Processes

J. D. Sease

Fast reactors that operate at high specific powers will require fuel pins of small diameter with fuel ranging from 80 to 90% of theoretical density and a high fissile loading. Our work is to develop procedures for Sphere-Pac and pelletization and for fabricating irradiation capsules.

Sphere-Pac (R. A. Bradley, W. J. Lackey)

The purpose of this work is to develop techniques for loading fuel pins to specified densities by the Sphere-Pac process. The development is being conducted concurrently with the loading of the fuel pins for the series II irradiation tests in the Experimental Breeder Reactor-II (EBR-II) (ref. 2).

In loading the first seven fuel pins, we observed that, in general, the smear density of the infiltrated bed increased linearly with the density of the coarse bed. There was, however, considerable variation in both the density of the coarse bed and final smear density of the pins loaded from the same batch of microspheres. In addition, we had noticed in previous test loadings[3] that the density of the coarse bed varied as much as 5% between batches, up to 1% between operators, and about 1.5% on duplicate loadings of the same batch by the same operator. These results were not conclusive, however, because the loading conditions were not standardized and the number of loadings was small. Therefore, we performed a statistically designed experiment to determine the source and magnitude of the variation in the density of the coarse bed.

Two riffled samples were obtained from each of 11 batches of microspheres. Two operators loaded each of these 22 samples into a 7-in.-long × 0.222-in.-ID tube in the same manner that the coarse microspheres are loaded into fuel pins. The position of the rod in the vibrator, the amplitude and time of vibration, and the rate of feed were constant. The densities obtained in these test loadings are summarized

in Table 1.1. Based on an analysis of variance of these data, we can draw the following conclusions:

1. We are more than 99% sure that there is a variation between batches.

2. There was not sufficient evidence to indicate a difference between operators.

3. There was not sufficient evidence to indicate a difference between the two samples from a particular batch.

4. The standard deviation describing a single operator's ability to reproduce his work with the same sample of microspheres was 0.40.

Table 1.1. Densities of Coarse Beds Obtained in Test Loading of PUM-13A Microspheres

Batch	Sample	Density of Coarse Bed, % of theoretical		
		Operator 1	Operator 2	Average of Four Loadings for Batch
Feed 1	1	56.88	58.04	57.61
	2	57.75	57.74	
Feed 2	1	59.48	58.40	58.72
	2	58.48	58.50	
Feed 3	1	60.02	59.53	59.73
	2	59.95	59.40	
Feed 4	1	60.71	60.79	60.81
	2	60.86	60.85	
Feed 5	1	60.58	59.66	60.24
	2	60.42	60.30	
Feed 6	1	61.20	60.16	60.65
	2	60.54	60.69	
Feed 7	1	61.34	61.14	61.27
	2	61.27	61.33	
Feed 8	1	61.02	61.34	61.16
	2	61.19	61.07	
Feed 9	1	60.98	61.07	60.92
	2	60.68	60.92	
Feed 10	1	60.90	61.08	61.08
	2	61.15	61.17	
Feed 11	1	61.29	59.97	60.92
	2	61.04	61.35	

As the data in Table 1.1 show, the average values for the densities of the coarse beds loaded from the 11 batches varied from 57.6 to 61.3% of theoretical. We believe that this variation is caused by variations in the densities of the different batches of microspheres.

This experiment shows that the density of the coarse bed from a given batch of microspheres can be reproduced to less than ±1% if the loading conditions are properly controlled. In subsequent experiments, we varied the feed rate and the time and amplitude of vibration, but none of these had a significant effect on the density of the coarse bed.

Since the density of the microspheres has the greatest effect on the density of the coarse bed and thus on the final smear density, it appears that altering the density of the microspheres is the most practical way of controlling the density of Sphere-Pac fuel pins.

Series II Unencapsulated Fuel Pins for Irradiation in the Experimental Breeder Reactor-II (R. A. Bradley, W. J. Leonard, T. B. Lindemer, R. B. Pratt, W. H. Pechin)

We are fabricating 19 unencapsulated fuel pins for irradiation in a 37-pin reactor subassembly shared with Babcock & Wilcox Company. Two spare fuel pins are being fabricated. Each site is responsible for design, fabrication, inspection, shipping, and postirradiation examination of its own fuel pins. Our test pins are fueled with pelletized and Sphere-Pac fuel produced by the sol-gel process.

During the past quarter we have been involved with fuel preparation, qualification and preparation of raw materials, welding development, fabrication and inspection of components and assemblies, and writing of process and quality assurance procedures. Analysis of activities listed by the critical-path schedule indicated that the project was 70% complete at the end of June.

Fuel Preparation. — The series II experiment for irradiation in the EBR-II requires 13 fuel pins loaded with $(U_{0.8},Pu_{0.2})O_2$ (93% enriched U) microspheres by the Sphere-Pac process, 8 fuel pins loaded with sol-gel pellets of the same composition, and 17 archive pins. The design specifies a fuel smear density of 80, 85, or 90% of theoretical for pellet fuel and 80 or 85% of theoretical for Sphere-Pac fuel and a ratio

of O:metal of either 1.940 ± 0.005 or 1.980 ± 0.005. The requirements for these pins were presented previously.[4]

All microspheres for the Sphere-Pac pins were received, examined by α autoradiography and by γ spectroscopy,[5] and found to be uniform in Pu content. After the microspheres had been blended into batches sufficiently large to permit loading all pins of a particular type from a single batch of microspheres, each batch of microspheres was heat treated to obtain the required ratio of O:metal. The ratios of O:metal achieved in these batches are given in Table 1.2.

Table 1.2. Ratio of Oxygen to Metal in $(U,Pu)O_2$ Microspheres

Batch	Desired Ratio O:Metal	Ratio O:Metal After Final Heat Treatment
SP 80C	1.980	1.985
SP 85C	1.980	1.976
SPF	1.980	1.988
SPL 80C	1.940	1.959[a]
SPL 85C	1.940	1.961
SPLF	1.940	b

[a]Preliminary result based on one sample.

[b]Not yet available.

Although the O:metal ratio of the Sphere-Pac fuel with 80 and 85% of theoretical density is 1.96 instead of the 1.94 desired, we have decided to accept this ratio rather than delay the loading of the fuel pins.

The fabrication of the pellets for the EBR-II fuel pins was described previously;[6] however, part of the pellets required heat treatment to reduce the ratio of O:metal to 1.94.

We produced part of the pellets with a low ratio of O:metal by heat treating presintered pellets at 1450°C in a cold-wall furnace with a W

element and Ti getter. The pellets with 85% of theoretical smear density and a portion of the pellets with 80% of theoretical smear density were produced in this manner.

Because of poor process control with this method and because of other demands on the furnace we were using, the work with the getter method was discontinued for the present. We plan to produce the remainder of the pellets with low ratio of O:metal and 80% of theoretical smear density by our usual heat treatment (reduction with Ar–4% H_2 in alumina tube furnaces).

Hardware Qualification. – In addition to 23 satisfactory fuel tubes, 7 additional tubes were taken through the chain of inspection, and 6 tubes satisfactorily met all the requirements. We qualified material for fabrication and inspected about 460 individual hardware components for the 21 fuel pins and 17 archive pins. After final inspection, each necessary component was assembled, packaged, and assigned to a specific fuel or archive tube.

Equipment Fabrication. – We modified the equipment built for calibrating the void volume of fuel pins to adapt it for loading fuel pins to a known volume of He and Xe in a measured ratio. Each fuel element is tagged with a unique mixture of normal and isotopic Xe that can easily be identified by reactor instrumentation to facilitate identifying any fuel elements that might fail during irradiation. This equipment has been used to charge all fuel pins manufactured to date.

Procedures. – All procedures for fabrication processes (except ceramic fuel processes), quality control, testing, and inspection have been prepared. These include (1) loading of fuel, (2) preparation and assembly of nonfuel components, and (3) final assembly and manufacture of the fuel pin. Each detailed operational, quality-assurance, standardization, and test procedure is arranged in a format as auxiliary procedures for use in conjunction with these process procedures.

Manufacture of Fuel Pins. – Nine Sphere-Pac and two pellet pins were loaded, and nine of these were tagged with Xe. The densities achieved in these 11 pins are summarized in Table 1.3. The smear densities of the nine Sphere-Pac fuel pins vary from 82.3 to 84.1% of theoretical. We have been unsuccessful in all our attempts to achieve a smear density of 80% of theoretical; therefore, we will use the fuel

Table 1.3. Densities of Fuel Pins for Series II Irradiation in Experimental Breeder Reactor-II

Fuel Pin	Fuel Pin Type	Smear Density, % of theoretical	
		Design	Measured
19-6-C	Sphere-Pac	80	83.4
19-8-A	Sphere-Pac	80	82.6
19-26-A	Sphere-Pac	85	82.5
19-37-A	Sphere-Pac	85	83.1
19-52-A	Sphere-Pac	85	84.1
19-56-A	Sphere-Pac	85	84.0
19-60-A	Sphere-Pac	85	84.0
19-60-B	Sphere-Pac	85	84.0
19-7-A	Sphere-Pac	85	84.0
19-66-B	Pellet 0.2182	85	86.3
19-76-A	Pellet 0.2182	85	86.1

pins as loaded. The remainder of the fuel pins have the bottom end plug welded to the tube, have been completely inspected to this stage, and are ready for fuel loading, insertion of top hardware components, Xe tagging, and final welding of the top plug and end cap.

We made two weld dummy pins and one Xe dummy pin before we manufactured the fuel pins. We shall make another Xe dummy pin when we have completed manufacturing the 21 pins.

Characterization of $(U,Pu)O_2$ Fuels

C. M. Cox J. D. Sease

The development of sol-gel fuel fabrication requires characterization of both the chemical composition and physical properties of the material to control the process and to interpret meaningfully the irradiation behavior. Thermodynamic studies will contribute to the development of the process for producing the fuel and will aid in predicting fuel performance for both irradiation testing and model studies.

Determination of Pu Content of $(U,Pu)O_2$ Microspheres by Gamma Spectroscopy (R. A. Bradley, W. J. Lackey, W. H. Pechin)

The $(U,Pu)O_2$ microspheres for six of the fuel pins for the series II irradiation in the EBR-II were prepared in 11 batches. Alpha-ray autoradiography showed no large variations in Pu content between microspheres within a batch, but variations of less than about 3% Pu cannot be detected by the technique used.[7] Therefore, γ-ray spectroscopy was used to determine whether there were variations in Pu content between batches or between microspheres within a batch.

Samples were riffled from each batch and analyzed by the technique described previously.[8] The ratios of Pu:(U+Pu) for two individual microspheres from each of the batches are shown in Table 1.4. This table also shows the average value for the two microspheres from each batch and the 95% confidence interval. One microsphere was counted six times to check the standard deviation of the analytical technique; we found it to be 0.465, which compared favorably with the 0.43 determined previously with a larger number of samples.[8]

An analysis of variance was performed to separate the sources of variation and to determine which ones were significant. We can say with 93% confidence that there is a variation in Pu content from batch to batch. Within the limits of detection, there was no variation of Pu content within a batch.

Precision and Source of Variation of Analyses of Ratio of Oxygen to Metal in $(U,Pu)O_2$ (W. J. Lackey, R. A. Bradley, W. H. Pechin, T. L. Hebble[9])

It is generally agreed that the O:metal ratio of $(U,Pu)O_{2\pm x}$ is an important parameter in determining the performance of fuel pins. Thus, to conduct meaningful irradiation tests, it is necessary to be able to fabricate in a reliable manner mixed oxide fuel with a known ratio of O:metal. The purpose of this investigation was to determine the ratio of O:metal for fuel from six sintering runs and at the same time to determine the sources that lead to variations in this ratio and to determine the precision of the gravimetric analytical technique used at ORNL.

We decided that these objectives could best be accomplished by basing the selection and order of submission of samples on a modification

Table 1.4. Plutonium Content of $(U,Pu)O_2$ Microspheres (PUM-13A) as Determined by Gamma-Ray Spectroscopy

Batch	Sample	Ratio Pu:(U+Pu)	
		Measured	Average[a]
		$\times 10^{-2}$	$\times 10^{-2}$
Feed 1	1	21.32	21.08 ± 0.81
	2	20.84	
Feed 2	1	21.08	21.20 ± 0.81
	2	21.31	
Feed 3	1	19.96	19.82 ± 0.81
	2	19.67	
Feed 4	1	20.76	21.03 ± 0.81
	2	21.30	
Feed 5	1	20.50	20.96 ± 0.81
	2	21.42	
Feed 6	1	20.42	20.25 ± 0.81
	2	20.08	
Feed 7	1	20.93	21.18 ± 0.81
	2	21.43	
Feed 8	1	20.93	21.35 ± 0.81
	2	21.77	
Feed 9	1	20.85	20.87 ± 0.81
	2	20.88	
Feed 10	1	21.57	21.71 ± 0.81
	2	21.84	
Feed 11	1	20.96	21.86 ± 0.81
	2	22.77	

[a]Range indicates 95% confidence interval.

of a statistical experimental design called Graeco-Latin Square.[10] The sources of variation investigated were analysis days, position in the analysis furnace, sintering runs, and position in the sintering furnace. By using the Graeco-Latin Square design, it was possible to determine without bias whether the sources of variation listed above influenced the result of the analysis for the ratio of O:metal.

The results of the statistical analysis are summarized in Table 1.5. This analysis of variance showed a large effect associated with analysis

Table 1.5. Analysis of Variance for Determination of Ratio of Oxygen to Metal

Source	Degrees of Freedom	Sum of Squares	Mean Square	Calculated F Value	95% Critical F Value
Analysis days	5	0.00375489	0.00075098[a]	24.54	2.77
Position in analysis furnace	5	0.00007222	0.00001444	0.47	2.77
Sintering runs	5	0.00046856	0.00009371	3.06	2.77
Position in sintering furnace	2	0.00002272	0.00001136	0.37	3.55
Residual	18	0.00055084	0.00003060		
TOTAL	35				

[a]When the calculation was repeated with the results of the bad analysis day excluded, the mean square for analysis days was 0.00004540 with four degrees of freedom.

days and a small but real effect associated with sintering runs. The variation associated with analysis days was almost entirely caused by the analyses for one day all being low by about 0.027 ratio units; the reason for this bias is not definitely known, but weighing errors are suspected. Neither the position in the analysis furnace or the sintering furnace caused a detectable effect.

Confidence intervals for the average ratio of O:metal in a future sintering run are shown in Table 1.6. From these confidence intervals, we conclude that the ratio of O:metal in future sintering runs should be determined by analyzing one sample per sintering run on each of three days. Assuming that days on which biased analyses occur can be detected, the 95% confidence interval for the average of three measurements obtained in this manner would be 0.007 ratio units. A report describing this investigation in detail is being prepared.

As a result of the statistical investigation described above, the Analytical Chemistry Division installed a new balance for determining the ratio of O:metal, and we have been submitting samples from a given sintering run on different days. An analysis of variance on 48 determinations of 19 sintering runs with the old balance and 41 determinations of 17 sintering runs with the new balance disclosed a marked improvement in the precision of the analysis. With the old balance, the standard deviation of the analysis, including variations between pellets and between days, was 0.011 ratio units; with the new balance, the standard deviation is 0.0039 ratio units.

The current method of submitting samples will permit the use of a control chart to detect errors beyond that associated with the variation of the analysis. This chart will be based on the fact that the range in the results of three analyses of the same sintering run should have a normal distribution. Any set of samples for which the range exceeds the 95% confidence interval has probably been affected by human error and will be analyzed again.

Microstructure of Unirradiated $(U,Pu)O_2$ Fuel for Instrumented Tests in the Engineering Test Reactor (W. J. Lackey, R. A. Bradley)

Optical microscopy, replica electron microscopy, and α-ray autoradiography have been used to characterize the microstructure of the

Table 1.6. Confidence Intervals[a] for the Average Ratio of Oxygen to Metal of a Single Sintering Run

Number of Analysis Days	Number of Analyses Per Day	90% Confidence Interval		95% Confidence Interval		99% Confidence Interval	
		Biased Analysis Days Detected	Biased Analysis Days Not Detected	Biased Analysis Days Detected	Biased Analysis Days Not Detected	Biased Analysis Days Detected	Biased Analysis Days Not Detected
1	1	0.010	0.023	0.012	0.029	0.017	0.043
2	1	0.007	0.016	0.009	0.021	0.012	0.030
3	1	0.006	0.013	0.007	0.017	0.010	0.025
1	2	0.008	0.023	0.009	0.028	0.013	0.043
2	2	0.005	0.016	0.007	0.020	0.009	0.030
3	2	0.004	0.013	0.005	0.016	0.007	0.025

[a]The confidence intervals are constructed by subtracting and adding the tabulated uncertainty to the average value of the ratio of O:metal determined for any particular sintering run.

sol-gel $(U_{0.8},Pu_{0.2})O_2$ fabricated for the instrumented tests in the Engineering Test Reactor (ETR). Briefly, all of these tests showed the fuel to be of excellent quality.

Knowledge of the microstructure of the fuel serves three purposes: it helps ensure that high-quality fuel is being fabricated; it reveals information concerning the effect of fabrication variables on the pore morphology and grain size of sol-gel-derived fuel; and it will be used for future comparison with the microstructure of the irradiated fuel.

The fuel examined was in the form of coarse microspheres (batch PM-11C), fine microspheres (batch PM-11F), and a cold-pressed and sintered pellet (batch ET3N). During fabrication, all of the fuel was sintered at 1450°C for 4 hr or longer. Details of the fabrication procedure have been reported elsewhere.[11,12]

Coarse Microspheres. — Both α-ray autoradiography and limited electron microprobe analyses showed the Pu content to be uniform between spheres within the limits of detection, which are estimated as ±4% Pu for autoradiography and ±0.5% Pu for microprobe analysis.

Optical and electron photomicrographs of the coarse microspheres are shown in Fig. 1.1. At magnifications below about 100×, the spheres appeared almost fully dense, but numerous, small, sintering pores were apparent at higher magnifications. In the electron photomicrographs, pores appear as dark areas and cast a light shadow. The quantity of porosity varied from sphere to sphere. The density of the most porous sphere observed in electron photomicrographs was 95.4% of theoretical, while that of the most dense sphere was 99.1% of theoretical; the average density is thought to be 96 to 97% of theoretical.

Nearly all of the porosity in the most porous spheres was located at grain boundaries, but that in the dense spheres was trapped inside the grains.

The grains were fairly equiaxed, and their size was relatively uniform within a sphere; but the grain size varied from sphere to sphere depending on the porosity. The grains of the more porous spheres were about 1.7 μm in diameter, while those of the most dense spheres were 3.2 μm in diameter. A diameter of 2.0 μm is suggested as typical.

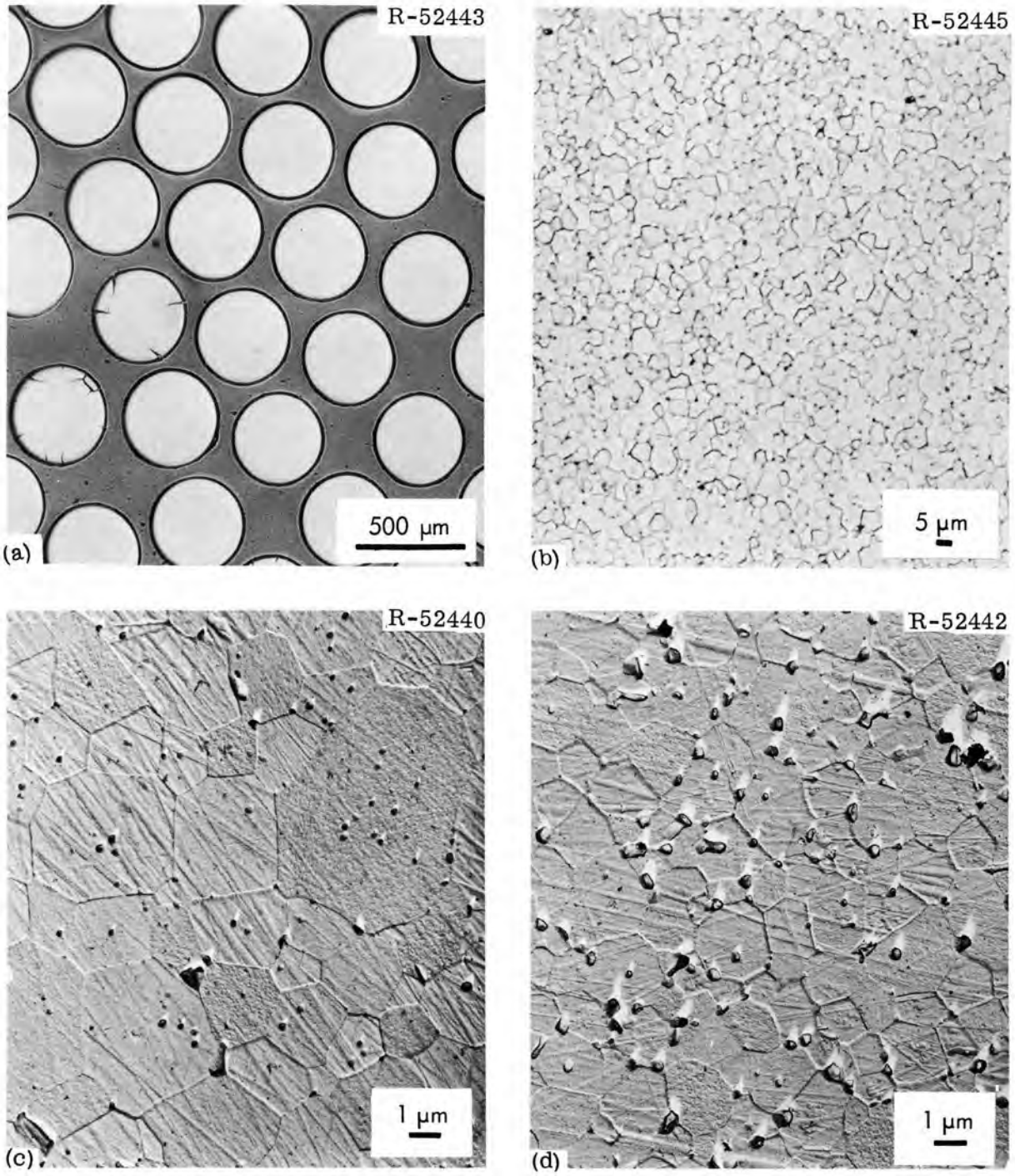

Fig. 1.1. Coarse $(U_{0.8},Pu_{0.2})O_2$ Microspheres for Instrumented Tests in the Engineering Test Reactor. (a) Optical photomicrograph. 35×. (b) Optical photomicrograph of a dense sphere. 500×. (c) Electron photomicrograph of a dense sphere. 4800×. (d) Electron photomicrograph of a porous sphere. 4800×.

Fine Microspheres. – Photomicrographs of the fine microspheres are shown in Fig. 1.2. Because of our inability to separate the shapes of the fine microspheres, this material contained some aspherical particles, but it was considered to be of excellent quality since nearly all of the particles were spherical. Approximately 2 to 4% of the spheres were hollow. Excluding the hollow spheres, electron microscopy showed the spheres to be very dense, perhaps exceeding 99.5% of theoretical.

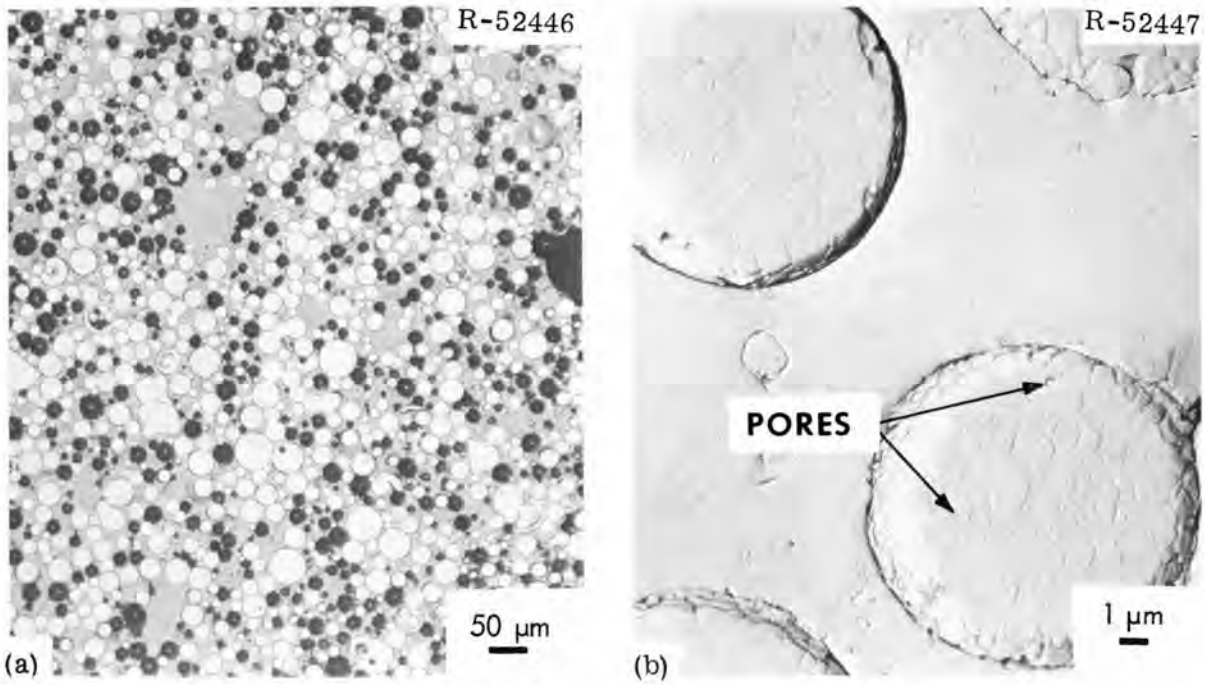

Fig. 1.2. Fine $(U_{0.8},Pu_{0.2})O_2$ Microspheres for Instrumented Tests in the Engineering Test Reactor. (a) Optical photomicrograph. 100×. (b) Electron photomicrograph of typical spheres showing high density and small grain size. 3320×.

The grain size was uniform within a given sphere and varied only slightly from sphere to sphere. The grains of essentially all of the spheres examined were in the range 1.2 ± 0.2 μm in diameter.

The surfaces of both the coarse and fine microspheres were of an "orange peel" texture as a result of grooving along the grain boundaries caused by thermal etching during sintering.

Pellets. – Alpha-ray autoradiography was used to determine if there were any inhomogeneity in the distribution of Pu in the pellets. From the examination of one pellet, it appears that there was no segregation of Pu.

The pellets were 84 ± 1% of theoretical density. On the basis of the amount and morphology of the porosity, there are three different types of microstructure in the pellets as shown in Fig. 1.3. First, there is a very porous matrix containing elongated, irregularly shaped pores interconnected with the surface of the pellet. Dispersed throughout the matrix, there are very dense areas as large as about 40 μm in diameter. Finally, about 5% of the pellet consists of areas frequently as large as 75 μm in diameter and occasionally larger with an intermediate amount of generally spherical porosity that is probably not interconnected with the surface of the pellet. These observations agree with results of analyses by mercury porosimetry that show that nearly all of the porosity is of the open type.

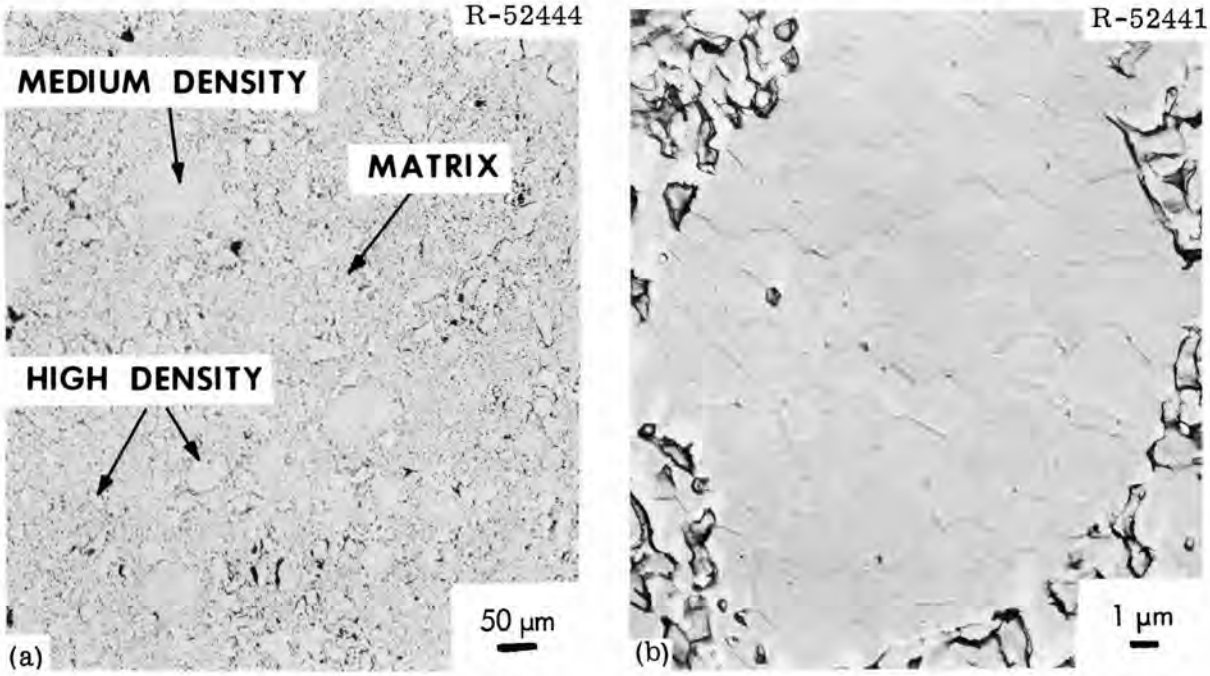

Fig. 1.3. Cold-Pressed and Sintered $(U_{0.8},Pu_{0.2})O_2$ Pellet for Instrumented Tests in the Engineering Test Reactor. (a) Optical photomicrograph. 100×. (b) Electron photomicrograph of an area of high density surrounded by the porous matrix. 3320×.

This triplex microstructure results from the process used to prepare powder for pelletizing. The sol-gel-derived shards are ground to −325 mesh. During the grinding process, the extremely fine fraction of the powder is separated by the collection system from the bulk of −325 mesh material, and the fines are combined. A dense area in the pellet results from the sintering of a single piece of the −325 mesh shard. The large areas with intermediate porosity are thought to result from agglomeration of the extremely finely ground material. The porous matrix consists of a mixture of the −325 mesh material and fines. Some of the matrix porosity undoubtedly results from the shrinkage necessary to form the very dense areas.

The grains in the dense areas varied from 1 to 2 μm in diameter, with 1.7 μm being typical. The grain size of the matrix was difficult to measure, because of the shadows cast by the numerous pores, but was slightly less than that of the dense areas. The grains in the areas formed by agglomeration of the fines were about 0.8 μm in diameter. If it becomes necessary in some future analysis to characterize the pellets by a single grain size, the value 1.5 μm is recommended. A report describing this work in greater detail is being prepared.

Irradiation Testing of $(U,Pu)O_2$ Fuels

C. M. Cox

The performance characteristics of mixed $(U,Pu)O_2$ fuels are being evaluated in a variety of irradiation tests for potential application in an LMFBR. We are now concentrating on comparative tests of sol-gel fuel fabricated as pellets or as microspheres and then compacted by the Sphere-Pac technique. The program includes thermal-flux experiments, which permit use of instrumented capsules and the achievement of high levels of burnup in relatively short times, and fast-flux experiments, in which the distribution of fission rate and the effects of radiation on the cladding are more typical of those for operating conditions anticipated in an LMFBR.

Uninstrumented Thermal-Flux Irradiation Tests (A. R. Olsen, D. R. Cuneo[13])

A series of uninstrumented capsules is being irradiated in the X-basket facilities of the ETR. Each capsule contains four test pins arranged in tandem. The initial objective of these tests was to investigate the effects of fabrication form with extended burnup on the release of fission gas, migration of fission products, and fuel swelling. Some capsules are now being irradiated specifically to provide short-cooled irradiated fuel for studies of LMFBR fuel reprocessing. The results from the first three capsules irradiated to low burnup in this series were discussed.[14] The current status of all the tests in this series is given in Table 1.7.

Experiment 43-113, the only capsule now being irradiated, was removed temporarily from the reactor because of an apparent change in the flux distribution in the ETR after the Be reflector was replaced after cycle 106. Rather than risk overpowering this experiment, we removed it until new flux monitoring data are available sometime in August.

The normal postirradiation examination of capsules 43-103 and 43-115 was completed during the past quarter. A report on these capsules will be presented at the American Nuclear Society Annual Meeting.[15] Data describing the eight pins from these capsules are given in Table 1.8. Figures 1.4 to 1.6 are composite pictures showing the autoradiographs with the comparable photomacrographs for two UO_2 fuel pins and one $(U,Pu)O_2$ fuel pin. Two interesting phenomena have been observed in the autoradiographic examinations.

The β-γ autoradiograph for the UO_2 pellet pin (Fig. 1.4) shows only a faint concentric-ring pattern of varying activity. Such patterns are often used to define the extent of melting of the fuel center.[16,17] The fact that this structure was not distinct indicates that even though the heat ratings and gamma scans[18] indicated melting of the fuel center, this condition did not exist during the latter stages of the irradiation. Even these faint rings were not seen on the comparable Sphere-Pac UO_2 pins shown in Fig. 1.5 or the Sphere-Pac $(U,Pu)O_2$ pin that operated at the highest heat rate, shown in Fig. 1.6.

Table 1.7. Uninstrumented Thermal-Flux Tests of $(U,Pu)O_2$ Fuels

Experiment	Fuel		Number of Pins	Peak Burnup (% FIMA)[a]	Peak Linear Heat Rate (w/cm)	Peak Temperature at Inner Surface of Cladding (°C)	Status June 1970
	Form	Composition					
43-99	Sphere-Pac	$(^{235}U_{0.80},Pu_{0.20})O_{2.00}$	2	1.5[b]	1640[b]	1000	Examined
43-100	Sphere-Pac	$(^{235}U_{0.80},Pu_{0.20})O_{2.00}$	2	1.4[b]	1470[b]	900	Examined
43-103	Sphere-Pac Pellet	$UO_{2.02}$ (20% ^{235}U) $UO_{2.00}$ (20% ^{235}U)	3 1	5	690	530	Examined
43-112	Sphere-Pac	$(^{238}U_{0.85},Pu_{0.15})O_{1.97}$ $UO_{2.02}$ (20% ^{235}U)	3 1	0.7	500	360	Examined
43-113	Sphere-Pac	$(^{238}U_{0.85},Pu_{0.15})O_{1.97}$ $UO_{2.02}$ (20% ^{235}U)	3 1	10[c]	500[c]	380[c]	In-reactor ≅ 9.7% FIMA
43-115	Sphere-Pac	$(^{238}U_{0.85},Pu_{0.15})O_{1.97}$ $UO_{2.02}$ (20% ^{235}U)	3 1	6.5	600	460	Examined
43-116	Sphere-Pac	$(^{238}U_{0.85},Pu_{0.15})O_{1.97}$	4	1.5[c]	600[c]	460[c]	Processed
43-117	FTR Pellets	$(^{238}U_{0.75},Pu_{0.25})O_{1.98}$	4	1.5	430[c]	360[c]	In preparation
43-118	FTR Pellets	$(^{238}U_{0.75},Pu_{0.25})O_{1.98}$	4	4.0	430[c]	360[c]	In preparation
43-119	FTR Pellets	$(^{238}U_{0.75},Pu_{0.25})O_{1.98}$	4	8.0	430[c]	360[c]	In preparation
43-123	FTR Pellets	$(^{238}U_{0.75},Pu_{0.25})O_{1.98}$	4	4.0	350[c]	310[c]	In preparation

[a] FIMA is fissions per initial actinide metal atom.

[b] Pins failed in reactor from overpowering.

[c] These are target design values.

Table 1.8. Fabrication and Operating Data for Intermediate Burnup Tests

Test Pin	Smear Density (% of theoretical)	Fuel Form[a]	Fuel Composition	Peak Linear Heat Rate[b] (kw/ft)	Peak Temperature at Inside Surface of Cladding (°C)	$\int_{400°C}^{\text{Fuel Center}} k\,dt$ (w/cm)	Peak Burnup (% FIMA)[c]	Days at Equivalent Full Power	Fission Gas Released (% ^{85}Kr)
103-1	74	SP	$UO_{2.02}$	16.4	380	34	4.2	126.3	30
103-2	84	P[c]	$UO_{2.02}$	25.9	540	64	4.9	126.3	47
103-3	73	SP	$UO_{2.02}$	21.6	470	44	5.5	126.3	44
103-4	74	SP	$UO_{2.02}$	17.9	400	38	4.5	126.3	41
115-1	80	SP	$(U_{0.85},Pu_{0.15})O_{1.97}$	18	400	40	5.6	174.2	36
115-2	74	SP	$UO_{2.02}$	17.0	390	31	5.9	174.2	47
115-3	82	SP	$(U_{0.85},Pu_{0.15})O_{1.97}$	20.6	460	46	6.5	174.2	44
115-4	81	SP	$(U_{0.85},Pu_{0.15})O_{1.97}$	13.4	370	32	4.2	174.2	38

[a] SP = Sphere-Pac; P = solid pellet.

[b] Time-averaged values based on the total exposure in equivalent full power days and an energy release of 177 Mev/fission.

[c] FIMA = fissions per initial actinide metal atom.

[d] Four mil average cold diametral gap between fuel and cladding.

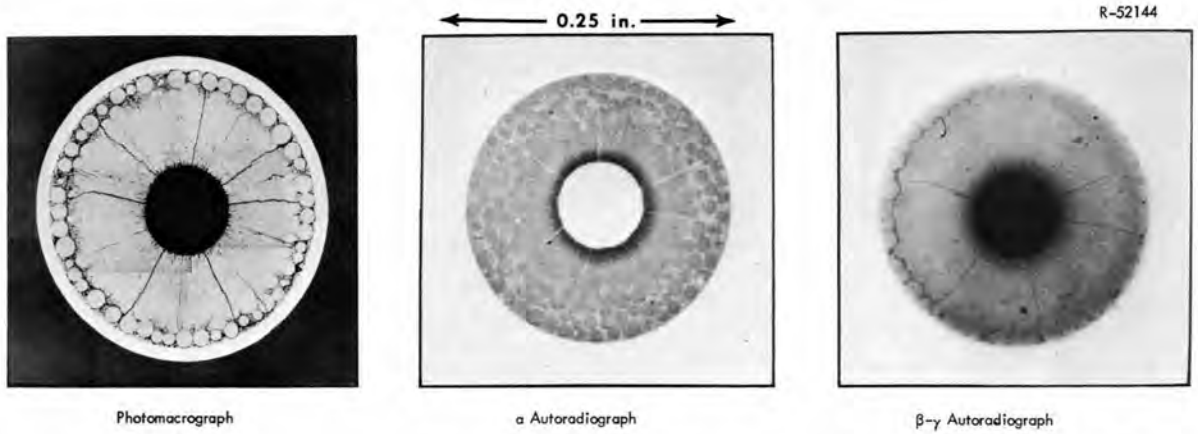

Fig. 1.4. Sphere-Pac $(U_{0.85},Pu_{0.15})O_{1.97}$ Irradiated at 14 kw/ft to 4.2% FIMA (Smear Density 81% of Theoretical).

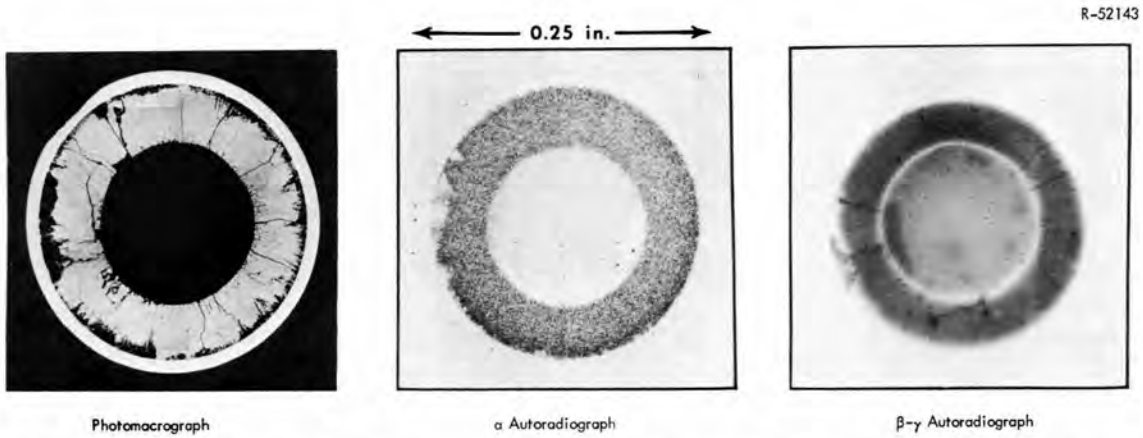

Fig. 1.5. Sphere-Pac UO_2 (20% Enriched) Irradiated at 21 kw/ft to 5.9% FIMA (Smear Density 74% of Theoretical).

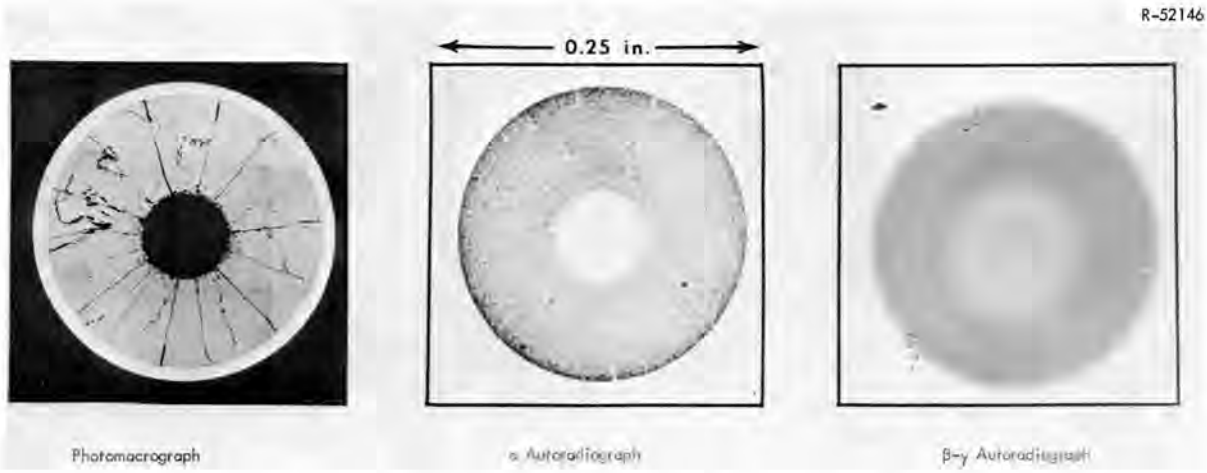

Fig. 1.6. Pelletized UO_2 (20% Enriched) Irradiated at 26 kw/ft to 4.9% FIMA (Smear Density 84% of Theoretical).

One of the most striking features of the autoradiographs was the spherical islands of higher Pu content in the cooler, peripheral areas of the columnar grains of all three $(U,Pu)O_2$ pins, as shown in the α-ray autoradiograph of Fig. 1.6. The appearance of the α-ray autoradiographs supports the vaporization-condensation theory of restructuring without melting in the region of columnar grain growth. The various modes of restructuring under consideration have been discussed in detail.[19] Briefly, for the $(U,Pu)O_2$ fuels, the vapor has a higher concentration of U (ref. 20). The movement of this vapor down the radial temperature gradient in the fuel leaves a higher concentration of Pu near the central void and reduces the relative concentration of Pu in the condensing area near the periphery of the region of columnar grains. These variations are shown by the relative α activities in the autoradiograph made after irradiation. The autoradiographs from these test pins also indicate fuel homogenization in the region of intermediate temperature near the central void. However, at the temperatures near the periphery of the region of columnar grains, even during 4000 hr of operation at power, the diffusion rates are too slow to homogenize the fuel in the large-diameter spheres with the surrounding condensate and fine microspheres. This phenomenon will be investigated more thoroughly with electron microscopy and microprobe analysis.

All hardware and fuel for capsules 43-117, 43-118, 43-119, and 43-123 is on hand. The capsule fabrication is about 50% complete; the performance and safety analyses have been finished; and irradiation will start during the first quarter of next year.

Instrumented Tests in the Oak Ridge Research Reactor (R. B. Fitts, V. A. DeCarlo,[21] D. R. Cuneo[13])

The instrumented irradiations in the Oak Ridge Research Reactor[22] (ORR) are designed[23] to monitor the thermal performance of test fuel pins. The temperatures of the cladding and fuel center and the rates of heat generation are continuously measured and recorded. These data are being used to evaluate the thermal characteristics of various fuels in-reactor and the effects of irradiation conditions upon the temperatures and rates of structural change within the operating fuels.

The irradiation of the third capsule in this series, SG-3, was completed. This capsule contains one fuel pin of $(U_{0.8},Pu_{0.2})O_2$ Sphere-Pac[24] fuel with a smear density of 82% of theoretical and a second fuel pin with 83.5% dense sol-gel pellet[25] fuel of the same composition and smear density. This experiment provided a direct comparison of these fuels to temperatures near 2000°C at the center of the fuel.

The temperatures of the cladding, NaK, and fuel center were reported[26] after about 60 days of operation of the experiment. The central temperatures measured in both fuels were consistent with calculated temperatures based upon the thermal conductivity given by Bailey et al.[27] for pellet fuel of the same density.

The irradiation of capsule SG-3 was successfully terminated on March 26, 1970. The Cd shield installed around the lower fuel pin (pellet) maintained the peak temperature at the center of the fuel in this pin at less than 600°C during the last reactor cycle, while the center of the fuel in the upper pin (Sphere-Pac) operated at 2000°C. The data obtained for the Sphere-Pac fuel during the final power reduction are plotted in Fig. 1.7. These results are compared with similar data obtained midway in the test and with the calculated relationship between temperature and rate of heat generation for a pellet fuel of comparable initial density. Despite the shift in the observed

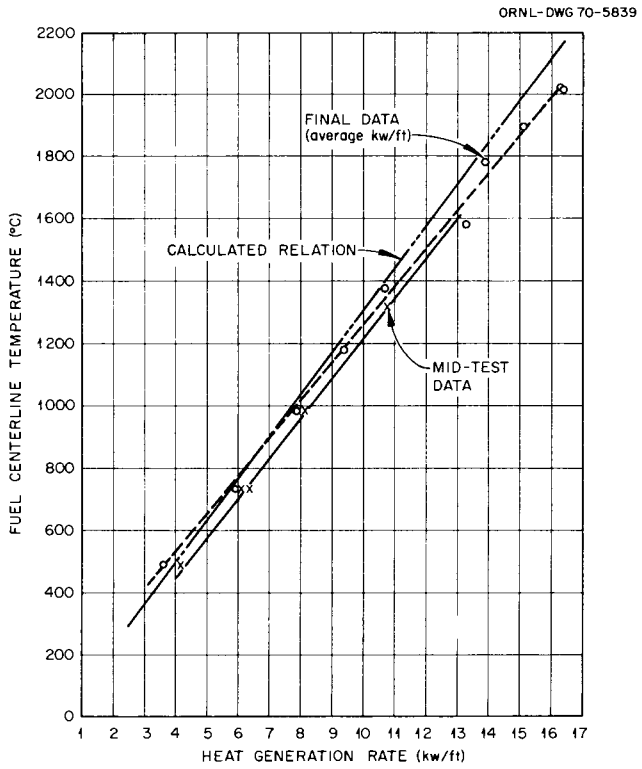

Fig. 1.7. Central Temperature of Sphere-Pac Fuel Versus Rate of Heat Generation.

relationship between heat generation and temperature over the course of the experiment, the measured and predicted temperatures remained within ±8% of each other. The shift that was observed and the detailed analysis of these data indicate that a few of the thermocouples drifted slightly. A final, detailed analysis of the data will be made to verify that the Sphere-Pac and pellet fuels have essentially the same effective thermal conductance during irradiation at low burnup.

The capsule is located in the ORR pool awaiting inspection by neutron radiography. After neutron radiography, the SG-3 experiment will be sent to the High Radiation Level Examination Laboratory for examination.

Instrumented Tests in Engineering Test Reactor (C. F. Sanders)

Two instrumented capsules (43-120 and 43-121) were constructed to investigate fuel swelling and the chemical interaction of fuel and cladding of Sphere-Pac and pellet fuels under peak LMFBR conditions.

These capsules were inserted into the ETR during cycle 107 (May 1970). Design parameters were previously reported.[28] The present operating conditions with the reactor at full power for these capsules are listed in Table 1.9.

Table 1.9. Operating Conditions for Capsules 43-120 and 43-121 in the Engineering Test Reactor

Pin Number	Thermocouple Number	Temperature of Inner Surface of Cladding (°C)	Heat Rate (kw/ft)
43-120-1	1	595	16.0
	2	575	15.4
43-120-2	3	625	17.0
	4	630	17.2
43-120-3	5	595	16.0
	6	545	14.5
43-120-4	7	440	11.0
	8	380	9.5
43-121-1	1	545	14.5
	2	545	14.5
43-121-2	3	565	15.0
	4	610	16.4
43-121-3	5	475	12.1
	6	a	a
43-121-4	7	407	10.0
	8	407	10.0

[a]Inoperative thermocouple; lost during shipment.

Transient Tests (E. J. Manthos, D. R. Cuneo[13])

Six fuel pins containing unirradiated sol-gel-derived $(U_{0.80},Pu_{0.20})O_{1.98}$ were subjected to power transients at the Transient Reactor Test Facility (TREAT). No failures occurred even though two Sphere-Pac pins received a transient that probably melted 50 to 60% of the fuel.

Design, operating conditions, postirradiation neutron radiographs, profilometry, and analyses of plenum gas were previously described.[29,30] Destructive examination of the fuel pins is in progress.

The fuel burnup determined by radiochemical and activation analytical techniques are summarized in Table 1.10. These data are transformed to values for power and energy release in Table 1.11. Although capsule TR-2 was subjected to a more severe transient, the cumulative burnups of capsule TR-1 were higher because of a calibration transient before test.

Metallography was completed for the three fuel pins in capsule TR-2, and typical results for fuel pin TR-2B are shown in Figs. 1.8 to 1.10. Figure 1.8 is a transverse cross section from 3/4 in. below the midplane of the fuel. The columnar grains are believed to have formed during cooling from a molten state, which included about 50 vol % of the fuel at this cross section. The interface between fuel and cladding after etching is shown at higher magnification in Fig. 1.9. Figure 1.9 shows appreciable grain growth even in the peripheral spheres and evidence of a localized hot spot on the inner surface of the cladding. We believe that the hot spot followed from a coarse microsphere being pressed against the cladding as the molten fuel expanded about 10%. During cooling, the fuel sintered and pulled away from the cladding, thus leaving the gap shown in Fig. 1.8.

Another interesting phenomenon is shown in Fig. 1.10, which is a longitudinal section taken 1 1/2 to 2 1/2 in. above the midplane of the fuel column. In this figure the circular surfaces along the axis of the central void are surfaces of large gas bubbles formed from the release of gases adsorbed from the molten fuel. Note that the gas bubbles seem to propagate both upward and downward.

Fast-Flux Irradiation Tests (A. R. Olsen)

The fast-flux irradiation tests in the EBR-II are designed to approximate conditions to be encountered in a commercial-scale LMFBR. The objective of these tests is to establish the effects of fuel fabrication form (Sphere-Pac or pellet), void distribution, and stoichiometry on the swelling of the fuel, mechanical and chemical interactions of

Table 1.10. Summary of Burnup Data for Fuel Pins Irradiated in Transient Reactor Test Facility

Fuel Pin	Distance From Top Capsule Flange (in.)	Burnup, as Determined by Indicated Method, % FIMA[a]							
		^{95}Zr	^{106}Ru	^{141}Ce	^{103}Ru	^{60}Co (interior)[b]	^{60}Co (exterior)[b]	Average	95% Confidence Interval
		$\times 10^{-6}$	$\times 10^{-6}$	$\times 10^{-6}$	$\times 10^{-6}$	$\times 10^{-6}$	$\times 10^{-6}$	$\times 10^{-6}$	$\times 10^{-6}$
TR-1A	56.7					4.40	3.98	4.19	±0.34
TR-1B	46.3	3.54	3.59	4.30	4.60	4.24	4.24	4.08	±0.21
TR-1C	33.6	2.60	3.04	2.65	4.02	3.49	3.17	3.16	±0.21
TR-2A	58.4	2.59	3.12	3.53	3.68	3.31	3.45	3.29	±0.21
TR-2B	46.8	2.65	3.00	3.57	4.25	3.16	3.42	3.34	±0.21
TR-2C	34.7					2.25	2.36	2.30	±0.34

[a] FIMA = fissions per initial actinide metal atom.

[b] Preliminary values.

Table 1.11. Summary of Power and Energy Release[a] Data for Fuel Pins Irradiated in Transient Reactor Test Facility

	Fuel Pin					
	TR-1A	TR-1B	TR-1C	TR-2A	TR-2B	TR-2C
Fuel fabrication form[b]	P	S	P	S	S	P
Fuel smear density, % of theoretical	88.9	80.9	79.7	82.0	80.9	80.2
Linear heat rate at 1 w reactor power,[c] w/cm × 10^5	2.86	2.50	1.91	2.85	2.64	1.70
Reactor integrated power, Mwsec	140	140	140	172	172	172
Reactor peak power, Mw	202	202	202	202	202	202
Fuel pin peak linear heat rate,[c] kw/ft	176	154	118	175	162	105
Fuel energy release,[c] cal/g	390	375	291	518	487	316

[a]Based on an energy release of 180 Mev/fission.

[b]P = solid pellets; S = Sphere-Pac microspheres.

[c]At the midplane of the fuel column.

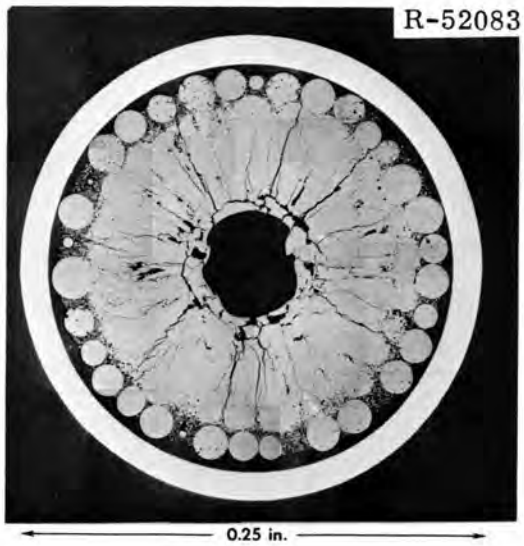

Fig. 1.8. Transverse Cross Section of Sphere-Pac Fuel Pin TR-2B. About 10×.

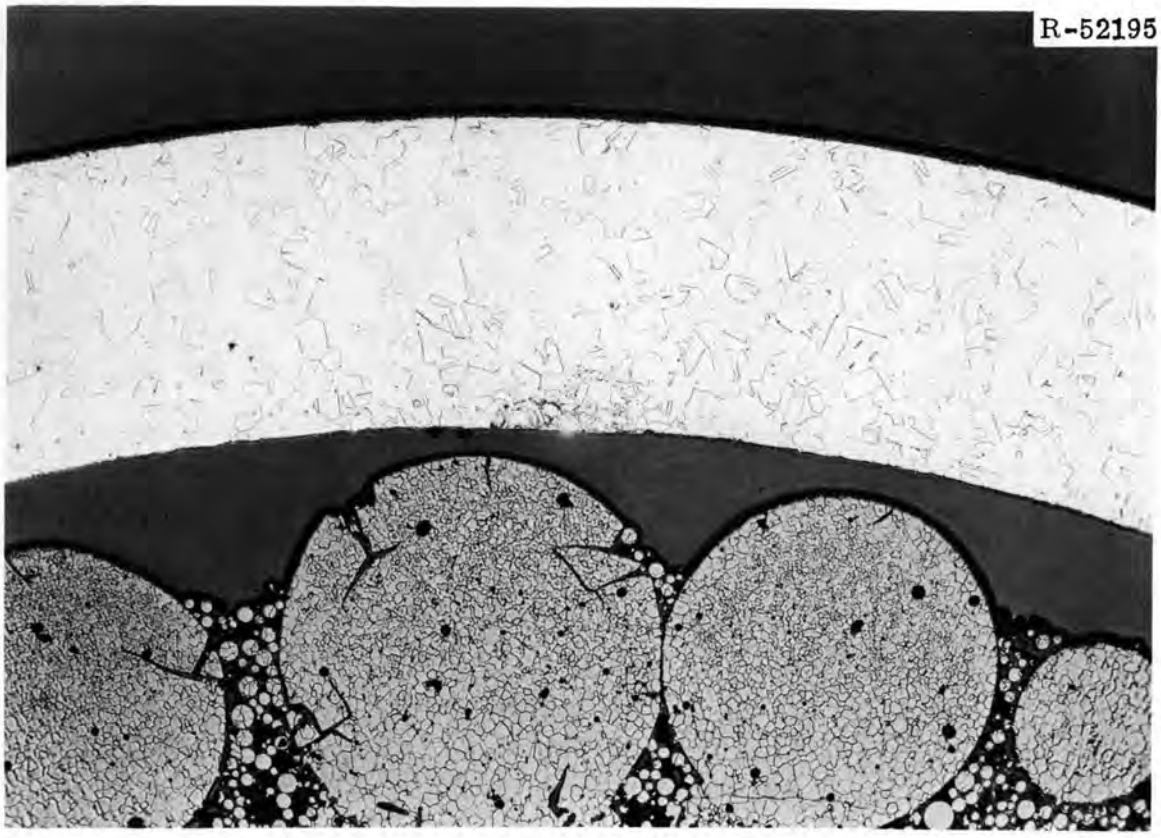

Fig. 1.9. Transverse Cross Section of Sphere-Pac Fuel Pin TR-2B. About 100×.

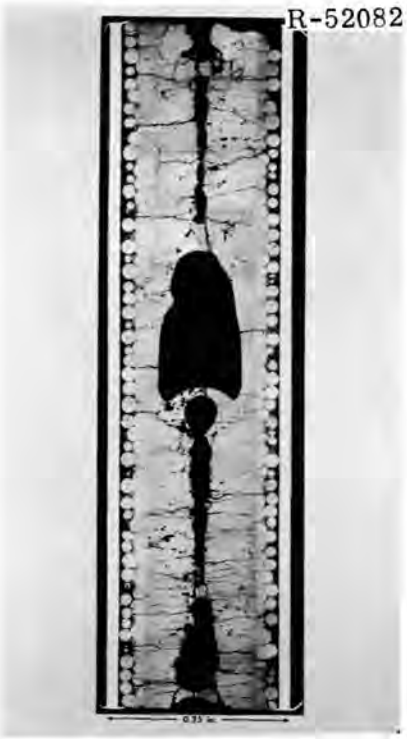

Fig. 1.10. Longitudinal Section of Sphere-Pac Fuel Pin TR-2B. About 4×.

fuel and cladding, release of fission gas, and distribution of fission products in a $(U,Pu)O_2$ fuel operating at typical heat rates to design levels of burnup.

The five series I encapsulated pins, all containing Sphere-Pac $(^{235}U_{0.8},Pu_{0.2})O_2$, were removed from the reactor with subassembly X050 at the end of cycle 42. The initial irradiation period was extended so that a calculated peak burnup of 6.2% fissions per initial actinide metal atom (FIMA) was achieved. The calculated burnup level for all pins is given in Table 1.12. Two of these pins will be returned to ORNL in July after neutron radiographs have been made; the other three are scheduled to be reinserted in a new subassembly for continued irradiation to a peak burnup of 11.8% FIMA. This additional burnup was approved so that these pins could serve as lead experiments for the series II tests. A revised safety analysis for this extended exposure was submitted to the EBR-II experiment manager.

Table 1.12. Calculated Burnup Levels for Series I Sphere-Pac $(U_{0.8},Pu_{0.2})O_{1.98}$ Capsules in Experimental Breeder Reactor-II

Capsule Identity	Type Stainless Steel Cladding	Fuel Smear Density (% of theoretical)	Peak Linear[a] Heat Rate (kw/ft)	Peak Temperature at Inner Surface of Cladding (°C)	Peak Burnup, % FIMA[b]	
					Current[c]	Target
S-1-A	304	83	12	500	4.6	4.6
S-1-B	304	86	15	580	5.6	5.6
S-1-C	316	83	15	580	6.2	11.8
S-1-D	316	80	14	540	5.7	11.8
S-1-E	316	82	14	540	5.6	11.8

[a]Calculated with EBR-II fission rates.

[b]FIMA = fissions per initial actinide metal atom.

[c]Calculated through EBR-II cycle 42.

The series II tests are unencapsulated pins to be irradiated in a 37-pin subassembly to be shared with pins fabricated by Babcock & Wilcox Company. Both Sphere-Pac and pellet fuel derived from the sol-gel process are included in the ORNL test series. These tests are coordinated with those of Babcock & Wilcox Company to provide comparative tests of a variety of fuel forms, densities, and ratios of O:metal. A preliminary subassembly layout (Fig. 1.11) and reactor test location were established. The fuel pin descriptions, assignments of pin positions, and proposed operating conditions are listed in Table 1.13.

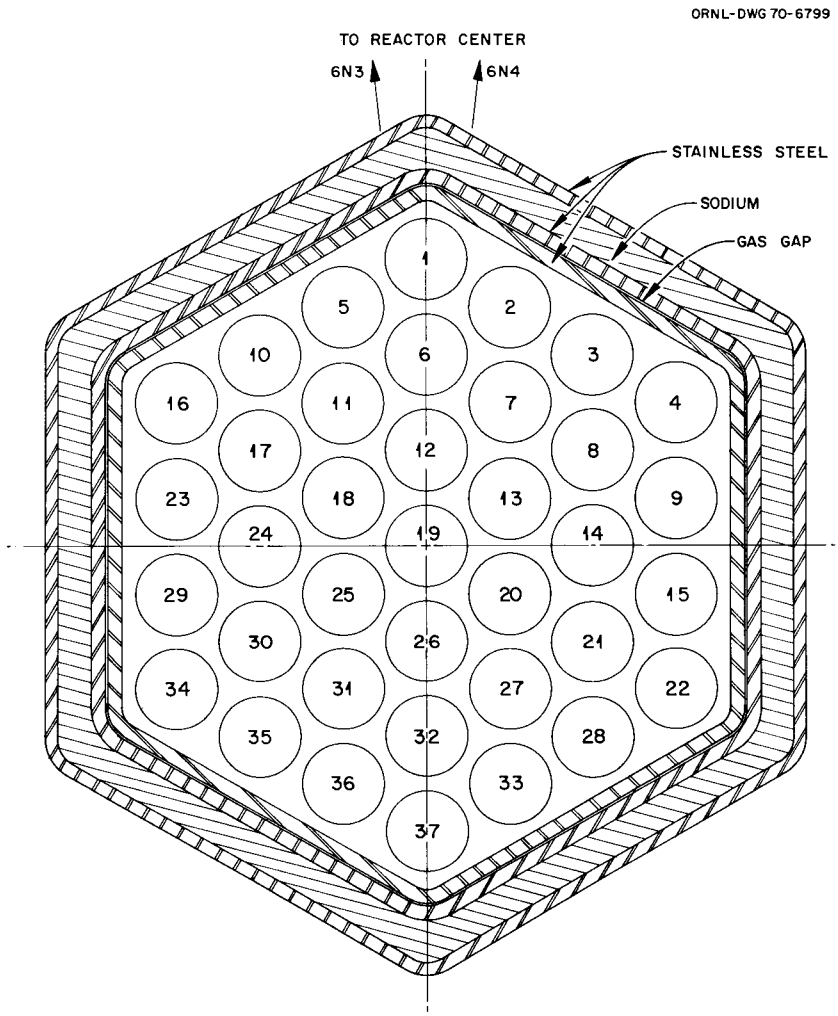

Fig. 1.11. Cross Section of J-37 Subassembly with Numbers Identifying Locations for Placement of Pins for ORNL Series II and Babcock & Wilcox Company Test Irradiations.

Table 1.13. Preliminary Assignments of Pin Positions

Subassembly Location	Pin Identification	Sponsor[a]	Fuel Type[b]	Smear Density (% of theoretical)	Peak Linear Heat Rate (w/cm)	Peak Linear Heat Rate (kw/ft)	Fission Heat Generation[c] (kw)	Peak Target Burnup (% FIMA)[d]
1	OS-1	ORNL	SP	80	450	13.7	13.8	6.0
2	OP-7	ORNL	PELL	80	450	13.6	13.7	12.7
3	OS-4	ORNL	SPL	80	440	13.4	13.5	5.9
4	OS-9	ORNL	SP	84–86	460	14.0	14.1	13.0
5	OS-11	ORNL	SPL	80	450	13.6	13.7	12.7
6	OS-8	ORNL	SP	80	440	13.4	13.5	12.5
7		B & W	VP	81–83	450	13.7	13.8	12.8
8		B & W	SP	81–83	440	13.5	13.6	8.7
9	OP-5	ORNL	PEL	84–86	450	13.6	13.7	12.7
10	OP-3	ORNL	PELL	80	440	13.4	13.5	5.9
11		B & W	SP	81–83	450	13.7	13.8	12.8
12		B & W	VP	81–83	440	13.5	13.6	8.7
13	OS-2	ORNL	SP	84–86	450	13.6	13.7	6.0
14	OS-6	ORNL	SP	84–86	440	13.4	13.5	8.6
15		B & W	VP	81–83	420	12.9	13.0	8.3
16		B & W	PEL	81–83	450	13.7	13.8	12.8
17		B & W	PEL	81–83	440	13.5	13.6	8.7
18	OS-12	ORNL	SPL	84–86	450	13.6	13.7	12.7
19	OS-7	ORNL	SP	84–86	440	13.4	13.5	8.6
20		B & W	SP	81–83	420	12.9	13.0	8.3

Table 1.13. Continued

Subassembly Location	Pin Identification	Sponsor[a]	Fuel Type[b]	Smear Density (% of theoretical)	Peak Linear Heat Rate (w/cm)	Peak Linear Heat Rate (kw/ft)	Fission Heat Generation[c] (kw)	Peak Target Burnup (% FIMA)[d]
21		B & W	SP	81–83	420	12.7	12.8	5.6
22	OP-4	ORNL	PELL	84–86	420	12.8	12.9	5.6
23	OS-10	ORNL	SP	84–86	450	13.6	13.7	12.7
24		B & W	SP	81–83	430	13.1	13.2	12.2
25		B & W	SP	81–83	420	12.9	13.0	8.3
26		B & W	VP	81–83	420	12.7	12.8	5.6
27	OS-3	ORNL	SP	84–86	420	12.8	12.9	5.6
28		B & W	SP	81–83	400	12.3	12.4	11.5
29		B & W	PEL	81–83	420	12.9	13.0	8.3
30		B & W	PEL	81–83	420	12.7	12.8	5.6
31	OS-5	ORNL	SPL	84–86	420	12.8	12.9	5.6
32		B & W	VP	81–83	400	12.3	12.4	11.5
33	OP-2	ORNL	PEL	90	430	13.1	13.2	5.8
34	OP-1	ORNL	PEL	84–86	420	12.8	12.9	5.6
35		B & W	PEL	81–83	400	12.3	12.4	11.5
36	OP-6	ORNL	PEL	90	430	13.1	13.2	12.2
37		B & W	VP	81–83	390	11.9	12.0	11.1

[a] ORNL = Oak Ridge National Laboratory; B & W = Babcock & Wilcox Company.

[b] VP = Vi-Pac; SP = Sphere-Pac; SPL = Sphere-Pac, ratio of O:metal = 1.95; PEL = pellet; PELL = pellet, ratio O:metal = 1.95.

[c] Assuming nominal density fuel and the subassembly located in a 6N3 or 6N4 position with the EBR-II operating at 62.5 Mw.

[d] FIMA = fissions per initial actinide metal atom.

These conditions were used to establish preliminary flow characteristics for the subassembly. The criterion for this design is a peak calculated temperature of 650°C (1200°F) at the inner surface of the cladding. Since the subassembly design is new and no details on flow are available, we submitted our preliminary calculations to ANL for comment. We are continuing with the necessary calculations for the data package. On May 28 we met with personnel from Babcock & Wilcox Company and established a schedule for this subassembly. The data package is scheduled for completion in August. Details of the fabrication status are reported elsewhere.[2]

Notes

1. Chemical Technology Division.
2. R. A. Bradley, W. J. Leonard, T. B. Lindemer, R. B. Pratt, and W. H. Pechin, "Series II Unencapsulated Fuel Pins for Irradiation in the Experimental Breeder Reactor-II," pp. 7–10 this report.
3. R. A. Bradley, Fuels and Materials Development Program Quart. Progr. Rept. March 31, 1970, ORNL-4560, pp. 6–7.
4. R. B. Pratt and R. A. Bradley, Fuels and Materials Development Program Quart. Progr. Rept. March 31, 1970, ORNL-4560, p. 12.
5. R. A. Bradley, W. J. Lackey, and W. H. Pechin, "Determination of Pu Content of $(U,Pu)O_2$ Microspheres by Gamma Spectroscopy," p. 11, this report.
6. R. A. Bradley, Fuels and Materials Development Program Quart. Progr. Rept. March 31, 1970, ORNL 4560, pp. 7–11.
7. R. A. Bradley and W. H. Pechin, Fuels and Materials Development Program Quart. Progr. Rept. March 31, 1970, ORNL-4560, pp. 15–18.
8. R. A. Bradley, W. J. Lackey, and W. H. Pechin, Fuels and Materials Development Program Quart. Progr. Rept. March 31, 1970, ORNL-4560, pp. 19–22.
9. Mathematics Division.
10. R. Lowell Wine, Statistics for Scientists and Engineers, Prentice-Hall, Inc., Englewood Cliffs, N.J., 1964.

11. R. A. Bradley and W. H. Pechin, Fuels and Materials Development Program Quart. Progr. Rept. Dec. 31, 1969, ORNL-4520, pp. 7–16.

12. R. A. Bradley and W. H. Pechin, LMFBR Fuel Cycle Studies Progr. Rept. December 1969, No. 10, ORNL-TM-2819, p. 61.

13. On loan from Reactor Chemistry Division.

14. A. R. Olsen, C. M. Cox, and R. B. Fitts, Trans. Am. Nucl. Soc. 12(2), 605–606 (November 1969).

15. A. R. Olsen, Trans. Am. Nucl. Soc. 13(1), 32 (June 1970).

16. J.A.L. Robertson et al., J. Nucl. Mater. 7(3), 225–262 (1962).

17. J. A. Christensen, Stoichiometry Effects in Oxide Fuels – 1. Power Rating Required for Melting and Oxygen Redistribution in Molten Center $UO_{2\pm x}$ Fuels, BNWL-536 (December 1967).

18. A. R. Olsen, R. B. Fitts, J. Komatsu, and C. M. Cox, Metals and Ceramics Div. Ann. Progr. Rept. June 30, 1969, ORNL-4470, pp. 134–136.

19. A. R. Olsen, R. B. Fitts, and J. Komatsu, Fuels and Materials Development Program Quart. Progr. Rept. Sept. 30, 1968, ORNL-4350, pp. 22–25.

20. T. L. Markin and M. H. Rand, Some Thermodynamic Aspects of $(U,Pu)O_2$ Solid Solutions and Their Use as Nuclear Fuels, AERE-R 5560 (August 1967).

21. Reactor Division.

22. D. B. Trauger, Some Major Fuel Irradiation Test Facilities of the Oak Ridge National Laboratory, ORNL-3574 (April 1964).

23. R. B. Fitts and V. A. DeCarlo, Fuels and Materials Development Program Quart. Progr. Rept. June 30, 1968, ORNL-4330, pp. 20–23.

24. F. G. Kitts, R. B. Fitts, and A. R. Olsen, "Sol-Gel Urania-Plutonia Microsphere Preparation and Fabrication into Fuel Rods," pp. 195–210 in Intern. Symp. Plutonium Fuels Technol., Scottsdale, Ariz., 1967, Nucl. Met. 13, ed. by K. E. Horton, R. E. Macherey, and R. J. Allio, American Institute of Mining, Metallurgical and Petroleum Engineers, New York, 1968.

25. R. A. Bradley, Fuels and Materials Development Program Quart. Progr. Rept. Sept. 30, 1969, ORNL-4480, pp. 7–8.

26. R. B. Fitts, V. A. DeCarlo, K. R. Thoms, and D. R. Cuneo, Fuels and Materials Development Program Quart. Progr. Rept. March 31, 1970, ORNL-4560, pp. 26–30.

27. W. E. Bailey, E. A. Aitkin, R. R. Asamoto, and C. N. Craig, "Thermal Conductivity of Uranium-Plutonium Oxide Fuels," pp. 293–308 in Intern. Symp. Plutonium Fuels Technol., Scottsdale, Ariz., 1967, Nucl. Met. 13, ed. by K. E. Horton, R. E. Macherey, and R. J. Allio, American Institute of Mining, Metallurgical and Petroleum Engineers, New York, 1968.

28. C. F. Sanders, Fuels and Materials Development Program Quart. Progr. Rept. March 31, 1970, ORNL-4560, p. 30.

29. E. J. Manthos and D. R. Cuneo, Fuels and Materials Development Program Quart. Progr. Rept. Dec. 31, 1969, ORNL-4520, pp. 45–50.

30. C. M. Cox, E. J. Manthos, and D. R. Cuneo, Fuels and Materials Development Program Quart. Progr. Rept. March 31, 1970, ORNL-4560, pp. 30–34.

2. DEVELOPMENT OF ADVANCED LMFBR FUELS

P. Patriarca J. L. Scott

The goals of this program are to investigate the properties and behavior of those U- and Pu-based ceramic fuels that we term conductors — such as the mononitrides, carbonitrides, and monocarbides — and to compare their potential as liquid-metal fast breeder reactor (LMFBR) fuel with that of $(U,Pu)O_2$, which by comparison is an insulator. Since the thermal conductivity of the ceramic conductors is about ten times that of $(U,Pu)O_2$, it is theoretically possible to operate a conductor at ten times the power density with the same temperature at the center of the fuel. In practice, heat-transfer limitations, thermal stresses in the cladding, and high rates of swelling at high temperatures limit the power density that can be achieved with thermal conducting fuels to about two or three times that of $(U,Pu)O_2$ — still a challenging improvement. Additionally, the margins for transient overpower in the ceramic conductors are much higher than those for $(U,Pu)O_2$.

We seek to provide the information necessary for evaluating the true potential of nitrides, carbonitrides, and carbides in comparison to each other and to mixed oxides. We must define the structures, composition, and quality control required to achieve 150,000 Mwd/metric ton at peak linear heat ratings of 30 to 50 kw/ft. We must also demonstrate the possibility of a low-cost fuel cycle for manufacturing fuel with the needed properties. And since austenitic stainless steel is a poor conductor of heat, we seek to establish the physical and thermodynamic criteria for the new cladding material that will probably be required to exploit the conducting fuels.

Our approach to establishing the potential of advanced LMFBR fuels is to emphasize irradiation testing of Na-bonded (U,Pu)N at high heat ratings to high burnups. Tests are being conducted in both thermal and fast reactors. Fabrication processes are being studied to provide material for irradiation testing and to establish the range of fuel densities and pore sizes that can be reasonably achieved. Compatibility is being studied to assess the importance of impurities in fuel, Na, and cladding

on compatibility and to resolve problems that arise from compositional changes in the fuel at high burnup. Emphasis is placed on type 316 stainless steel cladding throughout the program.

Synthesis, Fabrication, and Characterization of Nitride Fuels

V. J. Tennery

Synthesis and Fabrication of Mixed Nitrides (E. S. Bomar, F. J. Homan)

The purpose of this portion of our program is to develop methods for preparing (U,Pu)N powders of high purity and to fabricate pellets of variable but controlled density for use in irradiation test capsules. We primarily use cold pressing and sintering but have also used a limited amount of hot pressing. Starting powders are either prealloyed (U,Pu)N or physically mixed UN and PuN.

The densities of pellets fabricated for preparation of pins for irradiation in the Engineering Test Reactor[1] (ETR) were analyzed statistically to determine the source of observed variations. We found that the mean densities for an array corresponding to furnace position fell well within their calculated confidence intervals but that half the mean densities for an array corresponding to sintering runs fell outside their calculated confidence intervals. This led to the conclusion that pellet position in the furnace did not influence the sintered density but that there was a significant difference between the 13 sintering runs.

In the second step of the analysis, we assumed that the pellets made from a given batch of powder were divided into five different populations. Analysis of individual sets of data selected from each of the five sets of data used confirmed the assumption that the five represented different populations. Reexamination of the mean densities for the 13 sintering runs showed that the means fell well within the calculated confidence intervals for the respective batches of powder with two exceptions. These analyses therefore indicate that the sintered density was independent of furnace position, that the density (within the 85 to 90% observed) is strongly dependent on the batch of powder from which the

pellet was fabricated, and that the sintering run may have some small effect.

We also performed experiments to obtain additional information on the effect of several fabrication variables on the density and microstructure of sintered $(U_{0.8},Pu_{0.2})N$ pellets. This is an extension of the work reported previously,[1,2] in which we found that cold-pressed-and-sintered pellets that contained mechanical mixtures of UN and PuN densened only slightly when heated at 2100°C with a N_2 cover gas at 630 torr. The most weight lost during sintering at 2100°C was 4%.

Preparation of Pellets for Irradiation in the Experimental Breeder Reactor-II (E. S. Bomar)

We decided to prepare the (U,Pu)N pellets to be used in fabrication of fuel pins for irradiation in the Experimental Breeder Reactor-II (EBR-II) by conversion of prealloyed U and Pu by the hydride-nitride method.

We placed an order with WADCO for preparation by arc melting of 2 kg of 80% U–20% Pu alloy fully enriched in ^{235}U. Shortly after the initial casting, a 500-g ingot spontaneously ignited and burned in a glove box with an air atmosphere. Neither the box nor its other contents were damaged. The remaining ingots were transferred to a box with an atmosphere of N_2 with an impurity level of 2 to 6% O_2 for storage before shipment. The ingots were subsequently found to have oxidized extensively while in storage.

We believe the pyrophoricity of the 20% Pu alloy is due to the presence of the ζ phase of the U-Pu binary. The composition of replacement castings was lowered to 18% Pu to reduce the amount of ζ phase that could be formed. Ingots prepared a year ago that contained 18.4% Pu, as analyzed at WADCO, gave no difficulty.

A set of metal containers with O-ring seals were fabricated in which to place additional castings for shipment. Shipment is scheduled for October 21, 1970.

Characterization of Nitride Fuels (V. J. Tennery)

X-Ray Diffraction Studies of Uranium-Plutonium Nitrides. — We determined the x-ray lattice constant of a control sample from each of the 13 lots of fuel pellets for the irradiation tests in the ETR. The parameter was determined by the use of a Straumanis film loading Debye-Scherrer camera and an extrapolation calculated on a digital computer. We have established that compositions in the pseudobinary UN-PuN system exhibit self-damage by irradiation down to at least 20 mole % PuN. The lattice constant increases with time approximately according to the observation of Bjorklund and Douglass[3] for pure PuN except that the damage level at a given time decreases in the mononitrides in an apparently complicated fashion as a function of the Pu content. With $(U_{0.8},Pu_{0.2})N$, a change of 0.0007 A was observed in the lattice constant due to self-damage at 25°C in 79 days from the time the sample was cooled from high temperature. Therefore, the lattice constants reported here for the ETR capsule material were determined at sample ages between 39 and 68 days; the self-damage effect amounted to about 0.0006 A over this range of ages. The measured constants and sample ages on the day the x-ray pattern was made are given in Table 2.1. Only minor variations were noted in the constant

Table 2.1. Lattice Constants of $(U_{0.81},Pu_{0.19})N$ Fuel for Irradiation Tests in the Engineering Test Reactor

Sintering Lot	Pellet Numbers in Set	Period From Cooling to X-Ray Analysis (days)	Lattice Constant (A)
1	155–169	48	4.89093 ± 0.00034
2	170–184	42	4.89095 ± 0.00032
3	185–199	43	4.89149 ± 0.00033
4	200–214	42	4.89086 ± 0.00037
5	215–229	39	4.89103 ± 0.00026
6	230–244	50	4.89093 ± 0.00027
7	245–259	49	4.89090 ± 0.00019
8	260–274	62	4.89093 ± 0.00019
9	275–289	68	4.89080 ± 0.00018
10	290–300	65	4.89099 ± 0.00026
11	301–315	64	4.89061 ± 0.00016
12	316–330	62	4.89109 ± 0.00055
13	331–339	62	4.89067 ± 0.00011

in the 13 sets. Five lots of powder were used to produce the pellets, and no correlation was found between the constant and the powder lot. The only diffraction lines observed on the patterns were those of the mononitride phase.

We produced several samples of $(U_{1-x},Pu_x)N$, in which x had nominal values of 0.2, 0.4, 0.6, 0.8, and 1.0, by mechanically blending UN and PuN. We uniaxially pressed and heat treated pellets of these compositions at 1800°C in about 600 torr N_2. We then crushed, ground, and refabricated the pellets into right cylinders about 1/4 in. in outside diameter and 1/4 in. high. We ground these pellets to −80 mesh and again heat treated them at 1800°C for 6 hr in about 600 torr N_2. The specimens densened to about 80% of theoretical. The lattice constants of these mononitride compositions were determined within a few days after the heat treatment to preclude the effect of self-damage through irradiation on the measured lattice constants. The chemical content of each composition was determined and is given in Table 2.2 along with a typical spectrographic analysis. We assumed that the O and C impurities occupied N lattice sites in fixing the composition of the various pellets used in the study. The x-ray data obtained are shown in Fig. 2.1 and listed below:

PuN Content (mole %)	Lattice Constant (A)
0	4.88918 ± 0.00017
19	4.89060 ± 0.00022
38	4.89470 ± 0.00015
58	4.90018 ± 0.00025
79	4.90382 ± 0.00013
100	4.90486 ± 0.00008

The lattice constant of these solid solutions does not obey a Vegard relationship as reported by Anselin.[4] The lattice constants measured agree very well with published values for UN (ref. 5) and PuN (refs. 6, 7) when they have impurity levels of 800 ppm O or less. We believe the disagreement between our data and those of Anselin is due to the high O contents of the nitride samples reported. [4]

Table 2.2. Results of Chemical Analysis of (U,Pu)N Fuel for Irradiation in Engineering Test Reactor

Sintering Lot	Pellet Number	Aliquot Number	Composition, wt %					
			U	Pu	N	O	C	Mass Balance[a]
1	167	1	76.68	18.23	5.14	0.070	0.029	100.15
		2	76.42	18.19	5.15	0.070	0.018	99.86
2	182	1	76.13	18.51	5.10	0.030	0.021	99.80
		2	76.14	18.45	5.15	0.044	0.027	99.82
3	197	1	76.28	18.15	5.49	0.062	0.043	100.03
		2	76.12	18.36	5.63	0.081	0.034	100.23
4	212	1	76.31	18.22	5.30	0.075	0.039	99.94
		2	76.16	18.43	5.32	0.075	0.031	100.02
5	217	1	76.35	18.28	5.20	0.078	0.029	99.95
		2	76.24	18.34	5.25	0.065	0.031	99.93
6	242	1	75.70	18.29	5.46	0.029	0.019	99.50
		2	75.84	18.26	5.41	0.029	0.048	99.59
7	257	1	75.46	18.73	5.22	0.059	0.020	99.50
		2	76.14	18.86	5.08	0.048	0.027	100.16
8	272	1	76.36	18.42	5.19	0.098	0.013	100.08
		2	76.34	18.36	5.12	0.092	0.015	99.93
9	287	1	76.19	18.26	5.25	0.072	0.023	99.80
		2	76.49	18.30	5.29	0.089	0.011	100.18
10	298	1	75.99	18.48	5.32	0.029	0.015	99.84
		2	76.28	18.45	5.35	0.030	0.015	100.13
11	313	1	76.24	18.27	5.21	0.026	0.020	99.77
		2	76.32	18.36	5.39	0.020	0.020	100.12
12	328	1	76.46	18.34	5.19	0.039	0.018	100.06
		2	76.16	18.34	5.11	0.041	0.019	99.68
13	337	1	76.28	18.36	5.10	0.019	0.017	99.78
		2	76.46	18.40	5.12	0.021	0.016	100.02

[a]Mass balances are arbitrarily the sums of the numbers shown for a particular aliquot number. These balances do not include about 0.02% of trace metal impurities that were present.

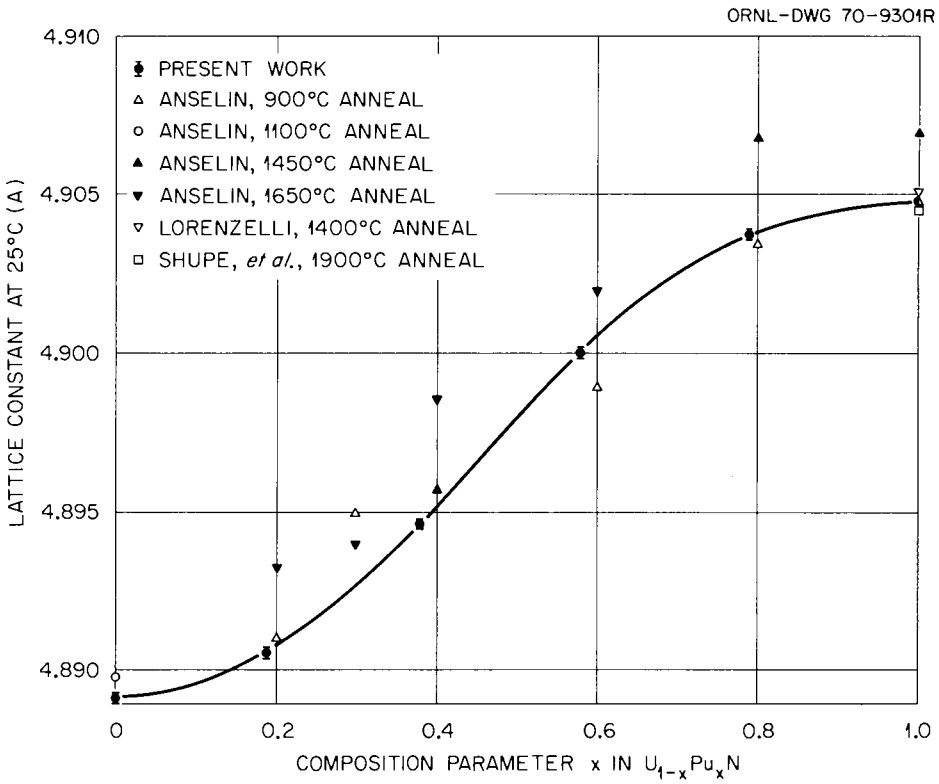

Fig. 2.1. Lattice Constant in the UN-PuN System. [Refs. F. Anselin, J. Nucl. Mater. 10(4), 301–320 (1963); R. Lorenzelli, Contribution to the Study of the System (U,Pu)C,N, ORNL-tr-3019 (March 1969); M. W. Shupe et al., Quarterly Status Report on the Advanced Plutonium Fuels Program, April 1 to June 30, 1969 and Third Annual Report, FY 1969, LA-4284-MS, p. 71.]

We are now measuring the self-damage by irradiation in the x-ray samples; preliminary results indicate that the self-damage at 25°C in UN-PuN solid solutions is not proportional to the Pu content.

Studies of the Analytical Techniques for Uranium-Plutonium Nitrides. — The chemical contents of a pellet selected randomly from each sintering lot of the ETR fuel were determined by the procedures described previously.[8]

The major analytical problem remaining for the nitrides represented by $(U_{0.8},Pu_{0.2})N$ is the dissolution method used in the analyses for N. The method now used consists of sealing a weighed amount of sample into a glass tube with a mixture of HCl and HF and heating the tube in a furnace for 24 to 36 hr. After complete dissolution, the sample is analyzed by the Kjeldahl method in the conventional manner. Nitrogen is often lost during this dissolution procedure. Recently, we developed a new

dissolution method for UN that is far simpler, provides greatly improved precision, and requires only about 15 min.

We determined the U and Pu contents of the ETR samples coulometrically and checked the results by titrating known solutions made from high-purity standard Pu and U. The O analyses were performed by inert-gas fusion, and the C was analyzed by a conventional combustion technique. The chemical contents of selected pellets corresponding to the sets listed in Table 2.1 are given in Table 2.2. Duplicate analyses were performed for each of the major elements, and, in some cases, triplicate analyses were performed when there was any question about the precision, primarily in the analyses for N. The values in Table 2.2 are those accepted as representative of the fuel for the irradiation test in the ETR.

We recently observed that UN could be readily dissolved in phosphoric acid in a matter of minutes in a beaker on a hot plate. Several of these specimens dissolved this way were analyzed for N by the Kjeldahl method. We also dissolved UN in phosphoric acid with a small addition of Devarda's alloy, a reducing agent often used in nitride dissolutions to prevent the transformation of the N to gaseous N_2. Essentially the same results were obtained with and without the use of Devarda's alloy. The phosphate apparently complexes the N in such a way that very little or none is converted to N_2 gas during dissolution and thus lost to the analysis. To date we have complete results for all major elements in four UN samples and results for N only, determined both with and without the use of Devarda's alloy, for two samples. Since each UN sample was sintered according to a slightly different program of temperature and N_2 pressure, some real variation may be expected in the N contents. The results are shown in Table 2.3. The nonmetal sums are very near the theoretical value for UN (5.556%). This dissolution method is now being tested for its applicability to mixed nitride specimens.

The results of chemical analyses for the various UN-PuN compositions listed previously are given in Table 2.4.

Table 2.3. Results of Nitrogen Analysis by Kjeldahl Method for Sintered UN Specimens Dissolved in Phosphoric Acid

Sample Number	Composition, wt %			Sum of Nonmetals (wt %)
	U	N	O + C	
1	94.61	5.40	0.07	5.47
2	94.60	5.38	0.07	5.45
3	94.52	5.45	0.05	5.50
4	94.49	5.42	0.09	5.51
5		5.34	0.04	5.38
		5.37	0.04	5.41
5[a]		5.40	0.05	5.45
		5.45	0.05	5.50
6		5.48	0.04	5.51
		5.46	0.04	5.50
6[a]		5.50	0.05	5.55
		5.48	0.05	5.53

[a]Devarda's alloy added to phosphoric acid for these aliquots.

Table 2.4. Results of Chemical Analyses of UN-PuN Solid Solutions

Specimen Number	PuN Content (mole %)	Composition, wt %				
		U	Pu	N	O	C
1	0	94.45	0	5.41	0.09	0.030
2	19	77.00	17.40	5.47	0.08	0.026
3	38	58.60	35.90	5.45	0.05	0.020
4	58	40.20	54.80	5.45	0.04	0.030
5	79	21.35	73.10	5.30	0.04	0.020
6	100		94.39	5.40	0.10	0.020

A typical spectrographic analysis for the specimens used in the UN-PuN x-ray study is shown below for specimen 2 from Table 2.4 which had the composition $(U_{0.8},Pu_{0.19})N$:

Element	Concentration (ppm)
Al	60
B	
Cr	
Cu	
Fe	120
Mn	
Mo	
Ni	
Pb	
Si	
Sn	
Ti	
V	
Zr	

The Pu and U were removed from the sample by ion absorption before analysis.

Compatibility of Mixed-Nitride Fuels with LMFBR Cladding Alloys

J. M. Leitnaker

Our approach to compatibility in high-performance fuel systems is to characterize interactions that can occur between the fuel and cladding material. A basic understanding of these reactions may point to methods for tailoring the fuel so that the reactions cannot occur and perhaps to methods for reducing reaction rates.

The Pu-Cr-N System (J. P. De Luca)

The first sample in the Pu-Cr-N system, a 1/4-in.-diam pellet with a Cr:PuN ratio of about 2:1, was heated at 1725°C for 2 hr under

200 torr N_2. It was then examined by optical microscopy and x-ray analysis. From Fig. 2.2 it appears that a liquid formed in the Cr-PuN pellets; however, the pellet did not slump during annealing. The phases have not yet been individually identified. X-ray analysis revealed predominantly PuN and also Cr_2N and several unidentified lines. Chromium

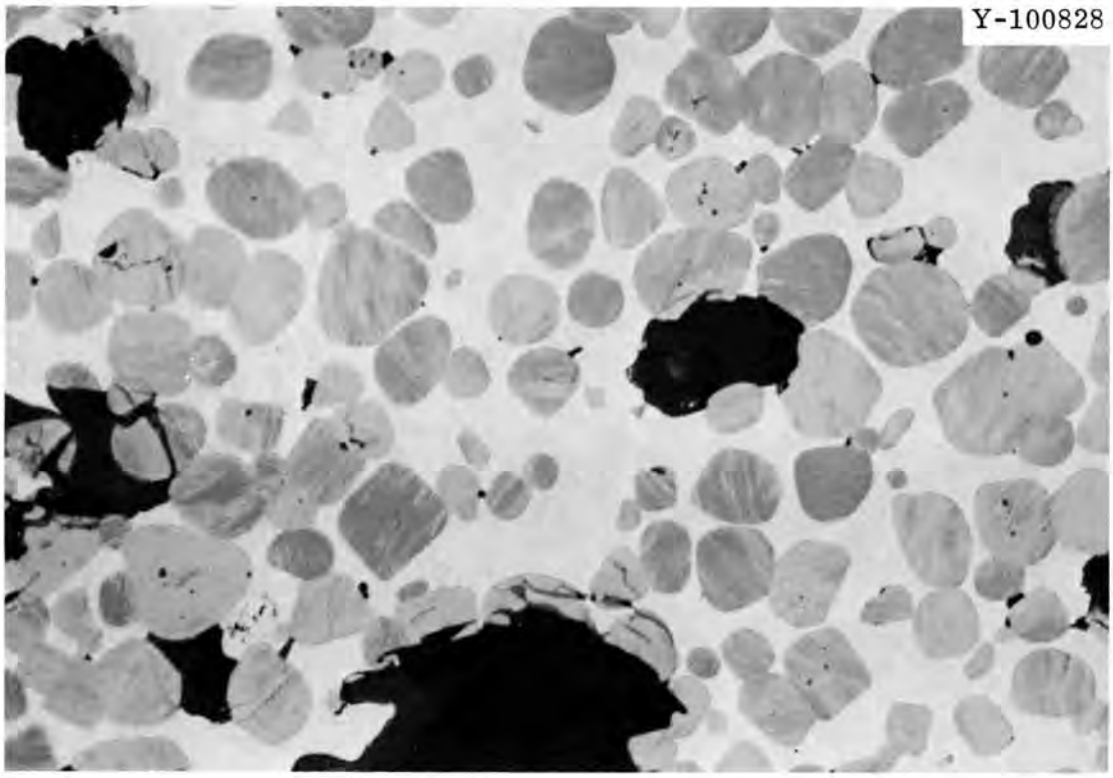

Fig. 2.2. Plutonium Nitride (−325 Mesh) and Chromium Metal (−325 Mesh) in a Molar Ratio of 1:2. Heated at 1700°C for 2 hr under 200 torr N_2.

metal was not identified, although the x-ray lines for PuN may have masked the Cr lines. The unidentified lines may indicate the presence of a Pu-Cr-N_2 phase analogous to the U-Cr-N_2 phase identified by Spear and Leitnaker.[9]

A second pellet of Cr_2N and PuN in a 1:1 molar ratio was annealed 8 hr under 200 torr N_2 at 1500°C. The resulting pellet is being analyzed.

Thermodynamic Investigations of High-Performance Fuel Systems

J. M. Leitnaker

The goal of our thermodynamics program for high-performance fuels, the carbides, nitrides, and carbonitrides, is to be able to predict the limiting equilibrium behavior of fuel and cladding in fast-reactor environments. Our experiments, though limited to measurements out-of-reactor, are of value for defining and understanding the factors that affect fuel performance.

Thermodynamics of Plutonium Nitride (J. P. De Luca)

For our study of the compatibility of mixed nitride fuels with cladding materials, we are building a system for measuring N_2 pressures over the nitrides and carbonitrides of Pu to define the effects of temperature, pressure, and composition on the behavior of the fuel toward cladding materials. The system was described previously.[10]

We continued to calibrate and check this piece of equipment. The residual-gas analyzer and microbalance were both put into operation and found to work satisfactorily.

Irradiation Testing of Nitride Fuels for LMFBR Applications

T. N. Washburn

The objective of this phase of the program is to establish the irradiation performance of the U-Pu nitrides and carbides. The nitrides and carbides have a thermal conductivity about 5 to 10 times higher, a theoretical density 30% higher, and a metal content in the compound 7% higher than the oxides. These properties make the nitrides and carbides strong contenders as advanced fuel for an LMFBR.

Thermal-Flux Tests (C. F. Sanders)

The initial series of thermal-flux irradiation tests consists of two uninstrumented capsules of four fuel pins each that will be

irradiated in the ETR. These tests are of the "screening" type and are being used to evaluate the performance of (U,Pu)N fuel synthesized from metal. The fuel pins operate at a peak linear heat rating of 30 kw/ft to burnups of 30,000 and 60,000 Mwd/metric ton.

The fuel is cold-pressed-and-sintered (U,Pu)N pellets with densities from 86 to 91% of theoretical. The fuel pin has a 0.010-in. radial gap between the fuel pellet and the inside surface of the type 316 stainless steel cladding. The gap will be filled with NaK-19 (Na–19% K) to enhance heat transfer.

We completed the fabrication of ten fuel pins, eight of which will be irradiated in capsules 43-N1 and 43-N2. The fuel and NaK-19 were loaded into the cladding, and the fuel pins were transferred in a sealed container for final closure welding. The NaK-19 was loaded[11] into each fuel pin and found to contain less than 95 ppm O. The quality and level of the NaK bond were determined by standard eddy-current techniques. At the time the fuel was loaded, we did not have a complete chemical analysis of the fuel; therefore, we decided to load each pin from one batch of fuel. This gave us a fuel column about 2.5 in. high instead of the design 3 in. high.

During the final inspection of the fuel pins, we found three defects. In one pin (45-1-C) the cold NaK level was about 3/32 in. below the top of the fuel column because the NaK loading tube was short. In another pin (45-1-J) we detected a broken pellet. Since this pellet had not been broken before loading, we concluded that it had been broken during handling or centrifuging of the fuel pin. The third defect (pin 45-1-G) was a void in the NaK-19 bond between fuel and cladding; we centrifuged the pin four more times but could not remove the void.

Since we had to use one of the pins with a defect, we chose pin 45-1-C, which had the low NaK level, because our calculations showed that the NaK level during operation will be above the fuel. The fabrication of the capsule will be completed next quarter.

Table 2.5 lists the design conditions, and Table 2.6 gives a summary of the measured characteristics of each fuel pin fabricated.

Table 2.5. Design Conditions for Mixed Nitride Capsules N-1 and N-2

Fuel	$(U_{0.8},Pu_{0.2})N$
Fuel diameter, in.	0.245
Fuel density, % of theoretical	88–90
Fuel length, in.	2.5
Cladding material	Type 316 stainless steel
Cladding diameter, in.	0.3
Cladding wall thickness, in.	0.0175
Bond between fuel and cladding	NaK-19
Gap between fuel and cladding, in.	0.010
Capsule material	Type 304 stainless steel
Capsule diameter, in.	0.501
Capsule wall thickness, in.	0.025
Instrumentation	None
Heat rating, kw/ft	30
Temperature of fuel center, °C	925
Temperature of fuel surface, °C	610
Temperature of inner surface of cladding, °C	585
Temperature of outer surface of cladding, °C	495
Number of pins per capsule	4
Number of capsules per test	1

The safety analysis for the irradiation experiment was completed and subsequently reviewed and approved by the ETR safety personnel.

After the Be reflector was changed in the ETR during April, there were uncertainties in peak flux in various locations. Therefore, we performed a new flux mapping for these experiments and decided to use positions L-12-SE and F-10-NW.

Table 2.6. Fuel Pins for Mixed Nitride Series I Irradiation Experiment

Tube	Fuel Pin	Pellet Batch	Pellet Density (% of theoretical)	Fuel Height (in.)	Pellet Diameter (in.)	Remarks
45-1-C	N1-1	A-7-C-2	90.2	2.473	0.240–0.243	NaK-19 level about 3/32 in. low
45-2-F	N1-2	A-6-C-2	87.2	2.453	0.245–0.248	
45-1-K	N1-3	A-6-C-1	87.8	2.448	0.245–0.248	
45-1-E	N1-4	A-5-C-2	85.5	2.573	0.240–0.245	
45-1-J	Sample	A-4-C-1	85.7	2.593	0.239–0.243	Broken pellet
45-1-D	N2-1	A-8-C-2	88.5	2.523	0.240–0.244	
45-2-G	N2-2	A-8-C-1	88.5	2.508	0.2405–0.244	
45-1-F	N2-3	A-7-C-1	89.2	2.487	0.240–0.243	
45-2-E	N2-4	A-6-C-3	86.8	2.441	0.247–0.248	
45-1-G	Sample	A-5-C-3	86.1	2.573	0.2405–0.244	Void in NaK-19

Notes

1. E. S. Bomar, Fuels and Materials Development Program Quart. Progr. Rept. March 31, 1970, ORNL-4560, pp. 40–45.

2. E. S. Bomar, Fuels and Materials Development Program Quart. Progr. Rept. Dec. 31, 1969, ORNL-4520, pp. 58–66.

3. C. W. Bjorklund and R. M. Douglass, Quarterly Status Report on the Advanced Plutonium Fuels Program, April 1 to June 30, 1969, and Third Annual Report, FY 1969, LA-4284-MS, pp. 73–75.

4. F. Anselin, J. Nucl. Mater. 10(4), 301–320 (1963).

5. J. M. Leitnaker, R. A. Potter, K. E. Spear, and W. R. Laing, High Temp. Sci. 1(4), 389–400 (1969).

6. M. W. Shupe et al., Quarterly Status Report on the Advanced Plutonium Fuels Program, April 1 to June 30, 1969, and Third Annual Report, FY 1969, LA-4284-MS, p. 71.

7. R. Lorenzelli, Contribution to the Study of the System (U,Pu)C,N, ORNL-tr-3019 (March 1969).

8. V. J. Tennery, J. L. Botts, and J. P. De Luca, Fuels and Materials Development Program Quart. Progr. Rept. March 31, 1970, ORNL-4560, pp. 49–55.

9. K. E. Spear and J. M. Leitnaker, "Phase Investigations in the U-C-N System." Submitted for publication.

10. J. P. De Luca, Fuels and Materials Development Program Quart. Progr. Rept. Sept. 30, 1969, ORNL-4480, p. 52.

11. C. F. Sanders and J. D. Sease, Fuels and Materials Development Program Quart. Progr. Rept. March 31, 1970, ORNL-4560, p. 61.

3. EFFECT OF POWER CYCLING ON LMFBR FUEL-CLADDING BEHAVIOR

P. Patriarca O. Sisman[1] A. L. Lotts

This program investigates the effects of power cycling and transients on fuel behavior and the mechanical interaction of fuel and cladding for a liquid-metal-cooled fast breeder reactor (LMFBR), first for mixed oxide fuel and stainless steel cladding and later for other fuels and claddings. The initial objectives of this study are to compare the mechanical interactions of fuel (flat-ended pellets, dished pellets, and particulate fuel) and cladding during thermal-cycling conditions typical of those to be expected in an LMFBR. The mechanical interactions between $(U,Pu)O_2$ fuel and stainless steel cladding will affect both the safety and economic characteristics of LMFBR's. Axial separations in the fuel column tend to make the reactor power coefficients more positive. In addition, concentrations of stress in the cladding due to fuel "hourglassing," cracking, and ratchetting combine with power cycling and reduced cladding ductilities to decrease the lifetime of the fuel elements. These mechanical interactions are quite important in defining allowable schemes of fuel management and reactor operating conditions and thus have a significant effect on the reactor economy.

Power Cycling Irradiation Tests

C. M. Cox

The intent of our program is to measure in-reactor the axial extension of the fuel column and cladding and the fuel pin internal gas pressure during operation under carefully controlled conditions, which include programmed power cycles and an occasional overpower cycle. The irradiation capsules will be designed so that the fuel pin operates at LMFBR prototypic power and temperature conditions. The irradiation tests will last 1 to 2 years and will give burnup levels of 5 to 9%.

Power Cycling of Mixed Oxide Fuel with Stainless Steel Cladding to Moderate and High Burnup (R. B. Fitts, R. L. Senn,[2] J. G. Morgan,[1] J. D. Jenkins[2])

As described previously,[3] the first two capsules for investigation of power cycling will be designed as prototype Fast-Flux Test Facility (FFTF) Reactor fuel pins and will operate in the poolside facility of the Oak Ridge Research Reactor (ORR).

The design effort on the first capsule (MINT-1) is progressing satisfactorily. The capsule is scheduled to be inserted into the reactor in September or November 1970. The conceptual design is illustrated in Fig. 3.1.

The fuel pin is to be fabricated from 9.6 in. of mechanically blended $(U_{0.75},Pu_{0.25})O_{1.97}$ solid pellets. The pellets are 0.1943 ± 0.0002 in. in diameter by 0.200 in. long, have a density of 89.4 ± 0.5% of theoretical, and have dished ends. The cladding is 20% cold-worked type 316 stainless steel, 0.230 in. in outside diameter and 0.015 in. in wall thickness. The resulting smear density of the fuel will be 84.4% of theoretical. The fuel pin will be immersed in NaK, which is to be used as a heat-transfer medium in the capsule.

There are 12 thermocouples in this capsule: 6 monitor the temperature gradient along the push rod and length-measuring system, and 6 are arranged in opposed pairs along the fuel pin. They are to be brazed to the inside of the primary containment in the NaK that surrounds the fuel pin to minimize the possibility of mechanical interaction between the thermocouples and fuel pin. Development work on this brazing operation is under way.

A pressure transducer was selected for measuring the internal pressure of the fuel pin during the test. It monitors the deflection of a diaphragm with a variable-permeance transducer. A conceptual design is shown in Fig. 3.2. An analysis of the expected buildup of pressure from fission gas within the fuel pin indicates that by the end of a 10% burnup test about 56 cm^3 of fission gases (45% of that generated) will have been released from the fuel column, and the internal gas pressure during operation will be about 20 atm.

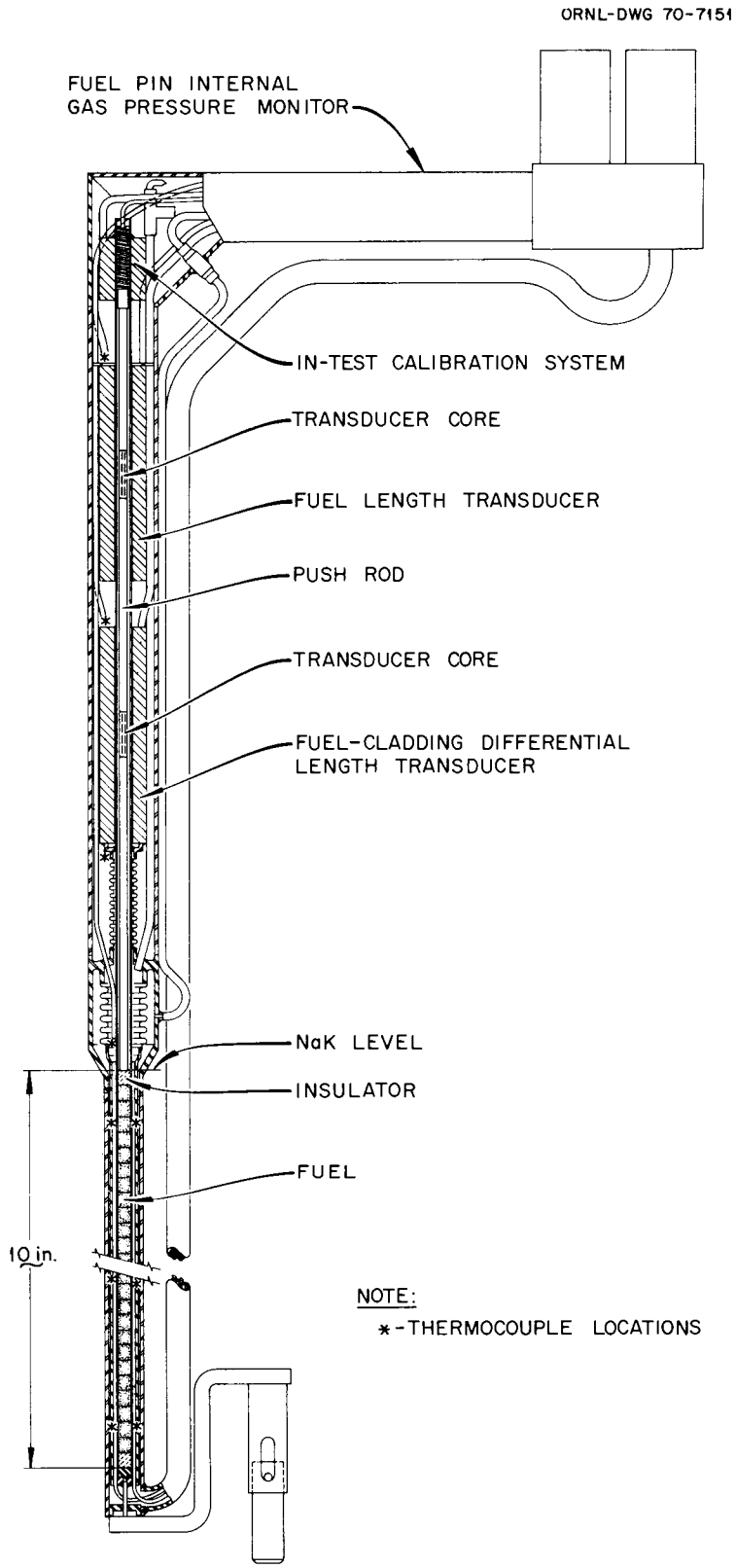

Fig. 3.1. Capsule for Studies of Mechanical Interaction of Fuel and Cladding.

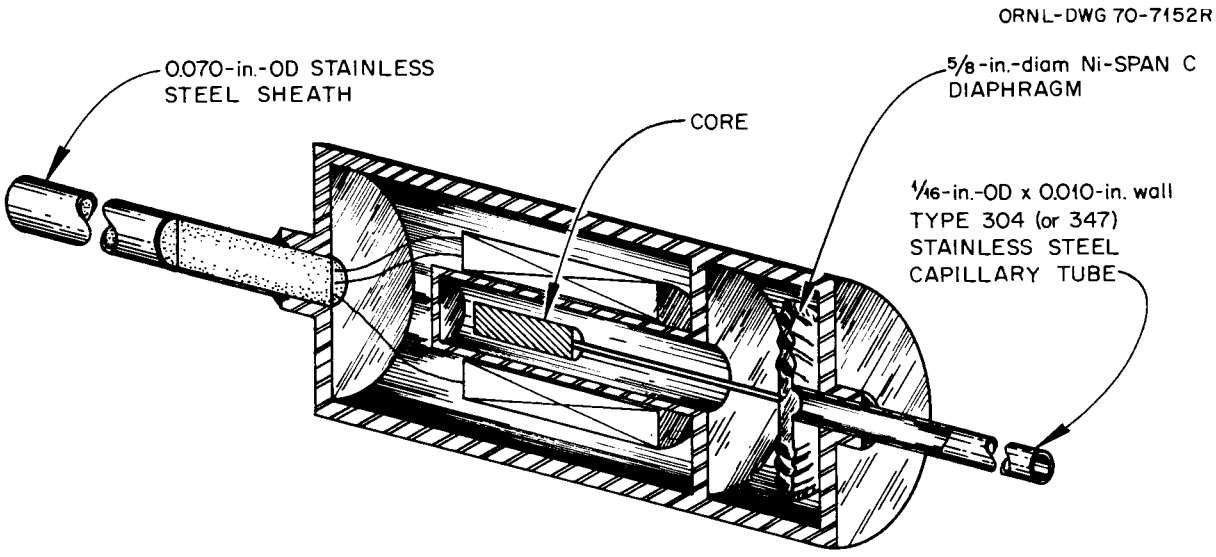

Fig. 3.2. Proposed Pressure Transducer.

The system for measuring changes in length, which will detect and monitor mechanical interactions of fuel and cladding, is based upon two variable-permeance devices similar to linearly variable differential transformers. These record the position of two magnetic cores in a push rod that rests on top of the fuel stack. One of the variable-permeance devices is attached to an extension of the fuel cladding and measures the relative change in length between fuel and cladding (differential transducer). The other is attached to the outer containment and measures the absolute change in the length of the fuel column (fuel-length transducer). Thus, we can monitor the growth of both fuel and cladding. A system for calibrating and zeroing the measurement system during testing is being designed to fit in the top of the cladding extension. The main approach now being considered employs an electromagnet to raise the push rod and thus the magnetic cores to two known positions to provide two points on the calibration curve of each variable-permeance device and permit the detection and correction of any calibration changes that might occur during the approximately 1 1/2-year duration of the test.

The expected movement of transducer bodies and cores during irradiation was analyzed to determine the desired location of these items in the capsule. In this analysis, the hardware components not associated with the fuel were assumed to operate at approximately 170°C based upon

temperatures measured in the extensometer capsules[4] for the Medium Power Reactor Experiment.

The design analysis is not sensitive to this assumption since 75% or more of the location changes are associated with the thermal expansion of the fuel[5] and the cladding[6] around it. The transducer readings calculated for the instrument that monitors the change in fuel length and for the one that monitors the length differential of the fuel and cladding are shown in Figs. 3.3 and 3.4. These calculated readings are based on the assumption that the capsules are assembled in such a way that the transducers and their cores are centered with respect to each other. As is apparent from these plots, the readings to be obtained are quite sensitive to, and thus will measure, the temperature (T_p) at which plastic deformation of the fuel due to internal and external stresses on the fuel eliminate the effects of thermal expansion. The curves were constructed using the simplified assumption that as soon as T_p is reached, there will be no more thermal expansion of the fuel. Thus, the transducer readings are a function of the temperature of the center of the fuel until that temperature reaches T_p. Creep deformation of the fuel and mechanical interaction of the fuel and cladding will affect these curves in the operating equipment. Creep of the fuel will not cause large changes, and mechanical interaction will produce greater changes on the transducer for fuel length than on the transducer for the length differential between fuel and cladding.

Based on the results of this analysis, we shall assemble the capsule so that the core of the transducer for the length differential between fuel and cladding is located 0.120 in. below the centered position and so that the core of the transducer for fuel length is 0.200 in. below center. These positions will provide maximum utilization of the ±0.200-in. range of optimum transducer operation.

We prepared a tentative operating sequence for the MINT-1 capsule based upon the plan to operate for one-half of the test [about 165 days to about 2.7% fissions per initial actinide metal atom (FIMA)] at 10 kw/ft and the remainder (165 days to 7% FIMA) at 16 kw/ft with occasional cycles of 20% overpower. This sequence will simulate the

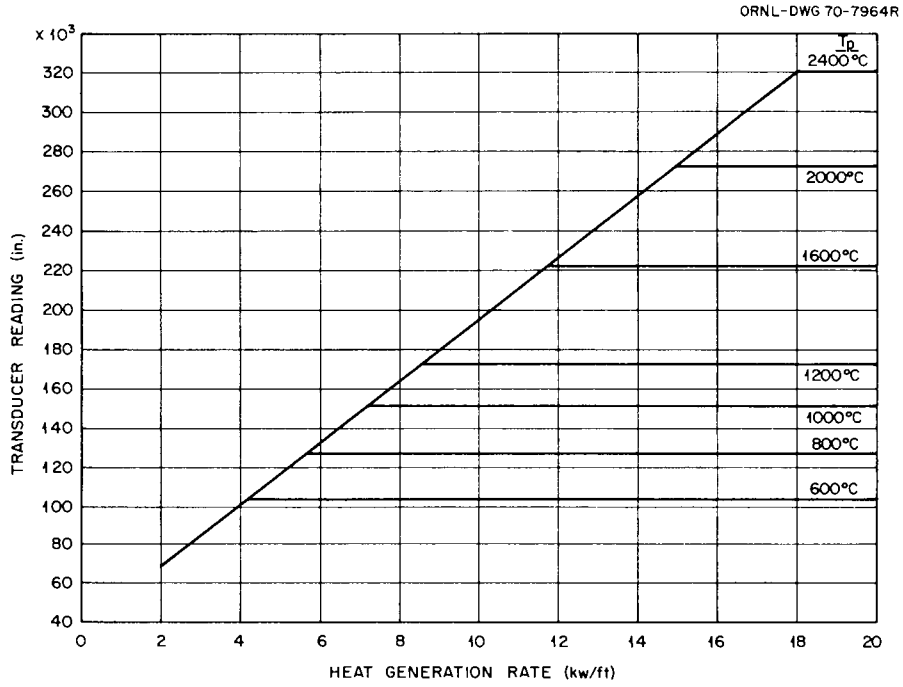

Fig. 3.3. Reading from Fuel-Length Transducer as a Function of Rate of Heat Generation and Temperature of Plasticity (T_p) for the Fuel. Transducer and core were initially centered.

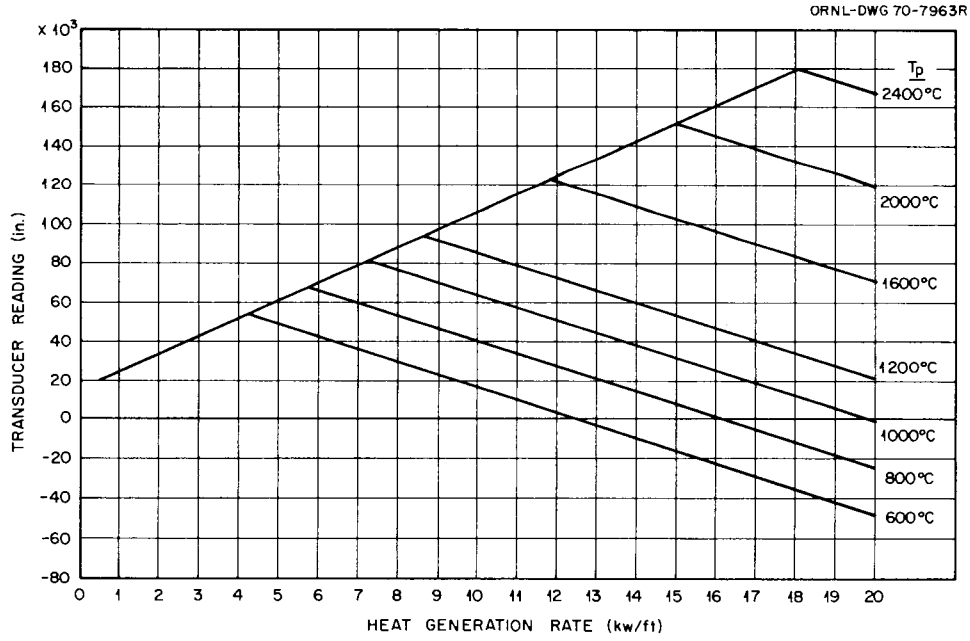

Fig. 3.4. Reading from Fuel-Cladding Differential Transducer as a Function of Rate of Heat Generation and Temperature of Plasticity (T_p) for the Fuel. Transducer and core were initially centered.

operation of a fuel pin in a peripheral position of the FFTF Reactor for one-half of its life followed by a movement into a central core location.

The irradiation tests of mechanical interaction will be used as one of the reference cases for the working group on LMFBR fuel element modeling.[7] We shall assume steady-state operation of the MINT-2 capsule at the overpower heat rate of 19 kw/ft for the first calculations. The principal differences between operation of this fuel pin in the ORR and in an LMFBR are the low cladding flux, shown below:

Burnup (% FIMA)	Neutron Flux [neutrons cm^{-2} sec^{-1} (> 0.1 Mev)]
	$\times 10^{13}$
0	1.50
2	1.54
4	1.57
6	1.61
8	1.66
10	1.71

The flux depression in the fuel is indicated in Fig. 3.5. The very large power depression follows from the high ^{239}Pu concentration in the 0.198-in.-diam 92% dense $(U_{0.75},Pu_{0.25})O_{1.98}$ fuel pellets.

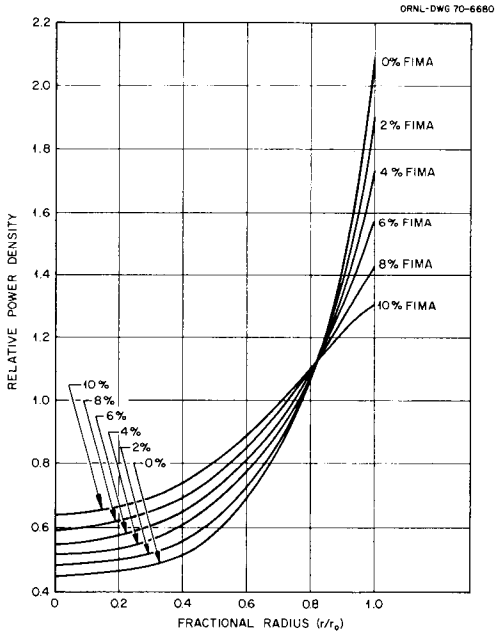

Fig. 3.5. Effect of Burnup on Radial Power Profile of Fuel for MINT Capsule.

Notes

1. Reactor Chemistry Division.

2. Reactor Division.

3. R. B. Fitts, V. A. DeCarlo, and J. G. Morgan, Fuels and Materials Development Program Quart. Progr. Rept. March 31, 1970, ORNL-4560, pp. 63–66.

4. S. C. Weaver, R. B. Fitts, et al., Results from Irradiation Testing of UO_2 Fuel Pins Designed for the Medium Power Reactor Experiment, ORNL-TM-2859 (August 1970).

5. A. Roth et al., Trans. Am. Nucl. Soc. 10(2), 457–458 (November 1967).

6. W. H. Bridges, The Physical and Tensile Properties of Type 316 Stainless Steel, ORNL-TM-3037, in press.

7. P. Patriarca, A. L. Lotts, and C. M. Cox, "LMFBR Fuel Element Design and Model Development," pp. 65–80, this report.

4. LMFBR FUEL ELEMENT DESIGN AND MODEL DEVELOPMENT

P. Patriarca A. L. Lotts C. M. Cox

The objective of this program is to develop analytical methods to predict and evaluate the performance of fuel pins and fuel elements for the liquid-metal-cooled fast breeder reactor (LMFBR). This work is closely coordinated with the related programs for development of fuel and cladding. It provides methods for designing and systematically evaluating irradiation tests, evaluating the influences of materials properties on the performance of fuel elements, and identifying specific areas in which experimental research needs to be intensified.

The program is divided into three areas: model integration, fuel performance, and cladding performance. The fuel and cladding performance tasks are oriented toward mathematical description of the various phenomena of the fuel and cladding under irradiation such as swelling, gas formation, and mechanical, thermal, and chemical behavior. These individual models are incorporated into a generalized computer program that simulates the performance of an operating fuel pin. The work on model integration emphasizes the behavior of fission gas and mechanical interactions of fuel and cladding.

Fuel Performance

The objective of this work is to develop improved analytical models to describe in-reactor swelling, release of fission gas, and restructuring of $(U,Pu)O_2$. During this reporting period, we emphasized in-reactor grain growth and redistribution of actinide metals. We expect grain size to have significant influence on the coalescence of bubbles of fission gas, which in turn will influence swelling of the fuel and release of gas. Nabarro-Herring creep of the fuel is also a function of grain size. Redistribution of the actinide metals alters the thermal gradient in the fuel as well as its physical, chemical, and mechanical properties.

Studies of Grain Growth (W. J. Lackey)

We determined the variation of grain size with radial position for a Sphere-Pac $(U_{0.85},Pu_{0.15})O_2$ fuel pin (43-112-4C) after thermal-reactor irradiation at a linear heat rate of 10.5 kw/ft to a burnup of 0.5% fissions per initial actinide metal atom (FIMA). The grain size of the sol-gel-derived coarse microspheres, as fabricated, was about 1.2 μm. As a result of the low heat rate, columnar grain growth did not occur, and the outlines of the spheres were clearly visible throughout the cross section of the fuel pin (Fig. 4.1). The variation of fuel temperature and the grain size of the coarse microspheres as a function of radial position is shown in Fig. 4.2. Temperatures were obtained from a PRØFIL[1] analysis. We estimated from Fig. 4.2 that grain growth occurred at temperatures as low as about 1100°C. The agreement of this

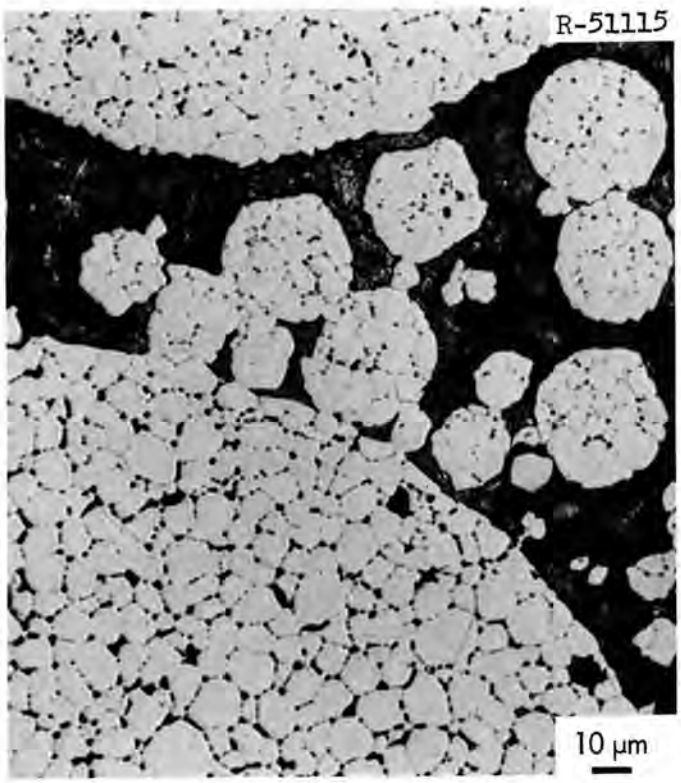

Fig. 4.1. Sphere-Pac $(U_{0.85},Pu_{0.15})O_2$ after Irradiation at a Linear Heat Rate of 10.5 kw/ft to 0.5% Fissions per Initial Actinide Metal Atom. Part of two coarse microspheres and several fine microspheres are shown. These spheres were located near the thermal center of the fuel pin. 500×.

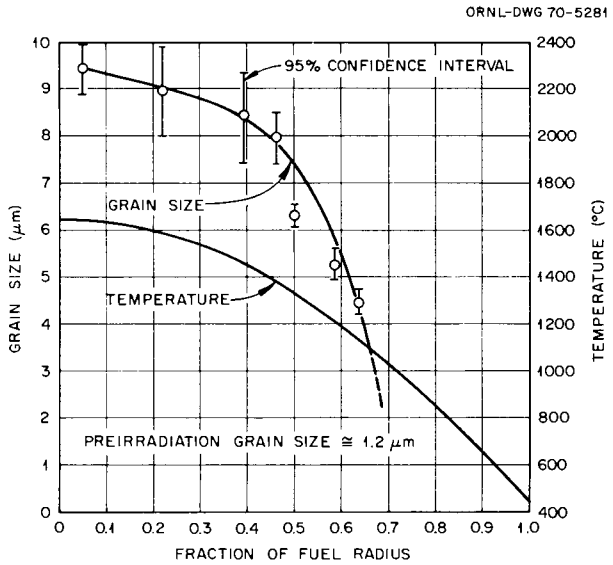

Fig. 4.2. Variation of Grain Size and Temperature with Radial Position for a $(U_{0.85},Pu_{0.15})O_2$ Fuel Pin Operated at a Linear Heat Rate of 10.5 kw/ft to 0.5% Fissions per Initial Actinide Metal Atom.

temperature with the sintering temperature (1100 to 1150°C) may or may not be coincidental.

Although grain growth theory is not highly developed, it is reasonable to fit the experimental data to

$$D^2 - D_0^2 = Kt^n \exp(-Q/RT) , \qquad (4.1)$$

where

D = final grain size, μm,

D_0 = initial grain size, μm

K = a constant,

t = time, hr,

n = time exponent, theoretically unity, and

Q = activation energy for grain growth, cal/mole.

The activation energy determined from Eq. (4.1) is given by the slope of the semilogarithmic plot of $(D^2 - D_0^2)$ vs 1/T, which is shown in Fig. 4.3. From a least-squares analysis, we determined that the activation energy was 16.9 ± 3.6 kcal/mole (90% confidence interval) less than one-fifth of that determined[2] for out-of-reactor grain growth in UO_2 and ThO_2.

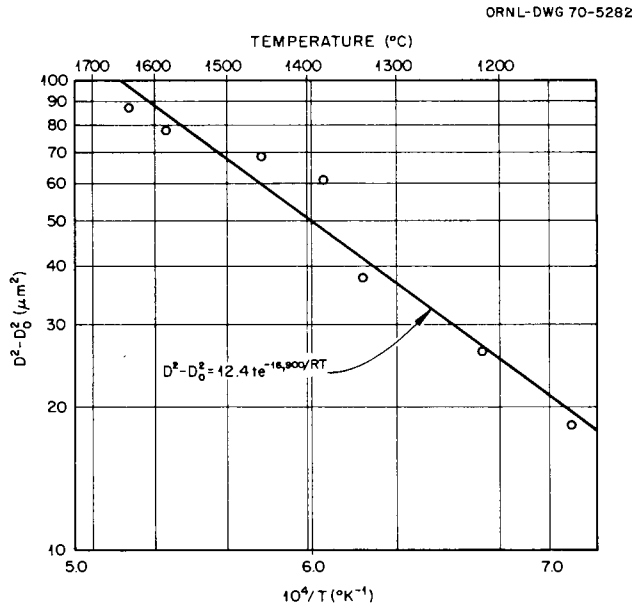

Fig. 4.3. In-Reactor Grain Growth in $(U_{0.85},Pu_{0.15})O_2$ Irradiated at a Linear Heat Rate of 10.5 kw/ft to 0.5% Fissions per Initial Actinide Metal Atom.

By assuming the time exponent, n, in Eq. (4.1) to be unity, which is the theoretical value, and by knowing that the equivalent hours at full power during the irradiation were 668, we obtained the following equation:

$$D^2 - D_0^2 = 12.4\ t\ \exp\ (-16{,}900/RT)\ . \qquad (4.2)$$

At 1550°C, the predictions of this equation generally agree with the observations of MacEwan[3] for out-of-reactor grain growth of UO_2. However, because of the smaller activation energy observed for in-reactor grain growth, Eq. (4.2) will predict significantly larger grain sizes at low temperatures and significantly smaller grain sizes at higher temperatures than those observed in the out-of-reactor investigation.

Equation (4.2) must be regarded as preliminary until the time exponent has been properly evaluated. Eventually it may also be necessary to account for the possibility of stabilization of grain size caused by the presence of porosity and fission products.

Distribution of U and Pu (W. J. Lackey, J. L Miller)

Electron microprobe analysis was used to determine the distribution of Pu across a transverse section of a Sphere-Pac $(U_{0.85},Pu_{0.15})O_2$ pin (43-112-3C) irradiated in the Engineering Test Reactor (ETR) at a linear heat rate of 13.6 kw/ft to a burnup of 0.7% FIMA.

Briefly, the microstructure was typical. There was a central void, columnar grains, equiaxed grains, and an unrestructured region consisting of the original microspheres. Fuel had been deposited at the region of transition from columnar to equiaxed grains, apparently by vapor transport down the temperature gradient onto the hot side of the microspheres.

The Pu and U concentrations were determined by measuring the intensities of the Pu Mβ and U Mα x rays. When these analyses were performed, a standard procedure had not been established for converting the x-ray intensities to Pu and U concentrations; therefore, several different standards were used for the analyses reported here. Consequently, close comparisons of Pu contents from one set of data with Pu contents from another data set are subject to an error of perhaps ±10% of the reported value. Within a given set of data, the standard deviation of the reported percentage of Pu is expected to be ±0.6% as determined from a statistical analysis of triplicate determinations of the Pu content of five coarse microspheres located adjacent to the cladding. The statistical analysis also showed that, within the limits of detection, there was no variation in Pu content from sphere to sphere.

A radial scan was made simultaneously for Pu and U in the region of columnar grains adjacent to the central void. The Pu and U contents read from the strip-chart recorder are plotted in Fig. 4.4 as functions of the distance from the periphery of the central void. Notice that the Pu content decreased and the U content increased with decreasing fuel temperature.

Figure 4.5 shows the variation in Pu content with radial position for a larger portion of the fuel radius. The data shown in Fig. 4.5 were obtained not by scanning but by measuring the x-ray intensity for a constant time with the electron beam at a fixed position. The intensities for U and Pu were measured simultaneously. Although these data

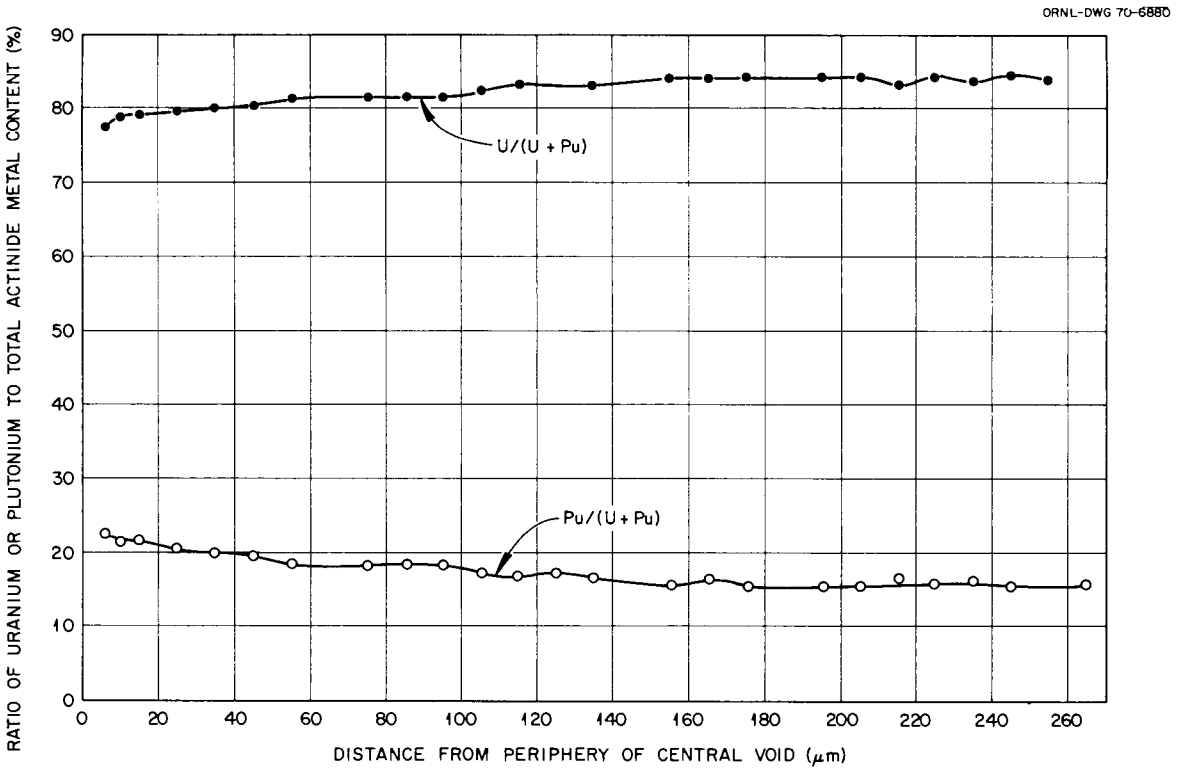

Fig. 4.4. Variation in Pu Content with Radial Position for the Columnar Grains Near the Central Void for $(U_{0.85},Pu_{0.15})O_2$ after Irradiation at a Linear Heat Rate of 13.6 kw/ft to a Burnup of 0.7% Fissions per Initial Actinide Metal Atom.

should be regarded as preliminary, several interesting trends are indicated. First, the Pu content near the central void decreased with decreasing fuel temperature, in agreement with the data of Fig. 4.4. The line between fractional fuel radii of 0.2 and 0.4 in Fig. 4.5 was drawn horizontally, based partially on the knowledge that a radial scan over much of this region showed essentially uniform Pu content. A second interesting region is that in the vicinity of the interface between columnar and equiaxed grains, where fuel was deposited on the surface of the microspheres. There appears to be a minimum Pu content in this region, as shown in Fig. 4.5 and, as indicated but not conclusively proven, by the results of two radial scans for Pu across the deposited fuel. Both the high Pu content near the central void and the low Pu content of the vapor-deposited fuel are consistent with transport down the temperature gradient of a gas phase rich in U.

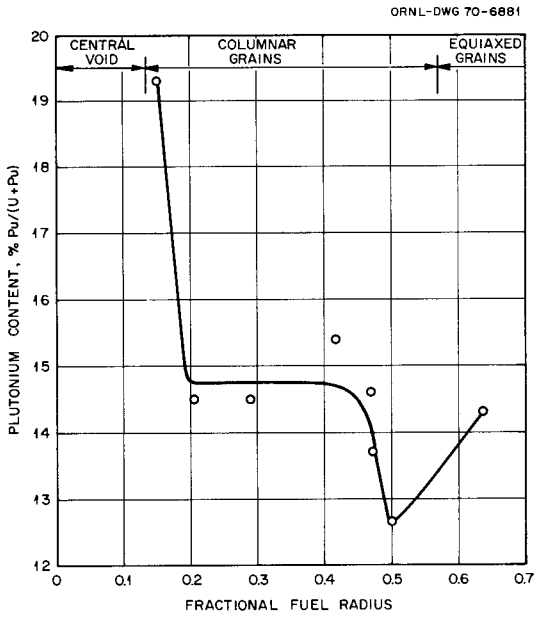

Fig. 4.5. Variation in Pu Content with Radial Position for $(U_{0.85},Pu_{0.15})O_2$ after Irradiation at a Linear Heat Rate of 13.6 kw/ft to a Burnup of 0.7% Fissions per Initial Actinide Metal Atom.

Release of Fission Gases from Mixed Oxide Fuels (W. H. Bridges)

The survey of the release of fission gas from mixed oxide fuels by Cox[4] is being continued and extended. An earlier version of the FMØDEL code was modified for use in a statistical analysis of the adjustable parameters used to describe empirically the release of fission gas from $(U,Pu)O_2$ fuels. The statistical analyses for a number of fuel pins will be performed simultaneously by means of a computer code for regression analysis.

Cladding Performance

Most of the work this quarter on models for cladding performance involved modifications to the mechanical analysis so that it would include load cycling. We continued evaluation of the properties of type 316 stainless steel and development of a discrete-element stress analysis.

Load Cycling (F. J. Homan)

The subroutine package used for mechanical analysis of cladding in the FMØDEL computer code was separated from that code and extensively

modified so that it can handle power-cycling conditions and calculate ratchetting of plastic strains during power cycling. Required for the use of this subroutine are analytical expressions for the pressures of fission gas and of contact between fuel and cladding as functions of time. This simplified model for the cladding provides a powerful tool for use in design studies, parametric analyses, and in fulfilling the analytical requirements for placing irradiation experiments into a reactor. The loss of precision associated with replacing a fuel model with mere analytical expressions seems less severe when one considers that the precision associated with such fuel models is only as good as the experimental data available, and data on many important fuel phenomena (such as creep and hot pressing of mixed oxide fuels while exposed to neutron flux levels typical of an LMFBR) can only be considered as preliminary. In addition, the simplified input and reduced computer time make a cladding model such as this very attractive.

A simple problem was formulated to illustrate the workings of the cladding subroutine. We assumed that the lifetime of the fuel pin was two power cycles, each 4000 hr long. The characteristics of each cycle are tabulated in Table 4.1, and the calculated results are plotted in Fig. 4.6.

Table 4.1. Power Cycle Characteristics Assumed for Test of Cladding Subroutines

	Power	No Power
Duration, hr	3000	1000
Neutron flux, neutrons cm^{-2} sec^{-1}	1.54×10^{15}	0
Cladding temperature, °C		
Inside surface	478	200
Outside surface	433	200
Cladding outer pressure, psi	60	60
Gas pressure, psi		
Cycle 1	Increasing 100 to 300	60
Cycle 2	300 to 600	60
Fuel-cladding contact pressure, psi	3000	0

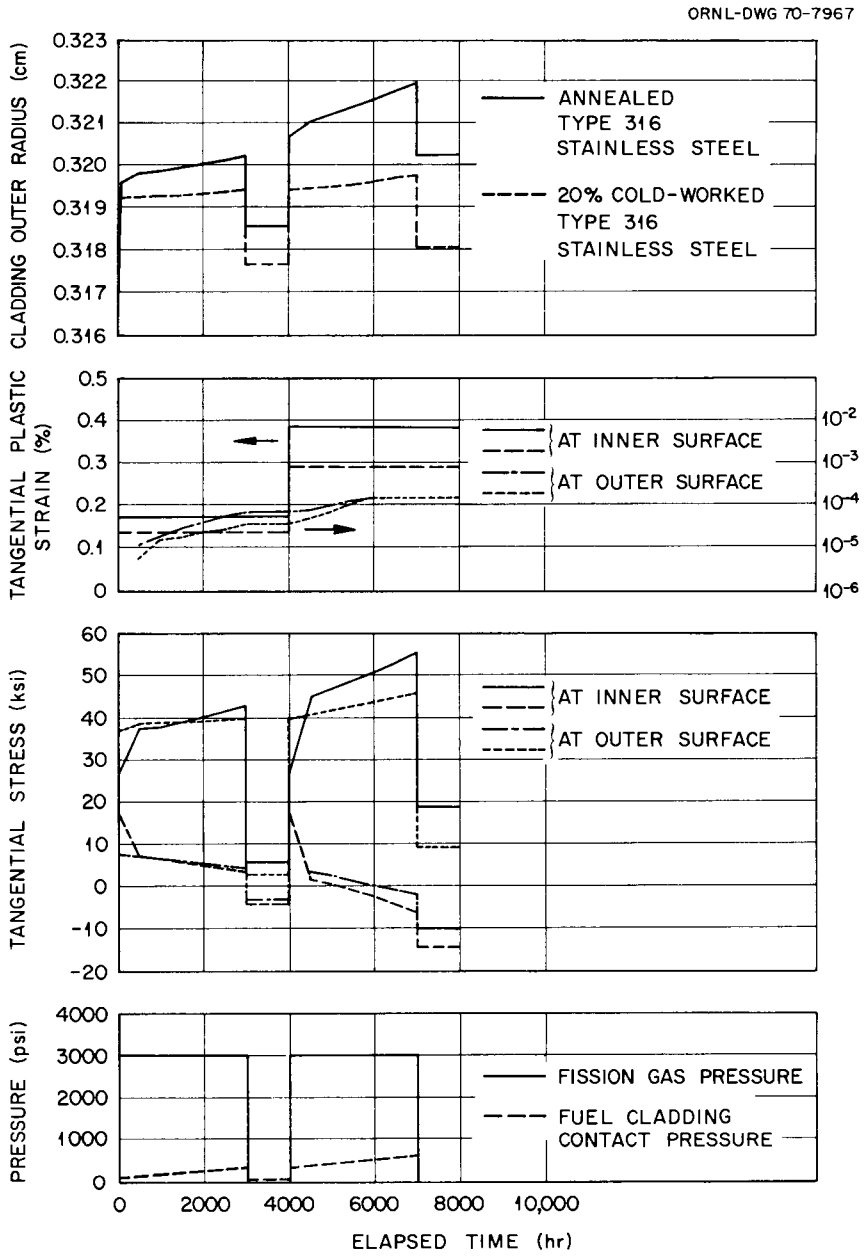

Fig. 4.6. Time Variation of Loads, Stresses, and Strains.

The problem was run for a relatively weak cladding (annealed type 316 stainless steel) and a strong cladding (20% cold-worked type 316 stainless steel). The tensile stress-strain curves used for the two claddings are plotted in Fig. 4.7 at 400 and 600°C. The strain-strain curves[5] derived from Fig. 4.7 are shown in Fig. 4.8. The slope of the strain-strain curve is a measure of the strain hardening that takes place during

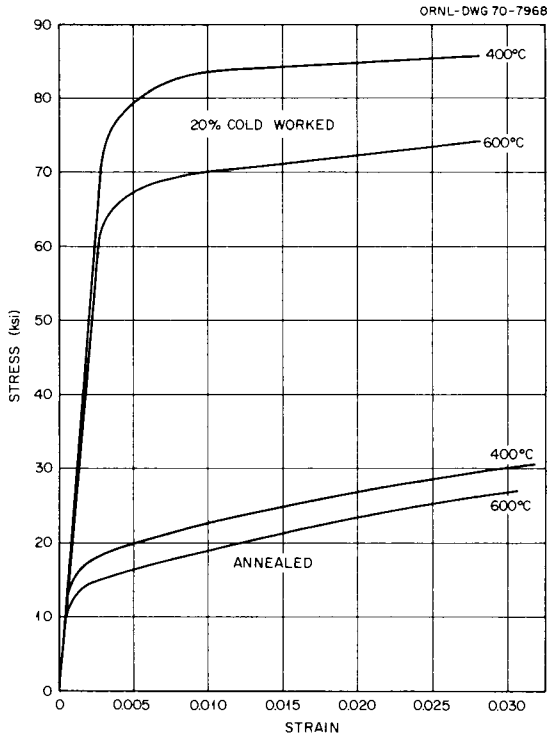

Fig. 4.7. Stress Versus Strain for Type 316 Stainless Steel, Cold Worked 20% and Annealed.

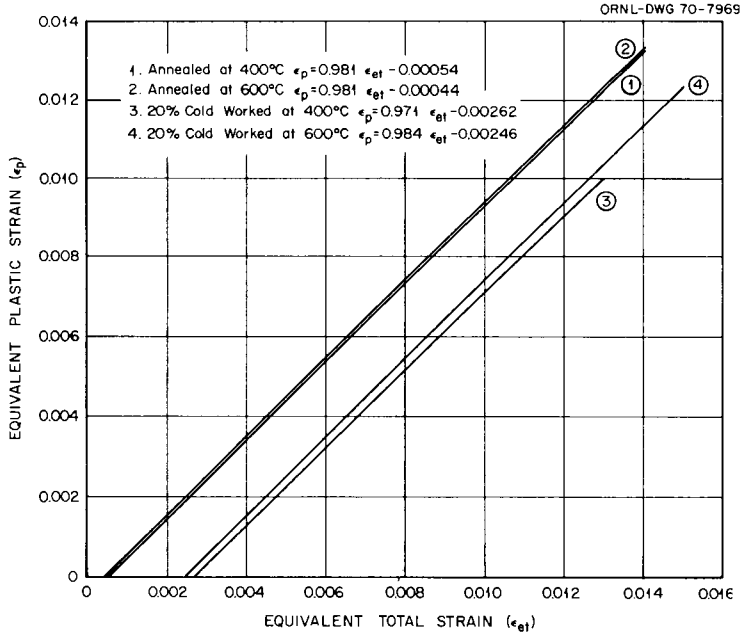

Fig. 4.8. Strain-Strain Curve for Type 316 Stainless Steel.

plastic deformation (a lower slope implies more strain hardening; a perfectly plastic material would have a slope of unity) and the Y-axis intercept is a measure of the elastic strain before plastic deformation. It is interesting to note that the strain-strain curves for all four cases from Fig. 4.7 have nearly the same slope. This greatly simplifies the task of accumulating data. Normally, it would be necessary to plot the strain-strain curves for each cladding material over a range of temperatures — a time-consuming and difficult procedure since a stress-strain curve is required for each strain-strain curve. But due to the similarity of slopes, a good approximation of the strain-strain curve at a given temperature can be obtained from the proportional limit and elastic modulus at that temperature. The 0.2% offset yield stress normally used is not sufficient for this type of analysis because significant plastic deformation has occurred at that stress level; instead, the true proportional limit must be used. The better agreement obtained with the strain-strain curve using the proportional limit is quite clear from the information presented in Table 4.2. Unfortunately, most tensile data are reported as the 0.2% offset yield stress rather than the proportional limit.

The plot of the tangential stress versus time in Fig. 4.6 reveals that the absolute stress level at the inner and outer surfaces of the cladding increases with time. This is due to the influence of that part of the swelling of the cladding due to decrease in void density. The hotter inner surface swells faster than the outer surface and thus increases the tensile stress at the outer surface and the compressive stress at the inner surface. As a result, the plastic strain on the second loading (at 4000 hr) is slightly larger than that at the initial loading, assuming that the tensile proportional limit does not change with time. Such an assumption, however, is not valid. Llewellyn[6] showed that warm working (plastic deformation at elevated temperatures) increases the yield stress and ultimate tensile stress. Claudson et al.[7] showed the increase in yield stress, proportional limit, and ultimate tensile stress caused by neutron bombardment and density loss. An analysis to describe the increase in proportional limit when these phenomena occur simultaneously would require an extensive evaluation of data and is not yet available;

Table 4.2. Summary of Calculated Stresses and Strains

Calculated Parameter[a]	Temperature (°C)	Annealed	20% Cold Worked
E,[b] psi	400	25.1×10^6	25.1×10^6
	600	22.5×10^6	22.5×10^6
PL,[c] psi	400	13,500	72,000
	600	10,000	61,000
0.2% ys,[c] psi	400	18,300	81,000
	600	15,000	67,500
PL/E	400	0.000538	0.00287
	600	0.000444	0.00271
0.2% ys/E	400	0.000730	0.00323
	600	0.000667	0.0030
ϵ_{et} at $\epsilon_p = 0$[c]	400	0.000550	0.00270
	600	0.000449	0.00250

[a] E = elastic modulus
PL = proportional limit
0.2% ys = 0.2% offset yield stress
ϵ_{et} = equivalent total strain
ϵ_p = equivalent plastic strain

[b] Linear interpolation from data presented in Pipes and Tubes for Elevated Temperature Service, USS Bull. 26, ed. 59, p. 62, National Tube Division, United States Steel Corporation, Pittsburgh, Pennsylvania, 1959. No distinction is made between annealed and cold-worked material.

[c] See Fig. 4.8, p. 77, this report.

but a parametric treatment of the problem of plastic-strain ratchetting while the proportional limit increases with time is presented in Fig. 4.9. Here there are five power cycles with characteristics similar to those described in Table 4.1, except that the duration of the cycles is different.

The cycle now has 1900 hr of operation at power followed by 100 hr with no power. In order to examine the effect of a proportional limit that varies with time on the plastic deformation ratchet, we established a factor to increase the initial proportional limit with time. Three cases have been considered: (1) a constant factor of 1, (2) a factor varying from 1 to 2, and (3) a factor varying from 1 to 5. The ratchet resulting from each case is shown in Fig. 4.9, with the tangential stresses at the inner and outer surfaces of the cladding for the first case.

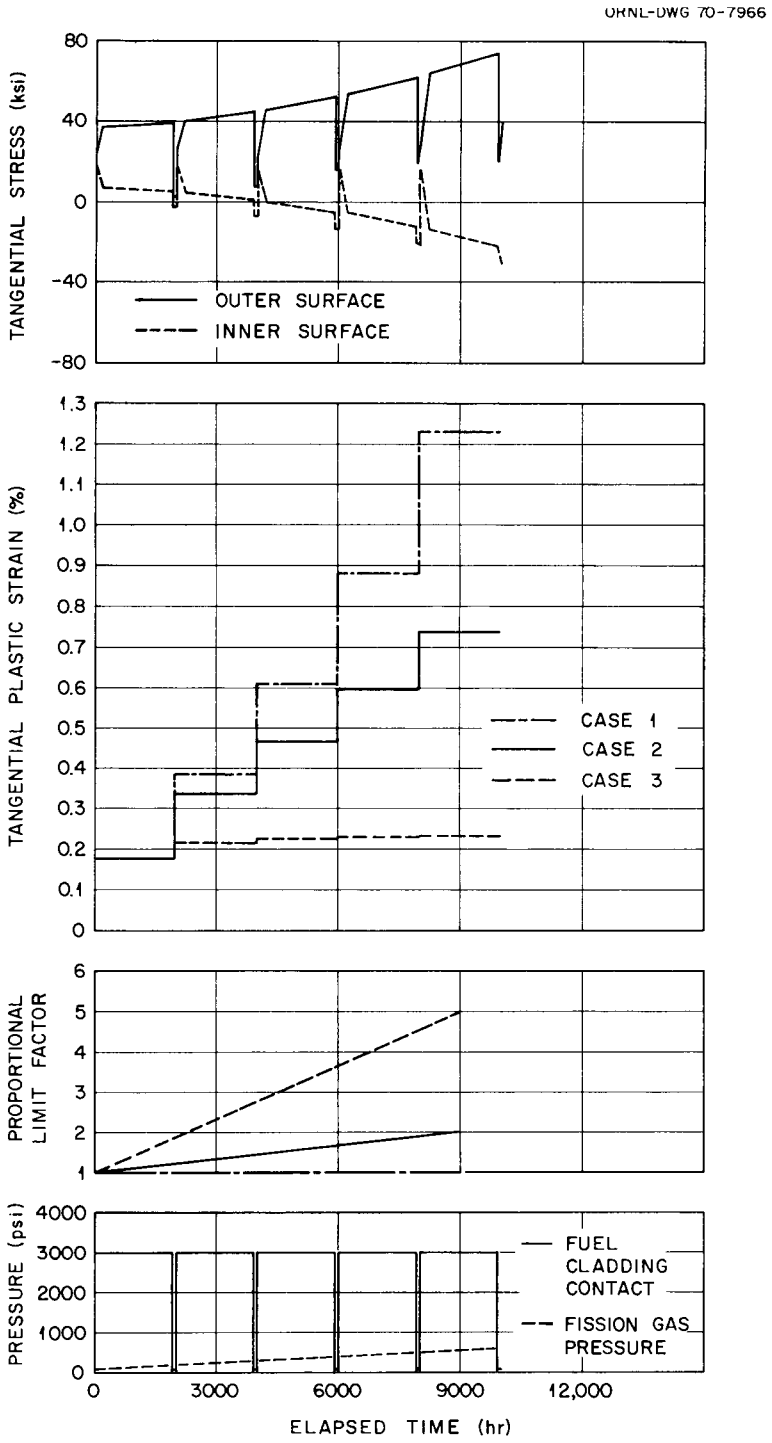

Fig. 4.9. Variation of Load, Porportional Limit, and Tangential Plastic Strain and Stress with Time.

Changes in the stress level after initial loading are dictated by the creep law used. Since the proportional limit and ultimate tensile strength change with time, it would be expected that the creep strength would also change. A truly rigorous analysis would include a creep law for each cycle; but, due to insufficient data, the same creep law was used for all cycles for the three cases plotted in Fig. 4.9.

We are altering the integrated model for performance of fuel and cladding to convert it for use with power cycling.

Physical and Tensile Properties of Type 316 Stainless Steel (W. H. Bridges)

The available data on the physical and tensile properties of type 316 stainless steel were compiled.[8] The data for physical properties cover the density, melting range, specific heat, thermal expansion, thermal conductivity, thermal diffusivity, emissivity, and electric resistivity. The data for tensile properties include the tensile and yield strengths at room temperature and elevated temperatures, Poisson's ratio, modulus of elasticity, and ductility. The available information was developed in the light of such influencing factors as cold work, the effect of Na and gas environments, and, in particular, the effects of irradiation on the various properties.

A continuation of this effort will include the creep and stress-rupture properties, fatigue, and other mechanical properties of value in reactor design and modeling studies.

Discrete-Element Analysis of the Creep of Stainless Steel Tubing for LMFBR Application (B. R. Dewey[9])

We completed a computer program for the analysis of stress in tubing where there exists a radial variation of temperature and material properties and ran limited test cases. This "discrete-element" analysis models the tubing as a series of concentric, hollow, circular cylinders and solves the interaction problem that results from the assemblage.

Some experimental data on the creep and stress rupture of type 304 stainless steel tubing have been reported recently by Shively and Mahoney,[10] who suggested the creep law

$$\dot{\epsilon} = A\sigma_e^n \exp\,[-Q/RT] \ ,$$

where σ_e is equivalent stress, T is temperature, and the other parameters are constants: A = 1.662 (10^5), n = 2.63, Q = 88,840, and R = 2. The material was tested as received. The computed comparisons are given in Table 4.3 and 4.4. At the specified initial loading, the tubing was not stressed above the proportional limit.

Table 4.3. Biaxial Creep of Cold-Worked Type 304 Stainless Steel Tubing at 649°C

Internal Pressure (psi)	Time (hr)	Experimental[a] Circumferential Strain (%)	Computed Circumferential Strains, %	
			Inner Wall	Outer Wall
1750	103	0.050	0.031	0.042
1750	408	0.168	0.121	0.178
1750	703	0.319	0.210	0.308
1750	1008	0.403	0.300	0.440
1460	103	0.084	0.016	0.028
1460	503	0.151	0.092	0.137
1460	1008	0.235	0.185	0.275
1460	2016	0.571	0.370	0.550

[a]J. H. Shively and M. W. Mahoney, Thermal Gradient Effects on Stress-Rupture Behavior of Thin-Walled Tubing, AI-AEC-12896 (January 1970).

Table 4.4. Stress Rupture of Cold-Worked Type 304 Stainless Steel with Inner and Outer Temperatures of 713 and 685°C

Internal Pressure (psi)	Rupture Time (hr)	Experimental[a] Peak Strain (%)	Computed Strains at Rupture Time, %	
			Inner Wall	Outer Wall
1530	177	2.2	1.6	2.9
1160	558	2.8	2.1	5.2
1160	392	2.5	1.5	3.7

[a]J. H. Shively and M. W. Mahoney, Thermal Gradient Effects on Stress-Rupture Behavior of Thin-Walled Tubing, AI-AEC-12896 (January 1970).

Note that the computed strain gradients shown in Tables 4.3 and 4.4 are enhanced by the thermal variation of material properties; the contribution due to thermal stress apparently relaxes rather quickly.

Notes

1. C. M. Cox and F. J. Homan, PRØFIL – A One-Dimensional FØRTRAN-IV Program for Computing Steady-State Temperature Distributions in Cylindrical Ceramic Fuels, ORNL-TM-2443, Addendum (August 1969).

2. C. S. Morgan and C. S. Yust, Metals and Ceramics Div. Ann. Progr. Rept. June 30, 1964, ORNL-3670, pp. 4–5.

3. J. R. MacEwan, J. Am. Ceram. Soc. 45(1), 37–41 (1962).

4. C. M. Cox, Nucl. Safety 10(5), 380–391 (September–October 1969).

5. For a discussion of the use of strain-strain curves in the calculation of plastic strains, see Donald F. Johnson, Analysis of Elastic-Plastic Stress Distribution in Thin-Wall Cylinders and Spheres Subjected to Internal Pressure and Nuclear Radiation Heating, NASA-TND-271, Appendix B (April 1960).

6. D. T. Llewellen and J. D. Murray, "Cold Worked Stainless Steels," pp. 197–212 in Metallurgical Developments in High-Alloy Steels, ISI Spec. Rept. 86, Iron and Steel Institute, London, 1964.

7. T. T. Claudson et al., Nucl. Appl. & Technol. 9(1), 10–23 (July 1970).

8. W. H. Bridges, The Physical and Tensile Properties of Type 316 Stainless Steel, ORNL-TM-3037, in press.

9. Consultant from The University of Tennessee.

10. J. H. Shively and M. W. Mahoney, Thermal Gradient Effects on Stress-Rupture Behavior of Thin-Walled Tubing, AI-AEC-12896 (January 1970).

CLADDING AND OTHER STRUCTURAL MATERIALS

5. MECHANICAL PROPERTIES OF ALLOYS IN REACTOR ENVIRONMENTS AND DEVELOPMENT OF LMFBR CLADDING AND STRUCTURAL MATERIALS

J. R. Weir, Jr. H. E. McCoy, Jr.

This program is concerned with the effects of irradiation on the mechanical properties of various metals of potential use in nuclear reactors. The materials of primary concern are types 304 and 316 stainless steel, both materials of interest for liquid-metal fast breeder reactors (LMFBR). These alloys are being exposed to high neutron fluences, and the resulting changes in density, microstructure, and mechanical properties are being measured. Other materials under study include Incoloy 800, V, and Nickel 270. Some attention is also being given to the use of particle accelerators to simulate neutron damage.

Austenitic Stainless Steels

Effect of Fast-Neutron Irradiation on the Creep-Rupture Properties of Type 304 Stainless Steel at 600°C (E. E. Bloom, J. O. Stiegler)

The effects of irradiation damage on the mechanical properties of cladding materials at temperatures above about 350°C are of concern for LMFBR applications. For specimens irradiated and tested at temperatures that produce a damage structure that consists of voids and dislocation loops, the tensile yield strength is increased and the uniform elongation is reduced.[1-3] Holmes et al.[1,2] investigated the tensile properties of type 304 stainless steel irradiated at 450 ± 50°C to 1.1×10^{22} neutrons/cm^2 (> 0.1 Mev). At test temperatures below 0.5 of the absolute melting temperature (T_m), the ductility was reduced by the onset of plastic instability (local necking) induced by the increased flow stress and reduced rates of work hardening. Above 0.5 T_m, He embrittlement was thought to control ductility. Carlander et al.[3] investigated the change in tensile properties as a function of fast-neutron fluence and postirradiation test temperature. For specimens irradiated at temperatures of 370 to 470°C

and tensile tested at 450°C, the changes in yield strength and uniform elongation were found to saturate at about 2×10^{22} neutrons/cm^2 (> 0.1 Mev).

Previous investigations, in which specimens were irradiated in thermal reactors, showed that at test temperatures above about 550°C the He produced by transmutation significantly reduced the ductility, particularly at the low strain rates encountered in creep-rupture tests.[4,5] This loss of ductility was ascribed to the increased rate at which cracks were initiated and propagated due to the presence of He at the grain boundaries. The effect of irradiation to high fast-neutron fluences on the creep-rupture properties has not been investigated. Of particular interest are the changes in properties that occur when the specimen contains the void and dislocation loop structure formed at irradiation temperatures below about 650°C and when the test is conducted at a temperature at which He embrittlement is an important factor (i.e., above about 550°C). The objective of this work was to study the creep-rupture properties of specimens that were irradiated under different conditions in order to relate the changes in creep-rupture properties to the microstructure produced by irradiation.

Sheet specimens of type 304 stainless steel were machined from a safety-rod thimble[6] irradiated in the Experimental Breeder Reactor-II (EBR-II). The thimble, a hexagonal tube about 3.2 cm across each flat, 0.10 cm thick, and 116.6 cm long, was placed in the reactor in the annealed condition and had an average grain diameter of 0.045 mm. It was irradiated in a row 3 position of the reactor to a peak fluence of 6.7×10^{22} neutrons/cm^2 (> 0.1 Mev). There was a gradient in both neutron fluence and irradiation temperature along the length of the thimble, as shown in Fig. 5.1. Because of the small dimensions of the thimble, only two specimens of a given irradiation temperature and fluence condition were obtained. We investigated the effects of varying fast-neutron fluence and irradiation temperature by removing specimens from those segments of the thimble located below and above the reactor core.

In order to expand the range of irradiation temperature beyond that available through an examination of the safety-rod thimble, specimens of type 304 stainless steel were irradiated in an experimental subassembly

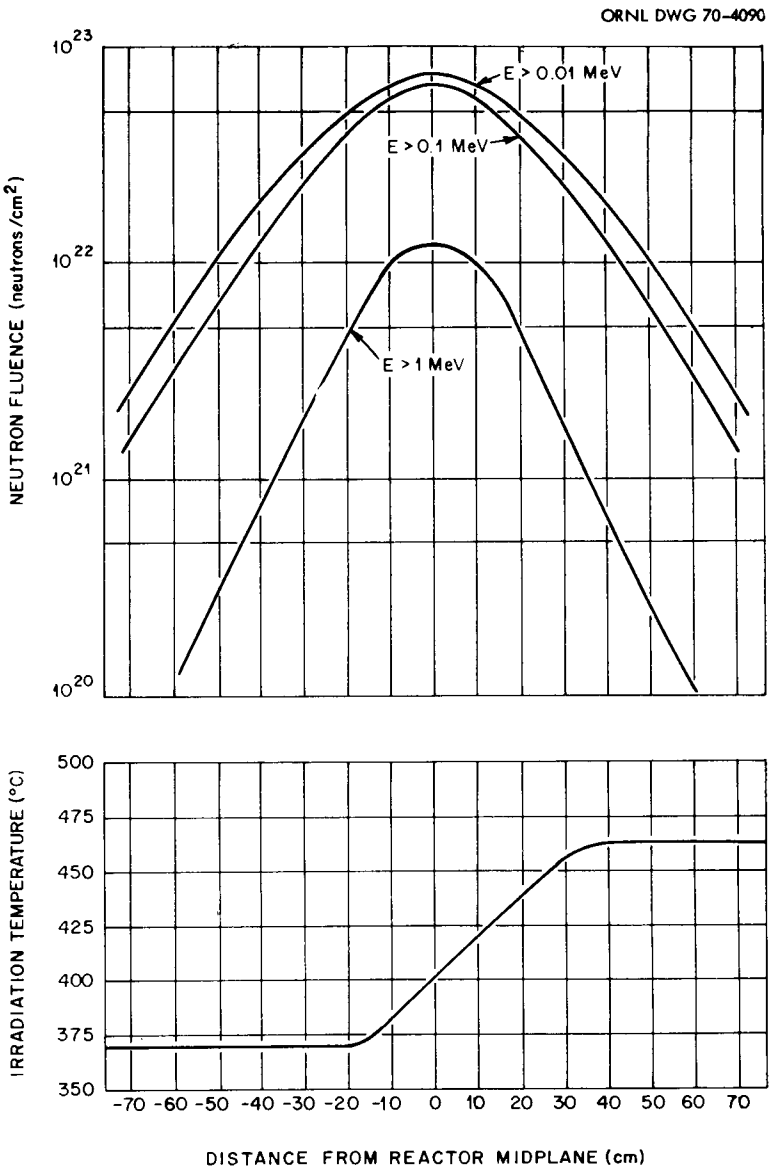

Fig. 5.1. Fast-Neutron Fluence and Irradiation Temperature for Experimental Breeder Reactor-II Safety-Rod Thimble.

located in row 2 of the EBR-II. The specimens were irradiated in specimen holders such as the one shown schematically in Fig. 5.2. A gas gap between the holder surface and the inside surface of the tube element provided a barrier to radial heat flow and allowed temperatures above that of the reactor coolant to be obtained. The experiment was designed and calibrated on the basis of nuclear heating rates as a function of position within the reactor as determined in a previous experiment. The

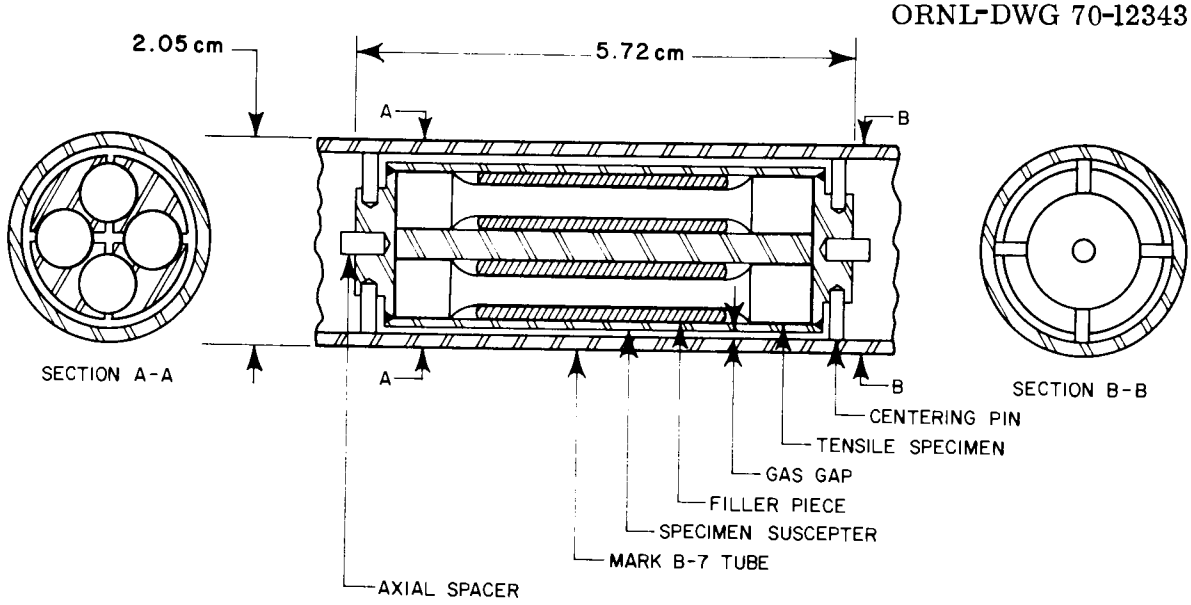

Fig. 5.2. Schematic Drawing of Specimen Holder Used in Irradiation Experiments in Experimental Breeder Reactor-II.

calculated irradiation temperature was 600°C for a peak gamma heating rate of 3.5 w/g. Gamma heating rates of 3.0 and 4.0 w/g would give irradiation temperatures of 570 and 630°C, respectively.

Postirradiation creep-rupture tests were performed in air at 600 ± 5°C in lever-arm creep machines located in hot cells. Specimen elongation as a function of time was determined by a linear differential transformer that measured the relative movement of the upper and lower specimen grips. Creep-rupture tests on specimens machined from an unirradiated EBR-II safety-rod thimble were run to determine the change in properties due to irradiation. Tested specimens were examined by optical metallography, transmission microscopy, and scanning electron microscopy.

Specimens irradiated to fast-neutron fluences of 2×10^{21} to 6.7×10^{22} neutrons/cm^2 (> 0.1 Mev) at temperatures between 370 and 470°C contained voids and faulted interstitial dislocation loops. The details of the microstructures were reported elsewhere.[7] At low fast-neutron fluences [below 10^{22} neutrons/cm^2 (> 0.1 Mev)] the damage was heterogeneously distributed. Dislocation loops were clustered around grown-in dislocation lines, and voids were often located on dislocation lines. For specimens irradiated to a constant fast-neutron fluence, the concentrations of voids and dislocation loops decreased and their size increased

with increasing temperature. Examples of the structures of dislocation loops and voids for specimens irradiated at 370 to 380°C and 460 to 470°C are shown in Figs. 5.3 and 5.4, respectively. Regions about 1000 A wide adjacent to grain boundaries were denuded of these defects. At fluences above about 1×10^{22} neutrons/cm^2 (> 0.1 Mev) the concentration of loops was so high that measurements by quantitative microscopy were impossible. After irradiation at 570 to 630°C to fluences of 2.5 to 3.5×10^{22} neutrons/cm^2 (> 0.1 Mev), the damage structure consisted of a dislocation network, a few unfaulted dislocation loops, and voids up to about 600 A in diameter. A typical microstructure is shown in Fig. 5.5. The dark, rectangular particle is a thin sheet precipitate.

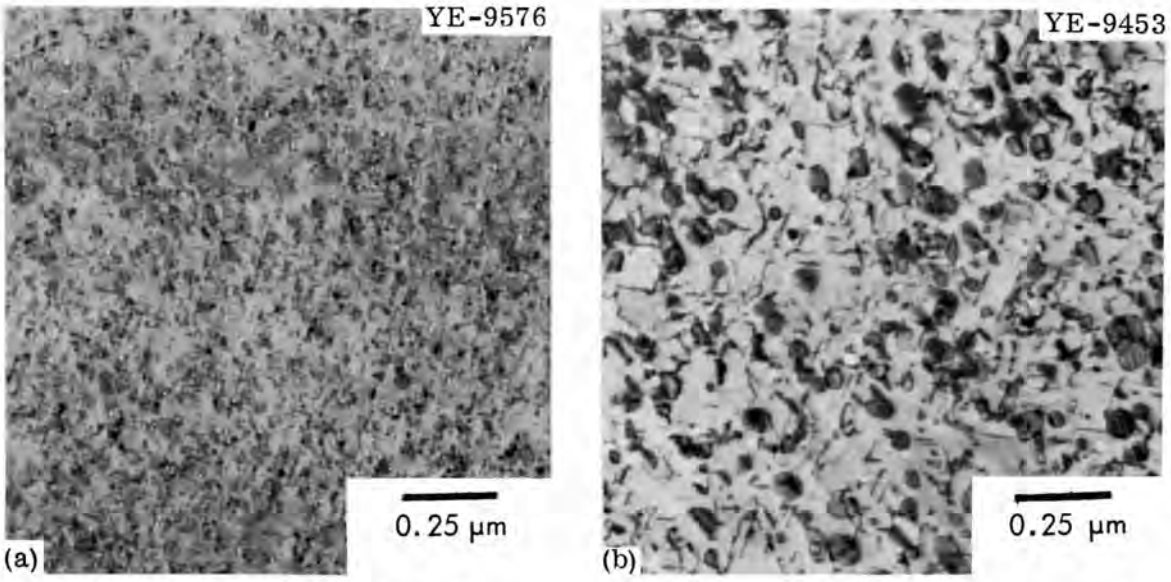

Fig. 5.3. Dislocation Loops in Type 304 Stainless Steel Irradiated at (a) 370°C to 0.8×10^{22} neutrons/cm^2 (> 0.1 Mev) and (b) 460°C to 0.9×10^{22} neutrons/cm^2 (> 0.1 Mev).

The creep-rupture properties at 600°C of sheet specimens removed from an unirradiated safety-rod thimble and of rod specimens of the same heat (BO) irradiated in the experimental subassembly are shown in Fig. 5.6. The strength properties of these two heats of type 304 stainless steel are typical for this alloy, and the variation in properties between these two heats is well within the variation between heats, as discussed

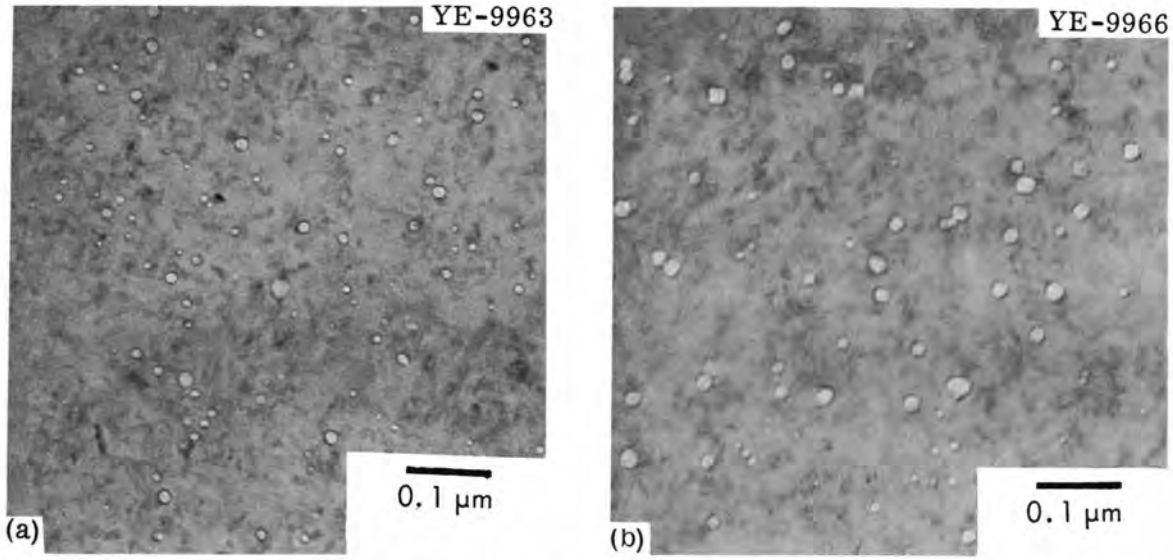

Fig. 5.4. Voids in Type 304 Stainless Steel Irradiated at (a) 370°C to 1.2×10^{22} neutrons/cm^2 (> 0.1 Mev) and (b) 460°C to 2.1×10^{22} neutrons/cm^2 (> 0.1 Mev).

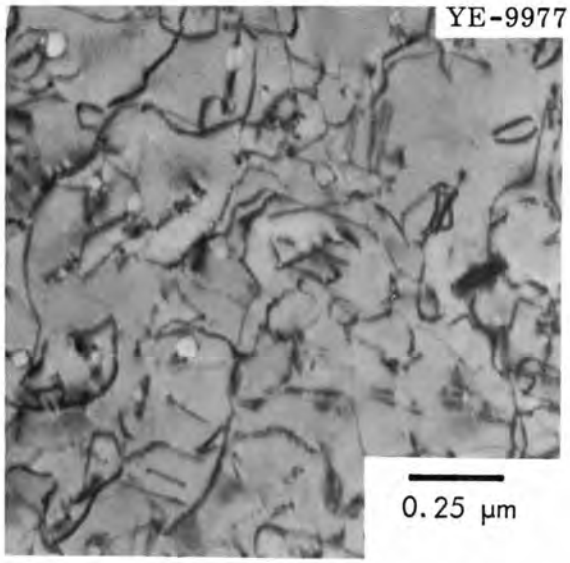

Fig. 5.5. Dislocation Network and Voids in Type 304 Stainless Steel Irradiated at 600°C to 3.5×10^{22} neutrons/cm^2 (> 0.1 Mev).

by Smith.[8] Ductility, as measured by total elongation, ranged from 16 to 40% for the safety-rod thimble specimens and from 9 to 25% for specimens from heat B0.

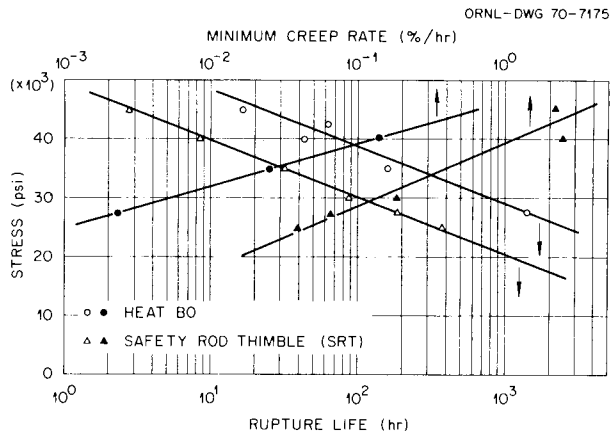

Fig. 5.6. Creep-Rupture Properties of Two Heats of Type 304 Stainless Steel at 600°C.

The effect of fast-neutron fluence on the rupture life of safety-rod thimble specimens irradiated at 370 to 460°C and tested at 600°C and 27,500 psi is shown in Fig. 5.7. The rupture life of the unirradiated safety-rod thimble at this temperature and stress was 185 hr. Specimens irradiated at 370°C ruptured sooner than specimens irradiated at 460°C. For each irradiation temperature, the rupture life decreased sharply with increasing fast-neutron fluence. A specimen irradiated at 410°C to about 6.5×10^{22} neutrons/cm^2 (> 0.1 Mev) had a rupture life of 0.55 hr, a factor of 330 less than that of the unirradiated material. The total elongation as a function of fluence for these specimens is shown in Fig. 5.8. The total elongation was reduced from values of 15 to 25% for unirradiated specimens tested at these conditions to values of 2 to 3% for specimens irradiated to fluences of 4×10^{21} neutrons/cm^2 (> 0.1 Mev). The ductility decreased continuously with increasing fast-neutron fluence and was essentially independent of irradiation temperature from 370 to 460°C.

Typical curves for strain versus time for specimens irradiated at 370°C are shown in Fig. 5.9. The primary stage of creep lasted only a very short time in irradiated specimens, usually less than 1 hr, as compared to 12 hr for an unirradiated specimen. Secondary creep rates were reduced by the irradiation, but for specimens irradiated to fluences greater than about 1×10^{22} neutrons/cm^2 (> 0.1 Mev) fracture occurred

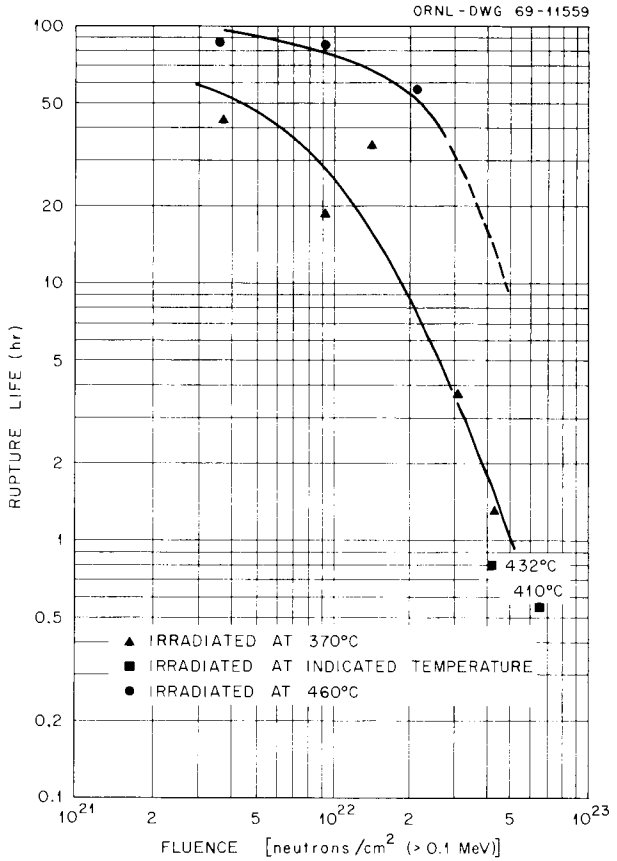

Fig. 5.7. Rupture Life of Irradiated Type 304 Stainless Steel at 600°C and 27,500 psi. The rupture life of an unirradiated specimen tested at this temperature and stress was 185 hr.

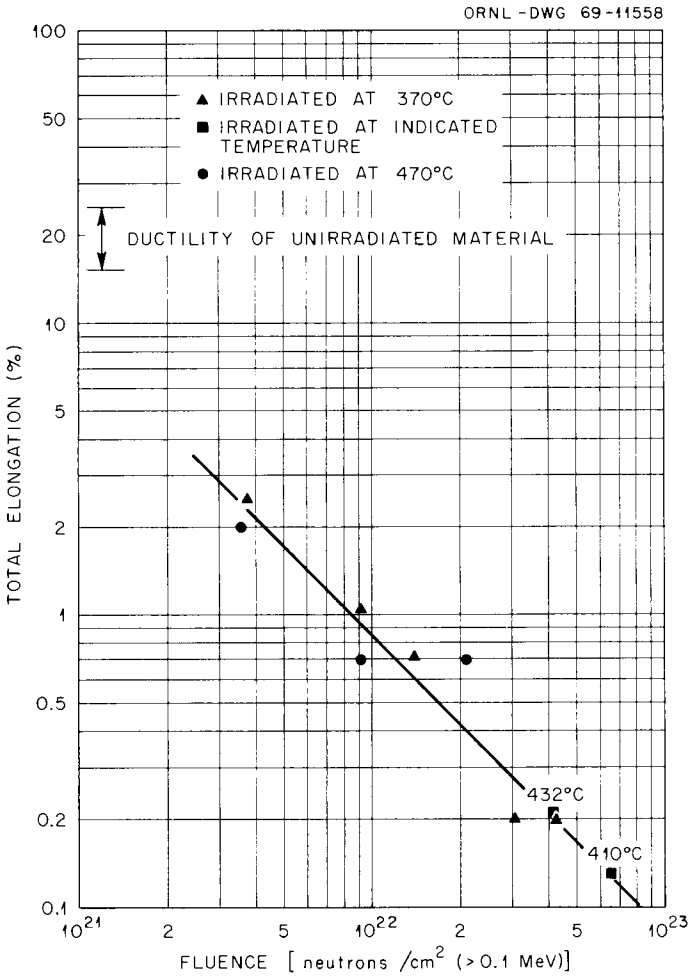

Fig. 5.8. Ductility of Irradiated Type 304 Stainless Steel Tested at 600°C and 27,500 psi.

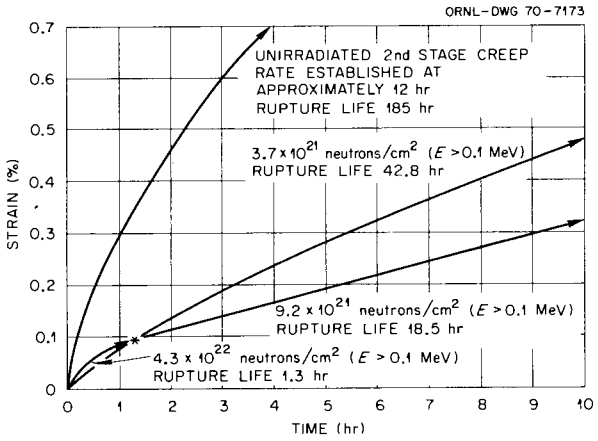

Fig. 5.9. Effect of Irradiation at 370°C on the Creep of Type 304 Stainless Steel at 600°C and 27,500 psi.

in such short times that the creep rates have little significance. None of the irradiated specimens entered tertiary creep.

Creep-rupture properties of specimens irradiated at 600°C to fast-neutron fluences of 2.5 to 3.5 × 10^{22} neutrons/cm^2 (> 0.1 Mev) are shown in Fig. 5.10. For these irradiation conditions, the rupture life changed little or not at all; however, the ductility was significantly reduced. For example, an unirradiated specimen tested at 27,500 psi had elongated about 5% at the onset of tertiary creep and a total of 9% at fracture as compared to an irradiated specimen tested at the same stress that

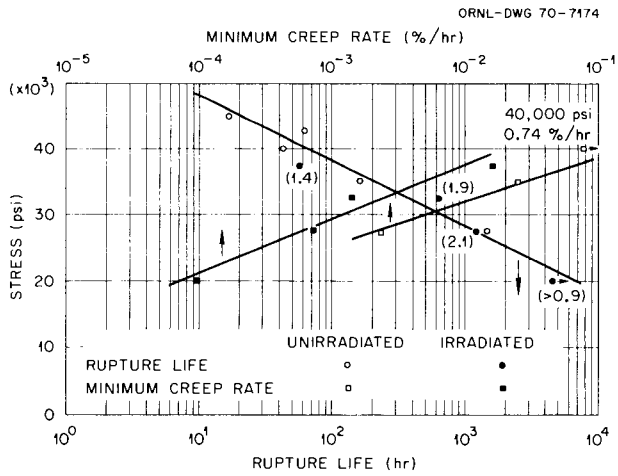

Fig. 5.10. Effect of Irradiation at 600°C to 2.5 to 3.5 × 10^{22} neutrons/cm^2 (> 0.1 Mev) on the Creep-Rupture Properties of Type 304 Stainless Steel at 600°C.

elongated a total of 2.1% with no tertiary creep. Minimum creep rates of irradiated specimens were about one quarter of those of the unirradiated material. The net result of the reduced minimum creep rates and reduced ductilities was that irradiation did not change the rupture life.

All irradiated specimens fractured intergranularly. Figure 5.11 is a scanning electron photomicrograph of a specimen irradiated at 410°C to 6.7×10^{22} neutrons/cm^2 (> 0.1 Mev) and tested at 600°C and 27,500 psi stress. The intergranular fracture began on the left side of the specimen and propagated to the right. The right portion failed last in a shear mode, presumably at a very high stress level and high strain rate. Optical metallography confirmed that even in those specimens irradiated to relatively low fluences the fractures were intergranular with no evidence of deformation within the matrix and little or no cracking at the grain boundaries in the region adjacent to the fracture. Thus, it appears that a grain-boundary crack, once initiated, propagates rapidly to cause failure.

For the specimens from the EBR-II safety-rod thimble, the irradiation temperature was lower than the test temperature. Thus, it was important to determine the changes in microstructure that occurred during the test. Figure 5.12 is a transmission photomicrograph of the area near the fracture of the same specimen as shown in Fig. 5.11. The specimen had been at 600°C for about 4 hr before failure occurred. Before testing, the structure consisted of voids and faulted dislocation loops. During the test, the dislocation loops unfaulted to produce the dislocation structure shown in Fig. 5.12. Previous results[9] showed that unfaulting of the dislocation loops can occur during annealing 1 hr at 600°C. Thus, it is probable that the dislocation loops unfaulted during the 3-hr hold at 600°C before application of the stress. The density and configurations of dislocations were very similar to those in a specimen irradiated under the same conditions and then annealed for 2 hr at 600°C. The lack of dislocation tangles and the similarity of microstructures between stressed and unstressed specimens are evidence that little deformation occurred within the matrix. The void concentration and distribution of void sizes in the tested specimen were about the same as those in specimens in the irradiated condition.

Fig. 5.11. Fracture of Type 304 Stainless Steel Irradiated at 410°C to 6.7×10^{22} neutrons/cm^2 (> 0.1 Mev) and Tested at 600°C and 27,500 psi.

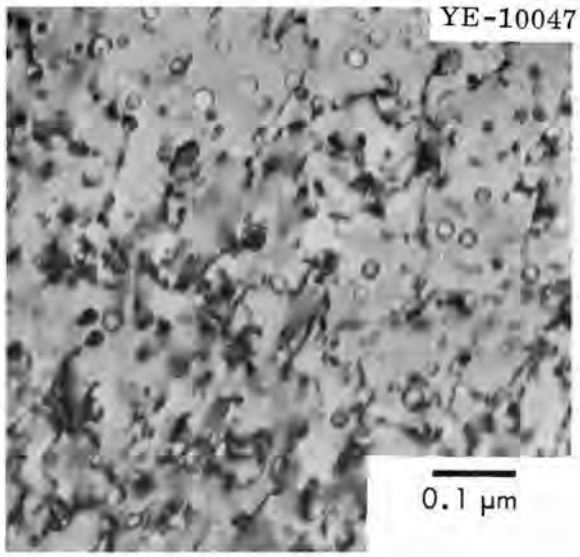

Fig. 5.12. Dislocation Structure of Type 304 Stainless Steel Irradiated at 410°C to 6.7×10^{22} neutrons/cm^2 (> 0.1 Mev) and Tested at 600°C and 27,500 psi.

It is well documented[4,5,10] that the He produced during the irradiation caused a reduction in ductility and rupture life due to its effects on grain-boundary fracture processes. The specimen irradiated at 410°C to 6.7×10^{22} neutrons/cm^2 (> 0.1 Mev) contained about 12 ppm He (ref. 11), exhibited about 0.1% total elongation, and ruptured in 0.5 hr (a factor of 330 less than the time for the unirradiated material). King[10] showed that a uniform concentration of 20 ppm He reduced the rupture life of annealed type 304 stainless steel from 900 to 40 hr at 600°C and 30,000 psi. The reduction in rupture life and ductility of the fast-neutron irradiated specimens cannot be entirely due to the He produced by irradiation. The intergranular fracture observed at elevated temperatures is believed to be initiated by grain-boundary sliding.[12] In the irradiated specimens, the regions adjacent to the grain boundaries were denuded of the damage structure, and deformation along the boundaries probably occurred similarly in unirradiated and irradiated specimens. When this deformation occurred, stresses were concentrated at constraints such as jogs and grain-boundary junctions. In an unirradiated specimen, these stresses can be reduced by deformation within the matrix. For irradiated specimens, deformation in the matrix is impeded by the defect

structure. The propagation of cracks nucleated in these regions of high stress along grain boundaries is likely to be enhanced by the presence of He.

Thermomechanical Treatments of Type 316 Stainless Steel (Dieter Fahr)

In many cases the mechanical properties after irradiation have been dependent upon the microstructure of the material. The specific effects of variables such as grain size, distribution and size of precipitates, and number and configuration of dislocations have not been clearly defined for type 316 stainless steel. Studies are under way to select thermomechanical treatments for future reactor experiments on the basis of the resulting microstructures. The principal criteria for selection consider the interrelation between precipitates and the nucleation of voids, the effect of dislocations (as vacancy sinks) on swelling, the possibility of trapping He bubbles by means of precipitates within the matrix to prevent their ultimate concentration within the grain boundary, irradiation-inducible precipitation, grain size, and effects of precipitation on creep properties.

Type 316 stainless steel specimens with 20% cold work were annealed for 1 and 10 hr at 450, 550, 650, and 750°C. Electron photomicrographs did not reveal any difference in microstructure between the cold-worked material and that annealed at temperatures as high as 650°C (Figs. 5.13 and 5.14). After 1 hr at 750°C, some recrystallized grains could be observed (Fig. 5.15), and recrystallization and grain growth had taken place after 10 hr at 750°C (Fig. 5.16), leaving many precipitates within the grains and only a few along the grain boundaries. The distribution of the precipitate particles strongly suggests that precipitation took place within the slip bands and along the grain boundaries of the cold-worked grains. There was practically no precipitation at twin boundaries that formed during grain growth.

The effects of small amounts of cold and "warm" work on the recrystallized grains and the interaction between dislocations and the established precipitation structure will be studied. Other investigations concentrate on improving the postirradiation mechanical properties of

Fig. 5.13. Electron Photomicrograph of Type 316 Stainless Steel after 20% Reduction in Area at Room Temperature. 52,000×.

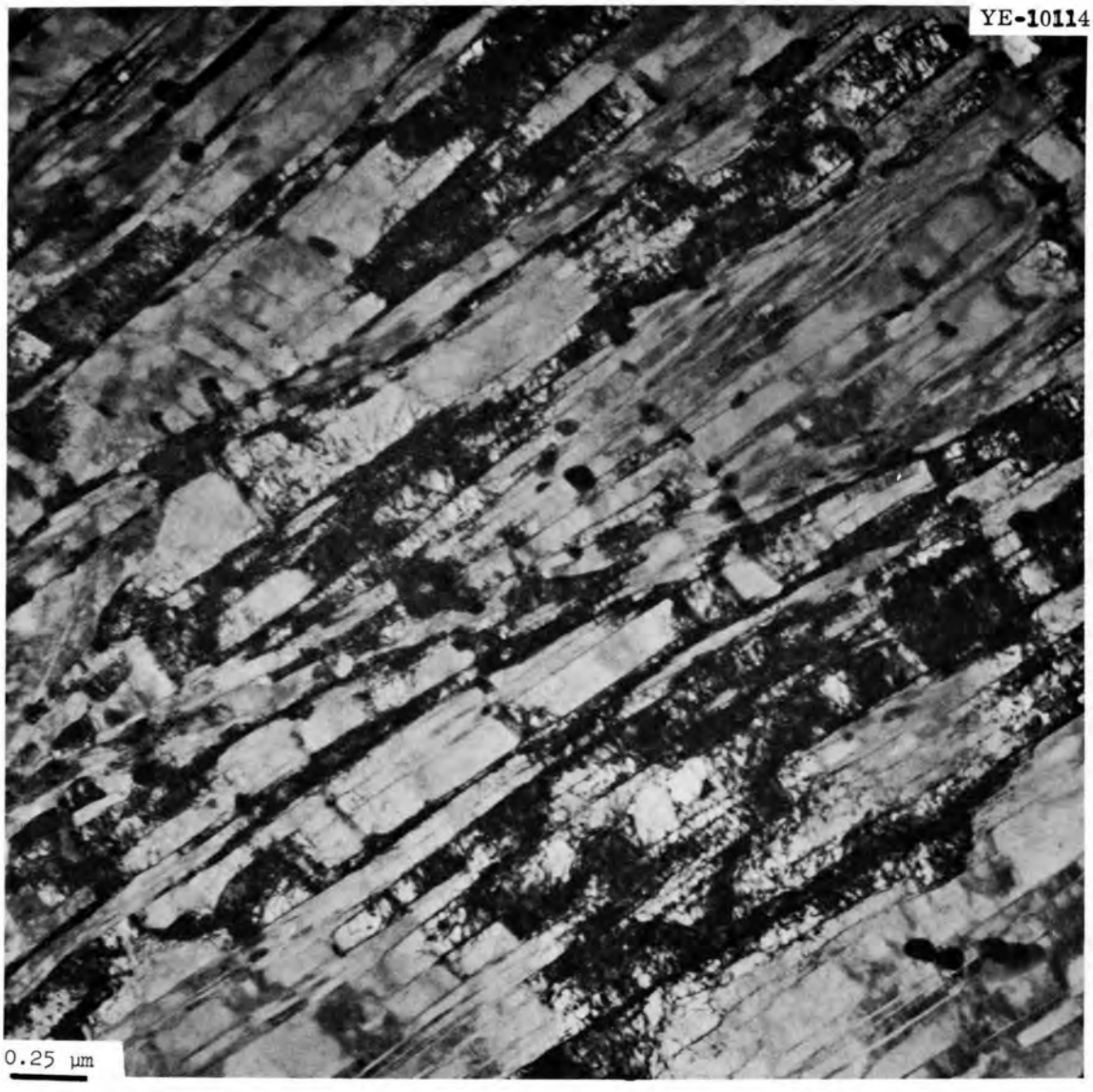

Fig. 5.14. Electron Photomicrograph of Type 316 Stainless Steel after 20% Reduction in Area at Room Temperature and Annealing for 10 hr at 650°C. 49,250×.

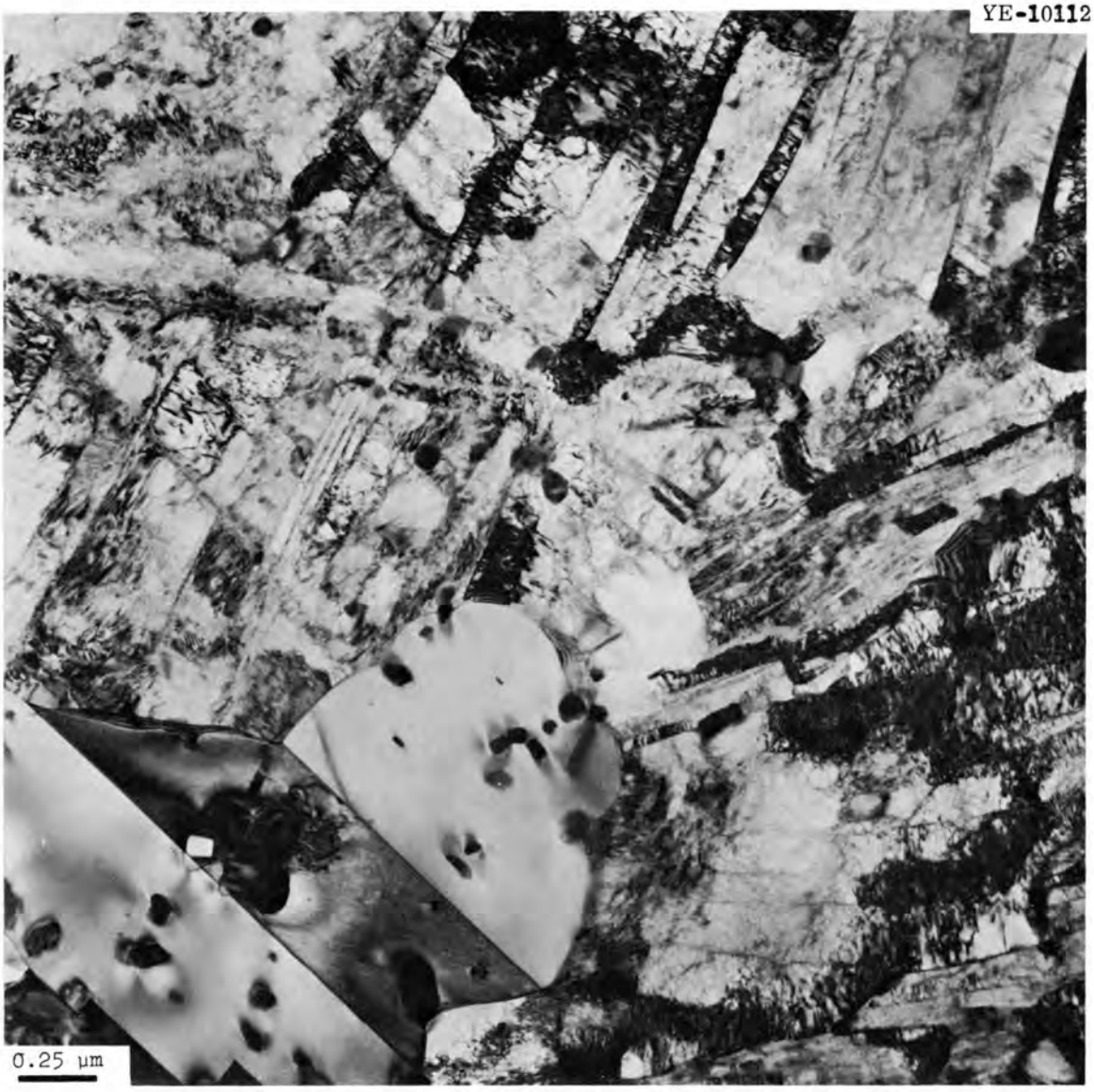

Fig. 5.15. Electron Photomicrograph of Type 316 Stainless Steel after 20% Reduction in Area at Room Temperature and Annealing for 1 hr at 750°C. 56,500X.

Fig. 5.16. Electron Photomicrograph of Type 316 Stainless Steel after 20% Reduction in Area at Room Temperature and Annealing for 10 hr at 750°C. 35,500×.

type 316 standard and Ti-modified st[illegible]less steels by means of thermo-mechanical treatments while maintaining an ultrafine grain size.

Formation of Voids in Irradiated Nickel 270 (J. O. Stiegler, E. E. Bloom)

Since the initial observation by Cawthorne and Fulton[13,14] that three-dimensional cavities or voids are produced in stainless steel during fast-neutron irradiation at elevated temperatures, many investigations have verified the phenomenon and shown it to be a common occurrence in metals and alloys irradiated between about 0.3 and 0.5 of their absolute melting temperature. Although voids are commonly observed, the kinetics governing their nucleation and growth vary widely between different materials.

For example, voids are observed in Ni (refs. 15, 16) after irradiation to fluences only slightly greater than 10^{19} neutrons/cm^2, while fluences in excess of 10^{21} neutrons/cm^2 are required to produce observable voids in stainless steel.[7] Relatively small differences in the impurity level in metals also influence the nature, amount, and distribution of the damage produced at elevated temperatures. At low fluences (about 10^{20} neutrons/cm^2), both voids and dislocation loops form in high-purity (99.9999%) Al, but only loops occur in materials of commercial purity.[17] Voids are eventually produced in the Al of commercial purity, but only at fluences in excess of 10^{22} neutrons/cm^2. Even among the austenitic stainless steels, wide variations in void sizes and concentrations are observed for equivalent irradiation exposures. Lauritzen et al.[18] showed that the voids produced in type 347 stainless steel irradiated in the EBR-II at about 660°C were both smaller and more numerous than those formed in type 304 stainless steel. Bloom and Stiegler[19] showed that the addition of 0.18 wt % Ti to type 304 stainless steel significantly reduced the concentration of voids after irradiation in EBR-II to a fluence of 1.6×10^{22} neutrons/cm^2 at about 450°C.

Helium has been shown to have a strong influence on void formation. In experiments in which damage was introduced by cyclotron irradiation, Nelson and Mazey[20] showed that a uniform concentration of a few parts per million of He (also introduced by cyclotron) greatly increased the concentration of voids. Bloom and Stiegler[21] verified this finding for neutron irradiation. Farrell, King, and Wolfenden[22] showed that

parts-per-million quantities of H or He, uniformly distributed, greatly increased void concentrations in Al.

It is clear from this discussion that material variables are at least as important as irradiation conditions in determining the damage produced in metals and alloys at elevated temperatures. Until the role of impurities in the damage process is clarified, a theoretical understanding of the mechanisms that cause nucleation and growth of voids will be clouded by apparently conflicting experimental observations.

In this report we present some observations on relatively pure Ni. Although the observations are in conflict with those of other examinations of Ni, we believe that the differences are real and significant and that an understanding of these conflicts will contribute to an understanding of the broader problem.

The material used in this investigation was the commercial product Nickel 270, which is 99.98% pure with respect to metallic elements. A chemical analysis, including nonmetallic impurities, is given below:

Element	Content (wt %)
Mo	< 0.02
Cr	0.03
Ti	< 0.02
C	0.004
Fe	0.07
Si	< 0.01
Mn	0.08
W	0.01
Zr	< 0.01
V	< 0.01
Co	0.10
Cu	0.04
Nb	0.005
Al	0.001
S	0.003
P	0.001
B	0.0006
O	0.0021
N	0.0011
H	0.0018
Ni	balance

The material was machined into tensile specimens 0.32 cm in diameter and 2.86 cm long (gage length), which were then annealed 1 hr in Ar at 700°C before irradiation.

The specimens were irradiated to fluences of 1.1×10^{18} to 1.4×10^{20} neutrons/cm^2 (> 0.1 Mev) in subassemblies in row 2 of the core of the EBR-II. Specimens were mounted in holders isolated from the inside surface of the tube element by a gas gap. Temperatures higher than ambient were obtained by varying the size of the gap and the gas — He or Ar. The temperatures reported were calculated from measured rates of gamma heating.

Disks about 0.5 mm thick were cut from the gage length of the specimens and thinned for transmission electron microscopy by the automated technique described by DuBose and Stiegler.[23] Foil thicknesses for quantitative measurements were determined by measuring the projected widths of twin boundaries. Foil thicknesses and the resulting void concentrations are believed to be accurate to within a factor of 2.

Voids were observed for all the irradiation conditions reported here. Although many of the void characteristics varied with temperature or fluence, the void concentration was reasonably constant. The values, given in Table 5.1, range between 2 and 3×10^{14} voids/cm^3, except for the specimens that received the lowest and highest fluence. For the specimen that received the lowest fluence (1.1×10^{18} neutrons/cm^2), all the voids were less than 60 A in diameter, and it is likely that a considerable fraction of the voids was not visible. In specimens that received the highest level of fluence the voids were large enough that the voids must have touched and merged, which would tend to reduce the concentration. Within the accuracy of our measurements, we can see no systematic variation in void concentration over the ranges of temperature and fluence reported here.

Although a variation in irradiation temperature did not influence the concentration of voids, it did alter the sizes and shapes of the voids that were present. Variations in shape are illustrated in Figs. 5.17 to 5.19. At the lower irradiation temperatures (385 to 410°C) the voids had well-defined cubic shapes. In seven of eight cases in which the shape of the voids was carefully analyzed, the projections were

Table 5.1. Summary of Void Characteristics

Irradiation Temperature (°C)	Fluence [neutrons/cm^2 (> 0.1 Mev)]	Concentration (voids/cm^3)	Average Size (A)	Calculated Fractional Volume Increase (%)
		$\times 10^{14}$		
385	1.4×10^{20}	2.9	126	0.05[a]
410	1.4×10^{20}	3.2	133	0.07[a]
440	1.4×10^{20}	2.0	151	0.06[b]
470	1.4×10^{20}	3.2	160	0.06[b]
525	1.4×10^{20}	2.4		
370	1.1×10^{18}	1.2	< 60	
370	3.2×10^{19}	2.9		
470	1.5×10^{22}	~ 1.0	> 300[c]	

[a]Assuming a cubic shape.

[b]Assuming a spherical shape.

[c]Voids ranged between 300 and about 1500 A in diameter. Since a large fraction intersected foil surfaces, no reliable size distributions could be obtained.

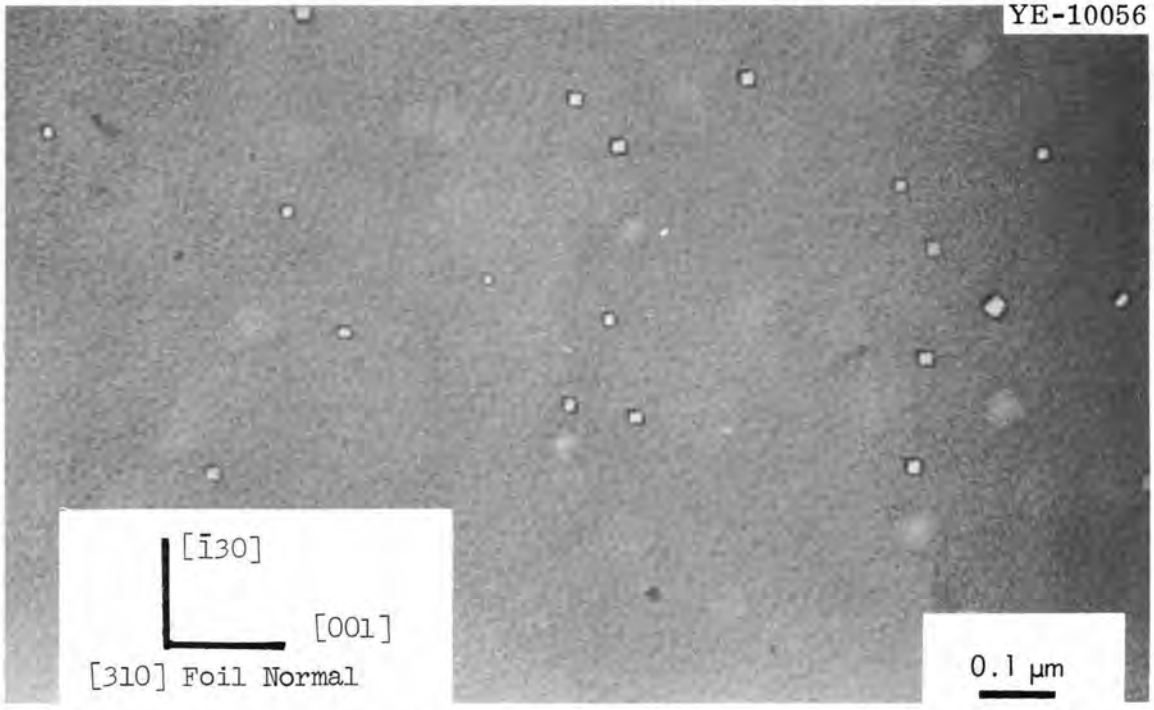

Fig. 5.17. Cubic Voids in Nickel 270 Irradiated in the Experimental Breeder Reactor-II at 385°C. Octahedral voids would show a similar projection but rotated about 45° in the plane of the photograph.

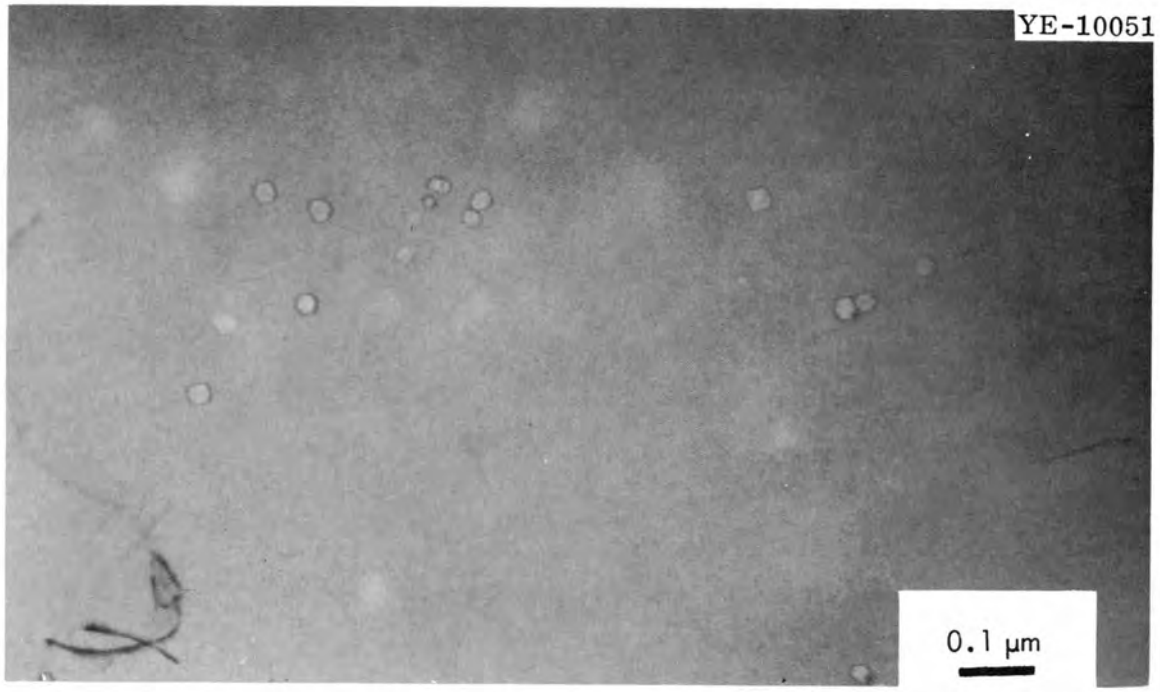

Fig. 5.18. Nearly Equiaxed Polyhedral Voids in Nickel 270 Irradiated in the Experimental Breeder Reactor-II at 470°C.

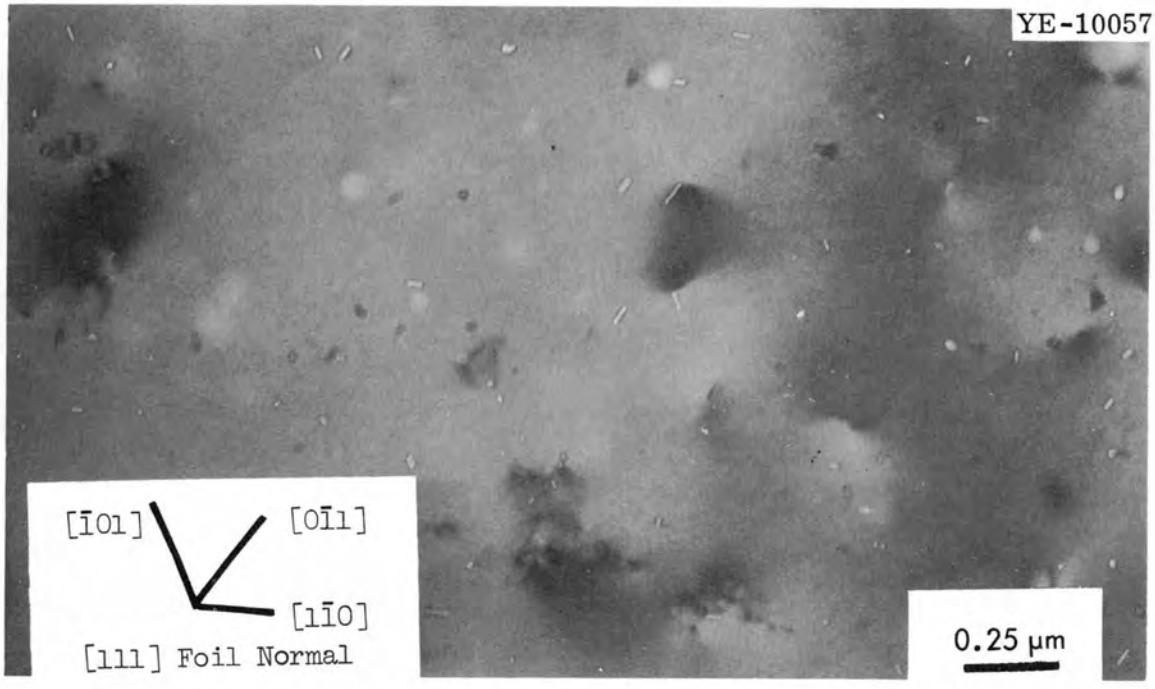

Fig. 5.19. Elongated Voids Formed in Nickel 270 Irradiated in the Experimental Breeder Reactor-II at 525°C. The voids are elongated along (110) directions.

consistent with a cubic shape and inconsistent with an octahedral shape. One case was ambiguous. At intermediate temperatures (440 to 470°C), many of the voids tended to become nearly equiaxed polyhedra. It was difficult to say whether they were truncated cubes or truncated octahedra, since the surfaces formed by the truncation could not be distinguished from the basic surfaces. At the highest irradiation temperature (525°C), about one-third of the voids were elongated along (110) directions, as can be seen in Fig. 5.20. The maximum ratio of length to width was about 5. Similar elongated voids on a much coarser scale have been observed in Al irradiated at about the same homologous temperature.[24]

Fig. 5.20. Clusters of Voids Formed in Nickel 270 Irradiated in the Experimental Breeder Reactor-II at 370°C to a Fluence of 3.2×10^{19} neutrons/cm^2 (> 0.1 Mev).

The average size of the voids appeared to increase with increasing irradiation temperature at constant fluence, as can be seen in Table 5.1. The average size of the diameter of the voids may be a misleading measure of their size, since the shape of the voids varies with irradiation temperature. At 385 and 410°C, it represents the average length of the edge of a cube, and at 440 and 470°C it represents the average diameter

of the more equiaxed polyhedra. Slight increases were noted in the length of the edges of the cubes between 385 and 410°C and in the diameter of the polyhedra between 440 and 470°C, but the much larger increase in the average size of the voids between 410 and 440°C may be associated with the change in shape. Since the volume of a cube with an edge length of d is appreciably larger than that of a more equiaxed polyhedron with an average diameter of d, the average void volume and consequently the swelling are much less sensitive to changes in irradiation temperature than is the average size of the voids.

Many instances of heterogeneous void distributions were observed. An extreme example, shown in Fig. 5.21, illustrates the tendency commonly observed for the voids to form clusters. The statistical test for randomness described by Ashby and Ebeling[25] and by Minter and Foreman[26] was applied to this material. Photomicrographs were marked into squares containing an average of about two voids per square, and the number of voids per square was counted. For a random distribution, the probability P(n) of finding n voids in a square, assuming a Poisson distribution, was

$$P(n) = \frac{\mu^n}{n!} e^{-\mu} ,$$

where μ is the average number of voids per square. A plot of the relative frequency of occurrence of voids per square for the area of Fig. 5.20 is shown in Fig. 5.21 along with a Poisson distribution for a random array

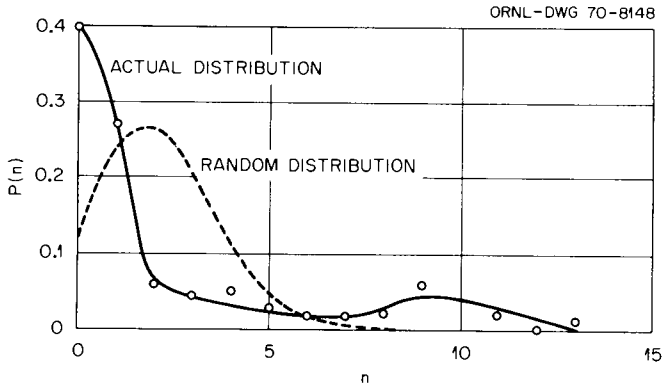

Fig. 5.21. Density Distribution Function for the Void Distribution (Solid Curve). The distribution for a random array is also given (dashed curve).

that has the same average number of voids per square. The curves bear no resemblance to one another. The maxima in the experimental curve at n = 0 and at n = 9 are characteristic of a clustering phenomena. In several cases in which the void distribution appeared superficially to be homogeneous, tails were observed at high values of n, again indicating clustering.

Examination of Fig. 5.20 indicates that size was influenced strongly by the local concentration of voids. The voids were appreciably smaller in regions of higher void concentration than in regions of lower void concentration. The detailed nature of the distribution of void sizes, therefore, reflects in part the spatial distribution of the voids. This will certainly have a pronounced effect in cases where heterogeneous distributions are involved, but also may influence the detailed shape of the distribution curve for homogeneous arrays.

Void concentrations and sizes also were influenced by grain boundaries and a dislocation loop structure that was present. Narrow bands adjacent to grain boundaries, poorly defined but about 0.1 μm thick, were denuded of voids. The void concentration did not suddenly jump to a constant value but gradually increased to a maximum at a distance of about 1 μm from the boundary. At somewhat greater distances, the dislocation structure began to develop, and the void concentration dropped by about 30%. A photomicrograph illustrates this phenomenon in Fig. 5.22, and void concentration is plotted as a function of distance from the boundary in Fig. 5.23. Void sizes in the region closest to the boundary were larger than in regions of highest concentration or in dislocation structures, where they were essentially equal. Because of difficulty in defining the size of the denuded zone, we did not attempt to measure the very small variations with irradiation temperature. Narrow denuded zones were also observed adjacent to coherent twin boundaries. We measured the concentration of voids adjacent to twin boundaries but in regions containing the dislocation structure, which should, therefore, have been typical of the grain interiors.

These results are basically different from those of a similar study by Straalsund[27] of Nickel 270 irradiated in the EBR-II in the same fluence range at 480°C. The results of this study are given in Table 5.2. The

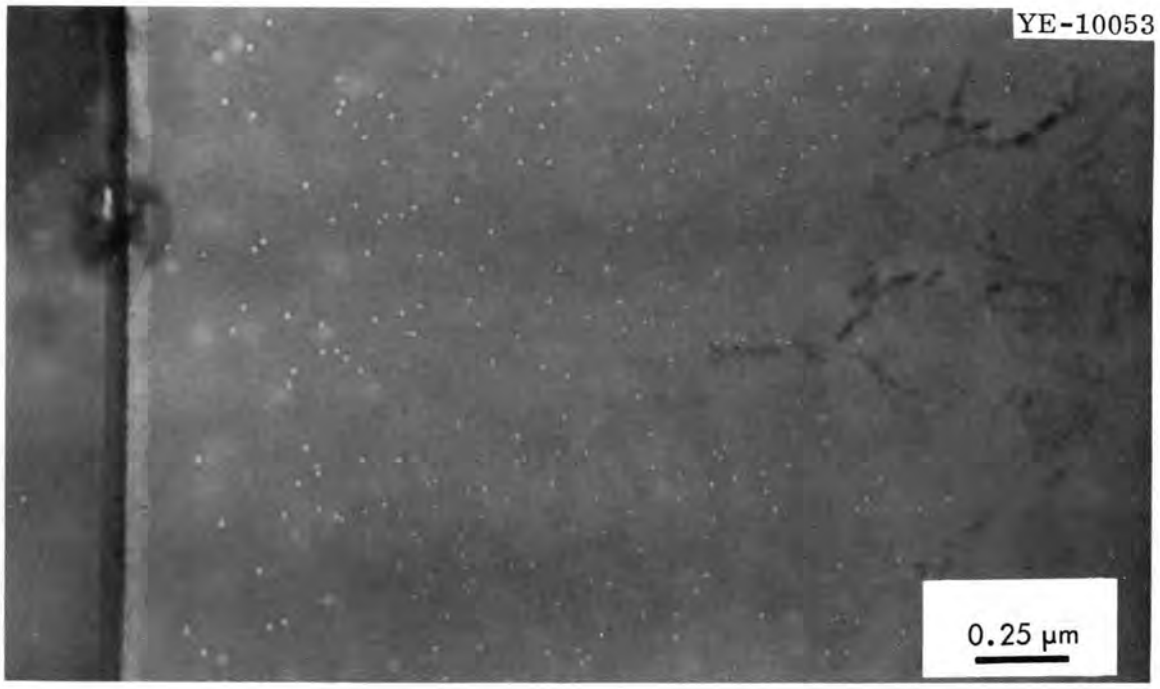

Fig. 5.22. Void Distribution Near a Grain Boundary.

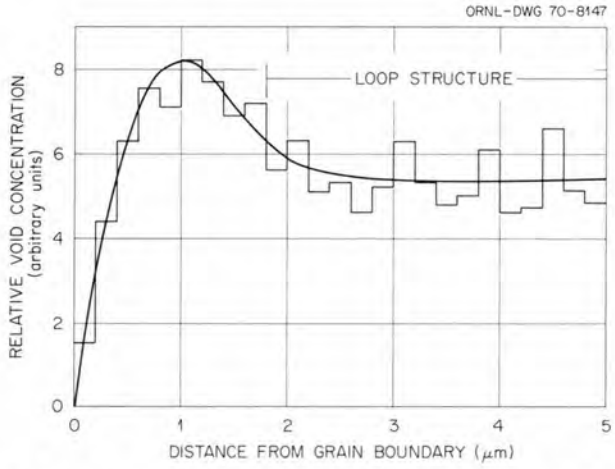

Fig. 5.23. Void Concentration in Strips Parallel to the Boundary as a Function of Distance from the Grain Boundary Shown in Fig. 5.22.

void concentrations are appreciably lower and the sizes larger than those that we measured (see Table 5.1). In addition, the concentration increased with increasing fluence. Other work[28] on material of higher purity than that used in these studies showed a third type of behavior, which is also presented in Table 5.2. The void concentrations were much higher than

Table 5.2. Void Statistics for Nickel Measured by Other Laboratories

Material Purity (%)	Irradiation Temperature (°C)	Fluence (neutrons/cm^2)	Concentration (voids/cm^3)	Average Size (A)	Calculated Change in Volume (%)	Reference
99.98	480	1.3×10^{20} (> 0.1 Mev)	9×10^{12}	250	0.012	a
99.98	480	1×10^{21} (> 0.1 Mev)	9.4×10^{13}	350	0.22	a
99.98	480	3×10^{21} (> 0.1 Mev)	1.8×10^{14}	360	0.51	a
99.997	380	5.2×10^{19} (> 1 Mev)	4×10^{15}	83	0.11	b
99.997	500	5.7×10^{19} (> 1 Mev)	8×10^{14}	165	0.16	b
99.997	575	6.2×10^{19} (> 1 Mev)	2.5×10^{14}	245	0.17	b
99.997	640	5.2×10^{19} (> 1 Mev)	8×10^{13}	270	0.07	b
99.997	750	5.2×10^{19} (> 1 Mev)	1×10^{11}	~ 400	< 0.001	b

[a] J. L. Straalsund, Battelle Memorial Institute Pacific Northwest Laboratory, private communication.

[b] J. L. Brimhall and B. Mastel, Scripta Met. 4, 51 (1970).

those we measured, and the concentration decreased with increasing irradiation temperature.

These differences, not only in numbers but also trends, are far greater than any possible experimental error. As such, they demonstrate that the response of Ni to neutron irradiation is dependent on more than the irradiation conditions alone.

In the specimens that we irradiated, a complex dislocation structure formed, the nature of which varied with irradiation temperature and fluence. The development of this structure at 370°C is illustrated in Figs. 5.24 through 5.26. After irradiation at a fluence of 1.1×10^{18} neutrons/cm^2, patches of perfect dislocation loops were dispersed throughout the specimen, as shown in Fig. 5.24. Because of the magnetic character of this material, we were unable to tilt the specimens through large enough angles to determine the character of the loops; we presume that they are interstitial. After irradiation at a fluence of 3.2×10^{19} neutrons/cm^2, the structure consisted of a coarse dislocation network

Fig. 5.24. Patches of Dislocation Loops Formed in Nickel 270 Irradiated in the Experimental Breeder Reactor-II to a Fluence of 1.1×10^{18} neutrons/cm^2 (> 0.1 Mev) at 370°C.

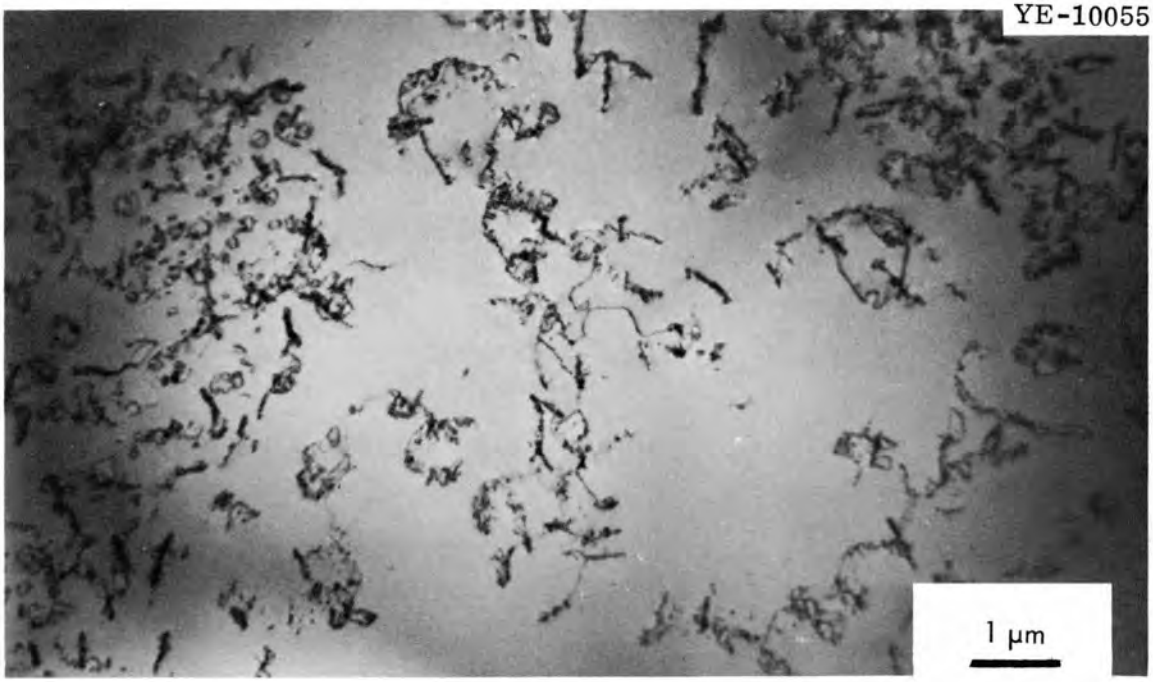

Fig. 5.25. Dislocation Structure in Nickel 270 Irradiated in the Experimental Breeder Reactor-II to a Fluence of 3.2×10^{19} neutrons/cm^2 at 370°C.

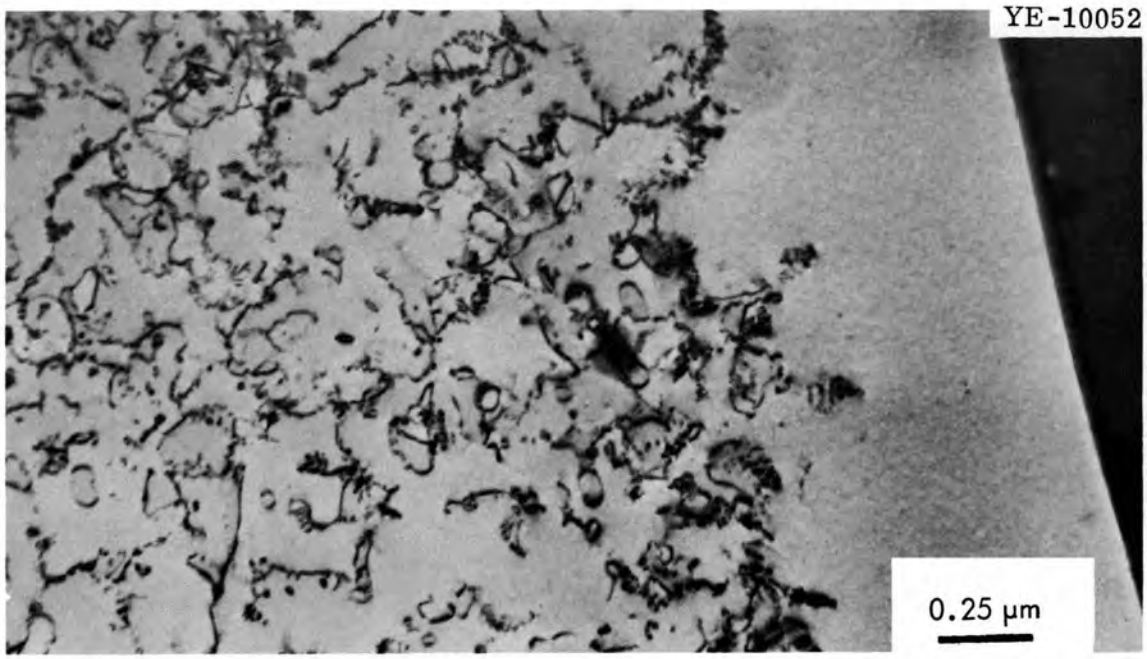

Fig. 5.26. Dislocation Structure in Nickel 270 Irradiated in the Experimental Breeder Reactor-II to a Fluence of 1.4×10^{20} neutrons/cm^2 at 385°C. Note the denuded zone near the grain boundary.

with a high concentration of small loops located near the dislocation lines as can be seen in Fig. 5.25. Relatively large patches were free of either dislocation lines or loops. After irradiation at a fluence of 1.4×10^{20} neutrons/cm^2, the structure was basically the same except that most of the patches were filled (Fig. 5.26). There were also large denuded zones near grain boundaries, as illustrated in Fig. 5.26. These denuded zones were 1 to 3 μm thick, but there was considerable variation within a single sample. No consistent trends with temperature or fluence were evident.

The dislocation structure became more coarse with increasing irradiation temperature, as shown in Fig. 5.27. In all cases the structure remained a coarse dislocation network with closely associated dislocation loops. Note the apparent displacement of the dislocations in the vicinity of loops. Similar effects were noted[17] in Al.

Fig. 5.27. Dislocation Structure in Nickel 270 Irradiated in the Experimental Breeder Reactor II to a Fluence of 1.4×10^{20} neutrons/cm^2 at 470°C. Compare with Fig. 5.26.

Mechanisms of Nucleation and Growth of Voids in Nickel 270 (J. O. Stiegler, E. E. Bloom)

Several mechanisms have been proposed to account for the nucleation of voids during neutron irradiation:

1. homogeneous nucleation,[29,30]
2. nucleation in displacement spikes,[30]
3. nucleation in spikes with the aid of He stabilization,[30]
4. nucleation on He bubbles,[13,14] and
5. preexisting nuclei.[30]

To date, none has won general acceptance.

Two pieces of evidence strongly suggest that in this case we are dealing with preexisting void nuclei: (1) the lack of a systematic variation of the concentration of voids with irradiation temperature or fluence and (2) the heterogeneous distribution of voids. Certainly the heterogeneous distributions of voids are at odds with a homogeneous nucleation process or with nucleation in displacement cascades. It is difficult to assign any role in the nucleation process to the He produced by transmutation, for at the fluence of 1.1×10^{18} neutrons/cm^2 about an order of magnitude more voids were present than He atoms.[31]

On the basis of any of these four mechanisms, we would expect a decreasing concentration of voids with increasing temperature due to a decrease in vacancy supersaturation with increasing temperature. This occurs for two reasons: (1) vacancy mobility increases with increasing temperature, and, hence, vacancy lifetimes and average vacancy concentrations decrease; and (2) the equilibrium concentration of vacancies against which supersaturation is measured increases with increasing temperature. The size of a critical nucleus increases with increasing temperature, and in terms of the first four mechanisms listed above, the rate of nucleation must decrease. Although this is commonly observed,[28] it did not occur in this system. We conclude that preexisting nuclei are responsible for the voids observed here and that all such entities present in the material are large enough to serve as void nuclei over the range of irradiation conditions encountered here.

The nature of the nuclei is not obvious from the photomicrographs; several possibilities exist. Small gas bubbles have properties consistent with the void characteristics that were observed. Such bubbles could be clustered or distributed nonrandomly as a consequence of a complex consolidation and fabrication history.[32] This particular grade of Ni is a powder-metallurgy product for which the powders are prepared by the carbonyl process. Gas bubbles can be formed in it in the absence of irradiation by high-temperature annealing treatments alone.

Nonwetting precipitate particles have most of the characteristics of bubbles or holes and could also serve as nuclei. The elongated voids produced during irradiation at 525°C suggest that precipitate particles may be involved in the nucleation of voids. In quenching experiments, elongated voids have occasionally been observed[33,34] and were shown always to be associated with precipitate particles. Elongated supervoids[24] produced in high-purity Al also have been shown to be associated with precipitate particles.

In summary, we cannot identify the nuclei, but have presented a considerable amount of circumstantial evidence that places the blame on structural defects, probably gas bubbles or particles.

Further evidence for the role of gas is given by the cubic shape of the voids produced at the lower irradiation temperatures. In studies of Ni of higher purity than that we used, Brimhall and Mastel[15,28] showed voids to be octahedral. Relative as well as absolute surface energies are believed to be influenced strongly by adsorbed gases.

The variability in the response of different Ni specimens to neutron irradiation supports the argument that chemical or structural defects influence the nature and extent of the damage. The opposite behavior observed for two lots of Nickel 270 cited in Tables 5.1 and 5.2 indicates that material variables are more important than irradiation variables in fixing the state of the damage. Since distributions of bubbles or particles would be sensitive functions of the entire processing history of the material, it is not surprising (in retrospect at least) to find such striking differences in the behavior of materials of like purity. Relative as well as absolute surface energies are believed to be influenced strongly by adsorbed gases.

It does not appear that any single mechanism of nucleation can explain the range of observations made on relatively pure Ni. We offer the following combination of processes, consistent within themselves, to account for the observations. We believe that small gas bubbles serve as the nuclei for voids. The bubbles may be preexisting, as we found in this work, in which case their concentration, size, and distribution will depend critically on the history of the material in question. Alternatively, bubbles may be produced by neutronically generated gases, namely He, which may precipitate heterogeneously, at least early in the irradiation. The concentration of such bubbles will increase until the probability that a newly generated He atom will reach an existing bubble greatly exceeds the probability that it will encounter a trap or interact with another atom or group of atoms to form a stable bubble. The latter condition also will depend critically on the chemical and structural state of the material.

We propose that in our Ni a grown-in population of bubbles or cavities served as the nuclei for voids. Helium generated during the irradiation was sufficiently mobile that most of it reached the existing voids and that few, if any, new voids were formed. In the case of the material studied by Straalsund,[27] few, if any, suitable nuclei must have existed before the irradiation, and the voids that were formed were generated during the irradiation. There is no obvious explanation for the differences between these two lots of material; both were annealed at 700°C immediately before irradiation. Evidently, there were slight chemical differences or variations in the histories of consolidation and fabrication. The same conclusion also holds for the higher purity material examined by Brimhall and Mastel.[28] Techniques of a higher level of sophistication than are currently available will be necessary before these differences can be unraveled. Perhaps, as has been suggested previously,[17] neutron irradiation at elevated temperatures may provide a useful means for developing or rendering visible small defect configurations present in high-purity materials.

The observation drawn from Fig. 5.20 – that in regions where there are high concentrations of voids the voids are smaller than in regions where there is a low concentration of voids – implies that vacancies move

appreciable distances during their lifetimes. Voids do not, therefore, grow independently of one another; the size of the void depends not only on the irradiation fluence and the temperature but also on the population of voids in its vicinity. This implies that the overall swelling or void volume is not greatly influenced by the void concentration. This is supported by the data in Tables 5.1 and 5.2. The material examined by Straalsund,[27] which contained a low density of large voids, showed only a slightly smaller change in volume than the material used in this study, which contained 30 times more voids. The data on higher purity material obtained by Brimhall and Mastel[28] showed a comparable change in volume, although direct comparison is not possible because of differences in fluence. The microstructure is very sensitive to subtle material variations, but the change in bulk density is not. Presumably, mechanical properties, which depend on the size and concentration of defects, will be sensitive to the material variations.

Irradiation Damage to Refractory Metals

Molybdenum Materials (F. W. Wiffen)

Specimens of refractory metals and alloys were irradiated in subassembly XO-34 in row 2 of the EBR-II in a program initiated by General Electric, Nuclear Systems Programs, Cincinnati. Examination of some of the specimens from this subassembly is under way at ORNL.

Molybdenum, Mo—0.5% Ti, and Mo—50% Re specimens from this subassembly were tested. The Mo and the Mo—0.5% Ti specimens were fabricated from arc-cast material supplied by Climax Molybdenum Company. This material was supplied as 1/4-in.-diam wrought bar and had been produced by reducing arc-cast material by extrusion, rolling, and swaging to final size. The Mo was stress relieved 15 min at 870°C, and the Mo—0.5% Ti was stress relieved 15 min at 1090°C. Standard buttonhead tensile specimens with a 1/8-in.-diam × 1 1/8-in.-long gage section were ground from the rods. After the specimens had been machined, they were given a final anneal of 1 hr at 1350°C in vacuum for the Mo, and at 1450°C for the Mo—0.5% Ti. The Mo—50% Re was supplied by the Chase Brass and Copper Company, Rhenium Division. It was produced from sintered powder and reduced by warm swaging.

Specimens machined from this material were given a final anneal of 1 hr at 1400°C in vacuum. The grain size and chemical analysis of the material used in this experiment are not yet available. A partial composition derived from the vendor's analysis of similar material is given in Table 5.3. A more complete chemical analysis of the irradiated specimens will be given later.

Table 5.3. Partial Chemical Composition of Molybdenum Alloys

Alloy	Element, %			Element, ppm			
	Mo	Re	Ti	C	N	O	H
Molybdenum	Bal			30	1	7	< 1
Mo–0.5% Ti	Bal		0.52	400	2	10	< 1
Mo–50% Re	Bal	50[a]		20	< 0.1	2	0.1

[a]Nominal, analysis not yet available.

Four tensile specimens of each of the three alloys were irradiated at 425°C in a He-filled tube of subassembly XO-34. The Mo specimens were 1 in. below the reactor midplane and received a fluence of 3.45×10^{22} neutrons/cm^2 (> 0.1 Mev); the Mo–0.5% Ti specimens were 3 1/2 in. below the midplane and received 3.0×10^{22} neutrons/cm^2; and the Mo–50% Re specimens were 10 in. below the midplane and received 1.5×10^{22} neutrons/cm^2.

The specimens were tensile tested in flowing He on an Instron Universal Testing Machine. Specimens were held for a constant equilibration time of 30 min between reaching test temperature and the start of the test. Test temperatures, strain rates, and test results are shown in Table 5.4. The control results were obtained from specimens in the annealed condition; they had not been aged to duplicate the thermal history of the irradiation exposure. The stresses shown in Table 5.4 are engineering values, based on the initial cross section, and the ductility values were taken from the crosshead motion. After irradiation, the tensile properties of the Mo and Mo–0.5% Ti were almost identical. Both materials increased greatly in strength properties due to irradiation for all of the test conditions investigated. Specimens tested at 400°C at strain rates of 0.02 and 0.002 min^{-1} had no ductility after irradiation.

Table 5.4. Tensile Properties of Molybdenum Alloys Irradiated at 425°C

Test Temperature (°C)	Strain Rate (min^{-1})	Yield Stress, psi		Ultimate Tensile Stress, psi		Uniform Elongation, %		Total Plastic Elongation, %	
		Unirradiated (0.2% offset)	Irradiated (maximum)	Unirradiated	Irradiated	Unirradiated	Irradiated	Unirradiated	Irradiated
		Molybdenum [3.45 × 10^{22} neutrons/cm^2 (> 0.1 Mev)]							
400	0.02	12,600	113,300	36,300	113,300	27.3	0.1	39.4	0.1
550	0.02	10,500	101,000	33,500	101,000	31.7	0.2	41.8	0.2
550	0.0002	9,400	85,000	32,100	85,000	28.1	0.1	37.1	6.5
650	0.02	10,700	86,300	32,400	86,300	29.7	0.1	42.3	8.4
		Mo–0.5% Ti [3.0 × 10^{22} neutrons/cm^2 (> 0.1 Mev)]							
400	0.02	14,400	118,000	44,500	118,000	34.0	0.1	50.1	0.1
400	0.002	15,000	102,600	41,700	102,600	32.9	0	47.5	0
400	0.0002	17,100	101,200	40,700	101,200	30.9	0.1	47.3	7.0
650	0.02	14,000	94,400	40,300	94,400	29.3	0.1	39.6	7.9
		Mo–50% Re [1.5 × 10^{22} neutrons/cm^2 (> 0.1 Mev)]							
400	0.02	63,300	144,300	87,400	144,300	20.8	0.1	31.7	0.1
650	0.02	45,000	147,300	76,100	147,300	12.5	0.2	20.3	0.2
800	0.02	41,900	141,400	68,000	141,400	12.1	0	21.1	0

At a strain rate of 0.0002 min^{-1}, the elongation to fracture at 400°C was 7%, but all of the elongation was nonuniform and the maximum load occurred at only 0.1% plastic elongation. Two tests at 550°C of the material irradiated at 425°C also showed the influence of strain rate. Both the Mo and the Mo–0.5% Ti elongated about 8% before failure in tests at 650°C at 0.02 min^{-1}. The specimens that did have ductility at 550 and 650°C had only nonuniform ductility. A typical stress-strain curve for an irradiated specimen that had some ductility is presented in Fig. 5.28 (note that the curve has not been corrected for machine modulus). In this test, as in all of the other tests on the irradiated specimens, the maximum load occurred at less than 0.2% plastic elongation. Detailed explanation of the tests at temperatures above the irradiation temperature must await further investigation of the effects of annealing at these temperatures on the microstructure produced by irradiation.

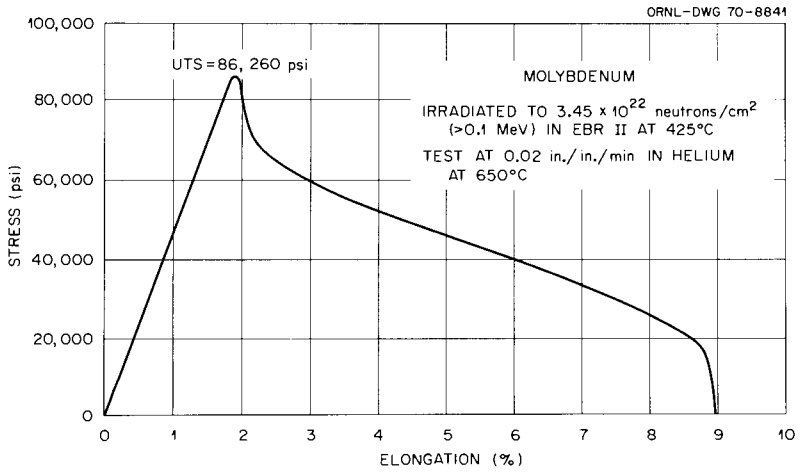

Fig. 5.28. Molybdenum Irradiated to 3.45 × 10^{22} neutrons/cm^2 (> 0.1 Mev) in the Experimental Breeder Reactor-II at 425°C. Tested at 0.02 min^{-1} in helium at 650°C.

The Mo–50% Re did not behave the same as the other two materials. It, too, showed a very pronounced hardening as a result of the irradiation but showed no ductility at 400, 650, or 800°C for tests at a strain rate of 0.02 min^{-1}.

This subassembly also included capsules that contained sheet specimens of several refractory metals and alloys. The three capsules were exposed to a fluence of 2.5×10^{22} neutrons/cm^2 (> 0.1 Mev) at a position centered 5 5/8 in. below the midplane of the reactor. The two capsules in He-filled tubes operated near 425 and 600°C. The third capsule was in an Ar atmosphere at a temperature near 800°C.

Preliminary microscopy on Mo and Nb samples from these capsules showed a very high density of small voids in the Mo at 600 and 800°C and in the Nb at 425 and 600°C. There are probably no voids in the Mo irradiated near 425°C, although examination is not yet complete. Niobium irradiated near 800°C contained voids of significantly lower density and larger size than in samples irradiated at 425 and 600°C.

Incoloy 800

Effect of Aging on Mechanical Properties (D. G. Harman)

The ASME Boiler and Pressure Vessel Code shows that for temperatures less than 650°C Incoloy 800, because of the lower 0.2% yield strength, has lower design stresses than do types 304 and 316 stainless steel. At higher temperatures, where creep and stress-rupture properties are limiting, the better creep resistance of Incoloy 800 results in higher allowable code stresses than those for the stainless steels. The ASME code stresses for these materials are listed in Table 5.5.

Our experimental Incoloy 800 with 0.1% C has appreciably higher yield strengths than does the commercial alloy, which has 0.04% C, and would have higher design stresses.

We previously reported that all of our Incoloy 800 alloys that contained 0.1% Ti had superior creep ductilities after irradiation, but that the alloy with 0.1% C was sensitive to the irradiation temperature. Creep ductilities after irradiation at 500°C were less than those after irradiation at 700 or 760°C. The alloys with lower C content and 0.1% Ti, on the other hand, showed equally good ductilities after irradiation at each of these temperatures.[35]

To aid in the interpretation of these results, we are running tensile and creep-rupture tests on samples aged for various times at 500°C.

Table 5.5. Maximum Allowable Design Stresses for Types 304 and 316 Stainless Steel and Incoloy 800

For Temperatures Not Exceeding (°C)	Maximum Allowable Design Stress, psi		
	Type Stainless Steel[a]		Incoloy 800 Grade II[b]
	304	316	
	× 10^3	× 10^3	× 10^3
38	20	20	15.6
93	20	20	13.4
149	19.8	20	12.1
204	17.6	19.4	11.1
260	16.4	18.2	10.4
316	15.6	17.1	10
371	15.1	16.2	9.6
427	14.8	15.6	9.3
482	10	10.3	9.1
538	9.45	9.8	8.9
593	8.25	9.45	8.8
649	5.5	6.95	7.1
704	3.4	4.0	4.15
760	2.05	2	2.5
816	1.25	1.15	1.5

[a]Values from 38 to 427°C from "Section III, Nuclear Vessels," pp. 28–29 in ASME Boiler and Pressure Vessel Code, The American Society of Mechanical Engineers, New York, 1965. Values from 482 to 816°C from "Additions and Revisions to Table PG-23.1," pp. 4–5 in Summer 1965 Addenda, ASME Boiler and Pressure Vessel Code, Power Boilers, The American Society of Mechanical Engineers, New York, 1965.

[b]"Case 1325," p. 166 in ASME Boiler and Pressure Vessel Code Case Interpretation, The American Society of Mechanical Engineers, New York, 1965.

We completed the tensile testing of two alloys with high C content (0.10 and 0.26% Ti) after they were aged for 1000 or 2000 hr at 500°C. These results are compared with those from unaged samples in Table 5.6. Tensile strength and ductility were particularly sensitive to strain rate in both the aged and unaged conditions. Annealed specimens had lower ductilities at the slower strain rates, while those treated to agglomerate carbides (100 hr at 500°C) showed just the opposite trend. This shows the importance of grain-boundary sliding in the deformation of these alloys and that the main effect of the anneal at 800°C was to agglomerate

Table 5.6. Tensile Properties of High-Carbon Incoloy 800 at 650°C after Aging for the Indicated Time at 500°C

	Strain Rate (min^{-1})	Strength, psi						Elongation, %/hr					
		0.2% Yield			Tensile			Uniform			Total		
		0 hr	1000 hr	2000 hr	0 hr	1000 hr	2000 hr	0 hr	1000 hr	2000 hr	0 hr	1000 hr	2000 hr
		$\times 10^3$	$\times 10^3$	$\times 10^3$	$\times 10^3$	$\times 10^3$	$\times 10^3$						
					Alloy with 0.1% Ti								
Annealed 30 min at 1150°C	0.05	15.8	20.0	18.5	56.0	79.0	70.7	33.9	35.6	32.3	38.6	37.2	35.2
	0.002	17.0	19.2	19.5	49.2	54.6	57.0	19.8	16.4	20.5	22.5	19.8	24.4
Annealed plus 100 hr at 800°C	0.05		13.5	19.7		62.4	59.5		23.0	20.9		30.4	31.5
	0.002	18.5	16.8	38.0	35.0	40.1	41.6	10.8	12.0	10.2	46.0	47.9	43.2
					Alloy with 0.26% Ti								
Annealed 30 min at 1150°C	0.05	18.5	22.1	15.9	72.2	69.2	64.6	32.8	32.1	36.3	36.8	37.1	40.7
	0.002	18.9	21.1	19.4	76.3	60.5	57.7	39.6	20.5	23.2	32.5	25.2	27.9
Annealed plus 100 hr at 800°C	0.05		17.9	17.1		52.0	52.0		22.1	24.2		36.2	38.5
	0.002		14.9	34.2		39.1	39.7		13.5	9.0		49.5	46.0

carbides along the grain boundaries. The alloy that contained 0.26% Ti had strengths similar to those of the alloy that contained 0.1% Ti but had consistently higher ductility values.

The results of creep-rupture tests at 650°C for the alloy that contained 0.1% Ti and 0.1% C after aging 2000 hr at 500°C are compared in Table 5.7 with those from the unaged material. Samples that were solution annealed and those that were treated to agglomerate carbides were strengthened as a result of thermal aging. The sample given the 800°C treatment showed no decrease in elongation due to aging, but the annealed specimen did. This is more evident in Figs. 5.29 and 5.30, where the creep curves from these tests are shown.

Table 5.7. Effect of Aging at 500°C on the Creep-Rupture Properties at 650°C of Incoloy 800 with 0.10% Ti and 0.1% C

	Time, hr		Total Elongation (%)	Minimum Creep Rate (%/hr)
	Aging	Rupture		
Annealed 30 min at 1150°C	0	146	39.6	0.040
	2000	216	29.3	0.0185
Annealed 30 min at 1150°C plus 100 hr at 800°C	0	22.7	57.8	1.10
	2000	67.7	56.8	0.44

Figure 5.31 shows both tensile and creep elongation as a function of the rate of deformation for the alloy that contained 0.1% Ti and 0.1% C and shows the superior performance of the samples given the 800°C treatment when tested at the slower rates. We had anticipated a greater loss in ductility due to aging the as-annealed samples because of the post-irradiation results. Apparently, the treatment to agglomerate carbides provided improved resistance to fracture at grain boundaries.

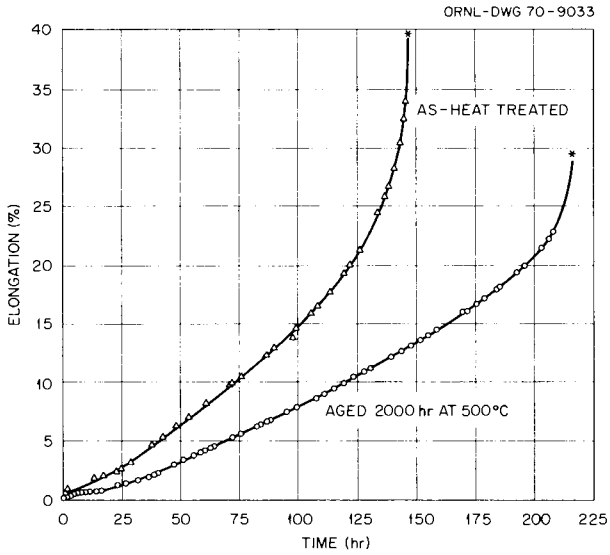

Fig. 5.29. Effect of Aging on Creep of Incoloy 800 Tested at 650°C and 30,000 psi. Specimens are from the heat with 0.1% Ti and 0.10% C and were annealed 30 min at 1050°C.

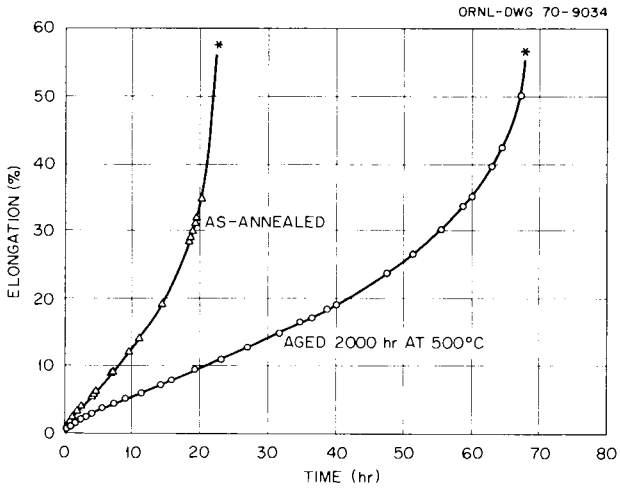

Fig. 5.30. Effect of Aging on Creep of Incoloy 800 Tested at 650°C and 30,000 psi. Specimens are from the heat with 0.10% Ti and 0.10% C and were held 100 hr at 800°C following the 1050°C anneal.

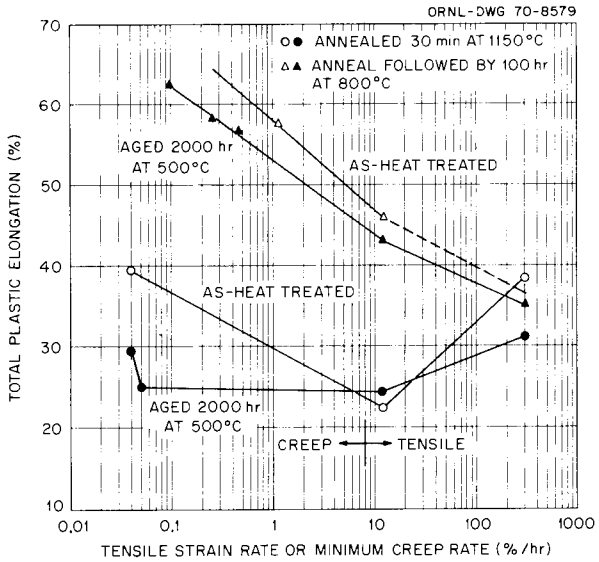

Fig. 5.31. Effect of Aging on the Elongation of Incoloy 800 at 650°C. Specimens contain 0.10% Ti and 0.10% C.

Notes

1. J. J. Holmes et al., Acta Met. 16, 955 (1968).

2. J. J. Holmes et al., J. Nucl. Mater. 32, 330 (1969).

3. R. Carlander et al., Nucl. Appl. 7, 67 (1969).

4. D. R. Harries, J. Brit. Nucl. Energy Soc. 5, 74 (1966).

5. E. E. Bloom and J. R. Weir, "Development of Austenitic Stainless Steels with Improved Resistance to Elevated-Temperature Irradiation Embrittlement," pp. 261–289 in Irradiation Effects in Structural Alloys for Thermal and Fast Reactors, Spec. Tech. Publ. 457, American Society for Testing and Materials, Philadelphia, 1969.

6. E. E. Bloom, Fuels and Materials Development Program Quart. Progr. Rept. Sept. 30, 1969, ORNL-4480, p. 73.

7. E. E. Bloom, "An Investigation of Fast Neutron Radiation Damage in an Austenitic Stainless Steel." Report in preparation.

8. G. V. Smith, "An Evaluation of the Yield, Tensile, Creep and Rupture Strengths of Wrought 304, 316, 321, and 347 Stainless Steels at Elevated Temperatures," ASTM Data Series DS 5S2, American Society for Testing and Materials, Philadelphia, 1969.

9. J. O. Stiegler and E. E. Bloom, J. Nucl. Mater. 33, 173 (1969).

10. R. T. King, "Cyclotron Simulation of Neutron Transmutation Produced Gases in Reactor Cladding and Structural Materials," paper presented at the International Conference on the Use of Cyclotrons in Chemistry, Metallurgy, and Biology, St Catherine's College, Oxford, England, Sept. 22–23, 1969. To be published in the proceedings.

11. Helium analysis was conducted by H. Farrar IV, Atomics International, Canoga Park, Calif.

12. N. J. Grant, "Intercrystalline Failure at High Temperatures," p. 562 in Fracture, ed. by B. L. Averbach, D. K. Felbeck, G. T. Hahn, and D. A. Thomas, Wiley, New York, 1959.

13. C. Cawthorne and E. J. Fulton, "The Influence of Irradiation Temperature on the Defect Structures in Stainless Steel," pp. 446–460 in The Nature of Small Defect Clusters, Vol. II, AERE-R-5269 (1966).

14. C. Cawthorne and E. J. Fulton, Nature (London) 216, 515 (1967).

15. B. Mastel and J. L. Brimhall, J. Nucl. Mater. 28, 115 (1968).

16. J. L. Brimhall and B. Mastel, J. Nucl. Mater. 29, 1231 (1969).

17. J. O. Stiegler, K. Farrell, C.K.H. DuBose, and R. T. King, "High Fluence Neutron-Irradiation Damage in Aluminum," p. 215 in Radiation Damage in Reactor Materials, Vol. 2, International Atomic Energy Agency, Vienna, 1969.

18. T. Lauritzen et al., Nucl. Eng. Des. 9, 265 (1969).

19. E. E. Bloom and J. O. Stiegler, "A Comparison of Irradiation Induced Swelling and Void Formation in Two Austenitic Stainless Steels." To be published in Journal of Nuclear Materials.

20. R. S. Nelson and D. J. Mazey, "Void Formation in Stainless Steel During Charged Particle Irradiation at Elevated Temperatures," p. 157 in Radiation Damage in Reactor Materials, Vol. 2, International Atomic Energy Agency, Vienna, 1969.

21. E. E. Bloom and J. O. Stiegler, "The Effect of Helium on Void Formation in Irradiated Stainless Steel." To be published in Journal of Nuclear Materials.

22. K. Farrell, R. T. King, and A. Wolfenden, Bull. Am. Inst. Mining Met. Eng. 4(1), 176 (1970).

23. C.K.H. DuBose and J. O. Stiegler, Semi-Automatic Preparation of Specimens for Transmission Electron Microscopy, ORNL-4066 (February 1967).

24. K. Farrell and R. T. King, "Supervoids in Irradiated Aluminum." Submitted for publication.

25. M. F. Ashby and R. Ebeling, Trans. Met. Soc. AIME 236, 1396 (1966).

26. F. J. Minter and A.J.E. Foreman, J. Mater. Sci. 4, 218 (1969).

27. J. L. Straalsund, Battelle Memorial Institute Pacific Northwest Laboratory, private communication.

28. J. L. Brimhall and B. Mastel, Scripta Met. 4, 51 (1970).

29. S. D. Harkness and Che-Yu Li, "A Model for Void Formation in Metals Irradiated in a Fast-Neutron Environment," p. 189 in Radiation Damage in Reactor Materials, Vol. 2, International Atomic Energy Agency, Vienna, 1969.

30. T. T. Claudson et al., "Fast-Reactor Radiation Induced Changes in Cladding and Structural Materials," p. 165 in Radiation Damage in Reactor Materials, Vol. 2, International Atomic Energy Agency, Vienna, 1969.

31. Chemical analysis by H. Farrar IV, Atomics International, Canoga Park, Calif., showed 0.0005 ± 0.00015 ppm (atomic) He for this irradiation. This is reasonable agreement with the calculated value.

32. R. C. Koo, Trans. Met. Soc. AIME 239, 1966 (1967).

33. K. H. Westmacott et al., Metal Sci. J. 2, 177 (1968).

34. I. A. Johnson et al., "The Heterogeneous Nucleation of Tetrahedra in Quenched Gold," pp. 140–153 in International Conference on Vacancies and Interstitials in Metals, Jülich, September 23–28, 1968, Vol. I. KFA-Jül-Conf-2, Kernforschungsanlage, Jülich, Germany.

35. D. G. Harman, Fuels and Materials Development Program Quart. Progr. Rept. June 30, 1969, ORNL-4440, pp. 123–128.

6. FABRICATION DEVELOPMENT FOR LMFBR STAINLESS STEEL TUBING

W. O. Harms W. R. Martin

This program for the development of techniques for fabricating cladding for fast reactors involves manufacturing thin-walled tubing of high quality. Our studies are designed to show the relationships among processing variables, mechanical properties at elevated temperature, and the physical defects of the tubing.

Effect of Fabrication Variables During Mandrel-Plug Drawing on the Quality and Properties of Type 316 Stainless Steel Tubing

W. R. Martin

Investigation of the Use of Artificial Defects to Simulate Natural Defects (R. W. McClung, K. V. Cook)

The second half of a series of tubular specimens[1] was prepared for tube-burst testing. The specimens are short lengths of 0.250 × 0.016-in. 20% cold-worked tubing that contain simulated flaws [notches produced by electrodischarge machining (EDM)] with depths of 10, 35, and 65% of the wall thickness and lengths of 0.125 and 0.030 in. A second series of specimens that duplicates these is being made for testing in the annealed condition. Twelve extra control specimens (without notches) are included for a total of 96 specimens. The last 54 specimens were sectioned from tubes drawn according to the "commercial" schedule BA1-1 (ref. 2).

As reported previously,[3] it appears that we can predict the effect of both a sinking pass and a drawing schedule on simulated flaws (EDM notches). We have inspected both 0.535- and 0.295-in.-OD type 316 stainless steel tubing designated BA2-1 and BA1-6, using a 0.002-in.-deep EDM notch as a reference standard. We are machining EDM notches that, when altered by the tubing fabrication schedule, should produce very narrow 0.0001-in.-wide × 0.250-in.-long simulated flaws. The depths of the altered notches in the 0.250-in.-OD × 0.016-in.-wall-thickness tubing should be about 10 and 20% of the wall thickness.

Effect of Planetary Swaging on the Structure and Creep Properties of Type 316 Stainless Steel

A. C. Schaffhauser

Drawing of Type 316 Stainless Steel Tubing by Planetary Swaging (G. A. Reimann)

We resumed the study of planetary swaging to determine its suitability as a process for producing high-quality cladding for reactor fuel. Since previous work[4] had indicated that the drive motor had insufficient capacity to fully utilize the capabilities of the planetary swager, a new 7 1/2-hp variable-speed motor was purchased and installed. This motor permitted us to eliminate the geared reducer, formerly needed to ensure sufficient torque, and resulted in a fivefold increase in speed, to 2100 rpm (no load).

We substituted WC balls for the ball bearings used previously, and surface finishes were markedly improved. Ball bearings, even with their high hardness (about 62 on the Rockwell C scale), tend to oblate, develop surface imperfections, and accumulate adhered metal particles.

Since we learned that tube working that involves sinking (substantial decrease of inside diameter) by planetary swaging produced premature tube failure,[4] we have concentrated on ironing steps (wall thinning with minimal decrease in inside diameter). Sinking, when required, was accomplished by conventional die and mandrel techniques.

The new drive motor permits us to operate the planetary swager at speeds of up to 2000 rpm in contrast with the previous maximum of 400 rpm. Efforts to planetary swage 1.0-in.-OD × 0.072-in.-wall-thickness type 304 stainless steel at 400 rpm were successful,[4] and this experiment was repeated at higher head and draw speeds. Planetary swaging was successful at 1000 rpm at a draw speed of 8 in./min, but excessive heat was generated in the deformation zone at the maximum speed of 2000 rpm, and the tube failed. At swager speeds of 1000 to 1200 rpm, draw speeds were varied between 6 and 48 in./min. A helical pattern on the tube surface became more pronounced as draw speed was increased, particularly above 36 in./min, and if such draw speeds appear advantageous, a coolant system should be

installed to remove the heat generated by correspondingly higher head speeds.

As noted previously, we obtained better results by several light passes rather than by few heavy passes, and reductions of much more than 10% seldom produced consistently good results, regardless of head or draw speed. Tubes of type 304L stainless steel were more amenable to planetary swaging than those of type 316 stainless steel when starting geometries and reduction schedules were similar. Tubes with a thick wall, relative to the outside diameter, are much more difficult to work without development of flaws. For example, surface cracks and flaking developed after a single 10% reduction on a 0.448-in.-OD × 0.044-in.-wall-thickness tube (wall about 10% of outside diameter), but the same reduction on a 0.415-in.-OD × 0.027-in.-wall-thickness tube (wall about 6 1/2% of outside diameter) was obtained with no difficulty, and several passes could be obtained on this tube by various combinations of draw and heat speeds. A similar relationship was found with 1-in. sizes: a 0.072-in. wall thickness could be worked successfully, while a 0.100-in. wall thickness could not.

To compare the properties of planetary-swaged tubing to those obtained by conventional drawing practice, we subjected several sections of tubing to burst tests at room temperature after swaging them to 0.250 in. in outside diameter by 0.015 in. in wall thickness. The samples were fabricated from type 316 stainless steel obtained from Allegheny-Ludlum Steel Corporation heat 65808, which had been evaluated previously after conventional drawing.

Planetary swaging was used to obtain the final 20% cold working needed to achieve final size from a sample measuring 0.258 in. in outside diameter by 0.219 in. in. inside diameter (0.0195 in. in wall thickness), which was obtained by conventional drawing. Except for the pass used to produce the sample for planetary swaging, the same drawing and annealing schedule was used that produced tubes tested as BA1-1 (ref. 5).

Five planetary-swaging passes and a 0.217-in.-diam mandrel were used. The tubing was deformed using 1/2-in.-diam WC balls and 1/4-in.-diam hardened steel balls at 1100 to 1200 rpm at draw speeds from 12 to

36 in./min. Since the final tube was 0.2190 to 0.2197 in. in inside diameter, depending on working variables, a reeling step was not required to loosen the tube from the 0.217-in.-diam mandrel. Five samples were cut from each tube and pressurized to failure. The results are presented in Table 6.1.

The level of cold work in the planetary-swaged samples was calculated to be 21.7%, compared to 18.9% calculated for the conventionally drawn tubing. This difference is insufficient to account for the great difference in properties. Also, note that with other factors remaining constant, the draw speed had a significant effect on properties. The tubes were ultrasonically inspected before planetary swaging, yet a number of defects were discovered in the specimens as a result of examination at 20× under a binocular microscope after bursting. It appears that the planetary-swaging process contributes to the generation of these defects.

Table 6.1. Room-Temperature Properties of Type 316 Stainless Steel Tubing Processed by Mandrel Drawing and Planetary Swaging

Sample Identification	Ball Diameter (in.)	Swager Speed (rpm)	Draw Speed (in./min)	Average Fiber Stress (psi)	Average Elongation (%)
BA1-1	Conventionally drawn			158,700	3.1
BA2-1	0.5	1100	12	168,100	1.6
BA2-1	0.25	1200	12	188,200	1.3
BA2-1	0.25	1200	18	194,200	1.1
BA2-1	0.25	1200	36	198,000	1.4

Notes

1. K. V. Cook, Fuels and Materials Development Program Quart. Progr. Rept. March 31, 1970, ORNL-4560, p. 110.

2. G. A. Reimann, Fuels and Materials Development Program Quart. Progr. Rept. Dec. 31, 1969, ORNL-4520, pp. 134–141.

3. K. V. Cook, Fuels and Materials Development Program Quart. Progr. Rept. Dec. 31, 1969, ORNL-4520, pp. 150–152.

4. G. A. Reimann, Fuels and Materials Development Program Quart. Progr. Rept. Sept. 30, 1969, ORNL-4480, p. 96.

5. G. A. Reimann, Fuels and Materials Development Program Quart. Progr. Rept. June 30, 1969, ORNL-4440, p. 178.

7. WELDING DEVELOPMENT FOR LMFBR VESSELS AND COMPONENTS

J. R. Weir, Jr. G. M. Slaughter

We are evaluating the behavior of weldments in austenitic stainless steel at 370 to 650°C as a function of both the welding process and the variables within a process for application to liquid-metal fast breeder reactor (LMFBR) vessels and components. The solidification substructure (the finest structural detail that can be resolved by an optical microscope) markedly influences the mechanical properties of a weldment at elevated temperatures. Since the size and type of substructure in a weldment are significantly influenced by factors that the welder can control, our approach is to determine the effects of different welding processes and of the variables within each process (current, voltage, travel speed, etc.) upon mechanical properties.

The research for this program is closely interrelated with that for Shielded Metal-Arc Welding for LMFBR Components.[1] For example, the mechanical properties and metallographic studies on the two programs directly complement each other, and occasional cross-referencing of information is useful.

Study of Submerged-Arc Process

Preparation of Weldment Specimens (G. M. Goodwin)

Weldments were prepared in 1-in.-thick type 304 stainless steel with a variety of commercially available fluxes and a range of energy input conditions.[2] We machined test specimens of several types from each weldment, including transverse and longitudinal (i.e., perpendicular and parallel to the welding direction) specimens of all weld metal and transverse specimens that contained weld metal, fusion line, and heat-affected zone.

Investigations of Mechanical Properties (D. G. Harman, G. M. Goodwin)

Our investigations of the mechanical properties of 1-in.-thick submerged-arc weldments are continuing on specimens from welds prepared

with the Arcos S-4 flux. These welds represent materials and procedures typical of those to be used for fabrication of LMFBR vessels. We controlled the travel speed at 30, 18, and 4.5 in./min to provide energy input values of 40.8, 68, and 272 kJ/in., respectively.

We previously reported[3] some preliminary creep-rupture results obtained at 650°C (1200°F) for welds made with medium energy input. We showed that the submerged-arc weld was consistently weaker (ruptured in about one-tenth the time) but much more ductile at the longer rupture times than shielded metal-arc welds tested at this same temperature. We also reported that the creep-rupture properties at 650°C were not deleteriously affected by annealing at 1065°C after welding or by such an anneal followed by aging 10 hr at 800°C. The treatment at 800°C is designed to avoid sensitizing the grain boundaries of the adjacent base metal at service conditions. Figures 7.1 and 7.2 show creep curves obtained at 650°C at 25,000 and 18,000 psi, respectively, from welded, annealed, and annealed-plus-aged specimens from a weld made with medium energy input and machined transverse to the weld direction with a fusion line within the gage section.

Although it is not possible to determine quantitatively the amount and rate of deformation from a specimen that contains the fusion line, valid comparisons can be made. Note that the total creep deformation decreases with increasing rupture time (compare Figs. 7.1 and 7.2). This was not true for the transverse specimens that contained all weld metal and that were tested under the same conditions. It is also apparent that both treatments after welding significantly increased the amount of third-stage deformation in the area of the fusion line.

In each case, the specimens that contained the fusion line ruptured within the weld metal. It will be shown later that the yield strength of the weld metal is considerably higher than that of the heat-affected base metal when tested as welded. Since we would then expect the weld-metal portion of such specimens to creep at a slower rate than the base-metal portion, it is surprising that they ruptured in the weld metal. Apparently the test is accelerated to failure as the weld metal reaches the creep strain necessary for initiation of the third stage of creep.

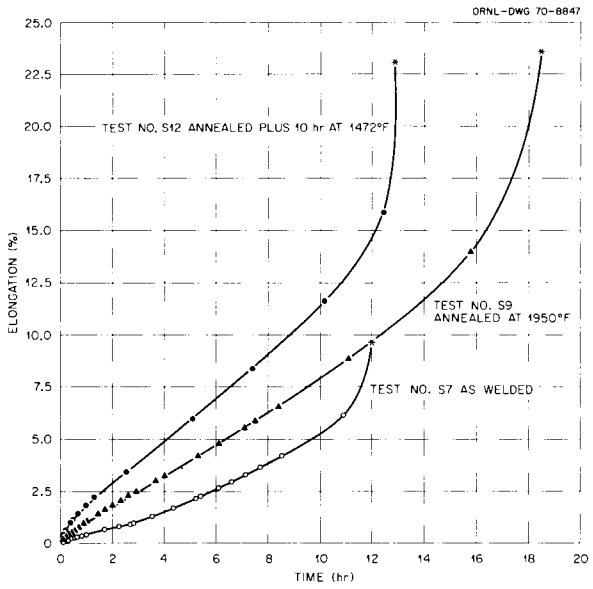

Fig. 7.1. Effect of Heat Treatment on Creep of Transverse Specimens That Contained the Fusion Line. Tested at 650°C (1200°F) and 25,000 psi. Specimens were welded with medium energy input and were tested in air in three conditions: (1) as welded, (2) after annealing 30 min at 1065°C (1950°F), and (3) after annealing 30 min at 1065°C (1950°F) and aging 10 hr at 800°C (1472°F).

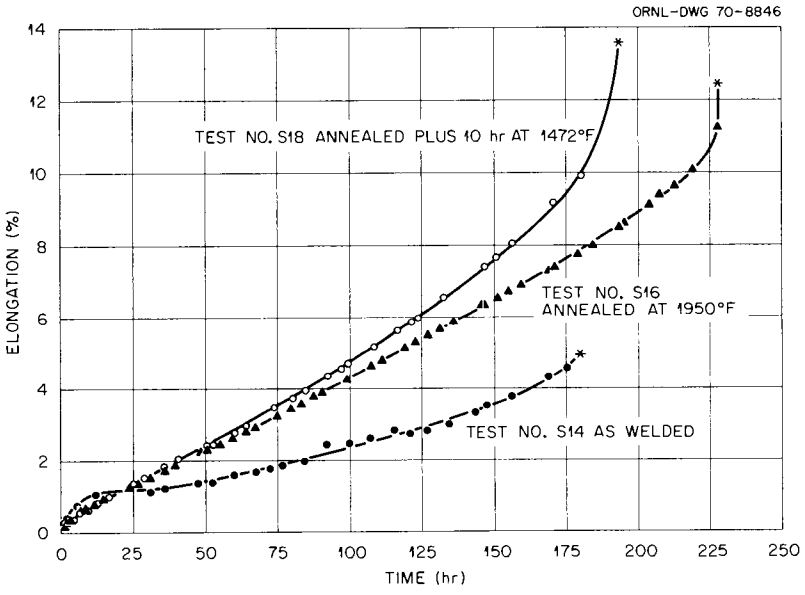

Fig. 7.2. Effect of Heat Treatment on Creep of Transverse Specimens That Contained the Fusion Line. Tested at 650°C (1200°F) and 18,000 psi. Specimens were welded with medium energy input and were tested in air in three conditions: (1) as welded, (2) after annealing 30 min at 1065°C (1950°F), and (3) after annealing 30 min at 1065°C (1950°F) and aging 10 hr at 800°C (1472°F).

Reduction in area is perhaps more significant than the creep extension for these composite specimens. The reductions in area for the specimens tested at 25,000 psi (see Fig. 7.1) are 16, 30, and 38% for the welded, annealed, and annealed-plus-aged conditions, respectively, while those for the specimens tested at 18,000 psi (see Fig. 7.2) were 6.8, 9.7, and 15.5%. Again, note the significance of heat treatment and stress level on creep ductility.

We continued our comparisons of the submerged-arc and shielded metal-arc processes by means of tensile tests at 650°C. We tested buttonhead specimens machined from 1/4 × 1/4 × 2-in. specimen blanks cut longitudinally to the weld direction from a layer midway through the weld depth (1 in. from both top and bottom surfaces). We found a variation in the properties of the specimens tested as welded as we traversed from base metal through the deposited weld metal and back to base metal. Since we included 1 to 1 1/2 in. of base metal from each side of the welds, we were able to measure the properties of both the base metal and heat-affected zone.

Figure 7.3 shows the tensile strength and ductility of a submerged-arc weld made with medium energy input and Arcos flux and of the standard shielded metal-arc weld made with an electrode coated with lime-TiO_2. As expected from our creep-rupture results, the submerged arc weld was not as strong as the shielded metal-arc weld. The overall observations, however, were identical for both welding processes. Both the 0.2%-offset yield strength and the ultimate tensile strength were highest at the fusion line. The ultimate strengths of the weld metal were comparable to those of the heat-affected zone, but the yield strengths were much higher. Because the yield strengths of the weld metal were near those for the ultimate strengths, the stress-strain curves peaked very early, and the uniform elongation was as low as 1%. The total elongation of the weld metal was about one-half that for the base-metal specimens most distant from the welds (25% compared with 50%).

We have tested the creep-rupture properties of specimens from the welds made with low, medium, and high energy input at 593°C (1100°F). The results from tests at 28,000 psi are listed in Table 7.1. The

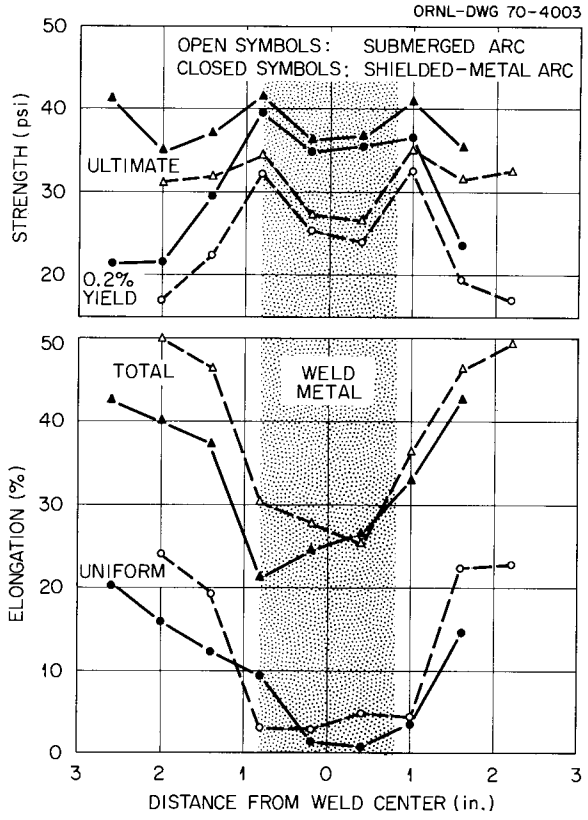

Fig. 7.3. Tensile Properties of Submerged Arc and Shielded Metal-Arc Weldments at 650°C (1200°F). Specimens were machined longitudinal to the weld direction from both base plate and weld metal and were tested in air at 0.002 min^{-1}.

Table 7.1. Effect of Energy Input on the Creep-Rupture Properties of Submerged Arc Welds at 593°C and 28,000 psi

Travel Speed (in./min)	Energy Input (kJ/in.)	Rupture Time (hr)	Elongation (%)	Minimum Creep Rate (%/hr)
30	40.8	119.7	24.0	0.1195
18	68	129.8	23.1	0.1190
4.5	272	123.5	16.4	0.0905

small difference in properties is surprising considering the wide range in energy input and resulting microstructure. The creep curves for these three tests are shown in Fig. 7.4. Preliminary results from tests at a lower stress of 25,000 psi indicate that some significant differences may show up after the longer test times. A specimen from the weld made with medium energy input ruptured after 283 hr, but one from the weld made with low energy input is still in test after 340 hr.

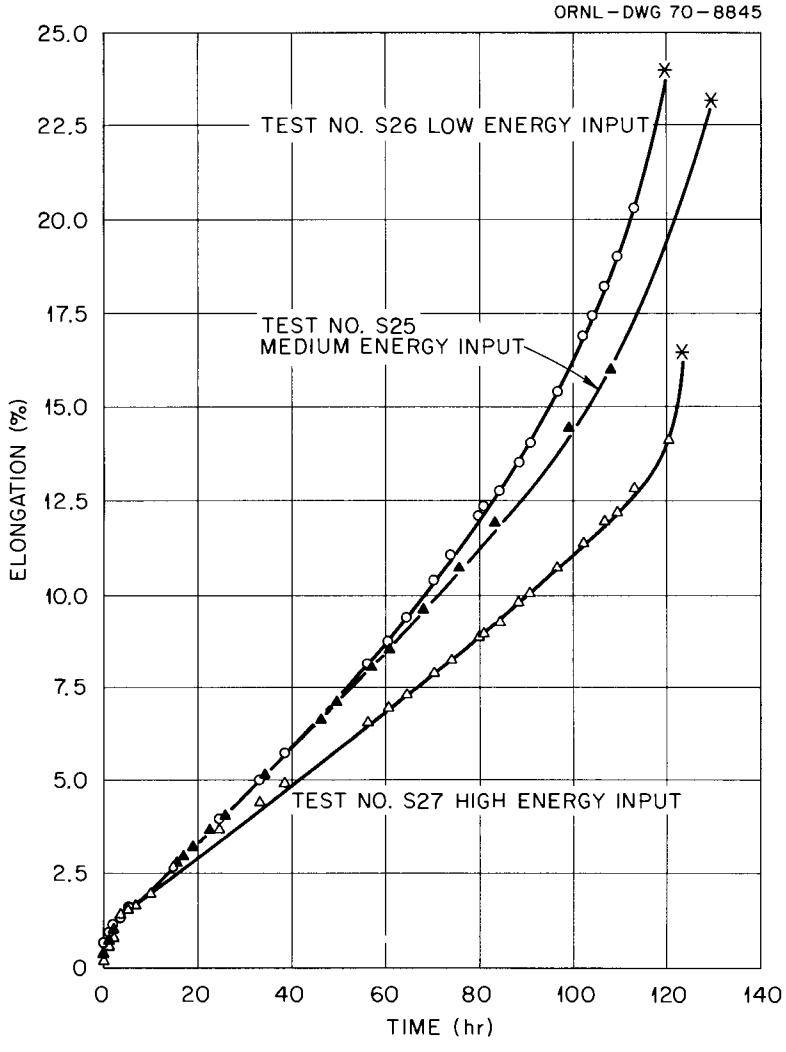

Fig. 7.4 Effect of Energy Input on the Creep Curves of Submerged-Arc Weld Specimens Tested at 593°C (1100°F) and 28,000 psi. Specimens were machined transverse to the weld direction, and the gage sections were all weld metal.

Corrosion Studies (G. M. Goodwin, Nancy C. Cole)

Considerable concern has been expressed about the possibility of corrosion damage – other than that associated with Na corrosion – to the vessel and components for the Fast-Flux Test Facility (FFTF) Reactor during fabrication, shipping, installation at the site, and outages after a time of operation. In order to evaluate the response of several types of weldments to a particular type of aqueous corrosion, we prepared composite wafer specimens, 1 × 2 × 1/4 in. thick, that contain weld metal, base metal, and heat-affected zones. These wafers were heat treated as shown in Table 7.2 and will be tested at Combustion Engineering, Inc., Chattanooga, Tennessee, by the Strauss Test (ASTM A393-63), which consists of a bend test after 72 hr in an acidified copper sulfate solution. The specimens will be examined metallographically after testing to determine the relationship between the structure produced by welding and heat treatment and its reponse to the Strauss Test.

Heat-Treatment Studies (Nancy C. Cole, G. M. Goodwin)

We are conducting extensive studies of the effect of heat treatment on base metal, heat-affected zones, and specimens of all weld metal from a number of different welds to determine, in general, the following.

The Required Relationship of Time and Temperature for Solution Treating. – We are studying a temperature range of 925 to 1120°C (1700 to 2050°F) and solution times from 1 to 10 hr, and have found that for certain compositions of weld metal, the ferrite phase is stable even after several hr at 1065°C (1950°F), though the ferrite does agglomerate considerably.

The Effectiveness of So-Called "Carbide Agglomeration" Treatments After Solution Treating at 1065°C (1950°F) for 1 hr. – We are examining the effects of holding temperatures of 730 to 855°C (1350 to 1575°F) for times from 1 to 100 hr.

The Relationships of Time and Temperature for the Formation of Sigma Phase and the Precipitation of Carbides. – The temperature range of interest is 540 to 800°C (1000 to 1472°F) for aging times from 1 to 1000 hr. We expect that we can metallographically discriminate

Table 7.2. Summary of Heat-Treatments for Weldment Specimens for Evaluation by Strauss Test

Specimen	Weld[a]	Heat Treatment[b]
1	FO1	
2	FO1	1065°C (2 hr), 65°C/hr to 800°C (10 hr), 40°C/hr to 455°C, WQ
3	FO1	1065°C (2 hr), 65°C/hr to 800°C (10 hr), 95°C/hr to 455°C, WQ
4	FO1	1065°C (2 hr), 65°C/hr to 800°C (10 hr), 150°C/hr to 455°C, WQ
5	FO1	1065°C (2 hr), 65°C/hr to 800°C (10 hr), 205°C/hr to 455°C, WQ
6	FO1	800°C (10 hr), 95°C/hr to 455°C, WQ
7	FO1	650°C (10 hr), 40°C/hr to 455°C, WQ
8	SA-6	
9	SA-6	1065°C (2 hr), 65°C/hr to 800°C (10 hr), 40°C/hr to 455°C, WQ
10	SA-6	1065°C (2 hr), 65°C/hr to 800°C (10 hr), 95°C/hr to 455°C, WQ
11	SA-6	1065°C (2 hr), 65°C/hr to 800°C (10 hr), 150°C/hr to 455°C, WQ
12	SA-6	1065°C (2 hr), 65°C/hr to 800°C (10 hr), 205°C/hr to 455°C, WQ
13	SA-6	800°C (10 hr), 200°F/hr to 455°C, WQ
14	SA-6	650°C (10 hr), 40°C/hr to 455°C, WQ

[a] FO1 = Shielded metal-arc weld, lime coating; Sa-6 = Submerged-arc weld, Hobart Flux.

[b] Times in parentheses indicate hour times at temperature. WQ = Water Quench. All heat treatments performed in air.

between ferrite, sigma phase, and carbides and have noted significant differences in the temperature and rate of formation of sigma phase in the weld metal as a function of the composition and structure of the weld metal. The longer-term heat treatments are continuing, and a detailed analysis will be presented in subsequent reports.

Irradiation Studies (G. M. Goodwin)

We prepared 226 composite samples composed of a sample of all weld metal and a sample of weldment for irradiation in the Experimental Breeder Reactor-II (EBR-II) during the first quarter of fiscal year 1971. Of these 226 specimens, 168 make up an 8 × 5 × 3-in. statistically designed experiment that involves eight different welds, five specimen positions, and three heat treatments. The remaining 58 specimens are comprised of additional welds, heat treatments, and specimen locations that could not be included in the main experiment because of the number of variables involved. All specimens were machined, and we began installing them into the irradiation assembly.

Metallographic Studies (Nancy C. Cole, G. M. Goodwin)

Extensive metallographic analyses are necessary to provide the link between various welding procedures, the solidification substructure that they produce, and high-temperature mechanical properties. The as-welded microstructure consists of austenite with a small amount of ferrite. This ferrite is desired for producing welds free of cracks; however, during service at high temperature, it tends to promote formation of the hard, brittle sigma phase, which in turn reduces the ductility of the weld.[4]

Since ferrite apparently plays an important role in determining the behavior of a weld in service, we are attempting to determine improved ways to measure its amount and characterize its morphology. The amount of ferrite is not easily determined, and much scatter is encountered. Many variables are involved, both in the production of the welds and the techniques for measuring the ferrite. We have chosen a destructive technique, which uses the quantitative television microscope, as the primary method for study.

We previously reported[5] a comparison of the amount of ferrite measured on welds from four different processes. The measured ferrite content varied from a mean of 3.1% for a shielded metal-arc weld to a mean of 8.2% for a gas metal-arc weld. The shielded metal-arc weld was made with a filler metal designed to have less than 3% ferrite; however, the other three welds were made with type 308 stainless steel filler metal. Also noted was the fact that the amount of ferrite measured within a given weld varied by a factor of 2 within each of the processes.

Subsequent studies on these welds confirmed this scatter, as shown in Table 7.3. The mean ferrite content listed represents an average of 12 or more readings on different areas within that location. Not only did the ferrite content vary between welding processes, but the amount of ferrite varied between welds made by a given process, between samples from a given weld, and between locations (e.g., the fusion line and the center of the weld) within the cross section of a given weld. Note

Table 7.3. Ferrite Measurements in Austentic Stainless Steel

Weld	Ferrite Content (%)	
	Range	Mean
Shielded Metal Arc	2.2–4.2	3.1
Submerged Arc	4.4–10	7.5
Gas Tungsten Arc	4.9–10.2	8.0
Gas Metal Arc	5.4–11.5	8.2
Submerged Arc		
Weld B, Sample 22	7.3–13.3	10.1
Weld A, Sample 64	10.3–15.3	12.6
Weld A, Sample 61	9.4–19.8	14.3
Gas Metal Arc		
Center	6.3–13.5	9.9
Root	4.6–8.3	6.6
Surface	9.3–13.7	11.7
Fusion Line	6.7–9.4	8.1

that the variation within one cross section is as large or larger than the variation between the submerged-arc, gas metal-arc, and gas W-arc processes. However, the distribution of the ferrite between processes varies considerably more than it does within one cross section of one weld. Thus, merely measuring the amount of ferrite in a weld does not give a complete picture of the morphology of the ferrite and how it affects the properties of the weld. Additional studies aimed at clarifying the situation are under way.

Notes

1. W. O. Harms and G. M. Slaughter, "Shielded Metal-Arc Welding for LMFBR Components," Chapter 8, p. 142, this report.

2. J. R. Weir and G. M. Slaughter, Fuels and Materials Development Program Quart. Progr. Rept. March 31, 1970, ORNL-4560, pp. 111–118.

3. G. M. Goodwin, D. G. Harman, and Nancy C. Cole, Fuels and Materials Development Program Quart. Progr. Rept. March 31, 1970, ORNL-4560, pp. 113–118.

4. T. L. Lyman (Ed.), Metals Handbook, 8th ed., pp. 419, 422, Vol. I, American Society for Metals, Metals Park, Novelty, Ohio, 1961.

5. G. M. Goodwin and N. C. Cole, Fuels and Materials Development Program Quart. Progr. Rept. June 30, 1969, ORNL-4440, pp. 167–174.

8. SHIELDED METAL-ARC WELDING FOR LMFBR COMPONENTS

W. O. Harms G. M. Slaughter

The objective of this program is to evaluate the shielded metal-arc (stick electrode) welding process for fabricating and repairing certain stainless steel components for liquid-metal fast breeder reactors (LMFBR). We very slightly modified the flux coatings of electrodes and are determining the influence of minor elements on the mechanical properties of the weld metal at elevated temperature. Flux coatings traditionally have been evaluated and selected by the relative ease with which weld metal can be deposited, and bead contour, arc stability, and deposition efficiency are usually prime considerations. The effect of the coating on the properties at elevated temperatures has not been seriously considered.

As part of this effort, we are also providing weld specimens to Battelle Memorial Institute Pacific Northwest Laboratory (BNWL) for a program of irradiations for the Fast Flux Test Facility (FFTF) Reactor.

Effect of Variations in Flux Coating

Preparation and Creep-Rupture Testing of Weldments (N. C. Binkley, G. M. Goodwin, D. G. Harman)

We reported[1] that the shielded metal-arc weldments display decreasing creep elongations with increasing time to rupture at 650°C (1200°F). We showed that, for the standard lime-TiO_2 coating, the ductility loss was associated with a metallurgical instability at the phase boundary. We suspect that the ferrite that is concentrated in these locations is perhaps transforming to the brittle sigma phase at the test temperature and that this is responsible for the loss of creep ductility for the welds of other compositions as well.

Sigma phase forms most readily at 650°C (1200°F) but has been reported for service temperatures ranging from about 500 to 760°C. We expected that the embrittlement that would occur at temperatures below 650°C would be more sluggish and, consequently, more difficult to demonstrate at testing times commensurate with the laboratory facilities committed to this program.

Creep-rupture tests of specimens from welds made with electrodes with the standard lime-TiO_2 coating at 593°C (1100°F) did show the embrittlement to be sensitive to temperature in the direction expected. The relationship of rupture time with stress and elongation is shown in Fig. 8.1 for both test temperatures for this weld. We were quite surprised that the creep

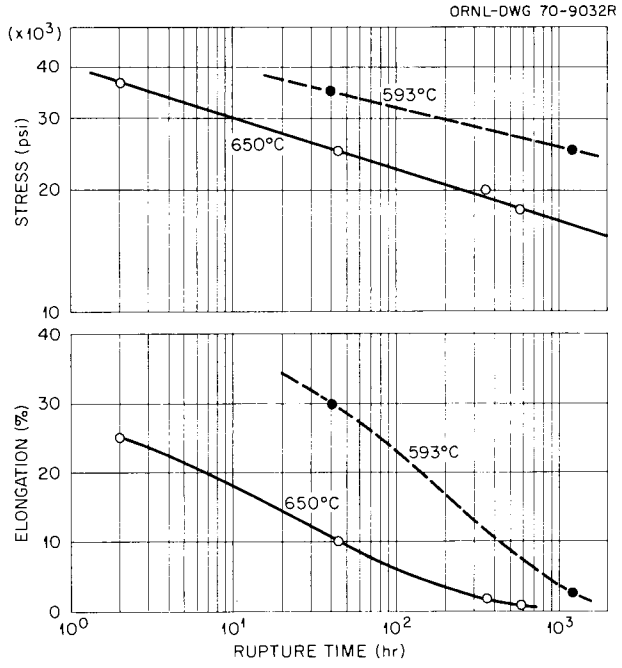

Fig. 8.1. Creep-Rupture Properties of Shielded Metal-Arc Weldment from Standard Lime-Titania Coated Electrode Tested in the As-Welded Condition.

ductility at 593°C decreased as rapidly as is shown here. Values of less than 5% can be expected for times greater than 1000 hr, even at the lower temperature. Since embrittlement due to formation of carbides at grain boundaries has generally been found to be most serious between 550 and 600°C for wrought austenitic alloys, the role of carbides in the instability of phase boundaries in weld metal is being investigated.

We recently included three experimental lime-base coatings in our studies of compositional variations. These were formulated by Combustion Engineering personnel at Chattanooga, Tennessee, and their tests show them to have improved ductility as compared with welds made with the standard lime-coated electrode. The new formulations contain a

ferro-titanium addition, ferro-titanium plus B, and ferro-titanium plus B and P. Figure 8.2 shows their test results along with ours for the weld from standard lime-coated electrode. We are preparing test specimens from the welds made at Combustion Engineering and have also obtained electrodes so as to prepare welds using equipment and personnel common to the rest of our program.

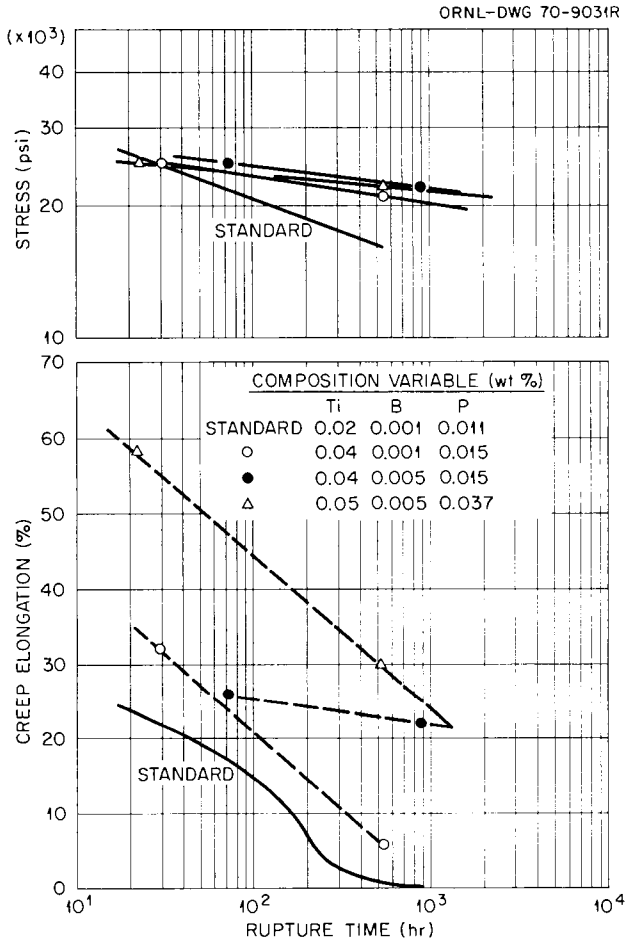

Fig. 8.2. Effect of Compositioned Variations on the Creep-Rupture Properties of Weldments from Lime-Base Coated Electrodes Tested at 650°C in the As-Welded Condition.

The status of our tests at 650°C and 18,000 psi of the welds made with the controlled lime-titania coatings is shown in Table 8.1. We previously showed C to be only moderately effective in increasing the rupture time.[1] Close examination of the creep curve from the high-C weld

Table 8.1. Effect of Compositional Variables on Creep Properties of Shielded Metal-Arc Welds in Stainless Steel at 650°C and 18000 psi

Coating	Rupture Life (hr)	Total Elongation (%)	Minimum Creep Rate (%/hr)
Commercial lime-TiO_2, 0.044C–0.47Si–0.012P–0.016S–0.001 B	576	0.50	1.9×10^{-4}
Low (0.035%) C	490	4.5	1.0×10^{-3}
High (0.074%) C	6000[a]	0.46	$< 5.0 \times 10^{-5}$
Low (0.29%) Si	592	3.2	1.0×10^{-3}
High (0.73%) Si	710	0.2	2.0×10^{-4}
Low (0.009%) P	To be tested		
Medium (0.023%) P	To be tested		
High (0.034%) P	1655	0.97	2.5×10^{-4}
Low (0.006%) S	526	0.75	8.3×10^{-4}
High (0.027%) S	548	0.67	3.9×10^{-4}
Medium (0.004%) B	2670	1.0	1.1×10^{-5}
High (0.006%) B	To be tested		

[a]Temperature drift caused specimen to rupture early. Rupture time extrapolated from tests of higher stress.

showed a slight increase in creep rate midway in the test due to a temperature drift caused by a faulty component in our temperature standard. Since the total creep strain is limited to very small values, a slight change in minimum creep rate severely affects the rupture time. Tests at two other stress levels substantiated this. These results show that additions of C increase strength but decrease ductility, while additions of B and P increase strength more and offer some promise in indicating solutions to the problem of loss of ductility.

Tensile properties of the standard lime-TiO_2 weld are compared with those of a submerged-arc weld elsewhere.[2]

Notes

1. N. C. Binkley, G. M. Goodwin, and D. G. Harman, Fuels and Materials Development Program Quart. Progr. Rept. March 31, 1970, ORNL-4560, pp. 119–126.

2. D. G. Harman and G. M. Goodwin, "Investigations of Mechanical Properties," pp. 131–136, this report.

9. PROPERTIES OF FERRITIC STEEL WELDS

J. R. Weir, Jr. G. M. Slaughter

The use of ferritic steels for tubing, piping, and headers in high-integrity steam generators requires that their overall weldability and the mechanical properties of weld metal and heat-affected zone at elevated temperatures (290 to 595°C) be assessed. The susceptibility of both the weld metal and the heat-affected zones to cracking is of particular interest.

This program deals with four classes of ferritic steel that are candidates for use in either liquid-metal-cooled or water-cooled reactors. The purpose of the program is to compare the weldabilities of these various steels and to determine the advantages and limitations of each. We emphasize determining susceptibility to cracking associated with the weld and the effects of welding on mechanical properties at the expected service temperatures.

Plain-Carbon Steels

Procurement and Preparation of Specimens (N. C. Binkley, D. A. Canonico)

We have procured a large plate (1 in. × 4 ft × 6 ft) of plain-C steel with the same C level (0.010% C) as the standard and stabilized varieties of 2.25% Cr–1% Mo ferritic steels. Lehigh restraint specimens (Fig. 9.1) are being prepared from this plate. In addition, some of the plate will be further reduced into test tubing, rod, and thinner plate for TIGAMAJIG specimens. Filler material for the plain-C steel (SAE 1010) is being procured.

Conventional 2.25% Cr–1% Mo Low-Alloy Steels

Procurement and Preparation of Specimens (N. C. Binkley, D. A. Canonico)

We procured a large plate (1 in. × 4 ft × 8 ft) of ASTM A387-D steel (standard 2.25% Cr–1% Mo ferritic steel). Lehigh restraint specimens were prepared from this plate with varying amounts of restraint dependent upon the depth of the sawcuts. Much of the plate remains for additional specimens.

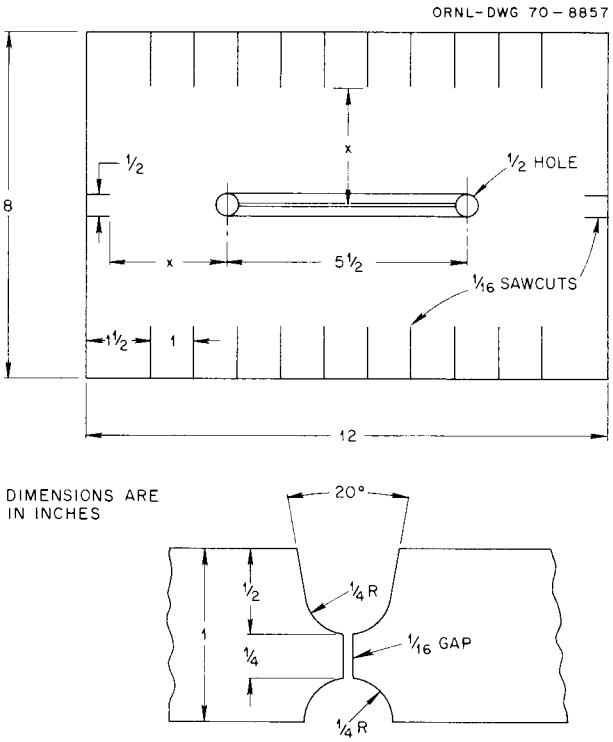

Fig. 9.1. Lehigh Restraint Specimen.

Low-Carbon Low-Alloy Steels

Procurement of Material (N. C. Binkley, D. A. Canonico)

We are attempting to procure an experimental heat of low-C (0.02% C) 2.25% Cr–1% Mo steel. This heat will then have to be rolled to shape.

Stabilized Low-Alloy Steels

Literature Search (N. C. Binkley, D. A. Canonico)

We began a thorough literature search into the weldability of these steels. As part of this search, we began correspondence and discussions with various domestic and European organizations and firms that may have experience in the welding of these steels, which have been used for some time in Europe in steam generators.

To date, two replies and an acknowledgment have been received from Europe. One reply, from Interatom (Internationale Atomreaktorban GmbH) of Germany, indicated that their experience with the welding of stabilized

2.25% Cr–1% Mo ferritic steel had been quite favorable. Interatom referred us to other sources, and we contacted these. Gebr. Böhler and Company of Germany sent us welding filler metal that they supply commercially in Europe specifically for welding the stabilized ferritic steels. A European supplier of these steels, Ugine-Kuhlmann of Paris, acknowledged our inquiry and should respond in the near future.

Discussions with manufacturing companies in this country revealed that they have not had the favorable experiences with the stabilized 2.25% Cr–1% Mo ferritic steels that the foreign companies report. They have encountered serious problems associated with hot cracking in the heat-affected zone (possibly due to the formation of Fe_2Nb).

Procurement of Materials (N. C. Binkley, D. A. Canonico)

Two different heats of Sandvik HT8×6 were received from Sandvik Steel, Inc. The HT8×6 is a Nb-stabilized 2.25% Cr–1% Mo steel that is being used in Europe in steam generators. One heat is in the form of seamless tubing typical of the tubing used for steam generator internals. The other heat of HT8×6 was received as bar stock in two 1-in.-diam × 2-ft-long rounds. We also attempted to procure some stabilized 2.25% Cr–1% Mo ferritic steel in plate form, but it appears that no plate products have ever been made of this material. Thus, we shall have to order an experimental heat and roll it to plate.

Preparation of Specimens (N. C. Binkley, D. A. Canonico)

Most of the specimens prepared to date have been from the limited amount of Sandvik HT8×6 stabilized 2.25% Cr–1% Mo steel. The 1-in.-diam bar of this steel was used to prepare a Jominy hardenability specimen. The results of this test, presented in Fig. 9.2, indicate that the hardenability of this material is poor, due, no doubt, to the formation of Nb carbides that decreases the amount of C available to enhance hardenability. The remainder of the bar stock was either flattened into 1/4-in. plate for TIGAMAJIG specimens or drawn into 1/4-in. rounds for Gleeble specimens. With the TIGAMAJIG, we hope to be able to determine the weld-associated susceptibility of this material to cracking. With the Gleeble, the material can be tested for hot ductility as well as

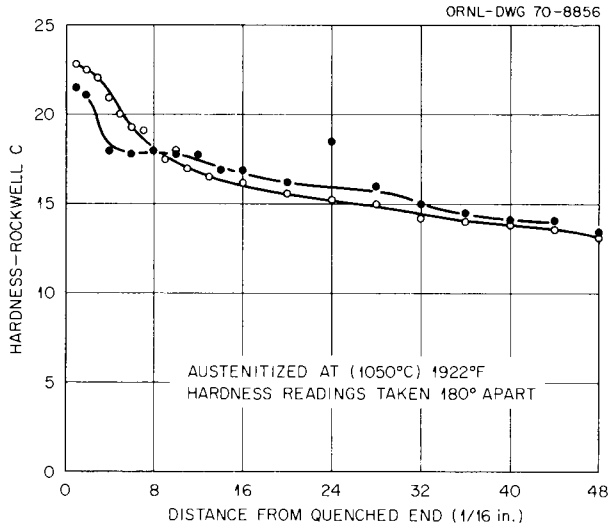

Fig. 9.2. Results of Jominy Hardenability Test.

subjected to various thermal cycles that simulate the cycling that would be encountered in various regions of a heat-affected zone. The HT8×6 tubing we received is from a different heat than the HT8×6 bar. Some of the tubing was slit longitudinally and flattened into strips about 1/16 in. thick. These strips were made into flat specimens for tests of hot ductility, both "on heating" and "on cooling." The zero ductility temperature will be established.

In all cases, the material, when reformed into different specimen shapes, was heat treated to produce the same microstructure as in the received material. The reported Sandvik heat treatment (1050°C normalizing for 20 min, air cooled to 500°C, tempered at 750°C for 1 hr, and air cooled to room temperature) was used with success. Microstructures of the received bar stock of HT8×6 (Fig. 9.3) compare favorably with that of the 1/4-in. plate heat treated for the TIGAMAJIG specimens (Fig. 9.4). Similarly, the microstructure of the received tubing (Fig. 9.5) compares favorably to that of the heat-treated strip rolled for Gleeble specimens (Fig. 9.6).

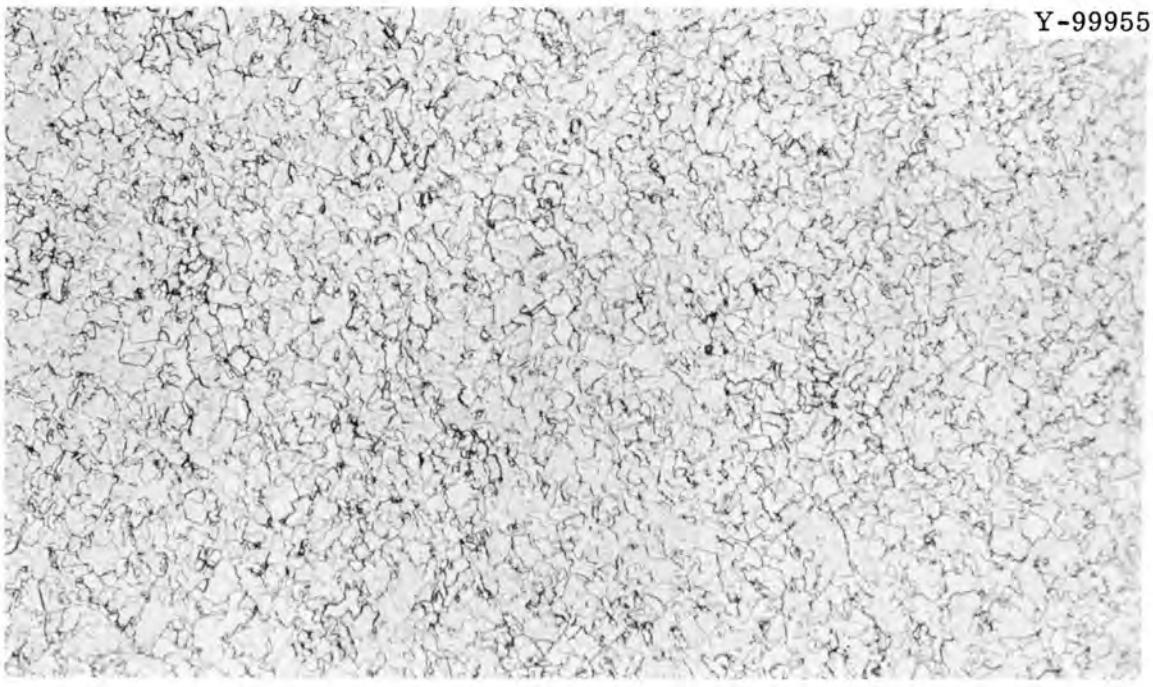

Fig. 9.3. Microstructure of Received Bar Stock of Sandvik HT8×6. 200×.

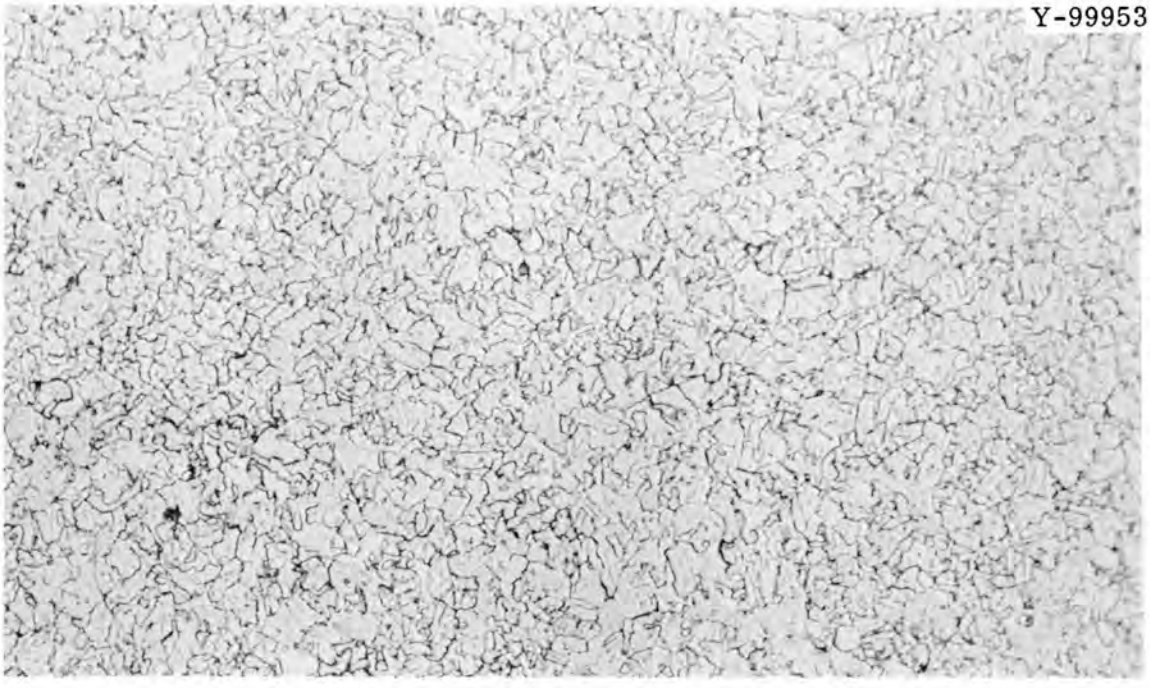

Fig. 9.4. Rolled Plate of Sandvik HT8×6 Heat Treated to Simulate Condition of Received Material. 200×.

Fig. 9.5. Microstructure of Tubing as Received from Sandvik Heat HT8x6. 200x.

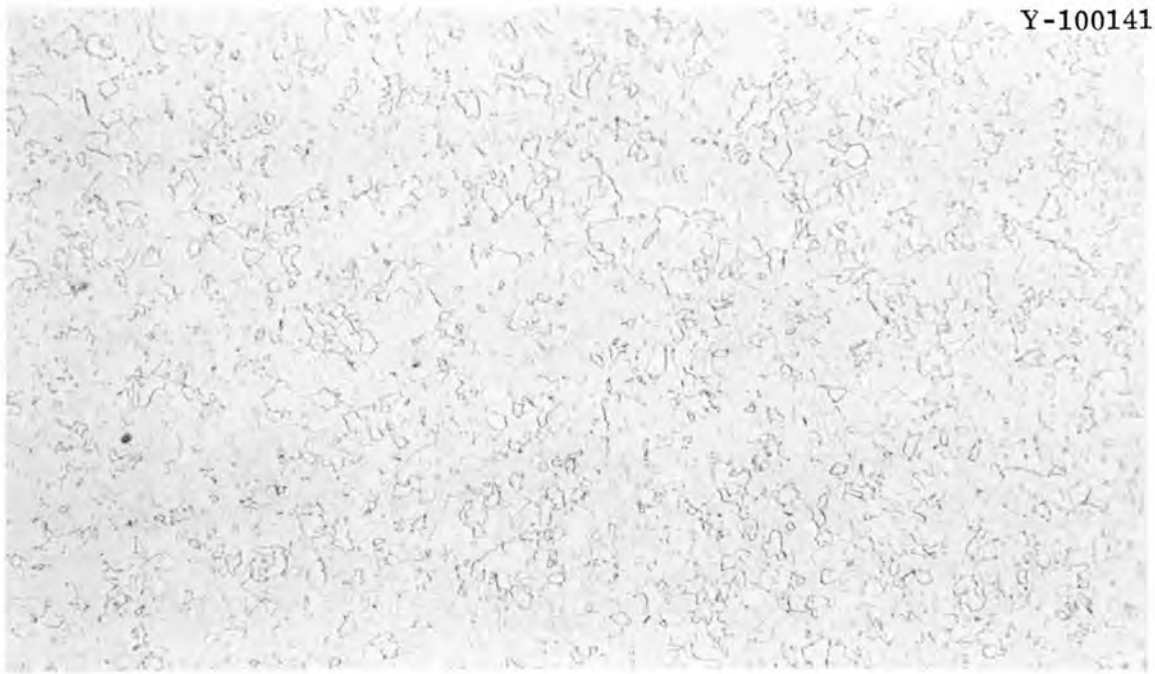

Fig. 9.6. Rolled Strip (0.063 in. Thick) of Sandvik Heat HT8x6 Heat Treated to Simulate Condition of Received Tubing. 200x.

10. NONDESTRUCTIVE TESTING TECHNIQUES FOR LMFBR

W. O. Harms R. W. McClung

We are developing new methods, techniques, and equipment for nondestructively evaluating materials or components related to the liquid-metal fast breeder reactor (LMFBR). Among the methods studied are electromagnetic induction, ultrasonics, and penetrating radiation. Special emphasis is being given to developing techniques for measuring the degree of cold work in stainless steel tubing with a small diameter.

Development of Advanced Nondestructive Testing

Development of Eddy-Current Instrument (C. V. Dodd)

We are continuing the development of an eddy-current instrument to measure both the size of defects and their depth below the surface. We have designed and constructed a video amplifier for the modular phase-sensitive eddy-current instrument that will be used in this program.

Ultrasonic Schlieren Techniques for Evaluation of Welds (H. L. Whaley, K. V. Cook)

We are using the schlieren technique in conjunction with two ultrasonic techniques for testing welds to study the response of ultrasound to various types of weld defects in samples of 1-in.-thick butt-welded Al and stainless steel plates. Weld samples for this study contain intentional defects such as porosity, inclusions, incomplete fusion, and incomplete penetration. The crown of each weld was ground flat before inspection. The three techniques by which each sample is being examined are described briefly below.

Schlieren. — The sample is scanned by means of a manually operated mechanical system in each of two different experimental configurations: (1) the transducer axis is aligned normal to the plate and centered on the weld; (2) the transducer is set at an angle of incidence needed to give a shear beam perpendicular to the weld interface. Because the sample plates are slightly bowed, maintenance of alignment is difficult. A

visual image of the ultrasonic pulse is observed as it travels through the water after having propagated through the weld area of the sample. Indications of the defects present in the weld are given by variations in the shape and intensity of the image of the pulse.

Conventional Pulse-Echo Ultrasonic Test. — The two basic systems of relative alignment of sample and transducer used in this test were the same as for the schlieren test. In this case, however, electronic instrumentation detects and displays (as traces on a cathode-ray screen) the ultrasonic signals reflected to the transducer from the sample. The disadvantage of this technique, as compared to the schlieren technique, is that all reflections that miss the transducer are "invisible." However, the sensitivity to small flaws may be significantly greater than for the visual technique. The mechanical system for scanning was manually controlled.

Delta Weld-Testing Technique. — The Delta technique[1] is a recently developed method of ultrasonically inspecting welds that utilizes the fact that ultrasound may be scattered from a discontinuity in a material in one or more of a number of ways. With the configuration shown in Fig. 10.1, a flaw so oriented as to prevent detection by a conventional pulse-echo test will still be detected if it scatters sufficient energy to the receiver. The transmitter and receiver are clamped in a single

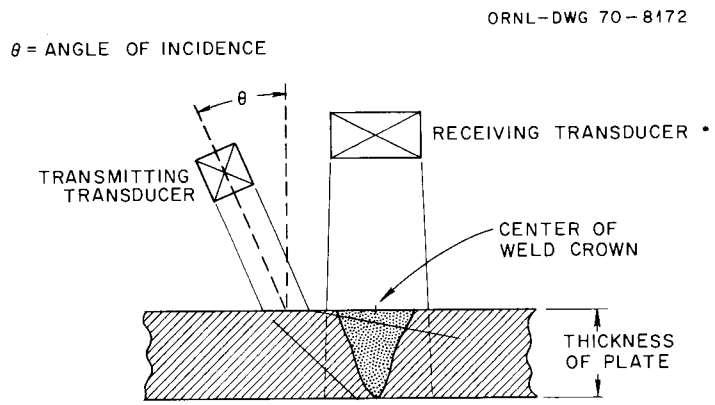

Fig. 10.1. Basic Delta Configuration.

mechanical fixture that maintains their relative positioning as they are scanned across the plate. The weld is scanned boustrophedonically by a precise automatic, mechanical system. A plan-view recording of the weld area is made for each sample. Interpretation of results is somewhat more difficult than for conventional techniques since a given discontinuity may be recorded more than once because various types of scattered energy (from a given flaw) may reach the receiver at different positions in its scan.

As data are accumulated, we are correlating the results between the different tests and with radiographs of each sample. Comparison of these data should increase our knowledge of the interaction of ultrasound with defects in welds.

Measurement of Cold Work in Stainless Steel Tubing

Design and Construction of Impedance Bridge (C. V. Dodd, W. A. Simpson)

We are investigating methods for nondestructively measuring the degree of cold work in stainless steel tubing that has a small diameter. We emphasize the use of electromagnetic induction for detecting the changes in magnetic permeability produced by cold work.

We constructed a high-impedance differential amplifier that will be used with the phase-sensitive eddy-current instrument to aid in the initial adjustment of the bridge. We received the stable alternating-current source that is needed for the impedance bridge.

Metallurgical Correlation

We are examining both the flat samples and the tubular samples of type 316 stainless steel with various degrees of cold work by means of the electron microscope. This will allow measurement of the relative amounts of martensitically-formed ferrite as a function of cold work for further correlation with the measurements of changes in relative permeability.

Notes

1. B. T. Cross et al., The Delta Technique — A Research Tool — A Quality Assurance Tool, TR-68-11, Automation Industries, Inc., Boulder, Colorado (March 1968).

11. SODIUM CORROSION STUDIES

W. O. Harms J. H. DeVan

The purpose of this program is to investigate the chemical and metallurgical effects produced in structural materials during exposure to molten Na. The program is designed to guide the selection of container materials for liquid-metal-cooled fast breeder reactor (LMFBR) systems and provide guidelines for specifying insulating materials for use with stainless steel components in the Fast Flux Test Facility (FFTF) Reactor.

Comparative Corrosion Tests on Refractory Alloys

J. H. DeVan

Although V alloys are highly resistant to dissolution by Na, they are quite reactive with nonmetallic impurities in Na, particularly with C, N, and O. Accordingly, we are investigating the mechanisms by which V alloys are attacked in Na at impurity levels typical of service conditions in a reactor. Our program is concerned with four basic aspects of the oxidation process for V alloys in Na: (1) the partitioning of O between V alloys and Na; (2) the effects of alloying additions of Cr and Zr on the diffusion coefficient of O in V; (3) the effects of Cr and Zr in V on the oxide formed and on the dissolution of the alloys in Na; and (4) the solubility of V in Na as affected by the presence of O in either metal. We are also examining the kinetics of the transfer of C, N, and O between V alloys and types 304 and 321 stainless steel in a Na circuit.

Effect of Oxygen on the Compatibility of Vanadium and Vanadium Alloys with Sodium (R. L. Klueh)

Static capsule tests are being used to study the effects of alloying additions on the oxidation behavior of V alloys in impure Na. We recently compared the oxidation behavior of V–1.3% Zr, V–5% Zr, and V–20% Mo with that of unalloyed V. Each of the alloys was encapsulated individually

with an unalloyed V specimen in a type 304 stainless steel capsule and exposed to Na with 2000 ppm O (added as Na_2O) for 100, 200, 300, and 600 hr at 600°C. All specimens gained weight and had black surface scales of varying thicknesses. Table 11.1 shows the changes in weight and O concentration as determined by fast-neutron activation analysis for the V and V alloy specimens. Generally the weight gains were commensurate with the change in O concentration and indicated that there was little or no mass transfer from the stainless steel capsules to the V.

Table 11.1. Oxygen Concentration of Vanadium and Vanadium Alloys Exposed to Sodium Containing 2000 ppm O at 600°C[a]

Time (hr)	Weight Change (mg)		Oxygen Concentration (ppm)		
			Vanadium	Vanadium Alloy	
	Vanadium	Vanadium Alloy	After Test[b]	Before Test	After Test
		V–1.3% Zr			
100	5.6	5.1	3940	175	4510
200	3.7	4.0	3030	110	3740
300	5.0	5.8	4250	132	5000
600	4.8	6.0	4020	121	5200
		V–5% Zr			
100	5.2	7.2	3910	228	5330
200	4.5	6.7	3850	220	5220
300	3.7	7.4	3600	212	5520
600	3.6	7.5	3320	196	5670
		V–20% Mo			
100	5.4	2.2	4090	184	2830
200	4.7	0.4	4120	134	2490
300	6.9	1.5	5980	155	2910
600	7.4	1.2	6470	133	2980

[a]All specimens were 1 × 1/2 × 0.04 in.

[b]Vanadium contained about 80 ppm before test.

The data in Table 11.1 indicate that O was redistributed between V–20% Mo and V during the first 300 hr of test and then remained fixed between 300 and 600 hr. Diffusion calculations show that equilibrium should be approached by 600 hr. As discussed previously,[1] these capsule tests allow a comparison of the equilibrium O distribution coefficient for unalloyed V (κ^V) with that of alloys in which O is in dissolved form. We showed[1] that $\kappa^{V\ alloy}/\kappa^V = C_O^{V\ alloy}/C_O^V$, where C_O represents the final concentration of dissolved O in the alloy and V, respectively. If we assume O in the V–20% Mo alloy to be completely in solid solution, the data in Table 11.1 show that the O distribution coefficient for the alloy is one half that for unalloyed V. This change in the O partitioning coefficient is very nearly the same as that reported[1] for a comparable Cr addition to V if we compare the additions on the basis of atomic percent.

These calculations of distribution coefficient are not applicable to the V-Zr alloys, since a major fraction of the O in these alloys is in precipitated form rather than solid solution. That is, the O diffuses into the V-Zr alloys, reacts with the Zr and precipitates an oxide of Zr. The kinetics of this process decrease with time, so equilibrium is approached very slowly. As is evident in Table 11.1, both V-Zr alloys continued to increase in O between 100 and 600 hr, an increase that has been verified metallographically.

Interstitial Contamination of Vanadium and Its Alloys (H. Inouye)

Unalloyed V was stressed to 12,000 psi at 600°C in N_2 at reduced pressures to determine the effects of N contamination on the creep properties. Table 11.2 compares the results of three tests in N_2 at pressures of about 10^{-6} torr with one test at a base pressure of 7×10^{-9} torr.

Based on the criterion of the minimum creep rate, this series of tests showed that the interaction of N with V to a pressure of 3.4×10^{-6} torr lowers the creep strength. However, on the basis of the time required to produce a given strain (up to 10%), V is stronger in 1.5×10^{-6} torr N_2 than in all the other environments tested, including

Table 11.2. Effect of Nitrogen Pressure on the Creep Properties of Vanadium Stressed to 12,000 psi at 600°C

Nitrogen Pressure (torr)	Time (hr) Required to Produce Given Strain				Minimum Creep Rate (hr^{-1})
	1%	2%	5%	10%	
					$\times 10^{-4}$
7.0×10^{-9}[a]	5.0	13.5	73	255	2.2
1.5×10^{-6}	26	50	136	327	2.8
3.4×10^{-6}	2.5	7.0	40	120	4.0
5.1×10^{-6}	2.5	5.5	8	8.5	b

[a]Base pressure. Nitrogen was not added to vacuum system.

[b]Specimen did not exhibit a definable creep rate.

the base pressure. This effect is attributed to the absence of a primary creep stage at this pressure.

The creep behavior in 5×10^{-6} torr N_2 was unusual in that an abrupt step in the creep curve occurred, as shown in Fig. 11.1. This specimen ruptured in 118 hr at a strain of 26%. Similar discontinuities in creep curves have been observed in Nb doped with O (ref. 2) and in Nb—0.6% Zr during contamination with O (ref. 3). The acceleration stage of creep in Nb-O alloys was attributed to "recovery" and in Nb—0.6% Zr to the precipitation of Zr from solution as a Zr oxide. The deceleration stage in the Nb-O alloys was attributed to the formation of a stable substructure and, in the case of Nb—0.6% Zr, to the formation of NbO at the grain boundaries. It is not known whether comparable mechanisms are responsible for the anomalous behavior of the V specimen tested in the program at a N_2 pressure of 5×10^{-6} torr.

Mass Transfer of Interstitial Impurities Between Vanadium Alloys and Type 304 Stainless Steels (D. H. Jansen)

We are operating a series of thermal-convection loops to determine the extent of interstitial mass transfer between V and stainless steel in Na. The heated portion of each loop is constructed of V, and the cooled portion is of either type 304L or type 321 stainless steel.

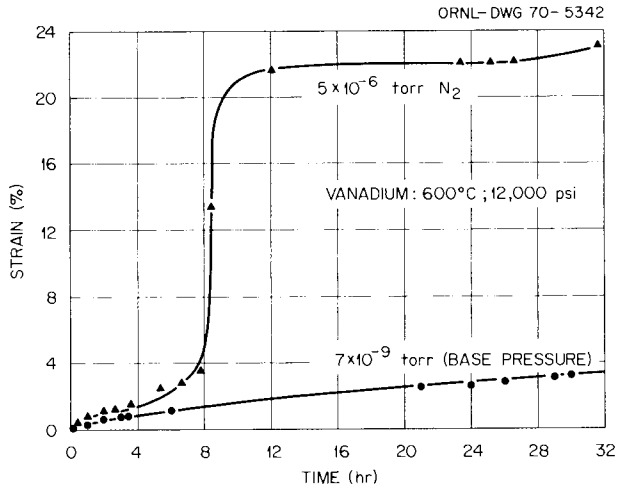

Fig. 11.1. Creep Behavior of 0.021-in.-Thick Vanadium Sheet in Vacuum and Low-Pressure Nitrogen. Specimens were creep tested at 600°C at a stress of 12,000 psi.

Results of the first test in this series, in which the cooled portion of the loop was constructed of type 304L stainless steel, were reported last quarter.[4] We have now examined a second loop that operated under test conditions[5] identical to those of the first loop but contained a cooled section of type 321 stainless steel. The loop operated for 3000 hr with Na that was hot trapped with Zr before it was filled. Sodium entered the heated section at 562°C and left it at 712°C. Seven V and three type 321 stainless steel inserts in the form of round tensile specimens[4] were positioned end-to-end in the heated V leg. Seven stainless steel and three V specimens were contained in the cold leg.

Figure 11.2 shows the weight changes of insert specimens according to their temperature and relative position in the loop. All V specimens [Fig. 11.2(b)] gained weight, as in the first loop.[4] However, the largest weight changes occurred near the entrance of the heater, and the changes decreased with increasing temperature along the heater, the reverse of what occurred in the first loop. Thus we suspect that the weight changes of V specimens in the heated entrance were not produced by Na but rather by a problem encountered before the loop was filled with Na. As the loop was being outgassed in preparation for filling, a leak developed in the braze joint that connected the dissimilar metals of the heater and cooler sections at the inlet to the heater. The braze

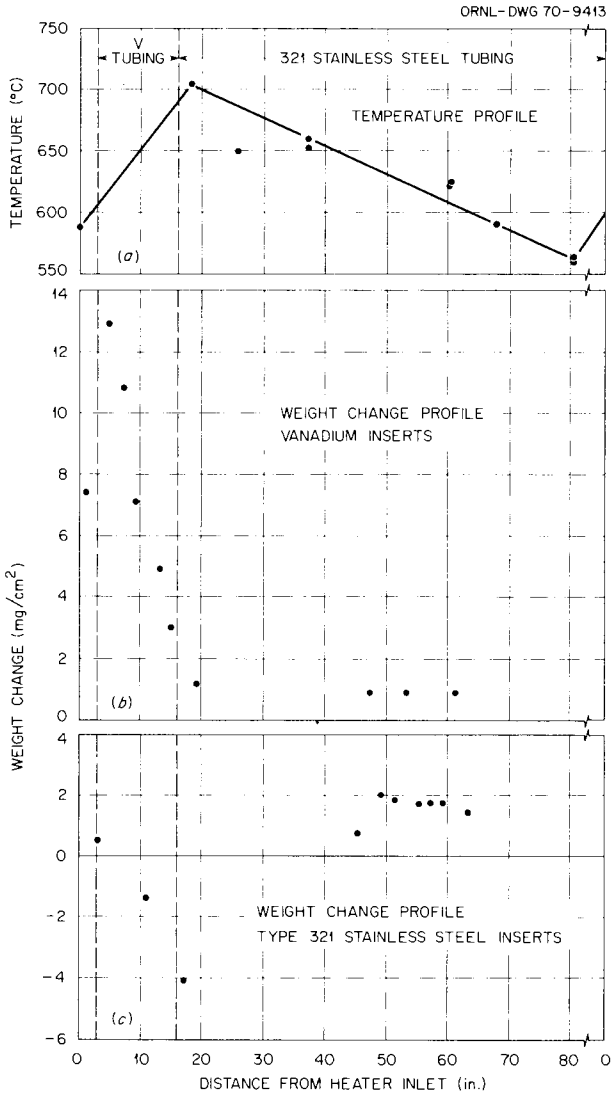

Fig. 11.2. Loop Temperatures and Specimen Weight Changes as Functions of Loop Position. (a) Loop temperatures as determined by Chromel-P vs Alumel thermocouples, (b) weight changes of vanadium specimens, and (c) weight changes of stainless steel specimens.

joint was subsequently repaired, and the loop was filled with Na and operated without further difficulty. However, although the loop was inside a vacuum chamber when the leak in the braze joint occurred, the V specimens in the heater section appear to have picked up N during the leak. This is also borne out by the relatively small weight changes of the V specimens in the cooled region, which were at a much lower temperature (300°C or less) at the time of the leak but whose temperature was comparable to that of specimens in the heated section during operation of the loop. These latter specimens, as well as the specimen at the heater exit, gained 1 to 3 mg/cm^2. Vanadium specimens from comparable positions in the first test (which incorporated type 304L stainless steel) were noticeably higher, 2 to 8 mg/cm^2. This comparison indicates that interstitial contamination of V at 600 to 700°C is somewhat less when coupled with type 321 stainless steel than with type 304L stainless steel.

The tensile properties at room temperature and interstitial content of selected V inserts are shown in Table 11.3. Note the relatively high N concentrations of specimens near the exit from the heater. Except for these latter specimens, the tensile properties of the V inserts were not noticeably changed by exposure to Na.

The stainless steel specimens in this test (type 321) showed essentially the same pattern of weight change as the type 304L stainless steel specimens in the first loop. As shown in Fig. 11.2(c), specimens at temperatures above 650°C experienced weight losses that increased with increasing loop temperature, and specimens below 650°C showed small weight gains. The interstitial changes for the stainless steel specimens and the corresponding effect on the tensile properties are compared in Table 11.4. Within the limits of analytical accuracy, there are no apparent changes in the bulk concentrations of N or C. Similarly, there was no substantial change in the tensile properties of the stainless steel specimens at room temperature. Thus, changes in the weight of the stainless steel specimens can be attributed, for the most part, to the movement of metallic rather than interstitial elements.

Table 11.3. Interstitial Content and Tensile Properties at Room Temperature of Vanadium Specimens After Exposure to Sodium for 3000 hr

Specimen Temperature[a] (°C)	Elongation (%)	Strength Properties (psi)		Interstitial Content (ppm)		
		Yield[b]	Tensile	O	N	C
		$\times 10^3$	$\times 10^3$			
592[c]	1.0	46.4	53.0	240	1500	160
632[c]	0.2	58.1	58.1	220	2500	150
702[c]	27.5	28.0	36.5	230	120	200
638[d]	41.0	19.7	30.7	120	51	200
606[d]	39.0	18.6	29.8	140	42	120
Control	40.0	13.6	26.6	180	72	290

[a] In sodium.

[b] At 0.2% offset.

[c] Located in heated region.

[d] Located in cooled region.

Table 11.4. Interstitial Content and Tensile Properties at Room Temperature of Type 321 Stainless Steel Specimens Exposed to Sodium for 3000 hr

Specimen Temperature[a] (°C)	Elongation (%)	Strength Properties (psi)		Interstitial Content (ppm)		
		Yield[b]	Tensile	O	N	C
		$\times 10^3$	$\times 10^3$			
605[c]	56.0	41.6	91.3	13	100	840
695[c]	44.5	41.0	96.3	32	110	920
643[d]	49.5	43.1	97.8	23	98	850
615[d]	44.5	44.7	98.2			
602[d]	48.0	42.2	96.1	22	79	840
Control				8	78	890

[a] In sodium.

[b] At 0.2% offset.

[c] Located in heated region.

[d] Located in cooled region.

Interactions of Sodium with Nonmetallic Materials

J. H. DeVan

Compatibility of Stainless Steel and Insulation for LMFBR Systems (C. D. Bopp[6])

The service temperatures of LMFBR's are considerably above those of present power reactors. Among the potential problems associated with higher operating temperatures are the possible interaction of thermal insulation with construction materials and the oxidation of these construction materials in the event of a Na leak. Accordingly, we are studying the reaction of commercial insulating materials with austenitic stainless steels between 370 and 760°C. A related study deals with the effect of Na on the oxidation of stainless steels, both insulated and uninsulated.

Effect of Sodium on the Oxidation of Stainless Steel. — We concluded our study of the effects of a Na leak on the oxidation behavior of austenitic stainless steels. This study was intended to evaluate the effect of the size of a leak on the rate at which Na escaped and on the interaction of Na with type 304L stainless steel and thermal insulation. The tests were conducted at 760°C in an atmosphere of 99% N_2, 1% O_2, and 100 ppm (by weight) H_2O.

In the final test in this series, we examined the effect of Na leakage on stainless steel and insulation when the stainless steel and surrounding insulation were each at 760°C (i.e., there was no temperature gradient through the insulation). The leak was an artificially induced crack in the stainless steel specimen that, at room temperature, produced an Ar leak rate of 2×10^4 atm cm^3/sec. This leak rate was the same as that of the fourth test[7] in which the stainless steel but not the insulation was heated to 760°C. In the fourth test, we observed a heavy concentration of Na oxides near the leak and rather extensive oxidation of the stainless steel specimen. In our last test, however, most of the leaking Na sublimed through the insulation and was deposited on the wall of our test apparatus. Accordingly, there was much less oxidation of the stainless steel than had occurred in the fourth test. This

finding corroborated our previous conclusion[7] that the damage to stainless steel from a Na leak is greatly reduced when thermal insulation or external surroundings afford a sink for Na.

Notes

1. R. L. Klueh, Fuels and Materials Development Program Quart. Progr. Rept. March 31, 1970, ORNL-4560, pp. 130–132.

2. J. Stoop and P. Shahinian, Effect of Oxygen on Creep-Rupture of Niobium, NRL-6095 (July 10, 1964).

3. T. K. Roche, Effect of Degree of Vacuum on the Slow-Bend Creep Behavior of Columbium-0.6% Zirconium at 1000°C, ORNL-3569 (June 1964).

4. D. H. Jansen, Fuels and Materials Development Program Quart. Progr. Rept. March 31, 1970, ORNL-4560, pp. 133–138.

5. D. H. Jansen, Fuels and Materials Development Program Quart. Progr. Rept. Sept. 30, 1969, ORNL-4480, p. 120.

6. On loan from Reactor Chemistry Division.

7. C. D. Bopp, Fuels and Materials Development Program Quart. Progr. Rept. March 31, 1970, ORNL-4560, pp. 139–141.

12. DEVELOPMENT OF FAST-REACTOR NEUTRON-ABSORBER MATERIALS

G. M. Adamson, Jr. W. R. Martin

The prime candidate material for the safety and shim rods in the Fast-Flux Test Facility (FFTF) Reactor and liquid-metal-cooled fast breeder reactors (LMFBR) is boron carbide (nominally B_4C) pellets in a stainless steel cladding. In spite of the widespread use of B_4C as a neutron absorber in thermal reactors, basic data have never been obtained. The material has never been fully characterized for structure, homogeneity range, effect of fabrication variables, and the effects of varying composition. The objective of our work is to characterize the material sufficiently to provide measurable control parameters to properly evaluate fabrication techniques and the effects of irradiation. The irradiation studies will emphasize basic effects of materials variables in both thermal- and fast-reactor environments. A secondary effort of this program will be the preliminary characterization of alternate materials that possess possible advantages over B_4C for use in fast reactors.

Characterization of Boron Carbide

Structural Changes that Result from Annealing of Powders (G. L. Copeland)

We completed mass spectrographic analysis of some of the Norbide 325F powders that increased in density when annealed rather than decreased as usual.[1] The results show no detectable differences in the heavy elements that were possible contaminants during annealing. Thus, the higher densities were probably due to erroneous measurements.

Transmission Electron Microscopy of Boron Carbide (C.K.H. DuBose, D. N. Braski,[2] G. L. Copeland)

We have developed a technique for preparing thin films of boron carbide (nominally B_4C) for transmission electron microscopy. Boron carbide has resisted successful thinning by conventional techniques due to its hardness, brittleness, and chemical inertness and because some voids are generally present that are attacked preferentially as the film

is thinned. These difficulties have been overcome through use of an ion-bombardment milling machine. A thin film of high quality was produced from a very dense B_4C pellet hot pressed from Norbide 325F powder. The electron transmission photomicrograph in Fig. 12.1 shows that the film was uniformly thinned in the area of the voids. The edges of the voids were parallel to crystal planes, as shown by comparison to dislocations in the film. The twins and grain boundaries are revealed clearly in Figs. 12.2 and 12.3. We are attempting to produce thin films from materials of lower density. Transmission electron microscopy should prove to be a valuable tool in the study of irradiated materials.

Chemical Composition and Size Distribution of a Coarse, Crushed Boron Carbide Powder (G. L. Copeland)

We purchased from the Norton Company 40 lb of nuclear-grade Norbide 4F B_4C powder from a single melt. The 4F designation indicates that the ingot was crushed to pass 4 mesh and that all finer sizes that resulted from the crushing were included with no further classification. We separated the powder into several size fractions to determine the size distribution and analyzed the various size fractions for B, C, and O. The results are shown in Table 12.1. The results do not completely agree with our previous results, which showed a marked decrease in the ratio of B:C as the size of the particles decreased.[3] In this case, the ratio of B:C tended to increase for the middle size ranges and decrease again for the finer size ranges. However, since most of the material was larger than 16 mesh, further crushing is required to provide significant separation of individual grains. Further characterization of this lot is in progress. The −20 +50 fraction was chosen for inclusion in the irradiation test in the Experimental Breeder Reactor-II (EBR-II). Pellets for the irradiation test were hot pressed from the −20 +50 fraction after further crushing to −80 +325 mesh and −325 mesh.

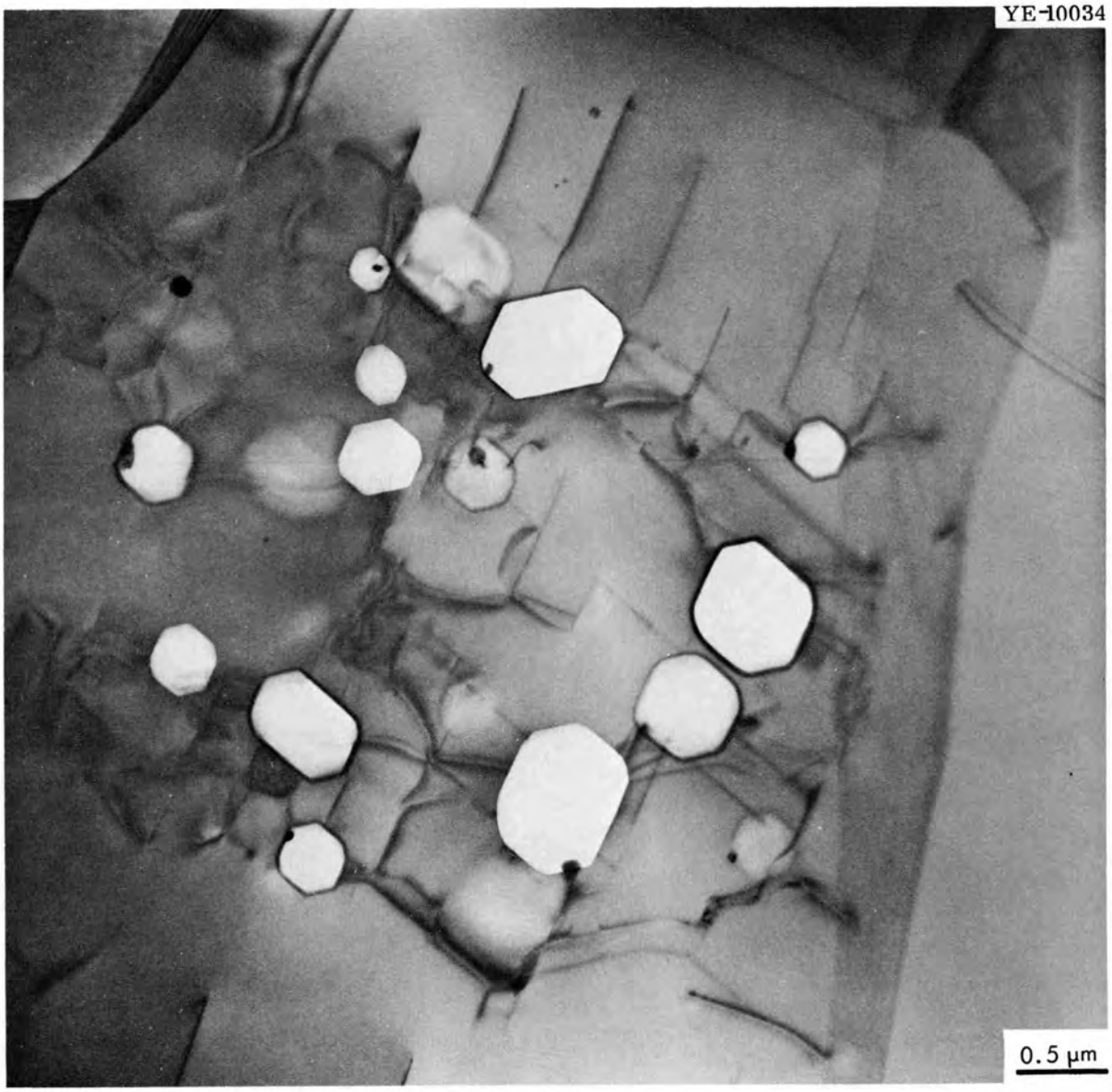

Fig. 12.1. Transmission Electron Photomicrograph of Hot-Pressed Boron Carbide Pellet Showing Polyhedral Voids.

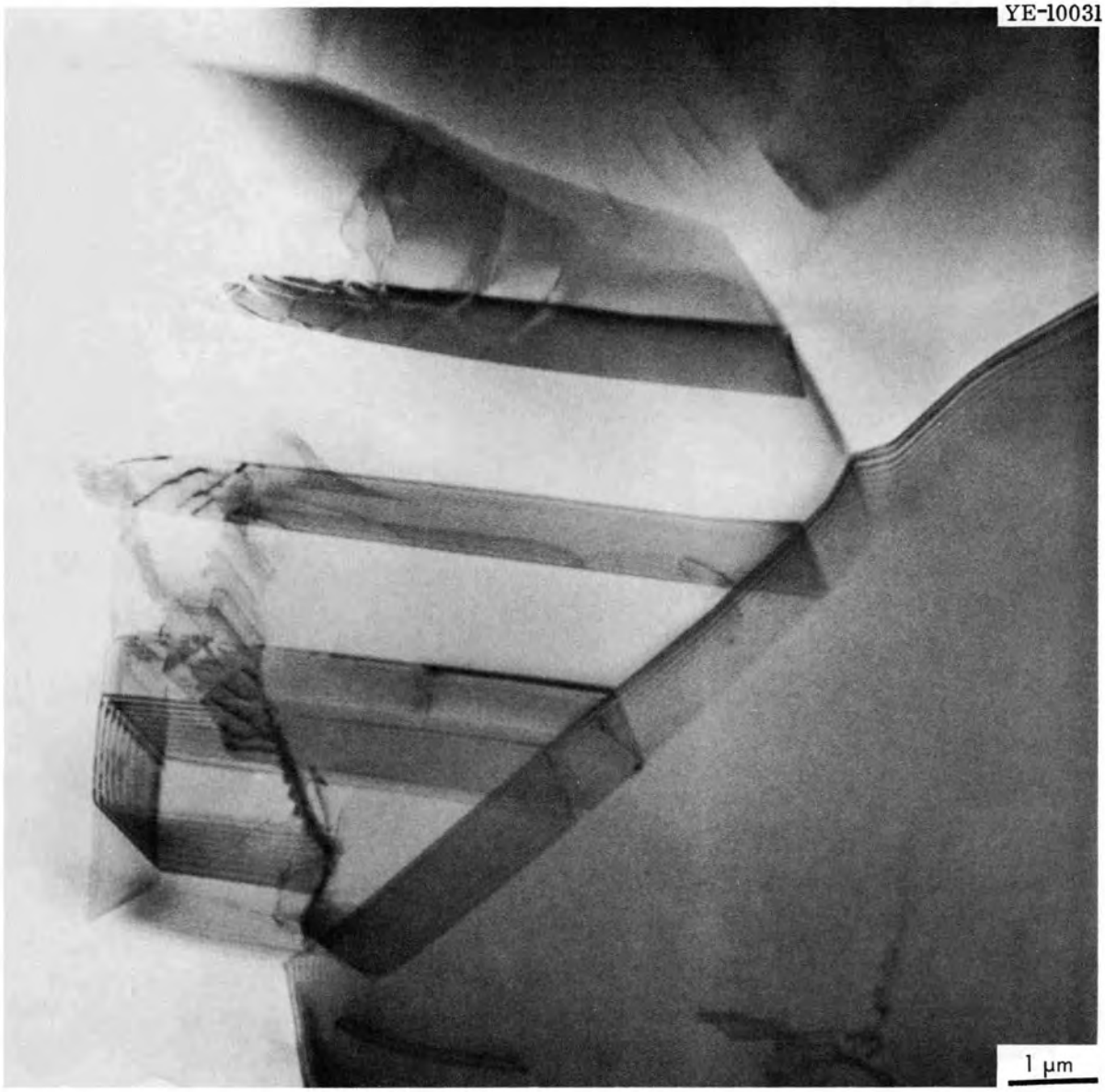

Fig. 12.2. Transmission Electron Photomicrograph of Hot-Pressed Boron Carbide Pellet Showing Twins.

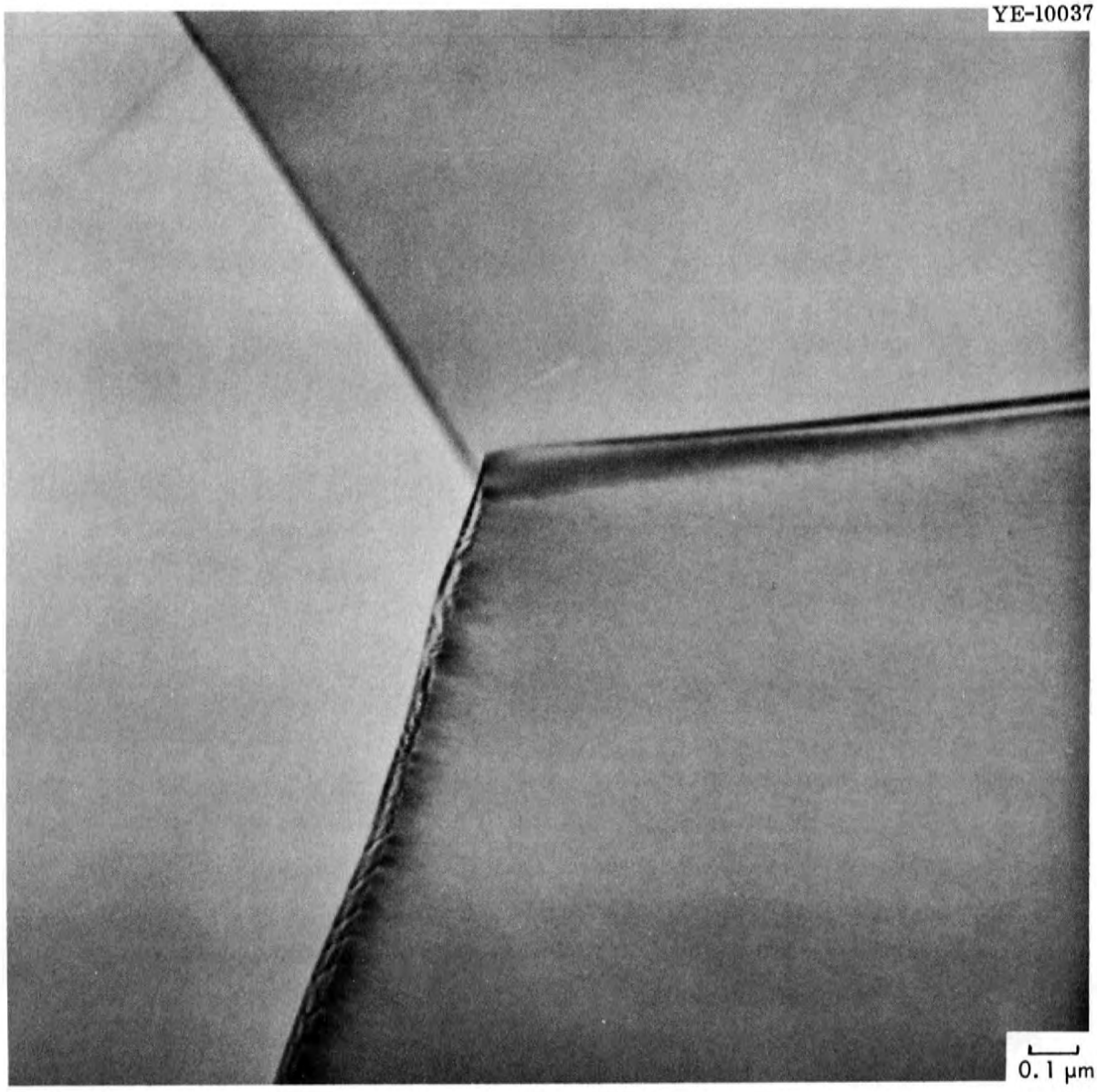

Fig. 12.3. Transmission Electron Photomicrograph of Hot-Pressed Boron Carbide Pellet Showing Grain-Boundary Triple Point.

Table 12.1. Size Distribution and Chemical Composition of a Sample of Norbide 4F Boron Carbide

U.S. Standard Mesh Size	Material in Size Range (wt %)	Chemical Composition (%)			Atomic Ratio B:C
		B	C	O	
+8	28.32	78.7	21.0	0.2	4.16
−8 +16	46.93	79.4	21.3	0.3	4.14
−16 +20	1.08	79.9	18.2	0.6	4.87
−20 +50	14.46	79.6	19.1	0.6	4.62
−50 +80	4.30	75.2	19.6	1.0	4.26
−80 +100	1.30	77.3	20.0	0.9	4.29
−100 +325	3.51	76.8	19.0	1.2	4.49
−325	0.09	67.8	18.0	7.2	4.17
WEIGHTED AVERAGE		78.9	20.7	0.4	4.23

Irradiation Behavior of Boron Carbide

Thermal-Reactor Tests (G. L. Copeland)

Nine additional capsules of the design previously used[4] are being irradiated in the isotopes stringer of the Oak Ridge Research Reactor (ORR). The materials include the three powders identical to those irradiated previously at 350°C that are now being irradiated at 500°C. These three are Norbide 325F powders, as received and after vacuum annealing 1 hr at 1500 and 2000°C. The other six capsules contain Norbide 235F blended with B to increase the ratio of B:C to 4.5. This material will be irradiated at 350 and 500°C after vacuum annealing for 1 hr at 1000, 1500, and 2000°C. The capsules are scheduled to be removed from the reactor in July, after about 15% burnup of ^{10}B (31×10^{20} depletions/cm^3).

Fast-Reactor Tests (G. L. Copeland, G. W. Keilholtz[5])

Fabrication of the pellets and capsules for the EBR-II irradiation tests are proceeding satisfactorily. All data packages necessary for

the review at the EBR-II site are near completion and will be transmitted near the end of July. The shipment of the experiment is scheduled for mid-August.

Investigation of Materials Other than Boron Carbide

Mixtures of Boron Carbide and Tantalum (G. L. Copeland)

Mixtures of B_4C and Ta (ref. 6) were blended, cold pressed, and vacuum sintered at 2000°C. These mixtures reacted completely to form TaB_2 and TaC during the 1-hr sintering. The B_4C was completely consumed in all the samples examined by x-ray diffraction. In samples where excess Ta was present, the B was completely converted to TaB_2 and some free C was present in addition to TaC. No other borides or carbides were observed. These results indicate that the reaction between B_4C and Ta is fast enough to preclude fabrication at reasonable temperatures even if the two were compatible for sufficient time at lower operating temperatures.

Characterization of TaB and TaB_2 (G. L. Copeland)

We have received samples of TaB and TaB_2 from the Shieldalloy Corporation that were manufactured by Hermann C. Starck of West Germany. We are now characterizing the materials. X-ray diffraction indicates that the TaB_2 is single phase whereas the TaB contains Ta_3B_2 and Ta in addition to TaB. Chemical analysis shows the compounds to be very pure: it showed the TaB sample to be 5.20% B and 94.32% Ta for a B:Ta atomic ratio of 0.922 and the TaB_2 sample to be 10.8% B and 88.84% Ta for a B:Ta atomic ratio of 2.03. Further investigation of these materials is in progress.

Notes

1. R. S. Mateer and G. L. Copeland, Fuels and Materials Development Program Quart. Progr. Rept. Sept. 30, 1969, ORNL-4480, p. 135.
2. Isotopes Division.

3. R. S. Mateer and G. L. Copeland, Fuels and Materials Development Program Quart. Progr. Rept. Sept. 30, 1969, ORNL-4480, p. 133.

4. G. L. Copeland, Fuels and Materials Development Program Quart. Progr. Rept. Dec. 31, 1969, ORNL-4520, p. 190.

5. Reactor Chemistry Division.

6. G. L. Copeland, Fuels and Materials Development Program Quart. Progr. Rept. March 31, 1970, ORNL-4560, p. 159.

PART II

SPACE POWER TECHNOLOGY

FUELS

13. DEVELOPMENT OF URANIUM MONONITRIDE FUELS

P. Patriarca J. L. Scott

Uranium mononitride (UN) is potentially attractive as fuel for space-nuclear reactors because of its excellent stability at high temperatures, high thermal conductivity, and good irradiation stability up to 1000°C. The purpose of this program is to determine the basic mechanisms of fuel swelling and gas release at temperatures above 1000°C. Results will be used to develop a model for predicting the performance of UN as a function of temperature, burnup, and cladding restraint.

Irradiation Testing

T. N. Washburn

The basic objective of the ORNL program[1] for irradiation testing of UN is to investigate the performance capability of this fuel material at high temperatures and low heat ratings. Fuel temperatures of interest are 1000 to 1500°C, with temperatures of 900 to 1400°C at the outside surface of the cladding and linear heat ratings from 5 to 10 kw/ft. Fuel properties of most interest are swelling rate, release of fission gas, and compatibility with the cladding materials. The irradiation tests are conducted in the poolside facilities of the Oak Ridge Research Reactor (ORR). These facilities allow adjustment of the position of the test capsule relative to the reactor face and thereby make it possible to maintain a constant temperature at a selected reference point on the test specimen as the reactor flux profile changes or as the fissile content of the test fuel is diminished.

Postirradiation Examination of Capsule UN-3 (D. R. Cuneo,[2] E. L. Long, Jr.)

We previously reported on the nondestructive portion of the postirradiation examination of the three fuel pins of capsule UN-3 (ref. 3) and the metallographic examination of the middle fuel pin that had failed during the irradiation test.[4]

The bottom fuel pin in this experiment was essentially a duplicate of the middle (failed) pin both in design and operation. The bottom pin was sectioned and examined by metallography. A transverse section is shown in Fig. 13.1. Cracks and voids evident in both the W liner and T-111 cladding were similar to those found in the middle fuel pin that led to its failure. We conclude that the same phenomenon that led to failure of the T-111 cladding in the middle fuel pin was also present in the companion bottom fuel pin and that additional time and/or localized temperature excursions would have led to its failure.

An electron microprobe analysis of the cladding of the middle fuel pin revealed no indications of U contamination from the fuel or of any diffusion of W from the liner into the T-111 cladding. This analysis did show very strong concentrations of Hf at the cracks and voids, both in the T-111 cladding and in the W liner. Although the data are not strictly quantitative, the concentrations are about 20 times that of the T-111 alloy content of 2 wt %. The Hf is not only segregated from the base alloy, it is also transported from the cladding and deposited in the W liner. The mechanism by which this transport occurs is not known, nor do we know whether the defects are caused by Hf concentrations or whether they are present by some other phenomenon and merely serve as sites for Hf concentration. Hafnium concentrations were not detected in either the preirradiation control sample or in the irradiated cladding except at visible voids or cracks.

The top fuel pin contained annular UN fuel pellets and W–25 wt % Re cladding. This fuel pin was sectioned, and metallographic examination is in progress.

The UN fuel appears to have performed very adequately in this experiment, which operated at the highest design temperature of any in the ORNL series of tests. The data for increase in fuel volume and release of fission gas shown in Table 13.1 are quite acceptable. There was no observed reaction between the UN fuel and either the W liner or the T-111 cladding.

The accumulation of fission gases at grain boundaries in UN is illustrated in the higher magnification views of the fuel in Fig. 13.1. Due to self-shielding in a thermal-neutron flux, the fission rate was

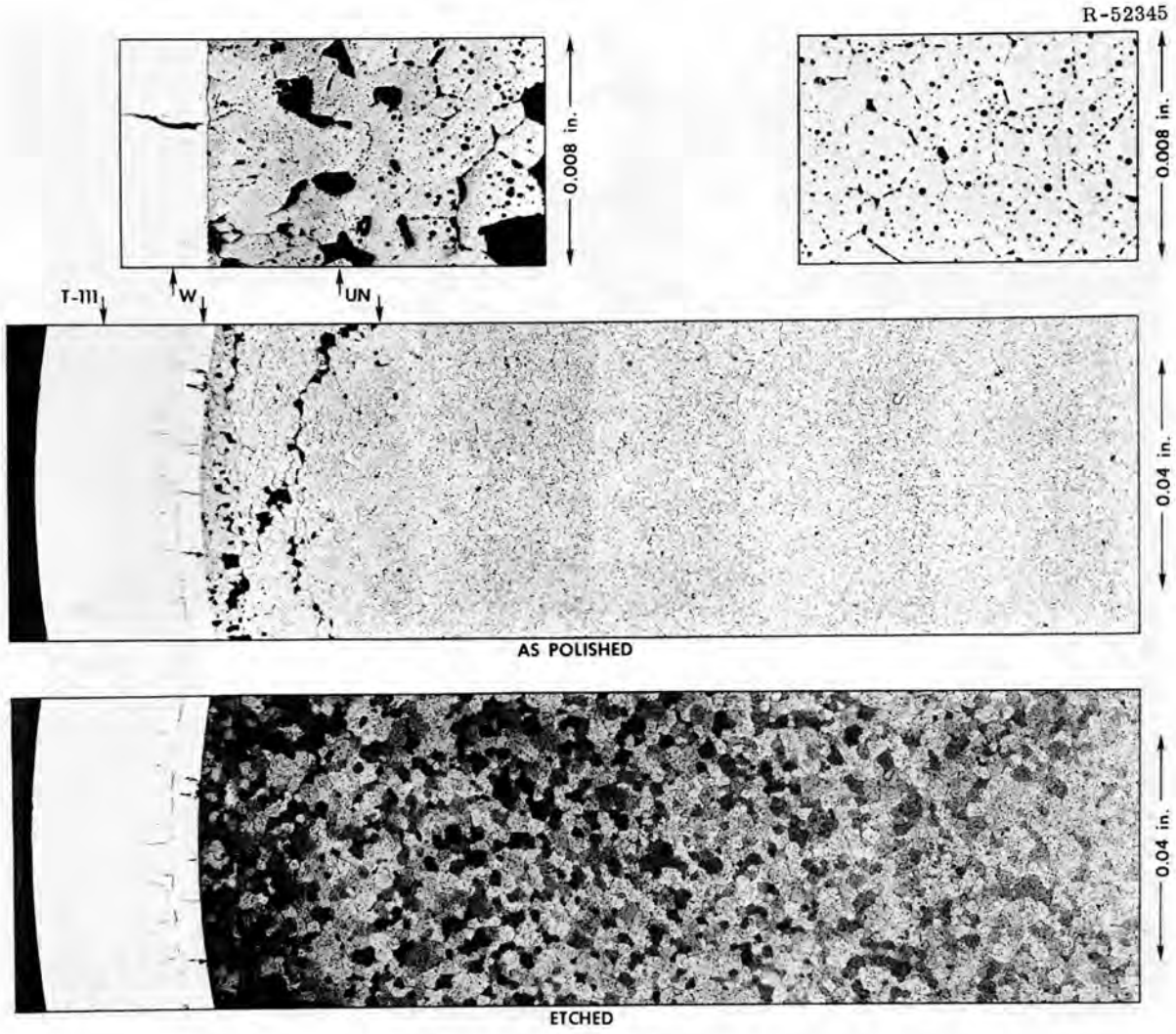

Fig. 13.1. Transverse Section of Bottom Fuel Pin of Capsule UN-3.

Table 13.1. Volume Increase and Release of Fission Gas for Capsule UN-3

Fuel Pin	Volume Percent Increase Per Atom Percent Burnup	Fission Gas Released (%)
Top	2.79	0.1
Middle	2.77	
Bottom	1.90	7.1

much higher near the outer periphery of the fuel, and accumulation of fission gas at the grain boundaries is sufficient to cause grain pull-out in this region during metallographic preparation.

Notes

1. The current program includes work sponsored by the AEC, and work sponsored by NASA under Interagency Agreement 40-184-69, NASA Order C-54536-B. Specifically, capsules UN-1, UN-2, UN-3, and UN-6 are funded by AEC, and capsules UN-4 and UN-5 are funded by NASA. Details of these capsule tests were reported previously.

2. On loan from Reactor Chemistry Division.

3. D. R. Cuneo, Fuels and Materials Development Program Quart. Progr. Rept. Dec. 31, 1969, ORNL-4520, pp. 195–201.

4. D. R. Cuneo and E. L. Long, Jr., Fuels and Materials Development Program Quart. Progr. Rept. March 31, 1970, ORNL-4560, pp. 165–172.

CLADDING AND OTHER STRUCTURAL MATERIALS

14. CLADDING MATERIALS FOR SPACE ISOTOPIC HEAT SOURCES

P. Patriarca R. G. Donnelly

The purpose of this program is to develop new cladding materials for containment of radioisotopes in power systems for use in space. We are attempting to develop a single alloy with an optimum combination of strength at high temperature, fabricability, environmental stability, and resistance to oxidation in air to take the place of the layered combination of strength member, diffusion barrier, and oxidation-resistant cladding used in present devices.

Development of Improved Alloys

H. Inouye

Platinum-Base Alloys (C. T. Liu)

Seven ternary Pt-base alloys with the nominal compositions listed in Table 14.1 were prepared by arc melting. Platinum atoms form the ordered phases Pt_3Ti and Pt_3Hf with Ti and Hf atoms, respectively. The critical temperature for ordering of Pt_3Ti is much higher (T_c = 1950°C) than that for alloy S-19, Pt_3Cr, (T_c = 1070°C). Therefore, adding Ti to alloy S-19 is expected to increase the critical temperature for ordering for alloys 1, 2, and 3 to 1230, 1360, and 1480°C, respectively.

The kinetics of the transformation from disorder to order in the ordered alloys was examined by Debye-Scherrer x-ray diffraction. Two important results were obtained. First, the ordering reaction in these ternary alloys is fast, and the disordered state cannot be retained by oil quenching from 1520°C. In the quenched condition, the intensity of superlattice reflections indicates that the formation of long-range order is more pronounced in the alloy 3 than in the other two alloys. Secondly, the rate of grain growth, even at temperatures above the critical temperature for ordering, such as 1520°C, decreases with increasing Ti content in these alloys. These results can be explained on the basis

Table 14.1. Experimental Platinum Alloys

Alloy	Composition (wt %)	Alloy State	Critical Temperature for Ordering[a] (°C)	Rockwell A Hardness
1	Pt–7.4 Cr–0.6 Ti	Ordered $Pt_3(Cr,Ti)$	1230	52.5
2	Pt–6.1 Cr–1.8 Ti	Ordered $Pt_3(Cr,Ti)$	1360	57.5
3	Pt–4.8 Cr–3.0 Ti	Ordered $Pt_3(Cr,Ti)$	1480	64.3
4	Pt–6 W–0.5 Hf	Solid solution and Pt_3Hf		54
5	Pt–6 W–1 Hf	Solid solution and Pt_3Hf		
6	Pt–5 Mo–0.5 Hf	Solid solution and Pt_3Hf		54
7	Pt–5 Mo–1 Hf	Solid solution and Pt_3Hf		55

[a]Calculated values.

of an increasing critical temperature for ordering with increasing Ti content in the alloys (see Table 14.1).

As also indicated in Table 14.1, the ordered alloys are hardened effectively by partially replacing Cr by up to 3 wt % Ti. Although these alloys, prepared in the 20-g button form, cannot be cold rolled satisfactorily because of cracks that form intergranularly, their forgeability improved with the addition of Ti. In fact, alloy 3, to which 3 wt % Ti was added, was forged successfully at room temperature.

We expect alloys 4 through 7, which contain 0.5 to 1 wt % Hf, to be strengthened by both solid solution and particles of Pt_3Hf. We also expect the stable particle Pt_3Hf to inhibit grain growth during aging at high temperature. The fabricability of alloys 4 through 7 is excellent. The two alloys with 0.5% Hf were cold rolled to 0.030-in.-thick sheet. These results indicate that the ordered phase Pt_3Hf does not impair the forgeability of the Pt-base alloys. The alloy sheet will be used for metallurgical study and evaluation of mechanical properties.

The oxidation behavior of ordered $Pt_3(Cr_{0.84},W_{0.16})$ and disordered Pt–6% W–1% Hf alloys were studied at 1000°C in air, and the results are shown in Fig. 14.1 together with the results for Pt_3Cr, which were reported previously.[1] The net weight change of Pt-base alloys on oxidation is a sum of the weight loss due to the formation of volatile Pt oxide and the weight gain due to the formation of a refractory oxide. The average weight gain of $Pt_3(Cr_{0.84},W_{0.16})$ was 6.5×10^{-4} mg cm^{-2} hr^{-1}. The alloys Pt–0.6% W–1% Hf and Pt_3Cr lost weight at rates of 6.8 and 9×10^{-4} mg cm^{-2} hr^{-1}, respectively. In contrast to the other alloys, no apparent oxide layer was observed on the surface of alloy Pt–6% W–1% Hf after a 100-hr exposure in air. Since unalloyed Pt loses weight at a rate of 7×10^{-4} mg cm^{-2} hr^{-1}, we conclude that the alloying with a limited amount of refractory elements does not impair the excellent resistance of pure Pt to oxidation.

We designed an apparatus for tensile testing experimental alloys in vacuum at high temperatures. The main part is a quartz tube furnace heated by an induction unit. The vacuum in the system is maintained by a VacIon pump. This apparatus was constructed and installed and is nearly ready for operation.

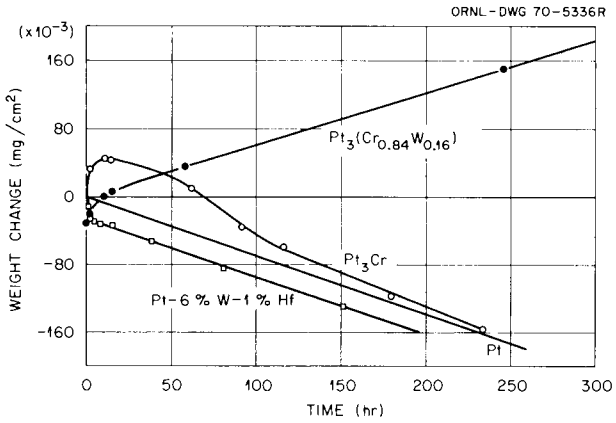

Fig. 14.1. Weight Change of Platinum-Base Alloys in Air at 1000°C.

Fabrication of Refractory Metals for Fuel Capsules

A. C. Schaffhauser

Back Extrusion (R. E. McDonald)

During this reporting period, we concentrated on evaluating back extrusion as an economical method for fabricating Ta–10% W and T-111 capsules for isotopes. Twelve starting blanks of each material were cut from extruded bar stock for back extrusion of capsule bodies and end caps. The blanks were annealed 1 hr at 1600°C and plasma spray coated with Mo. This coating protects the blanks from contamination during preheating in an Ar atmosphere and subsequent fabrication in air. Metallographic and chemical analyses showed that the resulting interaction layer was less than 0.010 in. deep. This layer was easily removed by machining.

Three Ta–10% W capsule bodies and four T-111 end caps were back extruded at 1450°C with a maximum stem load of 500 tons. Under these conditions, back extrusion produced capsule bodies extruded to a length of 4 to 4 3/4 in. These parts will be extruded again to produce the required 5 1/2-in.-long capsule bodies. The plunger design is being modified to reduce friction and thus enable back extrusion of longer capsules in a single step.

Notes

1. C. T. Liu, Fuels and Materials Development Program Quart. Progr. Rept. Dec. 31, 1969, ORNL-4520, pp. 205–210.

15. PHYSICAL AND MECHANICAL METALLURGY OF REFRACTORY ALLOYS

P. Patriarca R. G. Donnelly

The purpose of this program is to provide a broad, base-technology evaluation of high-temperature alloys for use in high-performance nuclear reactors and isotopic heat sources for advanced space, terrestrial, and civilian power applications. Principal emphasis is placed on materials problems that involve Ta-, Nb-, Mo-, and V-based alloys for systems that use alkali metals as thermodynamic working fluids and heat-transfer media.

Physical Metallurgy

H. Inouye

Effects of Interstitials on the Mechanical Properties of Refractory Alloys (H. Inouye)

The objective of this task is to determine the effects of low-pressure N_2 on the creep properties of T-111 to simulate its interaction with the N derived from the decomposition of UN. The major components of the creep apparatus were installed, but fabrication of minor items and installation of the instrumentation are being delayed. A vacuum of 1×10^{-9} torr is obtained in the system with a 400 liter/sec Orb-Ion pump.

Development of Age-Hardening Refractory Alloys (C. T. Liu, R. W. Carpenter)

The development of age-hardening refractory alloys for use at elevated temperatures focused on decomposition of an alloy in the Ta-Zr system. A Ta–43.5 wt % Zr alloy was electron-beam melted and drop cast into a 1/2-in.-diam ingot. After aging 2 hr at 1450°C and 10 hr at 1100°C, the alloy became soft [diamond pyramid hardness (DPH) = 195] and had excellent fabricability. With a few intermediate anneals, the alloy was cold swaged into 0.138-in.-diam rod. The stock will be used as swaged to evaluate its mechanical properties.

The decomposition of a specimen homogenized at 1815°C is not completely suppressed by oil quenching, since x-ray diffraction shows strong, diffuse streaks associated with the β-phase reflections. Diffraction patterns of two body-centered cubic (bcc) phases were clearly observed in a specimen aged at 1150°C; this confirms the reported existence of a stable miscibility gap associated with the bcc β phases.[1,2]

The hardness of the alloy is very sensitive to the heat treatment. Figure 15.1 shows the aging response of this alloy as a function of time up to 4×10^3 min at 850°C. The hardness of the alloy as quenched (DPH = 492) indicates the initiation of precipitation during quenching. After the alloy has been aged 1 min, the hardness drops continuously with time from 527 to 306 DPH. We are waiting for the results of detailed x-ray analysis and metallography before offering an interpretation of these data.

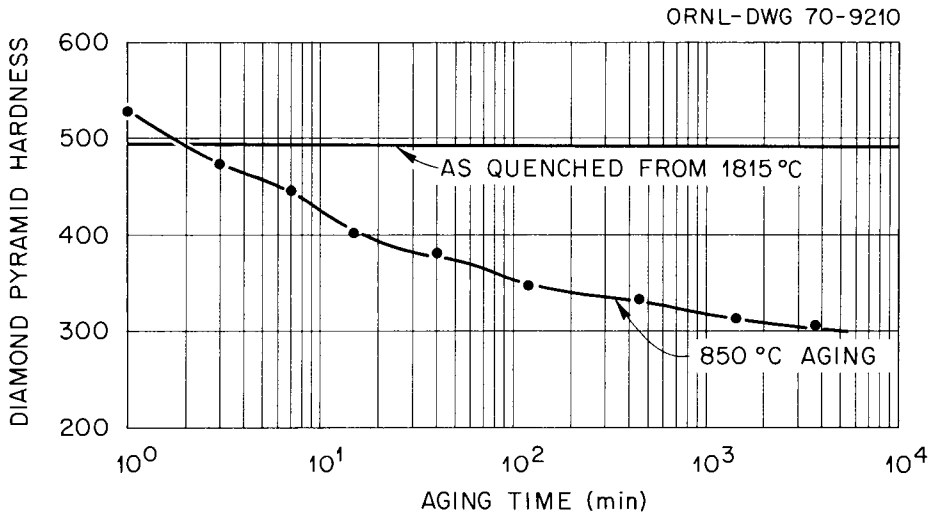

Fig. 15.1. Diamond Pyramid Hardness at Room Temperature Versus Aging Time for Ta–43.5 wt % Zr Alloy.

We calculated an approximate boundary between the $\alpha + \beta$ and β phases for the Ta-Hf system, using the measured lattice constants of the β phase for the Ta–30% Hf, Ta–50% Hf, and Ta–65% Hf alloys. The result is shown in Fig. 15.2 compared with the diagrams reported previously.[3,4] Note that the calculated phase boundary (the curve labeled A) is quite flat over the concentration range of 30 to 70 at. % Hf.

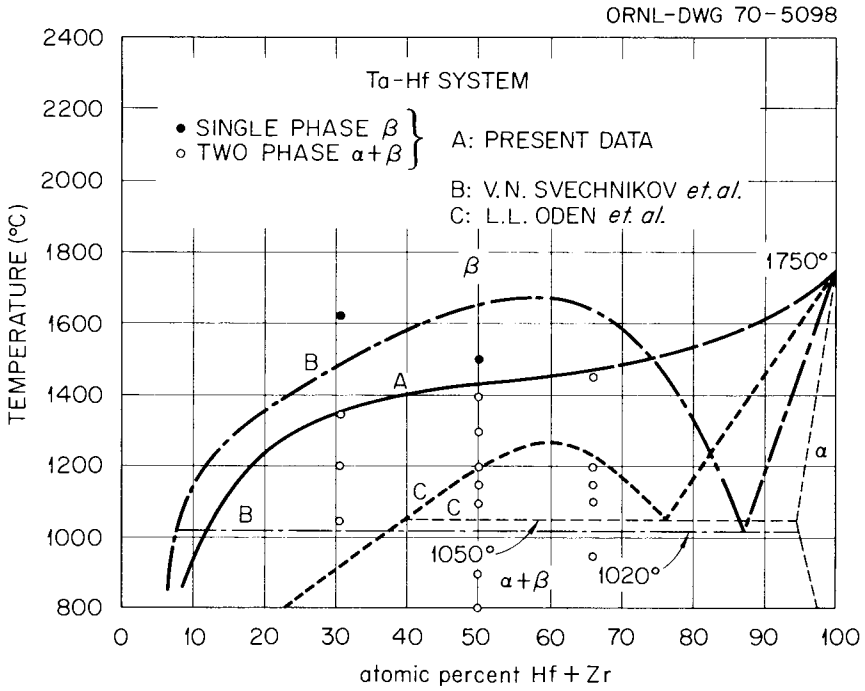

Fig. 15.2. Proposed Phase Diagrams for the Tantalum-Hafnium Alloy System and the Range of Stability of the α Precipitate Found in the Present Work. [Refs. V. N. Svechnikov et al., Phase Equilibrium Diagram of the Hf-Ta System, NASA-TT-F-10,280 (September 1966); L. L. Oden et al., Hafnium-Tantalum Equilibrium Diagram, BM-RI-6521 (1964)].

Thermodynamically, this indicates the possible existence of a metastable bcc miscibility gap with a critical temperature lower but close to the temperature of the stable boundary between the α + β and β phases (i.e., 1400°C in this case). The observation of uniform precipitation of fine particles in this system is closely related to this phase relationship.

The study of the isothermal aging of the Ta–65 wt % Hf alloy was completed. Figure 15.3 summarizes the hardness data, most of which were reported previously.[5] The aging reponse is quite typical. Both x-ray diffraction and metallography indicate that the features of these hardness curves resulted from the various stages of decomposition, which involve the clustering of Hf atoms on the β lattices (Guinier-Preston zones), precipitation of coherent and incoherent α-phase Hf, and coarsening of particles.

The oxidation behavior of two specimens of a Ta–65 wt % Hf alloy was studied in air at 1000°C. The specimens were heat treated to produce

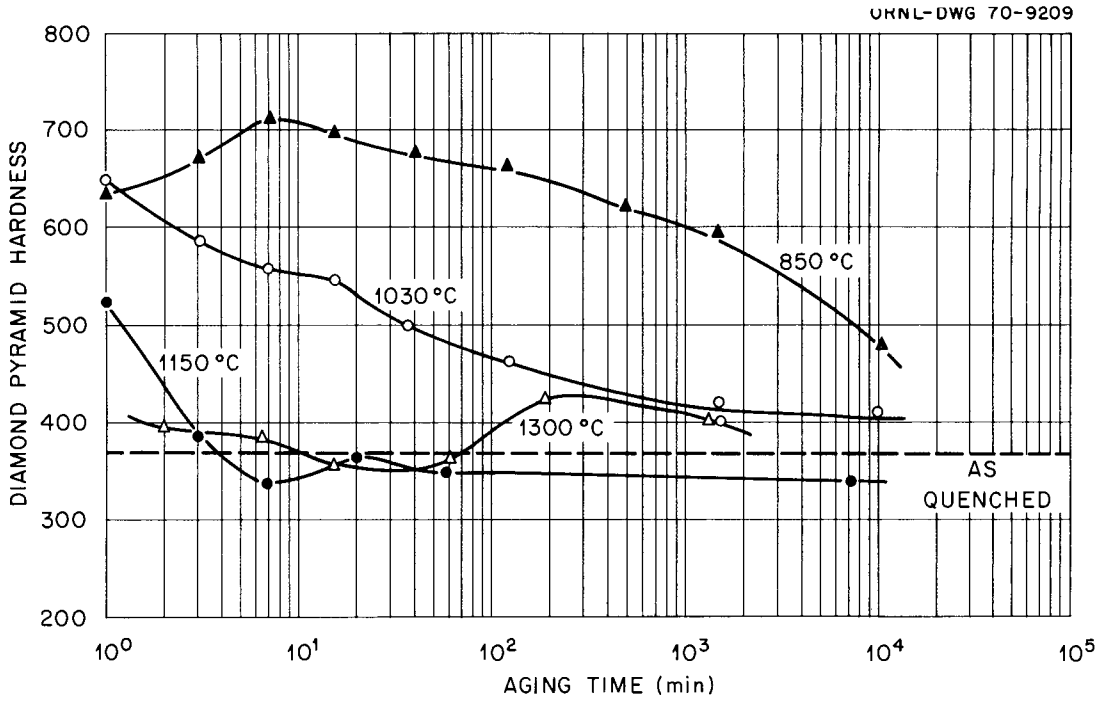

Fig. 15.3. Diamond Pyramid Hardness at Room Temperature Versus Aging Time for Ta–65 wt % Hf Alloy.

either a uniform or a heterogeneous (pearlitic structure) Hf-rich structure. The data summarized in Table 15.1 show that the weight gain due to oxidation was not sensitive to the structure of alloy. The average weight gain of this alloy in 450 min was 2.5 mg cm^{-2} hr^{-1}. As a comparison, this oxidation rate is about two orders of magnitude lower and one order of magnitude higher than those of the unalloyed Ta and Hf, respectively.[6] The weight change of the oxidation-resistant Hf-base alloy [Hf–24.5% Ta–2% minor elements (Cr, Al, Si, B, etc.)] was reported[7] to be 2.1 mg cm^{-2} hr^{-1}, and the oxidation rate of the Ta–65% Hf alloy was comparable.

Mechanical Properties

H. E. McCoy, Jr.

Long-Time Creep Properties of Alloy C-129Y (R. L. Stephenson)

We have studied the creep-rupture properties of alloy C-129Y (Nb–10% W–10% Hf–0.1% Y) and are now studying the microstructures of the

Table 15.1. Oxidation of Ta–65 wt % Hf Alloy in Air at 1000°C

Time (min)	Weight Change (mg/cm^2)	
	Heterogeneous Precipitation Structure	Uniform Precipitation Structure
10	2.5	2.5
100	7.2	8.0
200	11.0	12.0
300	14.5	15.8
450	20.4	

creep specimens. Figure 15.4 is typical of the microstructure of ruptured creep specimens of alloy C-129Y. All ruptured specimens show extensive intergranular cracking and, typically, a crack-free zone at each surface that grows wider with increasing time and temperature and that suggests that cracking is inhibited in a region into which interstitial contaminants have diffused.

For diffusion of an interstitial into a metal that contains a reactive substitutional solute, Rapp[8] gives the following equation for the distance penetrated (ζ) by the advancing front of precipitate:

$$\zeta = \left[\frac{2N_o^{(s)} Dt}{N_b^o \nu}\right]^{\frac{1}{2}}, \qquad (15.1)$$

where

$N_o^{(s)}$ = mole fraction interstitial at the surface,

N_b^o = mole fraction reactive solute in the bulk alloy,

D = diffusivity of the interstitial in the alloy base,

t = time, and

ν = number of interstitial ions per substitution atom in the compound.

The diffusivity (D) can be represented by

$$D = D_o e^{-\Delta H/RT} , \tag{15.2}$$

where

D_o = constant,

R = gas constant,

T = temperature, and

ΔH = activation energy.

Substituting Eq. (15.2) for D in Eq. (15.1), taking logarithms, and rearranging terms yields

$$\ell n\left(\frac{\zeta^2}{t}\right) = \ell n\left[\frac{2N_o^{(s)} D_o}{N_b^{(o)} \nu}\right] - \frac{\Delta H}{RT} . \tag{15.3}$$

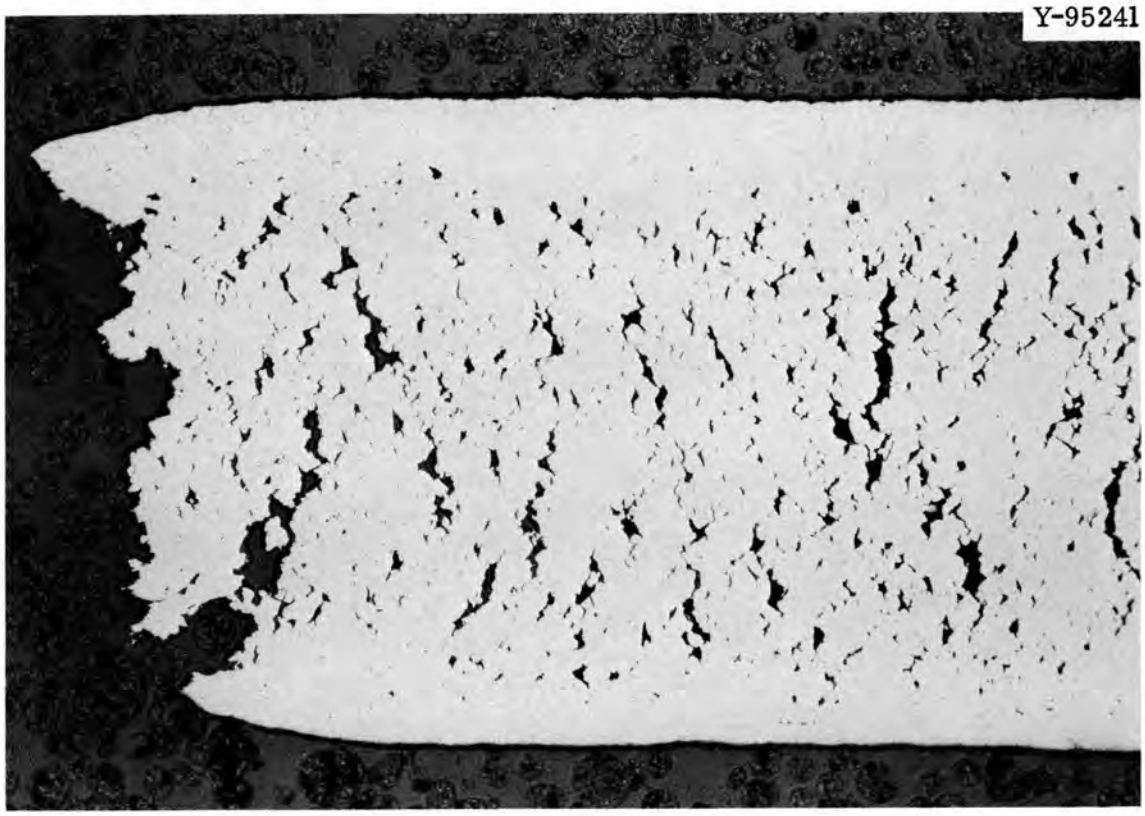

Fig. 15.4. Microstructure of Alloy C-129Y Tested 1291.5 hr at 1095°C. 100×.

It is now clear that if $\ell n(\zeta^2/t)$ is plotted versus $1/T$, a straight line should result whose slope would be $\Delta H/R$. Figure 15.5 is such a plot for 980, 1095, and 1205°C. Three measurements were made at each temperature. The slope of the line of a linear least-squares fit gives an activation energy of 39,000 cal/mole with a standard error of 7380 cal/mole. Reported values[9] for the diffusion of interstitials in Nb range from 26,000 to 35,000 cal/mole. For this plot, we assume that the surface concentration is the same at all three temperatures. This is probably not precisely true. Further, the depth of penetration cannot be measured very accurately. Considering the approximations made, this value could be considered in agreement with those for the diffusion of interstitials in Nb.

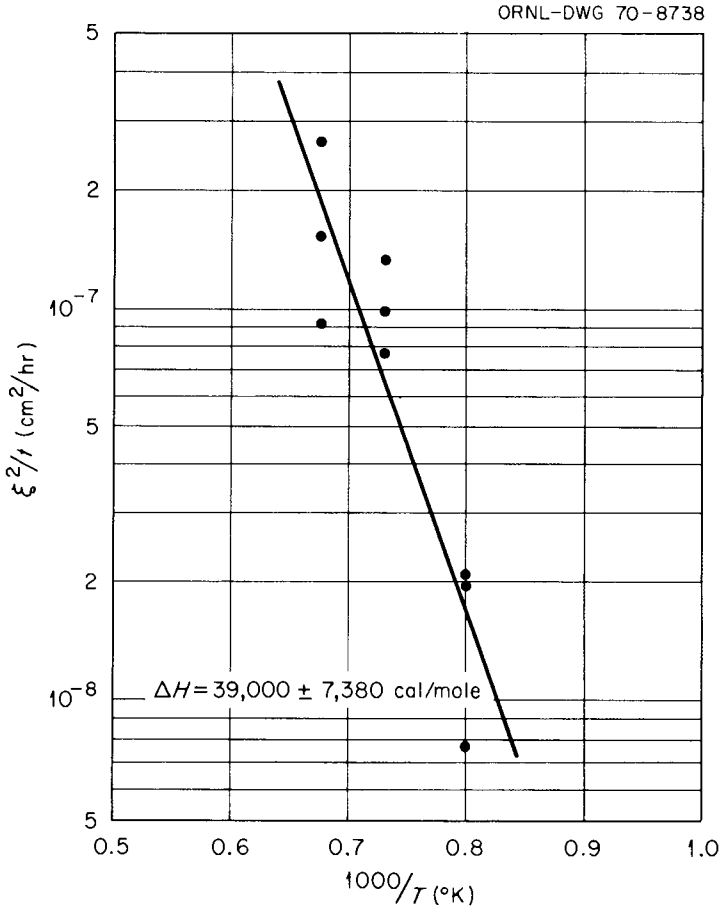

Fig. 15.5. Normalized Penetration Distance Versus Reciprocal Temperature for Alloy C-129Y.

Welding and Brazing

G. M. Slaughter

Joining Platinum to Refractory Metals (D. A. Canonico, G. M. Goodwin)

Previous efforts[10] showed that Kirkendall voids occurred in the Pt when couples of Pt and Ta–10% W were heated to 1200°C in vacuum for less than 100 hr. We did find, however, that interposing a transition layer of W between the Pt and Ta–10% W extended the life of the joint to between 500 and 1000 hr. This suggested an investigation of the applicability of various elements and alloys for use as transition layers.

We reviewed the availability of materials with melting points above 1400°C and prepared a multilayered assembly of these materials in contact with Pt and Ta. This series of diffusion couples was heated to 1200°C at 1000 psi for 100 hr. The results of a metallographic study of the composite are given in Table 15.2.

Figure 15.6 illustrates the results obtained from this study. Kirkendall voids are evident in the Pt at the interfaces with both the chemically vapor deposited W and the Ta. The Ta-Pt couple was more severely damaged, and at least four phases are evident.

We are continuing our study of the compatibility of the various materials with Pt and Ta at 800 and 1000°C. We expect that Pt will perform satisfactorily with certain elements (alloys) at lower temperatures. This study will identify those compatible combinations, and they will be used as transition materials for tubular welds.

Physical Properties

D. L. McElroy

Thermal Conductivity of Tantalum (R. K. Williams, J. P. Moore)

Good estimates of the thermal conductivity of metals and alloys at high temperatures can frequently be obtained by combining data for electrical resistivity at high temperature with data for electrical resistivity and thermal conductivity at low temperature. In fact, for

Table 15.2. Initial Metallographic Results of Dissimilar-Metal Diffusion Couples Aged 100 hr at 1200°C

Test Material	Void Indications	
	Pt Couple	Ta Couple
Pt		many
Ta	many	
Mo	few	none
Nb	few	none
Ti	few	none
V	many	none
Ni	many	many
W	few	none
Re	many	b
D-43	few	none
B-66	many	none
FS-85	many	none
Ta–10% W	many	none
T-111	many	none
T-222	many	none
TZM	many	a
W–25% Re	few	a
W–25% Re–30% Mo	few	none

[a]Couple not in contact.

temperatures above 1300 K, the estimates of thermal conductivity are usually more reliable than available measurements. We believe that experimentally derived values for phonon conductivity and the Lorenz function form the best available basis for these estimates of thermal conductivity and previously[11] reported a comparison for W and several W-base alloys. New measurements of thermal conductivity and electrical resistivity at 80 to 400 K on Ta, Ta–5% W and Ta–10% W and our previously reported data for the electrical resistivity of pure Ta at high temperature allow a similar comparison for Ta. Data for the Ta-W alloys were

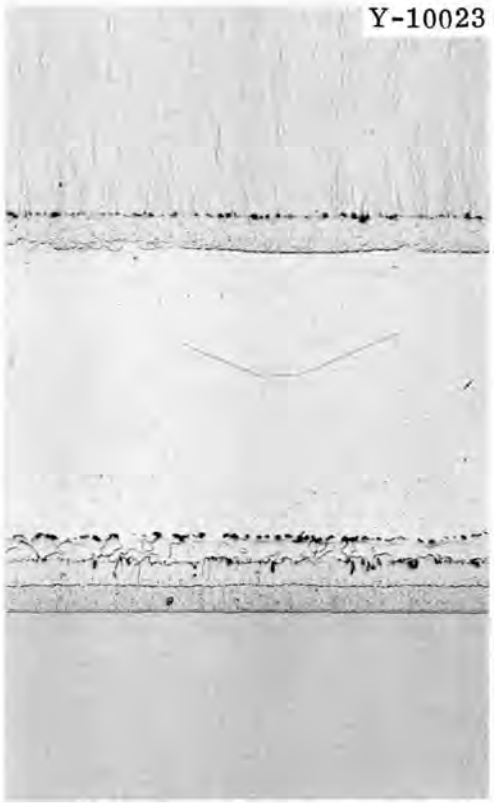

Fig. 15.6. Example of the Results of Studies of Diffusion in Multilayered Couples to Determine Materials Compatible with Tantalum or Platinum. This couple was held at 1200°C and 1000 psi for 100 hr. Kirkendal voids are evident at both interfaces.

used to substantiate the values for thermal conductivity and the Lorenz function obtained by fitting data from measurements of thermal conductivity and electrical resistivity at 80 to 400 K to a theoretically based equation. The results of this comparison are shown in Table 15.3. The excellent agreement between the estimated and recommended values shows that the thermal conductivity of Ta behaves about as expected from transport theory.

Table 15.3. Comparison of Thermal Conductivity Estimates for Tantalum

Temperature (K)	Electrical Resistivity ($\mu\Omega$ cm)	Recommended Value[a] (w cm^{-1} deg^{-1})	Range of Reported Experimental Values[a] (% Difference From Recommended Value)		ORNL Estimate[b] (w cm^{-1} deg^{-1})	$\frac{\text{Recommended Value}^{a} - \text{ORNL Estimate}^{b}}{\text{Recommended Value}^{a}} \times 100$
			Maximum	Minimum		
500	22.55	0.582	+4.3	−17.7	0.570	−2.1
1000	43.17	0.606	+21.1	−2.7	0.583	−3.2
1500	61.75	0.622	+22.8	−27.7	0.606	−2.6
2000	78.85	0.640	+26.1	−39.7	0.631	−1.4
2500	94.85	0.656	+6.7	−53.2	0.654	−0.3
3000	110.22[c]	0.665	−22.7	−32.3	0.674	+1.3

[a] C. Y. Ho et al., Thermal Conductivity of Selected Materials, Part 2, NSRDS-NBS 16, National Standard Reference Data Series, National Bureau of Standards, Washington, D.C. (February 1968).

[b] Estimated thermal conductivity = $2.462 \times 10^{-8} \left[1 - \exp\left(\frac{T}{75.0} + 0.214\right)\right] \frac{T}{\rho} + \frac{12.25}{T}$

[c] Extrapolated.

Notes

1. L. F. Pease and J. H. Brophy, Trans. Met. Soc. AIME 227, 1245–1249 (1963).

2. D. E. Williams et al., Trans. Met. Soc. AIME 224, 751 (1962).

3. V. N. Svechnikov et al., Phase Equilibrium Diagram of the Hf-Ta System, NASA-TT-F-10, p. 280 (September 1966).

4. L. L. Oden et al., Hafnium-Tantalum Equilibrium Diagram, BM-RI-6521 (1964).

5. C. T. Liu, Fuels and Materials Development Program Quart. Progr. Rept. March 31, 1970, ORNL-4560, pp. 179–180.

6. R. I. Jaffee et al., "Rhenium and the Refractory Platinum-Group Metals," pp. 383–463 in Refractory Metals and Alloys, Vol 11, ed. by M. Semchyshen and J. J. Harwood, Interscience, New York, 1961.

7. V. L. Hill, Development of Hafnium-Base Alloys, IITRI-B6090-4 (September 1969).

8. R. A. Rapp, Corrosion 21, 382–401 (December 1965).

9. R. W. Powers and M. V. Doyle, J. Appl. Phys. 30, 514 (1959).

10. D. A. Canonico, Nancy C. Cole, and G. M. Goodwin, Fuels and Materials Development Program Quart. Progr. Rept. Dec. 31, 1969, ORNL-4520, pp. 222–223.

11. R. K. Williams, J. P. Moore, W. P. Murray, and D. L. McElroy, Metals and Ceramics Div. Ann. Progr. Rept. June 30, 1969, ORNL-4470, p. 61.

16. TUNGSTEN METALLURGY

P. Patriarca A. C. Schaffhauser

The objective of this program is to provide the base technology on W alloys for advanced power applications in space. We are developing fabrication processes for W alloys based on modification of conventional extrusion and warm-drawing techniques, direct chemical vapor deposition, and welding. Since the primary criterion for the use of W alloys is based on the creep-rupture properties, we are conducting extensive long-time tests at the temperatures of interest. We are also determining the mechanisms that control the creep behavior and the effect of interactions with the vapor species from an isotope or reactor fuel.

Chemical Vapor Deposition

J. I. Federer

Deposition of High-Purity Tungsten Sheet

Previously we found that for small, tubular deposits the temperature of the wall of the deposition chamber affected the F content of the deposit.[1] We have confirmed these results for large sheet deposits. In the current experiments, the chamber wall was cooled either with cold (about 20°C) or hot (about 75°C) water. Without cooling water, the wall would attain a temperature of about 150°C. Deposits prepared with the wall at about 75°C contained 20 to 30 ppm F, while deposits prepared with the wall at about 20°C contained only 5 to 10 ppm F. The reason that the F content of the deposits varied with the temperature of the chamber wall when the other conditions are the same is not known. Possibly the lower temperature lowers the partial pressure of a constituent of the gas phase that bears F and causes F contamination by reaction or entrapment. An attempt to lower the F content further by using moist H_2 was not successful. About 100 times the stoichiometric amount of water required to react with 10 ppm F present as WF_4 was introduced into the reaction chamber. However, the F content was similar to that obtained with dry H_2.

Deposition of Chloride Tungsten

Tungsten deposited from WF_6 (fluoride tungsten) usually has the {100} orientation. Previous efforts to obtain the {110} orientation from WF_6 were not successful.[2] The {110} orientation can be obtained in W deposited from WCl_6 (chloride tungsten). Fluoride tungsten is usually finer-grained and exhibits less grain growth than chloride tungsten. Tungsten emitters in thermionic diodes that have the {110} orientation can be operated at a greater electrode spacing or at a lower temperature to achieve the same power as an emitter that has the {100} orientation.[3] Therefore, we have begun to investigate the deposition of chloride tungsten. Chloride tungsten is more difficult to deposit than fluoride tungsten due to the lower vapor pressure of WCl_6 compared to WF_6 and the higher temperature required for deposition (above 800°C). We hope to deposit a seed with the {110} orientation from WCl_6 and then obtain an epitaxial deposit from WF_6.

Initial experiments have involved only deposition from tungsten chloride. The apparatus consisted of a 1 1/4-in.-diam × 24-in.-long silica glass tube in which the tungsten chloride was prepared and then reduced with H_2. Fluoride tungsten chips in one end of the tube were chlorinated at 750°C with Cl_2. The tungsten chlorides passed onto a 3/4-in.-diam × 1-in.-long Ni substrate heated by induction where H_2 reduction to the metal occurred. In the first experiment, the chlorinator was heated to only 600°C. As a result, some Cl_2 passed unreacted through the W chips and attacked the substrate. The chlorinator was heated to 750°C for the next experiment, and a W deposit was obtained at a substrate temperature of 900°C. X-ray diffraction showed that the deposit was strongly {100} oriented, but, compared to fluoride tungsten, the {110} orientation was enhanced. In the next three experiments, the ratios of Cl_2:W used in the chlorinator at 750°C were 1.02, 0.78, and 0.88, which indicated that chlorides other than WCl_6 were being formed. The orientation of these deposits has not yet been determined. Increasing the H_2 content of the reacting gases from about the stoichiometric amount to about three times that amount increased the efficiency of deposition at 900°C from about 6 to 24%. Tungsten that is not deposited condenses as chlorides in cool parts of the apparatus.

Deposition of Tungsten-Rhenium Alloys

During the past year we attempted to minimize nodules and grown-in porosity because such defects in W–5% Re deposits seriously affect the mechanical properties. We tried to refine the structure by interrupting the deposition process by such techniques as pulsing the gas flows separately or in combination, periodically reversing the gas flows, lowering the deposition temperatures, and cycling the temperature. None of these methods completely interrupted deposition, since grains and nodules grew through lamination caused by interruptions. Smoother, less nodular deposits were obtained in deposits that contained less than 5% Re, as previously reported.[4] Chemical analysis revealed that the deposit intended to contain 1% Re actually had 0.06 to 0.34% Re and that the nominal 3% Re deposit actually had 1.6 to 2.3% Re. Although these deposits had fewer nodules than W–5% Re deposits, we wished to eliminate nodules entirely or alter their form to make them less deleterious to the deposits.

In recent experiments we began to study the effect of gas composition on the morphology of nominal W–5% Re deposits at 750°C and 5 torr. The deposits were formed on resistance-heated Mo substrates 4 in. long and 0.5 in. wide contained in a 4-in.-ID × 12-in.-long reaction chamber. The experimental arrangement was similar to that of the larger apparatus used to prepare sheet deposits. The principal difference between these experiments and those in which sheet deposits were prepared was a higher flow of WF_6-ReF_6 per unit area of substrate (25 vs 3.3 $cm^3\ min^{-1}\ in.^{-2}$). A series of deposits, shown in Fig. 16.1, was prepared in which the ratio of H_2:(WF_6 + ReF_6) was varied from 1 to 20 by varying the flow of H_2 while maintaining the temperature, pressure, and flow of WF_6-ReF_6 constant. The smoothest deposits occurred at ratios of H_2:(WF_6 + ReF_6) of 1 and 3 [Fig. 16.1(a) and (b)]; Fig. 16.1(b) represents a stoichiometric mixture of H_2, WF_6, and ReF_6. These two deposits had a few nodules of the type that usually has no porosity at the interface with the matrix. As the ratio increased to 5, 10, and 20 [Fig. 16.1(c), (d), and (e)], the deposits became more nodular, which is most easily observed on the edges, and the nodules had associated porosity. These results indicate

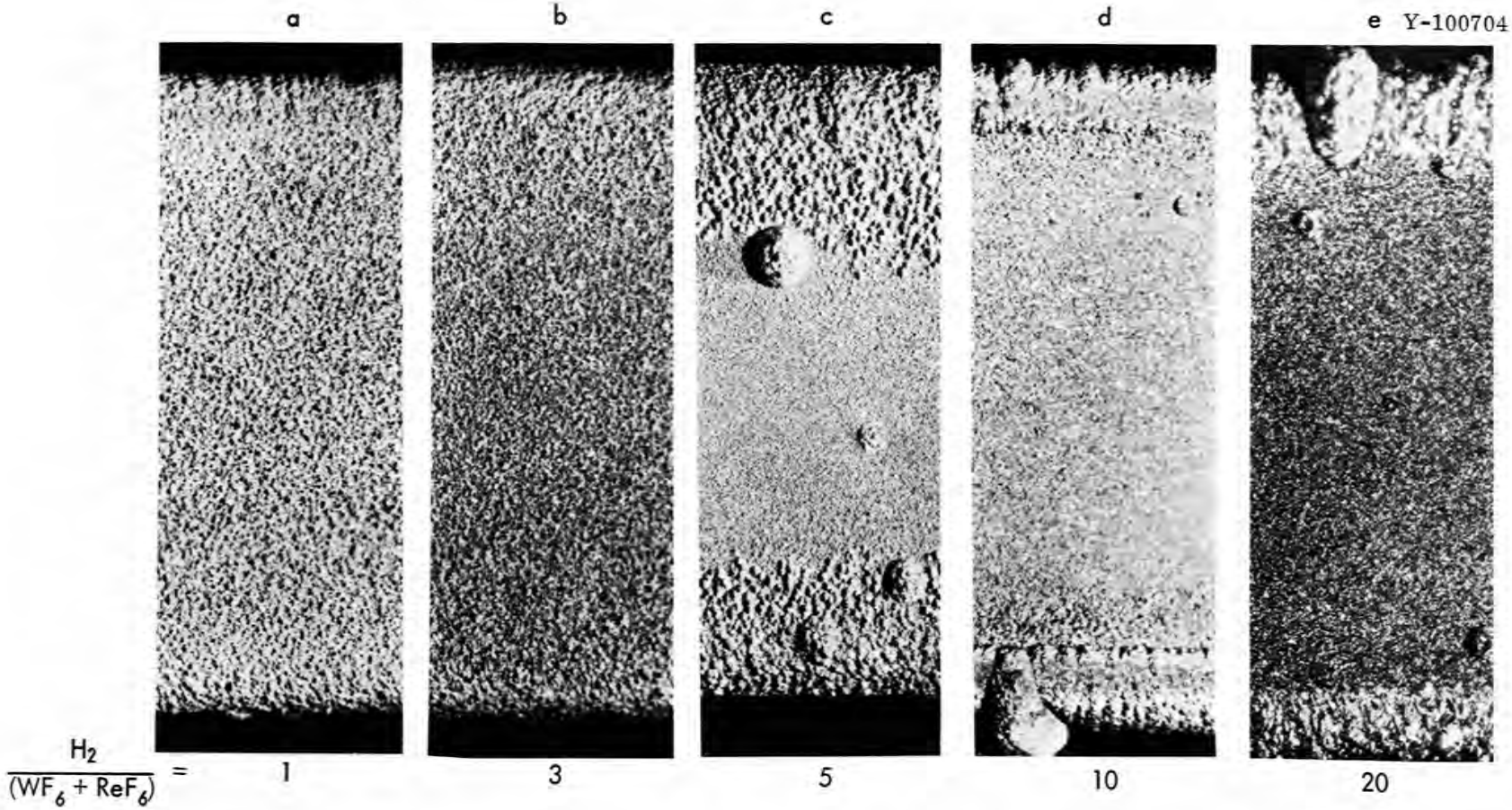

Fig. 16.1. Effect of H_2:(WF_6 + ReF_6) on Morphology of Nominal W–5% Re Alloy Deposited at 750°C and 5 torr at WF_6 Flow of 95 cm^3/min, ReF_6 Flow of 5 cm^3/min and H_2 Flows of (a) 100, (b) 300, (c) 500, (d) 1000, and (e) 2000 cm^3/min.

that smooth deposits are favored by a gas mixture rich in WF_6 and ReF_6 and that nodules occur most readily in mixtures that are lean or depleted in WF_6 and ReF_6. Chemical analyses and metallographic examination of the deposits shown in Fig. 16.1 are in progress. If these results confirm the visual observation that the best deposits are obtained with a near stoichiometric gas mixture, we shall attempt to deposit large sheets.

Evaluation of Methods for Joining Tungsten Alloys

G. M. Slaughter

Development of Improved Techniques (Nancy C. Cole)

We are continuing to make gas W-arc (GTA) welds in chemically vapor deposited W. We welded 0.030-in.-thick sheet with very few problems of cracking, as were previously encountered with the 0.050-in.-thick material.[5] The workpiece was electropolished, stress relieved at 1200°C for 2 hr, preheated to 150°C before welding, and stress relieved at 1200°C for 2 hr after welding.

We conducted bend tests on welds in both thicknesses of material, following the standards set by the Materials Advisory Board[6] as closely as possible. The bend radius was 4 times the sheet thickness, and the specimens were bent with the plunger transverse to the weld. Various strain rates from 0.5 to 0.005 in./min were used.

We were unable to obtain a 90° bend at temperatures up to 550°C in the welds in 0.050-in.-thick sheet, but, at temperatures above 450°C, we were able to produce 90° bends in the weld metal of the 0.030-in.-thick sheet. It is interesting to note that, although the weld metal achieved a 90° bend, the base metal and heat-affected zone cracked. We are attempting to determine the reasons for the observed behavior.

Long-Time Creep Properties of Tungsten Alloys

H. E. McCoy, Jr.

Long-Time Creep Properties of Tungsten and Tungsten-Rhenium Alloys (R. L. Stephenson)

We are studying the long-time creep properties of arc-melted and chemically vapor deposited W alloys. The times to rupture and to 1% creep for arc-melted W, W–5% Re, W–26% Re, W–25% Re–30% Mo, and chemically vapor deposited W were reported previously. Figures 16.2 through 16.6 show the secondary creep rate as a function of stress for these materials at 1200 to 2200°C. Comparison of the data shows that the W–5% Re alloy is the strongest on the basis of secondary creep rates between 10^{-2} and 10^{-4} hr^{-1}.

Correlation of Creep Data for Unalloyed Tungsten (R. L. Stephenson)

Sherby[7] suggested that for pure metals and dilute alloys at temperatures above 0.4 of the absolute melting point, creep strength is influenced by the elastic modulus, E, diffusivity, D, and grain or subgrain size, L.

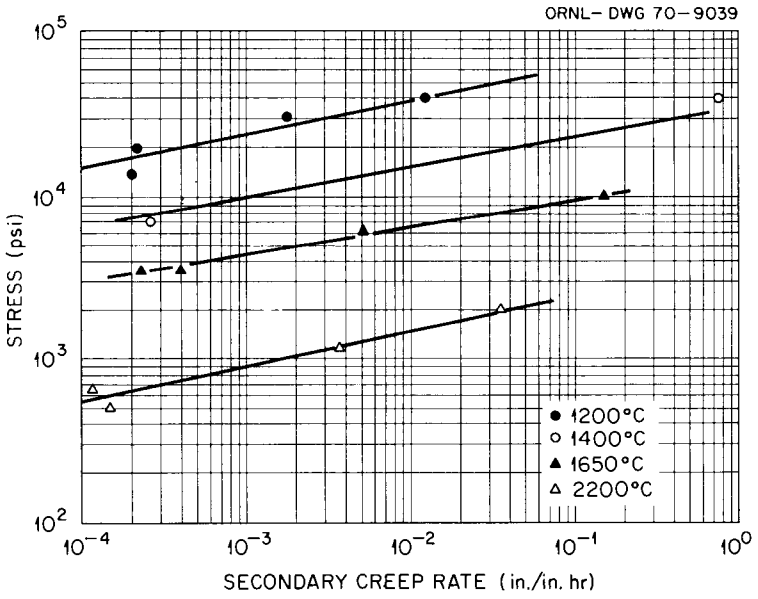

Fig. 16.2. Secondary Creep Rate Versus Stress for Unalloyed Tungsten.

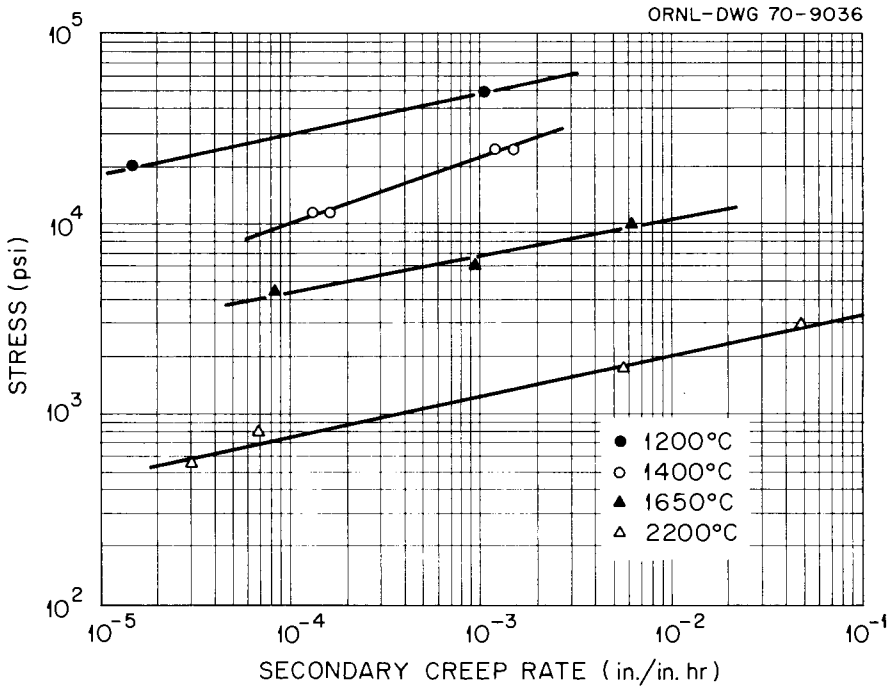

Fig. 16.3. Secondary Creep Rate Versus Stress for W–5% Re.

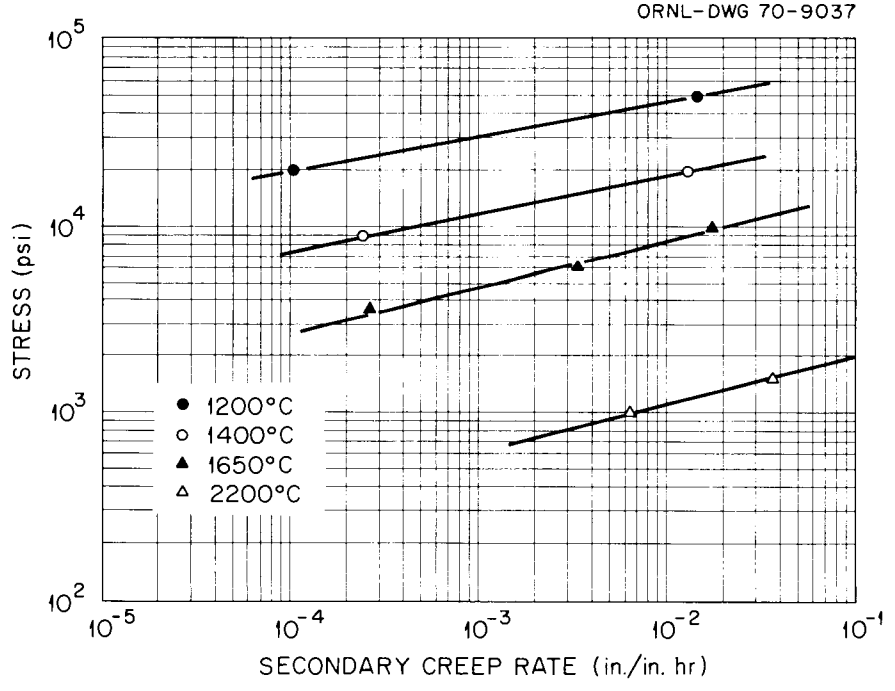

Fig. 16.4. Secondary Creep Rate Versus Stress for W–26% Re.

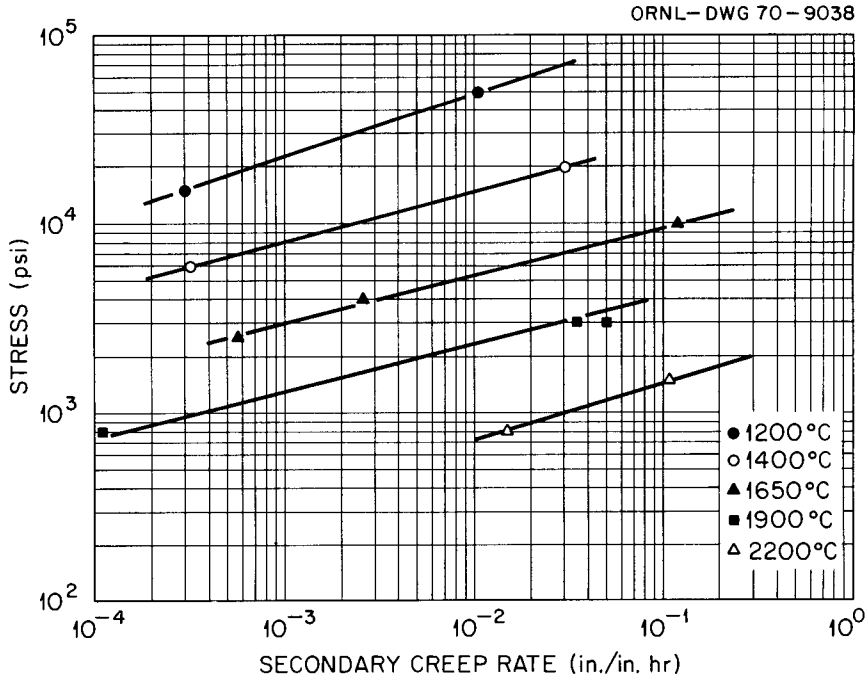

Fig. 16.5. Secondary Creep Rate Versus Stress for W–25% Re–30% Mo.

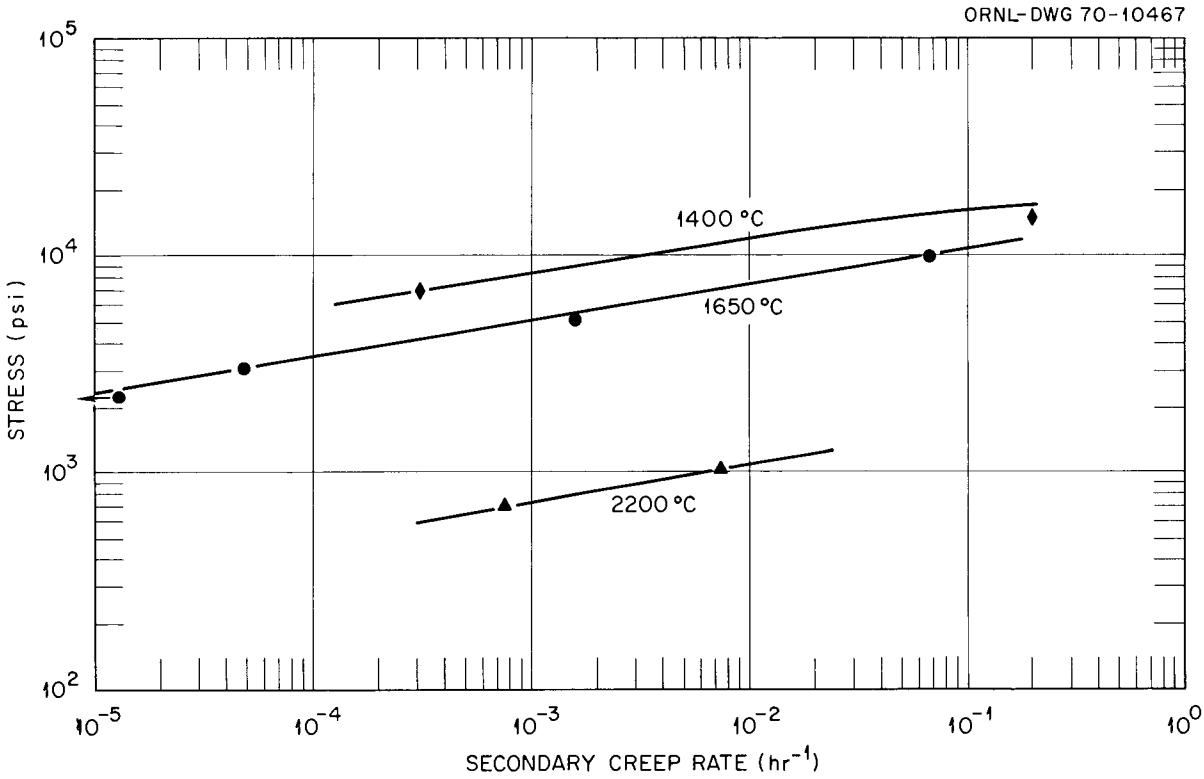

Fig. 16.6. Secondary Creep Rate Versus Stress for Chemically Vapor Deposited Tungsten.

Sherby further suggests that the creep data can be correlated by an equation of the form

$$\dot{\epsilon} = SL^2D\left(\frac{\sigma}{E}\right)^n \quad , \tag{16.1}$$

where S and n are constants, σ is the stress, and $\dot{\epsilon}$ is the creep rate.

Plots of $\dot{\epsilon}/D$ versus σ/E for several materials show a distinct curvature, frequently at values of σ/E that are about equal (between 1.5 and 2.0×10^{-4}). Garofalo[8] and others have suggested that the creep rate for many materials may vary as the hyperbolic sine of the stress. We have combined these two approaches into an equation of the form

$$\dot{\epsilon} = S'D\left[\sinh\left(\frac{\alpha'\sigma}{E}\right)\right]^n \quad , \tag{16.2}$$

where S' and α' are constants.

Figure 16.7 is a plot of $\dot{\epsilon}/D$ versus σ/E for data for the unalloyed W from this study and for data from three sources correlated by Robinson and Sherby.[9] Equation (16.2), represented by the dotted line, agrees well with all of these data.

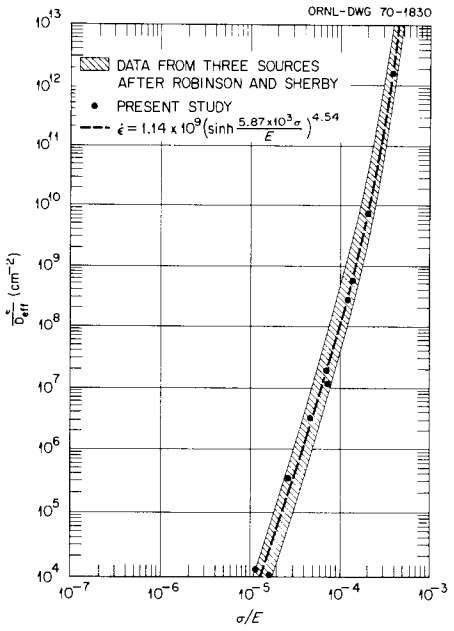

Fig. 16.7. Correlation of Stress and Creep Rate for Tungsten at 1400 to 2200°C. [Ref. S. L. Robinson and O. D. Sherby, Acta Met. 17, 109 (1969).]

We are examining this material by transmission electron microscopy to determine if the subgrain size can be correlated with this equation.

Metallurgical Properties of Tungsten Alloys

H. Inouye

Effect of Low-Pressure Oxygen on the Creep Properties of W–25% Re

The creep properties of 0.035-in.-diam W–25% Re wire produced by powder-metallurgy techniques are being measured in low-pressure O_2 and at thermionic temperatures to simulate the effects of its interaction with the O_2 derived from the decomposition of an oxide fuel.

Figure 16.8 is the creep curve for a specimen stressed to 1000 psi at 1800°C. When the environment was changed from a base pressure of 5×10^{-8} to 8×10^{-6} torr O_2, the minimum creep rate decreased ($\dot{\epsilon}_o/\dot{\epsilon}_v = 0.3$). Changing the environment from O_2 back to vacuum did not alter the creep curve. As reported previously,[10–12] O_2 increases the creep rate of W, which is the opposite of the effect on W–25% Re reported here.

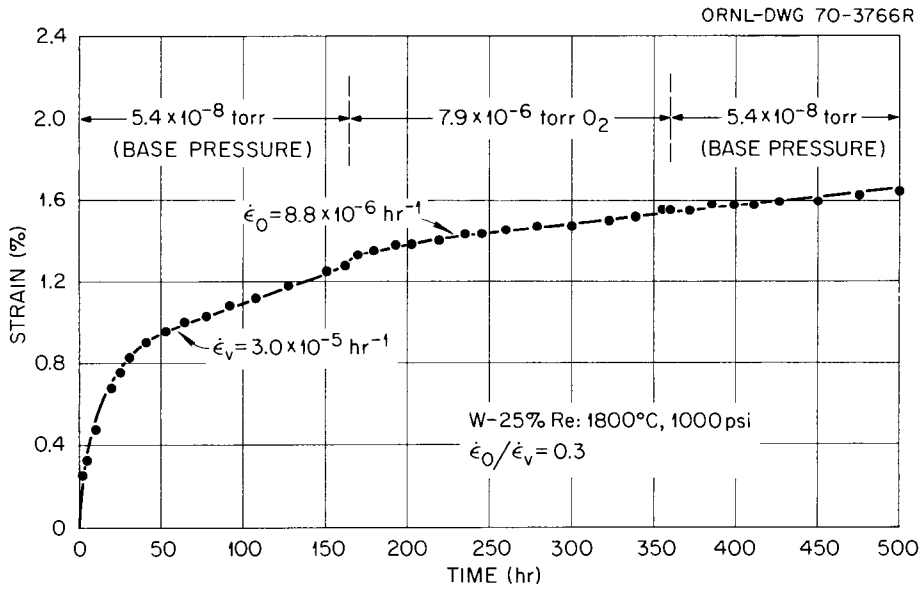

Fig. 16.8. Effect of Pressure Cycles on Creep Behavior of W–25% Re.

Creep curves for W–25% Re stressed to 2000 psi at 1650°C in either vacuum or 7.6×10^{-5} torr O_2 are shown in Fig. 16.9. Although the creep curves are nearly identical to about 300 hr, the specimen tested in O_2 had a lower minimum creep rate than did the specimen tested in vacuum. The beginning of the third stage of creep in O_2 coincided with lower requirements of current to maintain the temperature of the resistively heated specimen. Thus, it appears that this stage of creep results from the reduction of the cross section of the specimen by sublimation as oxides. A rupture ductility of about 2% indicates that O_2 embrittles the alloy at 1650°C.

Tentatively, we attribute the lower creep rates of W–25% Re in O_2 to the formation of a surface layer of sigma phase as a consequence of the fact that the reaction rate of W with O_2 is higher than that of Re with O_2 (ref. 13).

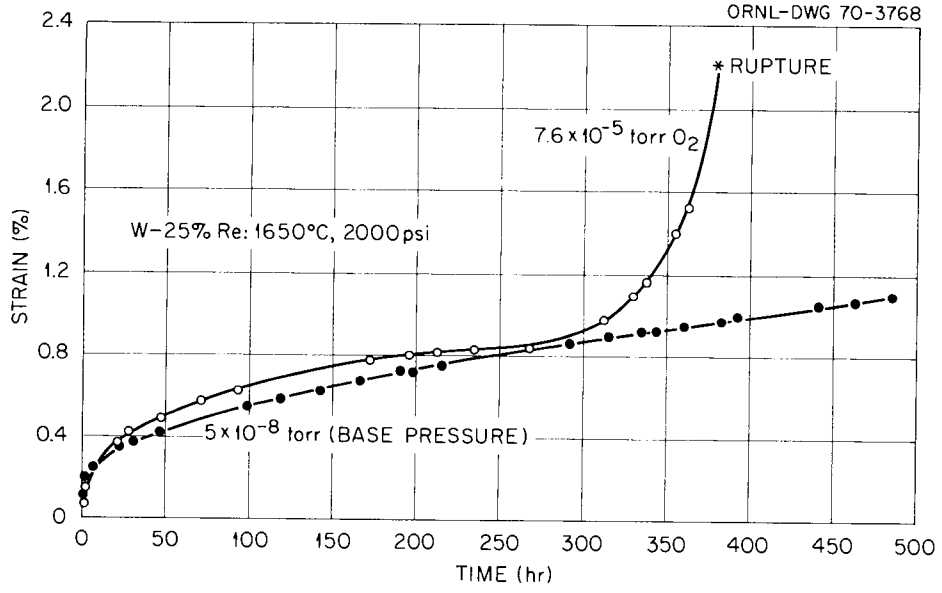

Fig. 16.9. Creep Curves of W–25% Re in Vacuum and in Low-Pressure Oxygen.

Notes

1. A. C. Schaffhauser and R. L. Heestand, "Effect of Fluorine Impurities on the Grain Stability of Thermochemically Deposited Tungsten," pp. 204–211 in 1966 IEEE Conference Record of the Thermionic Conversion Specialist Conference, Nov. 3 and 4, 1966, Houston, Texas, Institute of Electrical and Electronics Engineers, New York.

2. J. I. Federer, W. C. Robinson, Jr., and R. M. Steele, "Effect of Deposition Conditions on the Orientation of Chemical Vapor Deposited Tungsten and Molybdenum," pp. 287–295 in 1967 IEEE Conference Record of the Thermionic Conversion Specialist Conference, October 30–November 1, 1967, Palo Alto, California, The Institute of Electrical and Electronics Engineers, New York.

3. L. Yang and R. G. Hudson, "Evaluation of Chemically Vapor Deposited Tungsten as Electron Emitters for Nuclear Thermionic Applications," pp. 329–348 in Proceedings of the Conference on Chemical Vapor Deposition of Refractory Metals, Alloys, and Compounds, Sept. 12–14, 1967, Gatlinburg, Tenn., ed. by A. C. Schaffhauser, American Nuclear Society, Hinsdale, Illinois.

4. J. I. Federer, Fuels and Materials Development Program Quart. Progr. Rept. March 31, 1970, ORNL-4560, pp. 186–189.

5. Nancy C. Cole, Fuels and Materials Development Program Quart. Progr. Rept. March 31, 1970, ORNL-4560, pp. 195–197.

6. National Research Council, Materials Advisory Board, Evaluation Test Methods for Refractory Metal Sheet Material, MAB-192-M (April 22, 1963).

7. O. D. Sherby, Acta Met. 10, 135 (1962).

8. F. Garofalo, Trans. Met. Soc. AIME 227, 351 (1963).

9. S. L. Robinson and O. D. Sherby, Acta Met. 17, 109 (1969).

10. H. Inouye, Fuels and Materials Development Program Quart. Progr. Rept. June 30, 1969, ORNL-4480, pp. 176–180.

11. H. Inouye, Fuels and Materials Development Program Quart. Progr. Rept. Dec. 31, 1969, ORNL-4520, pp. 229–232.

12. H. Inouye, Fuels and Materials Development Program Quart. Progr. Rept. March 31, 1970, ORNL-4560, pp. 189–191.

13. L. H. Rovner et al., Mass Spectrometric Studies of the Vaporization of Refractory Metals in Oxygen at Low Pressure, AFML-TR-68-200 (July 1968).

17. FAST-NEUTRON IRRADIATION EFFECTS ON ELECTRICAL INSULATORS

G. M. Watson[1] G. W. Keilholtz[1]

The purpose of this program is to establish the effects of fast neutrons on the mechanical, physical, and electrical properties of materials suitable for use as electrical insulators in thermionic converters and to evaluate the mechanisms of neutron damage in these materials up to 1100°C.

General Survey of Fast-Neutron Effects on Electrical Insulators

R. E. Moore[1] D. A. Dyslin[2] H. E. Robertson[1]

A low-temperature (below 150°C) assembly containing three advanced materials as well as polycrystalline alumina was irradiated in the Engineering Test Reactor (ETR) for 6 months. The advanced materials were (1) synthetic sapphire Al_2O_3, (2) single-crystal MgO, and (3) transparent, polycrystalline zirconia-doped Y_2O_3. The maximum fast fluence of the assembly was estimated to be about 2×10^{21} neutrons/cm^2 (> 1 Mev).

One of the four MgO specimens and one of the six Y_2O_3 specimens were found to be broken in half after irradiation. The 6 sapphire Al_2O_3 specimens and the 16 specimens of polycrystalline alumina included in the assembly were undamaged. Metallographic examinations of specimens of the three advanced materials that had been irradiated to nearly the maximum fast fluence of the assembly revealed no microfracturing.

The volume increases of polycrystalline alumina and the three advanced materials are given in Table 17.1. The volume expansion of the polycrystalline alumina was about the same as that of the sapphire specimens, but the three sapphire cylindrical specimens that had received the highest fluences expanded in length by about 50% more than in diameter. The c axis was oriented in the direction of the length of the cylinders. The other three sapphire specimens irradiated at a lower fluence for the same time period expanded by about the same amount in length and diameter.

Table 17.1. Comparison of the Volume Expansions of Polycrystalline Alumina and Three Advanced Materials Irradiated at Low Temperature (Below 150°C)

Type of Specimen	Estimated Fast Fluence [neutrons/cm^2 (> 1 Mev)]	Volume Increase (%)
	$\times 10^{21}$	
GE Opaque Lucalox (polycrystalline)	0.4	1.6
	0.7	1.7
	1.3	1.5
	1.7	1.3
	2.0	1.2
Synthetic sapphire	0.4	1.6
	0.7	1.6
	0.9	1.6
	1.5	1.5
	1.8	1.4
	1.9	1.4
Transparent polycrystalline Y_2O_3	0.5	0.5
	0.7	0.4
	1.0	0.3
	1.5	0.4
	1.9	0.3
Single-crystal MgO	0.8	1.3
	1.6	1.2
	1.9	1.1

Cylindrical specimens of single-crystal MgO expanded in volume slightly more than polycrystalline specimens irradiated in previous experiments.[3]

The breakage of one MgO specimen and one Y_2O_3 specimen was not encouraging, since the maximum fluence of the assembly was moderately low. Additional irradiations of synthetic sapphire at high fluences would seem warranted.

Irradiation of High-Density Commercial Al_2O_3 Products Considered for Thermionic Insulators

R. E. Moore[1] D. A. Dyslin[2] H. E. Robertson[1]

Most of the postirradiation examinations of solid cylindrical alumina specimens irradiated in row 4 of the Experimental Breeder Reactor-II (EBR-II) are now complete. The assembly contained the same three commercial types of alumina that had previously[4] been irradiated in the ETR. The design temperature for the specimens was 800°C, but actual temperatures, which will be obtained from SiC temperature monitors included within the assembly, have not yet been measured. The results of dimensional measurements, visual inspections, and metallographic examinations are given in Table 17.2.

The expansion in volume is much greater than that found in specimens irradiated in the ETR under approximately the same conditions.[3] Figure 17.1 shows the volume increase of General Electric Opaque Lucalox for both reactors. Metallographic examinations of the specimens with the greatest volume increase revealed no separation at grain boundaries or transgranular fracture. The only way to account for the greater expansion in the EBR-II is through differences in the neutron-energy spectra. That is, the EBR-II spectrum, for measured fluences above 1 Mev, must contain a greater percentage of neutrons with damage potential than does the ETR spectrum.

Metal-Clad Al_2O_3 Specimens

R. E. Moore[1] D. A. Dyslin[2] H. E. Robertson[1]

The status of the irradiations of bilayers and trilayers is given in Table 17.3.

Table 17.2. Results of Postirradiation Examinations of Solid Cylindrical Alumina Specimens Irradiated in Row 4 of the Experimental Breeder Reactor-II

Type of Specimen[a]	Fast Fluence [neutrons/cm^2 (> 1 Mev)]	Volume Increase (%)	Results of Visual Examination	Results of Metallographic Examinations
	$\times 10^{21}$			
I	0.6	1.7	Chipped on one end	
	1.0	1.6		
	1.1	2.9	Longitudinal fracture	
	1.2	3.4	Longitudinal fracture	
	1.3	4.1	Longitudinal fracture	Some grain-boundary separation
II	0.7	2.0		No grain-boundary separation
	0.9	1.6		
	1.1	4.3		
	1.2	4.4		
	1.3	5.2		Very severe grain-boundary separation
III	0.7	2.1		
	0.9	1.7		
	1.2	2.7		
	1.1	3.5		No grain-boundary separation
	1.3	2.8		No grain-boundary separation

[a]I = Coors AD-995 (grain size, 13 μm); II = Wesgo AL-995 (grain size, 23 μm); III = General Electric Opaque Lucalox (grain size, 6 μm).

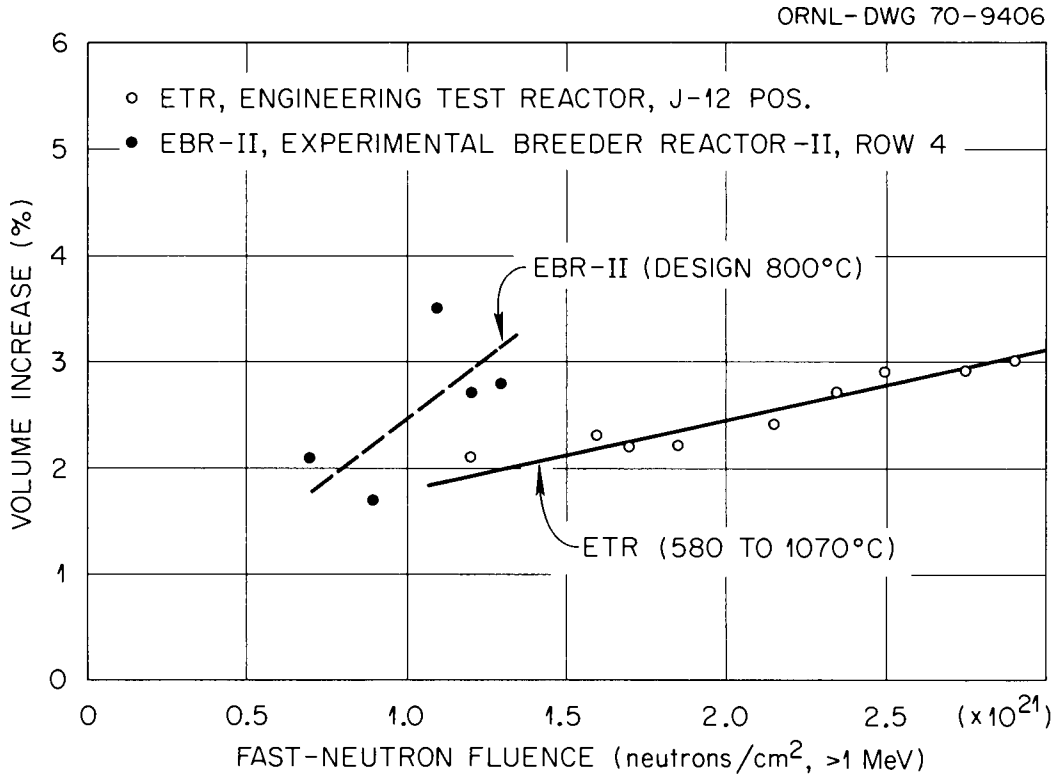

Fig. 17.1. Volume Increase of General Electric Opaque Lucalox (Grain Size 6 μm) after Irradiation in Two Reactors with Different Neutron-Energy Spectra.

Table 17.3. Irradiations of Bilayers and Trilayers

ORNL Experiment Number	Supplier	Design Temperature (°C)	Fast Fluence [neutrons/cm^2 (> 1 Mev)]	Status
41-40 (ETR)	NASA-Lewis Fairchild-Hiller Thermo Electron	600,800 1000,1100	0.6–2.8	Postirradiation examination completed
41-42 (ETR)	Thermo Electron Gulf General Atomic	600,800	0.6–2.8	Postirradiation examinations completed except for metallography
0-3 (EBR-II) Row 8	Thermo Electron	700–800		Undergoing irradiation To be completed September 1970

Notes

1. Reactor Chemistry Division.

2. General Engineering Division.

3. G. W. Keilholtz, J. E. Lee, Jr., and R. E. Moore, "Properties of Magnesium, Aluminum, and Beryllium Oxide Compacts Irradiated to Fast-Neutron Doses Greater than 10^{21} Neutrons cm^{-2} at 150, 800, and 1100°C," pp. 133–148 in Proceedings of the Conference on Nuclear Applications of Nonfissionable Ceramics, Washington, D. C., May 9–11, 1966, American Nuclear Society, Hinsdale, Illinois, 1966.

4. R. E. Moore, D. A. Dyslin, and H. E. Robertson, Fuels and Materials Development Program Quart. Progr. Rept. Dec. 31, 1969, ORNL-4520, pp. 245–252.

18. CORROSION STUDIES OF ADVANCED REFRACTORY METALS

W. O. Harms J. H. DeVan W. R. Huntley[1]

Requirements for auxiliary electricity or ion propulsion for space vehicles necessitate power plants of high efficiency that will operate at high temperatures. For these applications, nuclear power systems have been proposed in which alkali metals are used to transfer heat, drive a turbogenerator, and lubricate rotating components. Accordingly, we are investigating the corrosion properties of candidate alkali metals, primarily Li, K, and Na, under conditions of interest for space applications. Because of the relatively high temperatures (above 1000°C), the investigation is concerned largely with refractory-metal container materials.

Lithium Studies

J. H. Devan W. R. Huntley[1]

Lithium Forced-Circulation Loop Experiments (C. W. Cunningham,[1] B. Fleischer)

A T-111 forced-circulation loop (FCLLL-1) containing Li was shut down after completing its scheduled 3000-hr test. Operating conditions maintained during the test are summarized below:

Temperature, °C	
Maximum	1370
Minimum	1205
Flow rate, gal/min	5.2
Maximum velocity of Li, ft/sec	18
Maximum Reynold's number	89,000
Total pressure drop in system, psi	36
Resistance heater power, kw	30
Volume of circulated Li, $in.^3$	300
Number of corrosion specimens	
Flat	84
Annular	9

As discussed previously,[2] the test was interrupted after 1735 hr when a Li leak occurred in an auxiliary line leading from the hot leg to a surge tank. Operation of the loop and its surrounding vacuum system was essentially free of trouble during the 1265 hr after the the leak was repaired.

Loop Start-Up. – After the repair, the loop was brought to design conditions, and the following operations, performed in sequence, required about 11 calendar days:

1. The chamber was evacuated with the auxiliary roughing system and heated to 315°C. The chamber pressure peaked at 1×10^{-3} torr, and, within 24 hr after reaching 315°C, the pressure was less than 8×10^{-6} torr.

2. Lithium was pushed from the dump tank, circulated, and then dumped three times in succession. After the last dump, the Li was hot trapped in the dump tank 25 hr at 815°C. The loop was again filled with Li, which was circulated and then sampled. Flow through the sampler was sufficient for 18 changes of volume in the sample line. As a result of the analysis of this sample, the loop was dumped, and the Li was hot trapped another 7 1/2 hr at 815°C.

3. The loop was again filled with Li, and the Li was sampled again. Analysis showed less than 20 ppm O and less than 5 ppm N.

4. The vacuum chamber was cooled, and the loop was heated to design temperature. Maximum pressure during heating was 1×10^{-4} torr.

5. The auxiliary pump was valved off, and the ion pumps and sublimation pump were started.

Operating Experience. – Operation of the loop and the vacuum system was essentially free of trouble during the 1265 hr after the Li leak was repaired. A minor problem resulted from residual Li that could not be cleaned from inaccessible areas within the vacuum chamber. During bakeout of the chamber, some of this Li was deposited on the relatively cold viewports and obscured visibility into the chamber. However, there was no evidence of further Li leakage during repair operation after the repair. The Li level in the fill and drain tank remained constant, and no Li peaks were observed on the residual-gas analyzer except for a period when a Ti-sublimation vacuum pump was placed in operation. We

believe the Li peaks observed at that time resulted from heating of the pump that displaced residual Li to the cooler areas.

The chamber pressure peaked at 1×10^{-4} torr when the loop reached design conditions after the repair. This pressure decayed to 1×10^{-6} torr within 24 hr, to 1×10^{-7} torr within 48 hr, and to 1×10^{-8} torr at the end of the test. The relative proportions of residual gases at the end of the test period were estimated to be 72% H, 15% Ar, 10% N_2-CO, and 3% methane.

Evaluation of W–3% Re vs W–25% Re thermocouples continued during the recent 1265-hr operation. Nine sheathed thermocouples were reused after repair of the leak, but only one of these thermocouples was still operating satisfactorily at the end of the test period. Twelve new spot-welded bare-wire thermocouples were installed after the Li leak was repaired, and all were functioning properly at the end of the test. We periodically compared readings between the optical pyrometer and the spot-welded couples and confirmed that there was no significant thermocouple drift. Readings between thermocouple pairs as a function of time showed that measurements of the loop temperature made with spot-welded bare-wire thermocouples were accurate within ±0.5%. The only exception to this was the thermocouple located in the I^2R heated section, which was affected by the applied voltage.

The excellent performance of the spot-welded bare-wire thermocouples during the recent operating period gave us an opportunity to check loop flow rates and heat-transfer performance accurately. The flow rate indicated by the electromagnetic flowmeter was 5.4 gal/min or 1100 lb/hr. This compared with a heat balance at the I^2R heater section that indicated a flow rate of 1095 lb/hr. The heat-transfer performance of the tube and shell Li economizer also agreed well with theoretical predictions. The actual performance of the economizer was within 5% of the performance predicted with the standard calculations for heat transfer in liquid metal.

Lithium Sample. – A final Li sample was obtained after the loop had been cooled to about 500°C. At the time the sample was isolated, about 35 inventories of the Li in the loop had passed through the bypass sampling

tube. The O and N impurity concentrations throughout the test program were as follows:

	Concentration, ppm	
	O	N
Start of Test	12	< 5
Lithium Leak		
Before Repair	58	< 5
After Repair	20	< 5
End of Test	50	< 5

The sample for O analysis at the end of test was slightly contaminated during analysis.

Failure Analysis. — As discussed previously,[2] the Li leak that forced an interruption in loop operation occurred in a vent line close to where it connected to the loop heater. The outer surface of the failed area was generally eroded to a depth of about 1/32 in. over an area about 3/8 in. in diameter. The inner surface contained many small protuberances as well as crater-like spots. A crack through one of these spots appeared to be linked to the external eroded area.

To determine the chemical nature of these protuberances and craters, we first scanned the inside surface of the tube with an electron microprobe analyzer. The results indicated that the protuberances were rich in Hf. A metallic film was deposited uniformly around the inner surface of the tube about an inch from the failure; this film also was quite rich in Hf and showed a trace of Ni. Subsequent microprobe analysis of a cross section of the film failed to confirm the presence of Ni. We next made a metallographic examination through the failure site and through one of the protuberances. The section through the failure site revealed a wide intergranular crack with smaller separations of grain boundaries connecting to this crack near the outside surface of the tubing. As shown in Fig. 18.1, several light and dark phases were noted in the grain boundaries near the crack. Electron microprobe analysis showed that Hf was depleted from these grain-boundary areas and also from the corroded area near the outer surface. A slight trace of Ni was found in several small locations in the corroded material at the outer surface. No other foreign elements were detected.

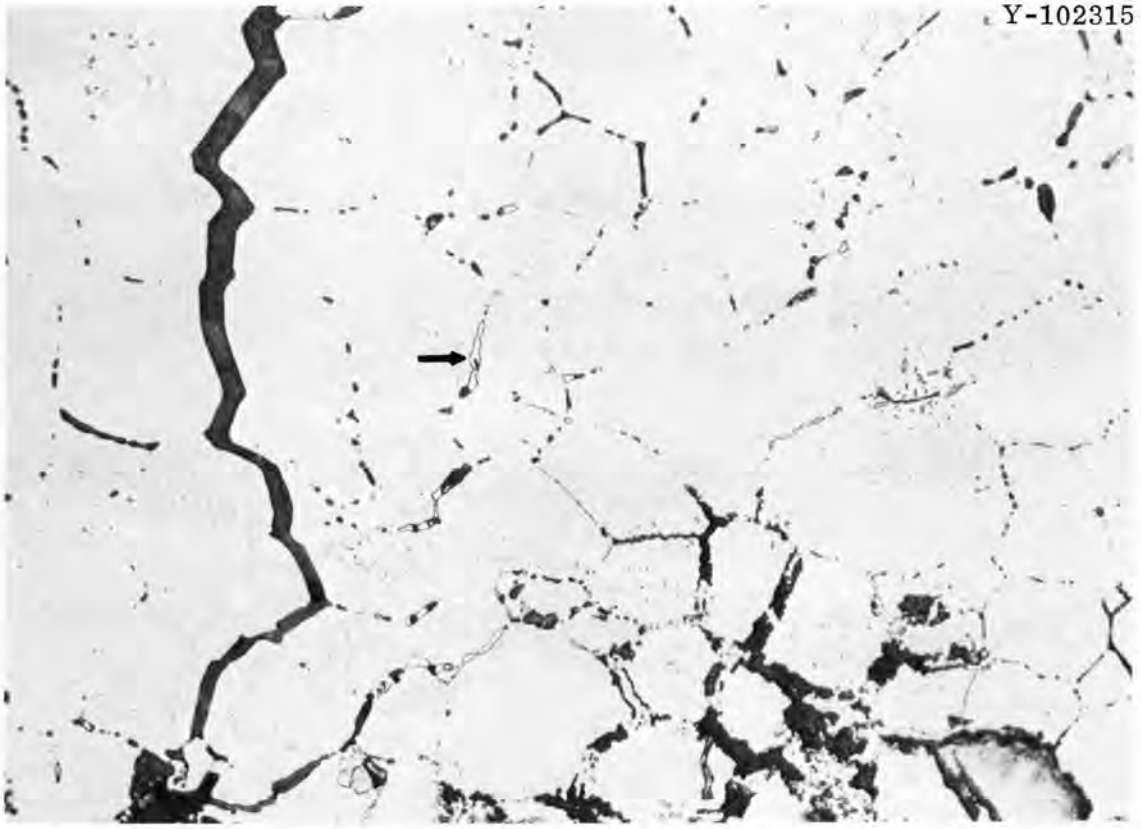

Fig. 18.1. Appearance of Grain Boundaries Near Failure of T-111 Vent Line. Note the light phase indicated by arrow. 500×.

The cross section through the protuberance revealed the two-phase structure shown in the center photograph in Fig. 18.2. A microprobe scan showed the darker primary phase to be rich in Hf (Fig. 18.2), and a microprobe trace for Hf through the protuberance showed that the lighter of the two phases was depleted in Hf. The surface under the protuberance showed no depletion of Hf. No foreign elements were found except for Zr, which occurs naturally in Hf.

Further visual examinations of the tubing surface adjacent to the failed section about 2 in. from the failure site showed some slight traces of what appeared to be foreign metallic-like material smeared on the inner surface.

The above findings and the general asymmetrical arrangement and appearance of the internal spots and protuberances near the weld and failure site lead us to believe that a foreign material was spattered over the inner and possibly the outer surface during welding. The

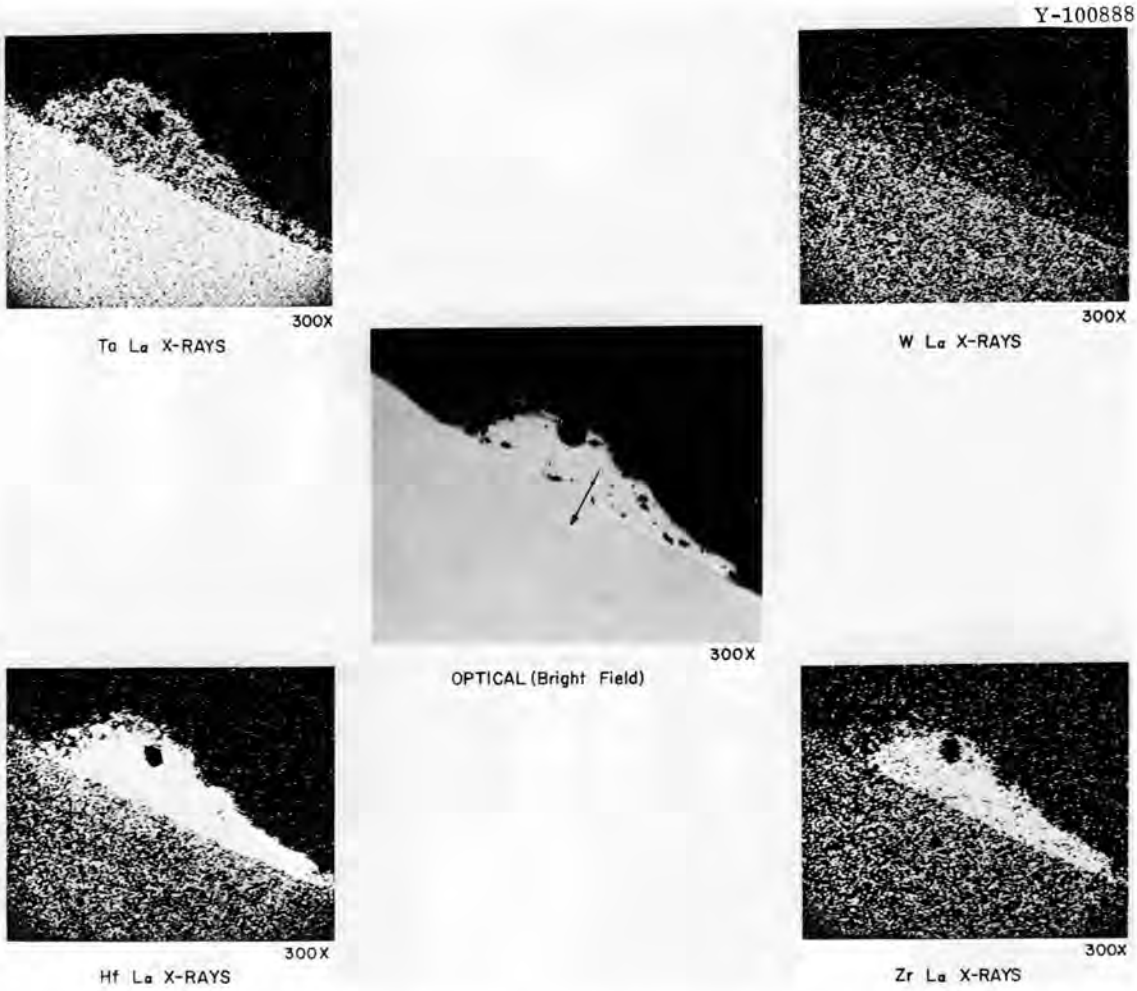

Fig. 18.2. Electron Microprobe Photomicrographs of Nodule Found on Inner Surface of T-111 Tubing in the Vicinity of the Failed Vent Line.

existence of trace quantities of Ni suggests that a Ni-Hf eutectic was present at some stage during welding; however, we believe that most of the Ni originally present was subsequently leached out by Li during operation. This would account for the Hf-rich protuberances deposited on the surface of the tubing. The Hf-rich film observed about 1 in. from the failure site appears to be the result of conventional solution mass transfer and not to be related to the failure.

Notes

1. Reactor Division.

2. C. W. Cunningham and B. Fleischer, Fuels and Materials Development Program Quart. Progr. Rept. March 31, 1970, ORNL-4560, pp. 202–210.

PART III

GENERAL REACTOR TECHNOLOGY

FUELS

19. FISSION-GAS RELEASE AND PHYSICAL PROPERTIES OF FUEL MATERIALS DURING IRRADIATION

O. Sisman[1]

The purpose of this work is to measure the variables that control the release of fission gas from highly characterized nuclear fuels and to evaluate these variables in terms of a generalized model for predicting release from operating fuel materials. Thermal diffusivity is measured in-reactor in analogous experiments. This is the final quarterly report on this program, but several open literature reports are being prepared.

Measurements of Thermal Diffusivity in UO_2 During Irradiation

R. M. Carroll[1] R. B. Perez[1]

Our method of measuring thermal diffusivity during irradiation is to make a stepped change in the fission power generated by the fuel specimen and then measure the dependence of the resulting temperature changes on time. One problem of measuring the thermal diffusivity of UO_2 during irradiation is that a large temperature gradient at any realistic power level makes it very difficult to measure the temperature at any point except at the center of symmetry of the specimen. By this method we are able to obtain measurements of thermal diffusivity by measuring only the time response of the temperature at the center of symmetry.

In attempting to develop this method, we solved many problems involving instrumentation, irradiation technique, computer processing of data, nonfission heating,[2] release of stored energy,[3] and mathematical formulations of the general theory into computer codes.[4] We completed the computer program for obtaining the values of thermal diffusivity from the general theory.

We discovered an error in the initial computer program, and only portions of the data were rerun. A preliminary evaluation shows that our measured values for thermal diffusivity agree with bench data to within about 20%. Since bench data between various experimenters show more variation than this, we consider the method to be working well.

Our original objective was to find if simultaneous fissioning and burnup at elevated temperatures had an effect on thermal diffusivity. The preliminary evaluation of data obtained from large-grained UO_2 showed that the thermal diffusivity increased with fission-rate density (fissions per cubic centimeter per second) at 600 to 1000°C. We also believe there is a good possibility of establishing a theoretical relationship between the release of fission gas and thermal diffusivity as a function of fission rate.

This is the last quarterly report for this project, but we are preparing a journal article that will contain the final evaluation of the data.

Behavior of Mixed Oxide Fuels During Irradiation

R. M. Carroll[1] O. Sisman[1]

Three specimens of $(U,Pu)O_2$ material manufactured in different ways were irradiated. Two of these were of pressed-and-sintered $(U_{0.75},Pu_{0.25})O_2$ specimens supplied by Battelle Memorial Institute Pacific Northwest Laboratory (BNWL); one of these specimens consisted of high-density (97%) sintered pellets, while the other consisted of 21 spheres (903 μm average diameter) ground from a production batch of candidate fuel for the Fast-Flux Test Facility Reactor. The third specimen was $(U_{0.8},Pu_{0.2})O_2$ prepared at ORNL by the sol-gel technique as spheres (546 μm average diameter).

The release of fission gas from each of these specimens was described in previous reports. However, the results of metallographic examination of these specimens after irradiation were completed, and a brief review is necessary to explain the results. The physical characteristics of all the specimens are summarized in Table 19.1.

Table 19.1. Characteristics of $(U,Pu)O_2$ Specimens

	Pressed and Sintered		Sol-Gel
	Pellets (C1-24)	Microspheres (C1-25)	Microspheres (C1-27)
Number of specimens	2	21	51
Density, g/cm^3	10.8	~10.8[b]	10.8
Outside diameter, cm	0.54	0.0903 ± 0.009	0.0546 ± 0.0017
Length, cm	0.58		
Inside diameter of axial hole, cm	0.127		
Ratio Surface Area:Volume (geometric, cm^{-1})	13.4	66.5	110
Sintering temperature, °C	1650	1650	1450
Uranium content, wt %	65.4	a	71.6
Plutonium content, wt %	22.1	22.4	17.4
Ratio O:metal	a	a	2.01
Total specimen weight, g	2.76	0.0784	0.047[b]
Impurities, ppm			
Ag	< 0.1	5	< 1
Al	50	50	18
C	< 50	< 25	a
Ca	2	< 1	10
Cr	< 25	< 25	5
Cu	10	5	10
Fe	10	20	94
Mg	< 5	< 5	20
Mn	4	2	5
Ni	< 10	20	15
Pb	< 50	5	10
Si	< 5	5	100
Sn	< 5	< 5	5
V	< 20		10
Zn	< 50	< 5	< 10

[a]Not available

[b]Estimated

Upon irradiation, the high-density pellets from BNWL showed evidence of some initial porosity that was decreased by irradiation sintering.[5] When the specimen temperature was raised to 1450°C, in an attempt to speed up this sintering process, the fission gases were released very rapidly. At this temperature, the mixed oxide specimen (unlike many previous tests with UO_2) apparently became sufficiently plastic to permit release of nearly all the fission gas produced. Examination after irradiation showed that the fuel specimen was broken into several large lumps.

The microstructure of a control pellet for the C1-24 experiment is shown in Fig. 19.1. The white specks within the microstructure were found to be W, apparently introduced during the milling operation. A typical midplane view after irradiation is given in Fig. 19.2, which shows the collection of bubbles of fission gas into grain boundaries and

Fig. 19.1. Microstructure of Control Pellet (C1-24) Before Irradiation. As polished.

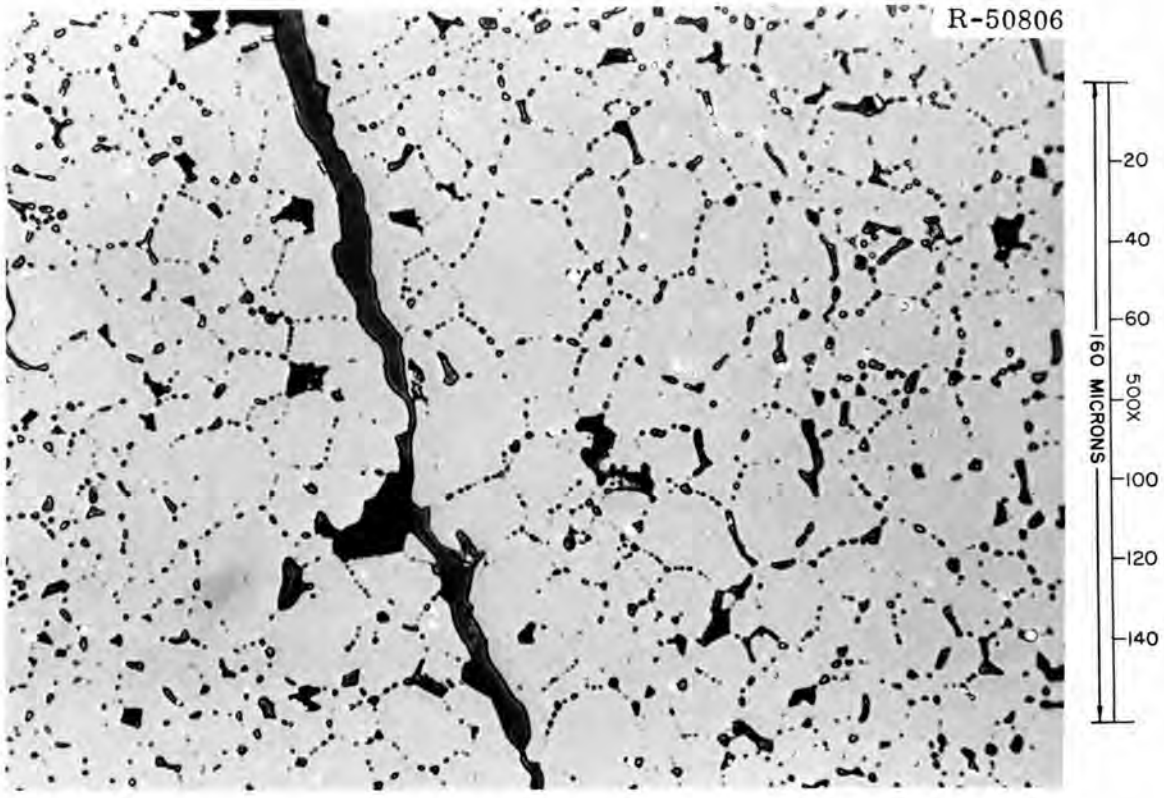

Fig. 19.2. Typical Midplane Section of Specimen (C1-24) After Irradiation. As polished.

the extensive linking. In Fig. 19.3 the inner surface of the cylindrical pellet is shown to have collected W particles at the surface that operated at the highest temperature. The most plausible explanation for the migration of the W particles is that they were swept along with migrating bubbles and deposited at the surface.

During irradiation, the pellet specimens (C1-24) were subjected to a temperature excursion to 1450°C for 20 min, which apparently was sufficient to allow rapid migration of bubbles.[5] It should be noted that the specimen was originally sintered at 1650°C. Thus, the differences between the microstructures shown in Fig. 19.1 and Figs. 19.2 and 19.3 were caused by the coupled effects of irradiation and temperature.

The ground spheres of the material from BNWL, specimen C1-25, also exhibited irradiation sintering and breakaway gas release at sufficiently high temperatures. By careful manipulation of the specimen temperature

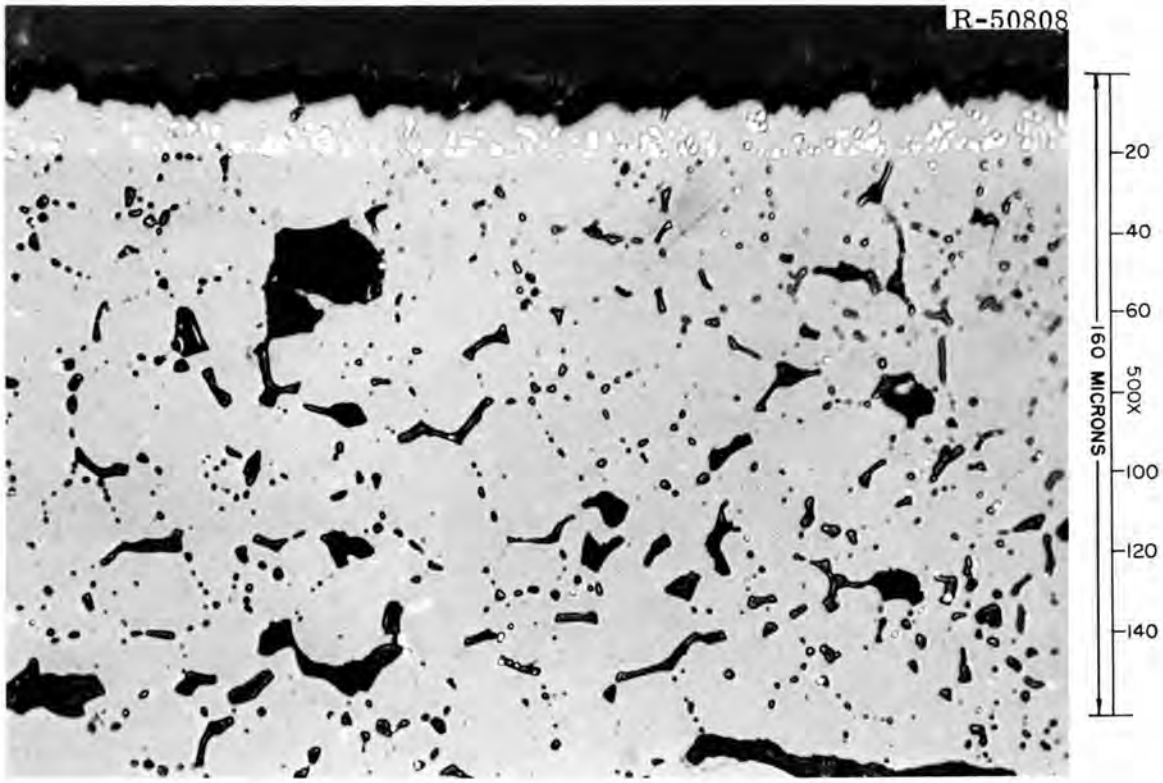

Fig. 19.3. Tungsten Concentrated at Inner Surface of Pellets (C1-24) After Irradiation.

we were able to determine the temperature at which breakaway gas release occurred as a function of burnup.[6]

The structure of specimen C1-25 before irradiation is shown by a control microsphere (Fig. 19.4). A different milling process was used for this material, and the powder was contaminated with Fe-Ni particles but not with W. The structure after irradiation is shown in Fig. 19.5. It should be noted that the damage to the microspheres, as shown in Fig. 19.5, is insignificant compared to the damage to the pellets, as shown in Figs. 19.2 and 19.3, yet the spheres had 4.5% burnup, whereas the pellets had only 0.28% burnup. The 1450°C peak temperature of the pellets, as compared to the 1050°C temperature of the spheres, apparently accounts for the difference. This leads to the conclusion that temperature is more important than burnup in causing changes in the microstructure of this material.

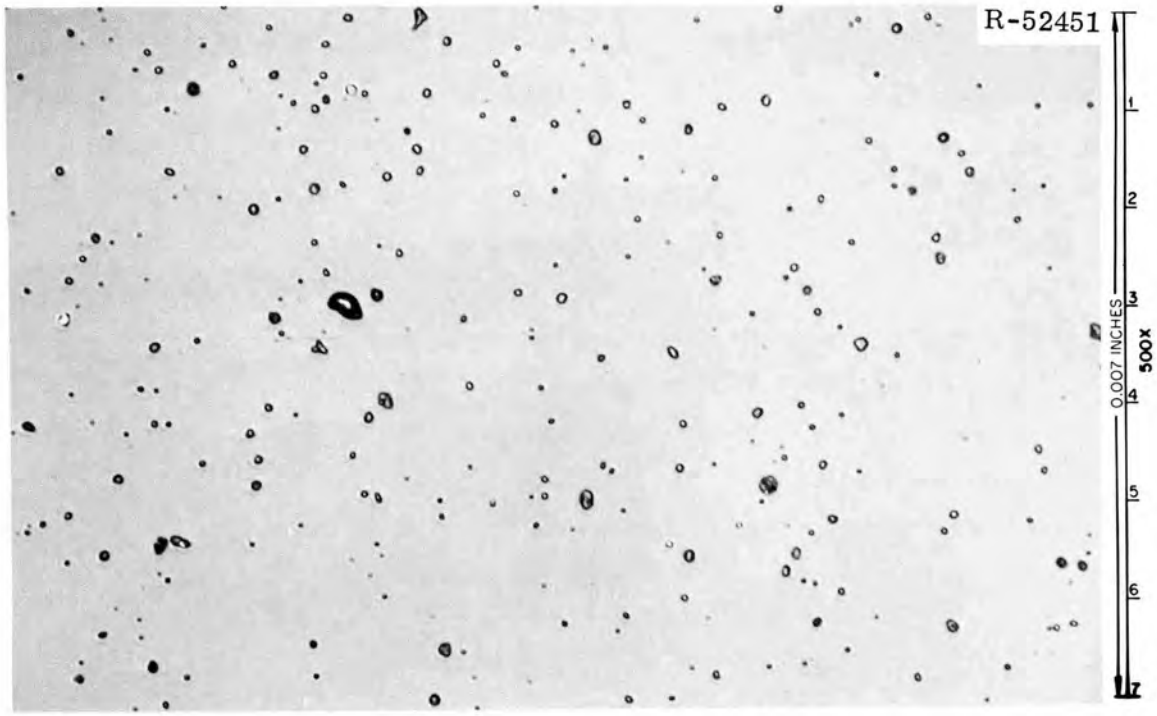

Fig. 19.4. Sintered Microspheres of Control Specimen (C1-25). As polished.

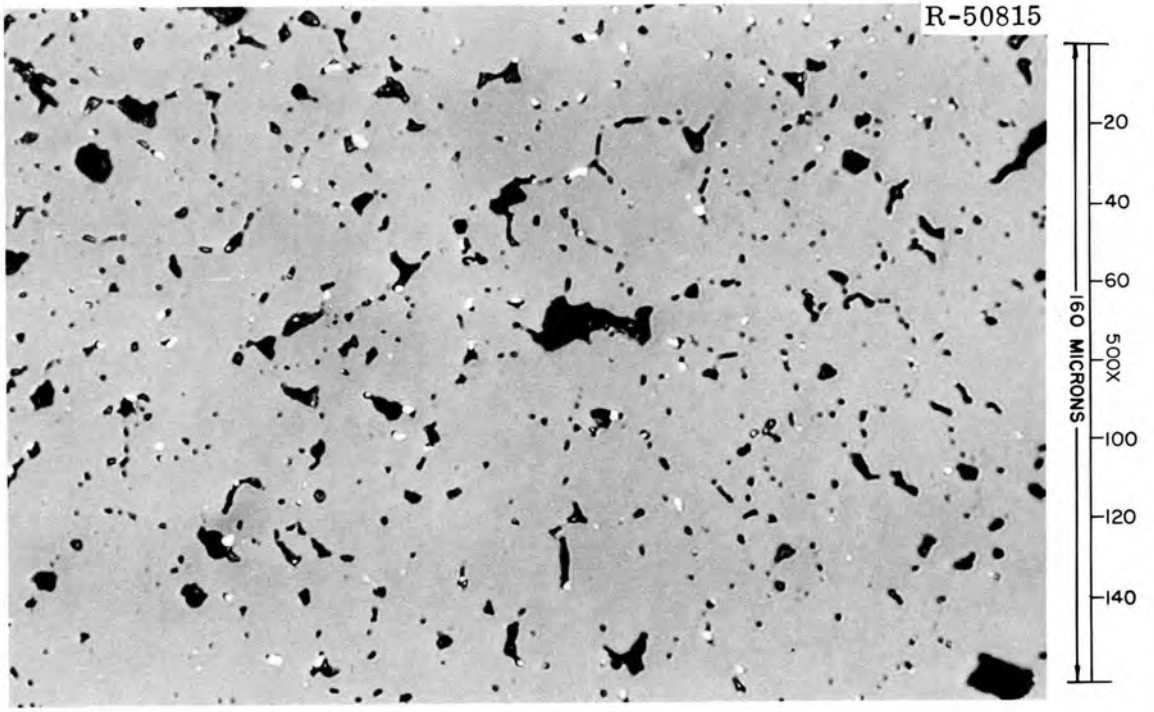

Fig. 19.5. Typical Microstructure of Sintered Microspheres (C1-25) After Irradiation. As polished.

The rate at which fission gas was released from the sol-gel specimens at the beginning of irradiation was about double that for the previous specimens (after corrections for the different ratios of surface area to volume). The sol-gel specimens did not sinter during irradiation to the extent that the other specimens had. There were no cooling bursts when the sol-gel specimens were cooled rapidly, and there was little of the trickle release of fission gas after cooling that had characterized the previous specimens. These observations all implied that the porosity in the sol-gel specimens was larger than that in the pressed-and-sintered mixed oxide specimens.[7]

The structure of control specimens before irradiation showed no evidence of porosity, and each sphere had been hand selected and individually examined by microscope.[8,9] The microstructure typical of the spheres after irradiation is shown in Fig. 19.6. There is no indication of the large, interconnected porosity indicated by the release of fission gas,[10] but about 10% of the microspheres had the appearance shown in Fig. 19.7.

Fig. 19.6. Typical Microstructure of Sol-Gel Specimens (C1-27) After Irradiation. As polished.

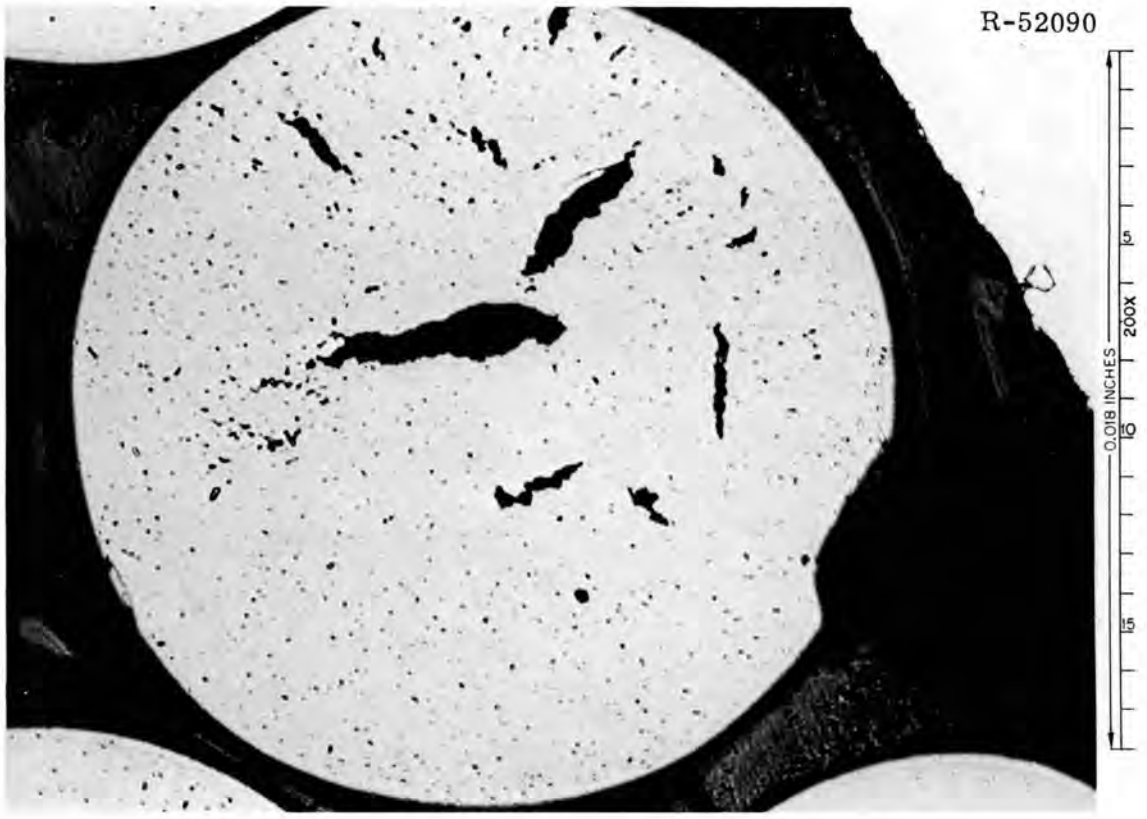

Fig. 19.7. Unusually Cracked Sol-Gel Specimen Included in Experiment C1-27. About 10% of the spheres had this appearance.

Analysis of the fission gas showed that the particles had the large internal cracks when irradiation began. Because the cracks did not grossly penetrate the surface, the internally cracked particles could pass optical inspection, whereas obviously cracked specimens were rejected. The gas release from these cracked specimens dominated the total gas release. We suggest that another irradiation test should be done in which the internally cracked specimens are also culled, since this test was inconclusive.

The results of these irradiations and other measurements of fission gas are being gathered into two journal articles.

Notes

1. Reactor Chemistry Division.

2. R. M. Carroll et al., Nucl. Sci. Eng. 36, 232–237 (1969).

3. R. M. Carroll et al., Nucl. Sci. Eng. 39(1), 123–126 (1970).

4. R. B. Perez et al., The Theory of a Time-Dependent Heat Diffusion Determination of Thermal Diffusivities with a Single Temperature Measurement, ORNL-4478. In press.

5. R. M. Carroll and J. G. Morgan, Fuels and Materials Development Program Quart. Progr. Rept. Dec. 31, 1968, ORNL-4390, pp. 65–68.

6. R. M. Carroll, Fuels and Materials Development Program Quart. Progr. Rept. March 31, 1969, ORNL-4420, pp. 72–74.

7. R. M. Carroll and R. B. Perez, Fuels and Materials Development Program Quart. Progr. Rept. March 31, 1970, ORNL-4560, pp. 216–217.

8. R. M. Carroll and R. B. Perez, Fuels and Materials Development Program Quart. Progr. Rept. Dec. 31, 1969, ORNL-4520, p. 261.

9. R. M. Carroll, R. A. Bradley, and H. E. Robertson, Fuels and Materials Development Program Quart. Progr. Rept. Dec. 31, 1969, pp. 261–264.

10. R. M. Carroll and O. Sisman, "Evaluating Fuel Behavior During Irradiation by Fission-Gas Release." Submitted for publication.

20. DEVELOPMENT OF FUEL ELEMENT FABRICATION

G. M. Adamson, Jr.

The purpose of these programs is to devise new combinations of materials or new fabrication techniques to advance the technology for fabricating fuel elements and components for research reactors. We are attempting to improve the performance of advanced research reactors, such as the High Flux Isotope Reactor (HFIR) and Advanced Test Reactor (ATR), by developing fuel elements with lower production cost, longer lives, increased safety or reliability, or all three. The studies include factors that affect both fabrication and irradiation performance. We must also develop sufficient knowledge of the processes used for fabricating Al-base dispersion fuel elements so that we can adequately assist commercial fabricators, purchasers, specification writers, and technical inspectors. Other studies are aimed at improving the reliability and reducing the cost of the required nondestructive inspection techniques.

Irradiation Studies

W. R. Martin

Postirradiation Examination of HFIR Fuel Element 49-I (R. W. Knight, A. E. Richt)

Irradiated fuel element 49-I was analyzed in the High Radiation Level Examination Laboratory (HRLEL) to determine dimensional stability during irradiation. Figure 20.1 shows top and side views of the element. In general, the element looked good; there was no apparent oxide spalling.

The fuel element operated for 2319 Mwd and was moved to the HRLEL 9 months after removal from the reactor. The average temperature of the element in the HRLEL was 95°C; the minimum temperature was 89°C, and the maximum temperature was 99°C. Figure 20.2 is a top view of the element with back lighting; no adverse oxide buildup or blisters were apparent.

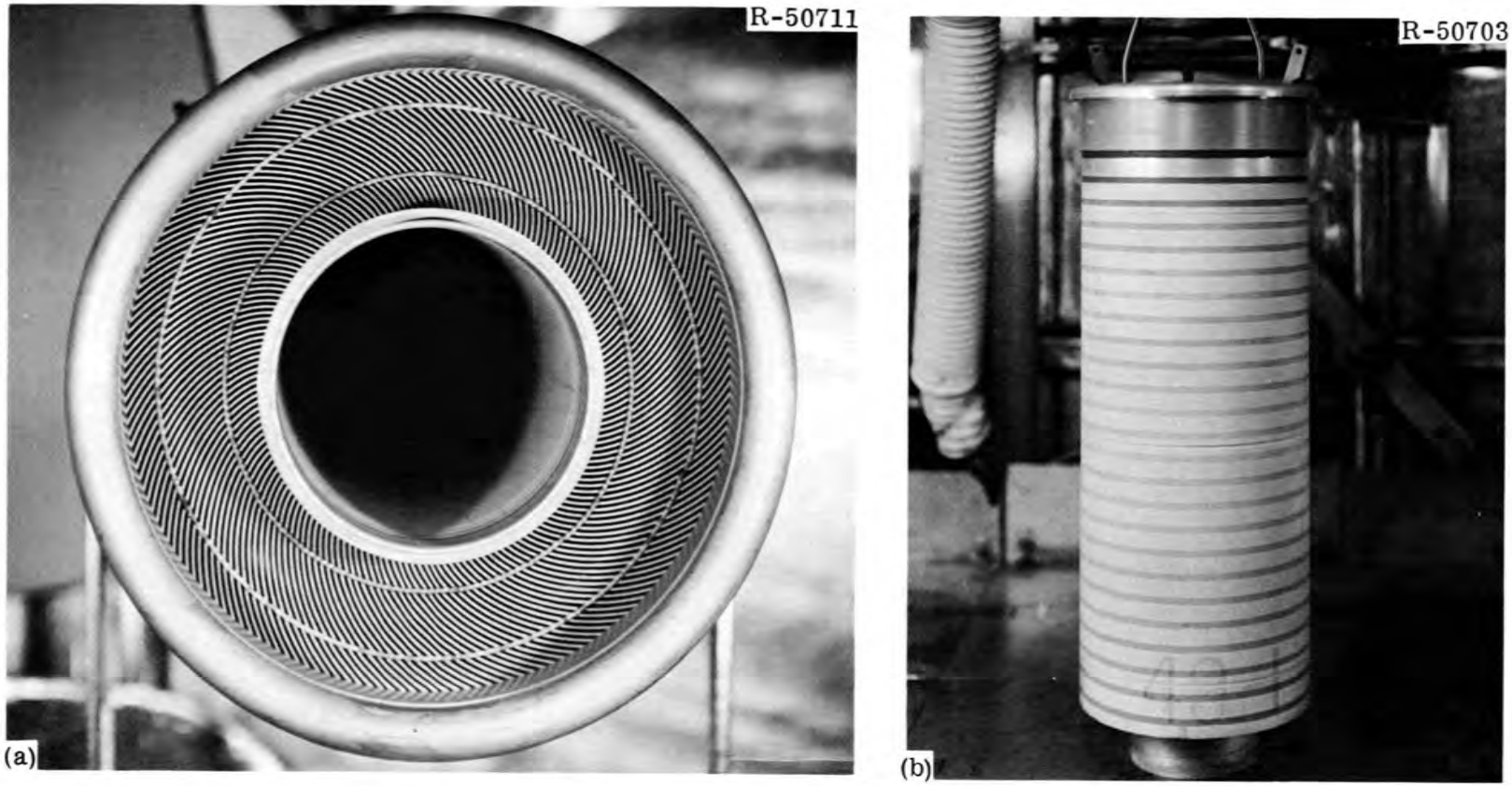

Fig. 20.1. Top and Side Views of Irradiated High Flux Isotope Reactor Fuel Element 49-I. (a) Top and (b) side view.

R-50710

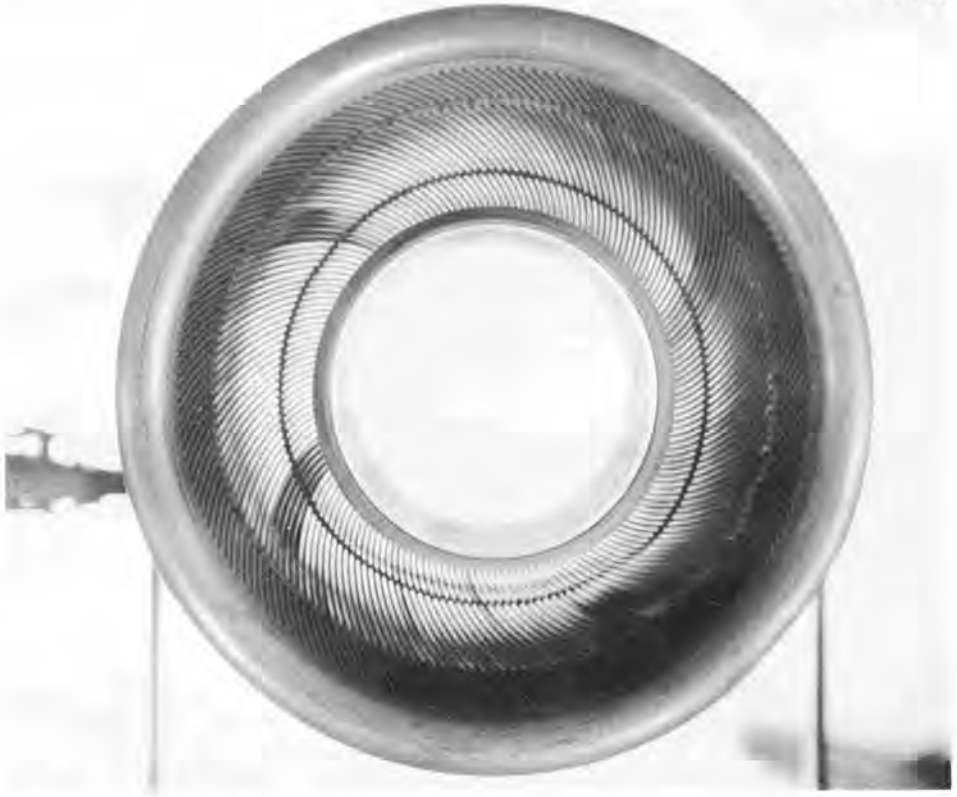

Fig. 20.2. Top View of Irradiated Fuel Element 49-I with Back Lighting.

The channel spacings of the fuel element were probed in four groups of five channels. The channels probed can be seen in Fig. 20.2. The results of this probing can be seen in Table 20.1. The differences shown in the table indicate a measure of the oxide buildup; no channels were out of specification.

Three other dimensions were measured, the inside and outside diameters and the shoulder-to-shoulder length of the inner end fittings. The results of these measurements are shown in Table 20.2.

The dimensions shown in Table 20.2 show a greater variation than was apparent on fuel element 5-I (ref. 1); however, fuel element 5-I operated only 2046 Mwd, and the average temperature was only 55°C in the HRLEL. The increased variability shown in the table may be real or may indicate the increased difficulty in taking the measurements. Taking the dimensions at face value, the shoulder-to-shoulder length is out of

Table 20.1. Measurements of Channel Spacing in High Flux Isotope Reactor Fuel Element 49-I

	Channel Spacing (in.)			
	As Manufactured		When Examined in HRLEL[a]	Difference
	All Channels	20 Channels	20 Channels	
Element overall grand average	0.0503	0.0501	0.0483	−0.0018
Maximum spot average	0.0530	0.0527	0.0508	−0.0019
Minimum spot average	0.0470	0.0476	0.0461	−0.0015
Maximum local	0.0570	0.0540	0.0540	
Minimum local	0.0450	0.0455	0.0415[b]	

[a]High Radiation Level Examination Laboratory.

[b]Scale buildup on probe fell off at minimum point, reprobed at 0.0470.

Table 20.2. Dimensional Comparison of Fuel Element 49-I

Location	Dimension (in.)		
	As Manufactured	Irradiated	Difference
Shoulder-to-shoulder length of inner end fittings	27.937	27.930	−0.007
Outside diameter			
Top	10.5925	10.5988	+0.0063
Middle	10.5925	10.5922	+0.0067
Bottom	10.5925	10.5961	+0.0036
Inside diameter			
Top	5.0735	5.0776	+0.0041
Middle	5.0735	5.0732	−0.0003
Bottom	5.0735	5.0707	−0.0028

specification by 0.002 in., and the outside diameters at top and middle are out of specification by 0.0013 and 0.0017 in., respectively.

Evaluation of this fuel element will continue. Fuel plates are presently being removed for evaluation of burnup, core swelling, and oxide thickness.

Evaluation and Design of Cermet Fuel Plate for Irradiation Experiments in HFIR (M. M. Martin)

Our objective is to determine those factors that influence the performance of Al-clad UAl_x and U_3O_8 dispersions in the ATR and HFIR at fission densities of up to 2.5×10^{21} fissions/cm^3. An experimental facility that would allow this maximum fission density to be achieved in five reactor cycles is being designed for the reflector region of the HFIR. Each experiment will consist of 18 uninstrumented plates and 3 instrumented plates. Temperatures will be measured by means of thermocouples inside the instrumented plates; the other plate temperatures will be calculated.

Discussions with Idaho Nuclear Corporation on May 27, 1970, have permitted us to integrate our experiments more properly in support of ATR cycle extension. As a result of these talks, we fully defined and agreed upon the core compositions for the first capsule for irradiation in the HFIR. The test plates are described in Table 20.3.

The two-number indexing scheme for the reference irradiation position in Table 20.3 identifies the location of the plates in the VXF-17 reflector hole of the HFIR. The first number gives the radial column (0 to 3) with respect to the center of the active reactor core; the second number gives the vertical orientation from top to bottom (1 to 6). The unperturbed thermal-neutron flux in VXF-17 is greatest near the 03–04 plate and smallest for both 31 and 36 plates, since the vertical flux pattern is nearly a symmetrical distribution about the horizontal midplane of the reactor.

The differences between Table 20.3 and the tentative capsule loading we previously reported[1] involve the distribution of fuel particle sizes (plates 21, 24, and 25), substitution of enriched UAl_x for depleted UAl_x (plate 24), and substitution of a dispersion of 24 wt % α Al_2O_3 in Al

Table 20.3. Description of Test Cermet Fuel Plates for the First Capsule to be Irradiated in the High Flux Isotope Reactor to a Target Fission Density of 2.5×10^{21} fissions/cm^3 (Maximum for UAl_x-Bearing Plates)

Reference Irradiation Position	Type of Test Plate[a]	Core Composition[b] (wt %)	Core Composition[b] Type of Dispersoid	^{235}U Enrichment in Fuel Particle (wt %)	^{235}U Loading Total (g)	^{235}U Loading Volumetric Core Composition (g/cm^3)	Distribution of Fuel Particle Sizes Upper Range (μm)	Distribution of Fuel Particle Sizes Diameter < 44 μm (wt %)
11	Mini[c]	52	Arc-cast UAl_x	0.2	0.002	0.00	44–149	25
21	Mini[d]	53	Arc-cast UAl_x	0.2	0.002	0.00	44–149	25
31	Mini[d]	54	Arc-cast UAl_x	0.2	0.002	0.00	44–149	25
12	Mini	47	High-fired U_3O_8	93.2	1.105	1.42	44–88	10
22	Mini	50	Burned U_3O_8	93.2	1.105	1.42	44–88	10
32	Mini[c,e]	51	Arc-cast UAl_x	93.2	1.012	1.30	44–149	25
01–02	Instrumented	47	High-fired U_3O_8	93.2	2.432	1.42	44–88	10
13	Mini	40	High-fired U_3O_8	93.2	0.887	1.14	44–88	10
23	Mini	42	Burned U_3O_8	93.2	0.887	1.14	44–88	10
33	Mini	53	Arc-cast UAl_x	0.2	0.002	0.00	None	100
14	Mini	53	Arc-cast UAl_x	93.2	1.012	1.30	44–149	25
24	Mini[c]	52	Arc-cast UAl_x	93.2	1.012	1.30	44–149	25
34	Mini	53	Arc-cast UAl_x	93.2	1.012	1.30	None	100
03–04	Instrumented	44	High-fired U_3O_8	93.2	2.226	1.30	44–88	10
15	Mini	63	Arc-cast UAl_x	93.2	1.253	1.61	44–149	25
25	Mini[d]	64	Arc-cast UAl_x	93.2	1.253	1.61	44–149	25
35	Mini	63	Arc-cast UAl_x	93.2	1.253	1.61	None	100
16	Mini	40	High-fired U_3O_8	0.2	0.002	0.00	44–88	10
26	Mini	40	High-fired U_3O_8	0.2	0.002	0.00	44–88	50
36	Mini	24	Alpha Al_2O_3		0.000	0.00	149–44	> 50
05–06	Instrumented[f]	51	High-fired U_3O_8	93.2	2.757	1.61	44–88	10

[a] Cladding is type 6061 Al alloy.

[b] Matrix is type 101 Al alloy.

[c] Plates hot rolled to final gage.

[d] Plates cold rolled 40% in thickness to final gage.

[e] Plates may be pressed after hot rolling to lower fabricated void content.

[f] Maximal operating core temperature of 150°C for the capsule will occur in this plate.

for depleted U_3O_8 (plate 36). We are considering using α Al_2O_3 in the filler section of HFIR fuel plates to reduce blistering during fabrication. Our expected accomplishment remains unchanged.

We formulated an experimental review procedure for the design and construction of our proposed irradiation capsule:

1. conceptual design, including preliminary drawings and flow diagrams;
2. safety and/or hazards analysis based on ORNL's Experiment Review questionnaire;
3. determination of quality assurance (QA) levels by experimenter, his QA coordinator, and General Engineering (GE) design personnel including GE QA coordinators as needed;
4. review by the Operations Division;
5. meeting to resolve any differences on experiment and QA levels;
6. approval or disapproval by the Operations Division for the conceptual design and QA levels;
7. review and either approval, conditional approval, or disapproval by ORNL's Reactor Experimental Review Committee (RERC);
8. review and approval of the QA levels by the QA Director;
9. final design;
10. fabrication plus installation of auxiliary equipment;
11. completion and/or revisions to Experiment Review questionnaire;
12. QA audits by Division QA coordinator and perhaps by Laboratory QA staff;
13. review by Operations Division;
14. review by RERC;
15. insertion of capsule.

The design and quality assurance for the experiment have progressed to step 4 above. The heat transfer, radioactivity, and hazards and shielding sections of the Experimental Review questionnaire are near completion. Since the Operations Division has not determined the necessary safety tie-ins to the HFIR, if any, and what effect the experiment will have on the reactivity of the HFIR, these portions of the heat transfer and hazards sections of the questionnaire have not yet been evaluated. We anticipate that capsule construction, step 10 above, will

begin in August. Our goal for inserting the capsule into the reactor is October.

Development of a HFIR Core with Increased Fuel Loading

W. R. Martin

Modifications and Improvements to HFIR Fuel Plates (R. W. Knight)

During the past year Texas Instruments, Inc., manufactured every other lot of fuel plates for the outer annulus of the HFIR element with a clearance fit of 0.005 in. between frame and compact rather than the 0.003- to 0.007-in. shrink fit used in the reference process. To date the blister rate has not changed due to the clearance fit, and assembly time was shortened.

Eight lots of fuel plates using burned U_3O_8 rather than the high-fired U_3O_8 were manufactured according to the HFIR reference process. No problems were encountered in manufacturing these fuel plates. Permission was requested of the Reactor Safeguards Committee to use six inner-annulus and six outer-annulus fuel plates in a fuel assembly for evaluation of fuel element irradiation performance.

Dummy fuel plates were manufactured with additions of Al_2O_3 in the filler section of the fuel plate core. The addition of the Al_2O_3 increased the void volume of the filler section about 2%. With rectangular cores fabricated from Al powder, one can expect approximately 37.5% rejection. None of the 72 plates rolled with this addition were rejected for blisters. Further work with this material will include fabrication of samples for studies of irradiation damage.

Fabrication Development

W. R. Martin

Void Content of HFIR Fuel Plates (M. M. Martin)

We determined the density of three groups of inner-annulus and three groups of outer-annulus HFIR fuel plates fabricated at Texas

Instruments, Inc., to establish the level and reproducibility of void concentration in the ^{235}U-bearing region of the fuel core. The three groups for each annulus contained the following replicate composites: (1) 16 standard plates from 10 production lots, (2) 14 experimental plates (one production lot) with increased fuel loading as high-fired U_3O_8, and (3) 14 experimental plates (one production lot) with increased fuel loading as burned U_3O_8. We examined a total of 88 plates.

All plates were manufactured in accordance with standard HFIR processes except for the U_3O_8 content. The inner- and outer-annulus plates with increased fuel loading contained 35 and 25% more ^{235}U, respectively, than the standard fuel cores. As described more fully elsewhere,[2] the increase in U_3O_8 content caused little difficulty in fabrication and inspection operations at Texas Instruments, Inc.

Figure 20.3 summarizes the results of our measurements of density and subsequent calculations of void volume. As expected from previous measurements[3] on plates fabricated at ORNL, the void content of the fueled region of the core depends upon the type and concentration of the U_3O_8 dispersoid. For comparison, recent data[4] on HFIR fuel plates fabricated at ORNL are included in Fig. 20.3. There was exact agreement for plates that contain burned U_3O_8 fabricated at ORNL and at Texas Instruments, Inc., but the commercial product with high-fired U_3O_8 contained about 0.7 vol % less voids. Perhaps the difference results from the use of three batches of high-fired U_3O_8. We plan to investigate this possibility.

The void concentrations in groups of plates that contained high-fired and burned U_3O_8 were very uniform, as shown by the ranges indicated in Fig. 20.3. The total range for the 14 plotted averages was less than ±0.5 vol %. The four groups composed of a single production lot of plates fabricated at Texas Instruments, Inc., showed minimal variations in void content. An estimate of the standard deviation for a plate within one of the four groups, which applies uniformly to the average void contents for that group, is ±0.064 vol % with 52 degrees of freedom. The standard deviation of two groups fabricated at Texas Instruments, Inc., of ten production lots each, however, was only ±0.151 vol % with 30 degrees of freedom. We conclude that the void content of HFIR fuel

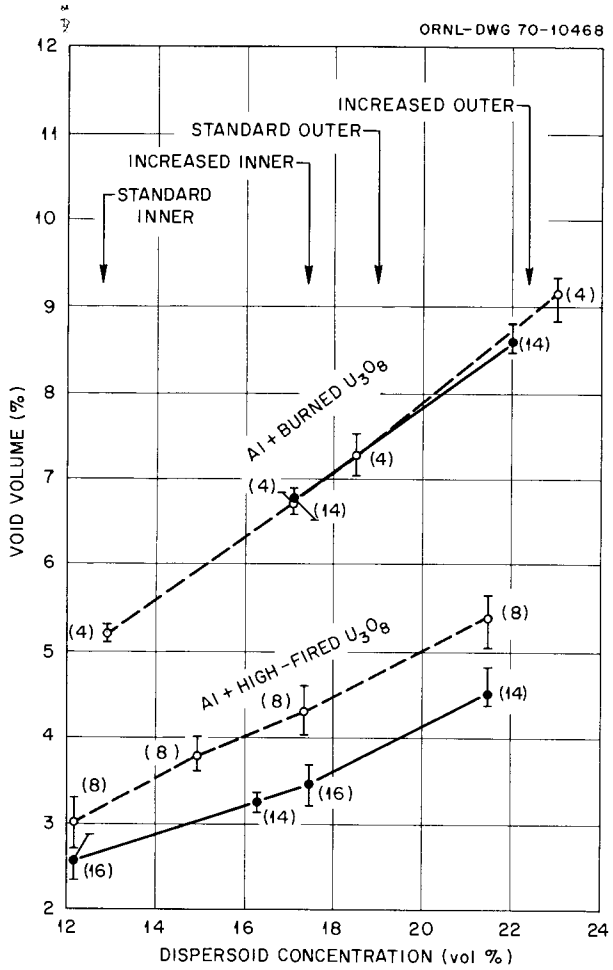

Fig. 20.3. Effect of Dispersoid Concentration on Void Volume in Fueled Section of Experimental Fuel Plates for High Flux Isotope Reactor. Solid and broken lines denote plates fabricated at Texas Instruments, Inc., and ORNL, respectively. Numbers in parentheses indicate the number of replicate plates.

plates fabricated at Texas Instruments, Inc., can be predicted to a precision of better than ±0.5 vol % about the average void concentration established for that particular production plate. Since fabrication voids play an important role in accommodating fission products,[5] we believe the addition of a void requirement to the specification would be a valuable procedure for quality control.

Deformation Behavior of Shaped Fuel Cores During Rolling of Aluminum Dispersion Fuel Plates (J. H. Erwin)

In a continued effort to solve problems that confront fabricators of roll-bonded fuel plates, we examined the deformation of shaped fuel

cores, which are sometimes used to prevent the excessive concentration of fuel that accompanies thickening of the core ends or "dogboning." We hot rolled at 490°C standard HFIR duplex billets containing a 46 wt % U_3O_8-Al core and a simulated core of wrought type 2219 Al alloy of identical geometry and examined the lengthwise cross section after each consecutive rolling reduction. We noted progressive changes in thickness from that of the original core, blistering, and cracking. For comparison with unshaped cores, we arbitrarily selected cores shaped on the leading and trailing ends to either a 1/8- or 1/2-in. radius, which extended 0.070 in. down the edges, on all corners tangent with the surface.

The deformation of fuel cores that are stronger than the cladding (type 2219 Al alloy) differs significantly from that of similar cores that have strengths more nearly equal to that of the cladding material (46 wt % U_3O_8-Al). For both types of cores, the void in the billet assembly as a result of the shaped ends is filled during billet reduction by a combination of sinking of the cover plate and swelling of the end of the fuel core. After the void is filled by a few roll passes, all parts of the fuel core, except the extreme ends, are reduced in thickness in about constant proportion. At the core end, the reduction differs with material strength. The ratio of end thickness (0.010 in. from original core end) to the average thickness for each of the fuel cores as a function of reduction is presented in Fig. 20.4. The curves for the two shaped cores of each material are parallel, differing only in the intercept that is the difference in thickness of the two radii used. From these observations, we conclude that shaping or reduction in core thickness is useful only in the vicinity of the dogbone formation, which is limited to the extreme end of the core, and that necking, as reported by some fabricators of ATR fuel elements, is, perhaps, the uniform reduction of shaped cores adjacent to the dogbone end development shown in Fig. 20.4.

No blisters were observed on the plates that contained the 46 wt % U_3O_8-Al compacts; but, of the plates that contained cores simulated with type 2219 Al, the shaped cores and a majority of the rectangular cores blistered at the core ends. The ability of powder-metal

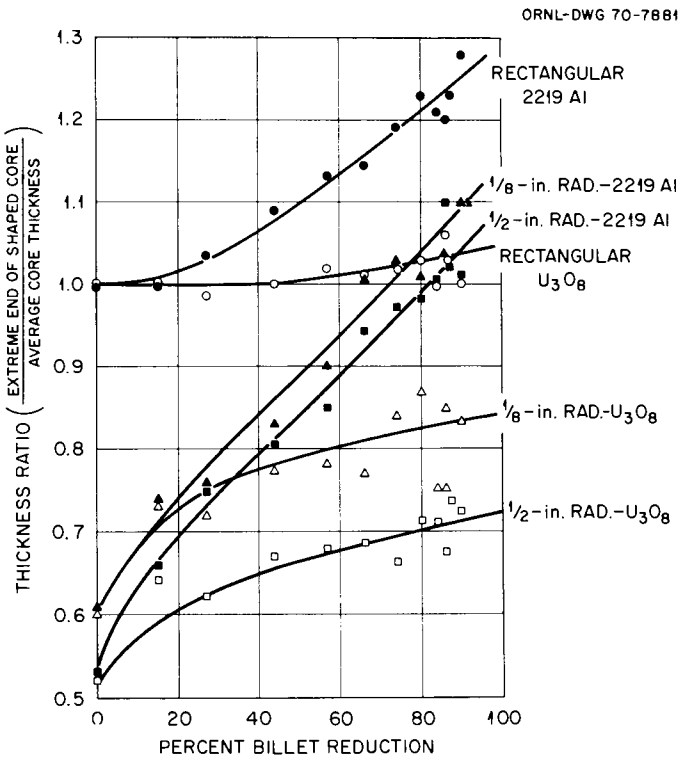

Fig. 20.4. Effect of Rolling on Ratio of Core End Thickness to Average Core Thickness.

cermets to accommodate trapped air without blistering has been recognized previously.[6]

Development of Nondestructive Inspection Techniques

R. W. McClung

Radiation Scattering (B. E. Foster, S. D. Snyder)

Our studies continued on the use of scattered and fluorescent radiation for measuring the thickness of Al cladding on fuel plates. We established a preliminary rough calibration of the thickness of type 1100 Al on a U metal base versus count rate. For the technique now being studied, the Al attenuates the 18-kev x ray that is produced by the excitation of the depleted U by the 38-kev x ray from our ^{147}Pm source. The range of Al thicknesses used is from 0.0003 to 0.0307 in. In the range of Al thicknesses from 0.001 to 0.023 in., there is about a 5%

change in count rate per 0.001-in. change in Al thickness. Above 0.023 in. of Al, the sensitivity decreases to about a 2% change in count rate per 0.001-in. change in Al thickness. Refinement of this calibration by the use of smaller increments of change of Al thickness has been temporarily interrupted by a malfunction of the 1600-channel analyzer.

Establishment of Standards for Burned U_3O_8 and High-Loaded, High-Fired U_3O_8 HFIR Plates (B. E. Foster, S. D. Snyder)

We completed the x-ray attenuation scanning at both 50 kilovolts constant potential (kvcp), 2.5 ma and 60 kvcp, 2.5 ma of the sample areas of the following eight HFIR fuel plates: one inner- and one outer-annulus plate containing high-fired U_3O_8 in accordance with the standard HFIR loading; one inner- and one outer-annulus plate loaded to 134.95% of standard; and four similar plates loaded with burned U_3O_8. The samples were machined from the plates and submitted for determination of U content by chemical analysis. Instead of machining the usual 2-in.-long strips, we machined 4-in.-long strips and divided each strip into two 2-in.-long samples. This provided us with a duplicate set of samples. The results of chemical analysis will be used to establish the calibration curves of U content versus x-ray attenuation for the two types of U oxide over a wide loading range. In turn, these calibration curves will be used in conjunction with the relationship of Al thickness to x-ray attenuation to design the contoured Al standards necessary for inspecting for fuel homogeneity in the plates that contain burned oxide and the high-loaded, high-fired oxide.

Notes

1. M. M. Martin and W. K. Crowley, Fuels and Materials Development Program Quart. Progr. Rept. March 31, 1970, ORNL-4560, pp. 222–224.

2. R. W. Knight, M. M. Martin, and J. H. Erwin, Fuels and Materials Development Program Quart. Progr. Rept. March 31, 1970, ORNL-4560, pp. 224–225.

3. M. M. Martin, Metals and Ceramics Div. Ann. Progr. Rept. June 30, 1967, ORNL-4170, pp. 177–179.

4. M. M. Martin and W. R. Martin, Fabrication Voids in Aluminum-Base Fuel Dispersions, ORNL-4611 (in press).

5. A. E. Richt and M. M. Martin, Fuels and Materials Development Program Quart. Progr. Rept. Sept. 30, 1969, ORNL-4480, pp. 218–219.

6. J. H. Erwin, Metals and Ceramics Div. Ann. Progr. Rept. June 30, 1969, ORNL-4470, p. 105.

21. TECHNICAL ASSISTANCE IN PROCUREMENT OF FUEL ELEMENTS

G. M. Adamson, Jr. W. R. Martin

The purpose of this program is to provide technical assistance and inspection surveillance to the U.S. Atomic Energy Commission (AEC) Division of Reactor Development and Technology (RDT) in its effort to procure fuel and neutron-absorber components from commercial sources for research reactors owned by the AEC.

Technical Assistance in Solving Manufacturing and Inspection Problems

Embedment of Abrasive Particles in Surface of Type 6061 Al Plate (J. H. Erwin)

Various possibilities are being examined to explain why some fuel plates have small holes or cracks in the cladding that expose the fuel composite to the reactor coolant.

Samples of Al plate about $2 \times 3 \times 1/4$ in. in the T-6 aged, fully annealed, hot-, and cold-rolled conditions were sanded with 100-grit Al oxide and with 60- and 100-grit SiC belts to produce a metallic luster on the surface. The sanding was followed by etching for 30 sec in Oakite 160 and pickling in HNO_3.

All plates, regardless of temper or heat-treatment condition, contained embedded abrasive. These particles of abrasive, from less than 0.003 to 0.012 in. in diameter, could completely penetrate the thin cladding over the "dogbone" region of an Advanced Test Reactor plate. If the embedded particle were removed during reactor operation, the resulting penetration through the cladding would expose the core of the fuel plate to the reactor water and allow the release of fission products to the coolant stream.

CLADDING AND OTHER STRUCTURAL MATERIALS

22. BEHAVIOR OF REFRACTORY MATERIALS UNDER IRRADIATION

G. M. Watson[1] G. W. Keilholtz[1]

The purpose of this program is to evaluate the effects of high fast-neutron fluences at temperatures up to 1100°C on the properties of refractory nuclear materials for both space and civilian power reactors. The program was terminated on June 30, 1970. The status of each of the three tasks of the program is given below.

Irradiation Damage to Nonfissionable Refractory Materials

R. E. Moore[1] D. A. Dyslin[2] H. E. Robertson[1]

The most recent work under this task involved an investigation of fast-neutron damage to carbides of Ti, Zr, Ta, Nb, and W at 60 to 1100°C.[3] Reports describing this work in detail and describing a damage model for carbides will be issued soon.

Effects of Irradiation on LMFBR Fuels

R. E. Moore[1] D. A. Dyslin[2] H. E. Robertson[1]

This task was aimed at evaluating the effects of the generation of He gas through the $^{14}N(n,\alpha)^{11}B$ reaction within nitride fuels.[3] A low-temperature (about 150°C) assembly and a high-temperature (about 1000°C) assembly that contained depleted fuels were irradiated in the J-12 core position of the Engineering Test Reactor. The depleted fuel specimens will be examined under another program.

Fast-Neutron Effects on Materials for Neutron Absorption in Fast Reactors

R. E. Moore[1] D. A. Dyslin[2] H. E. Robertson[1]

This task was aimed at the development of B_4C as a neutron absorber for control of reactivity in fast reactors.[3] The work will continue after July 1, 1970 as part of another program.

Notes

1. Reactor Chemistry Division.
2. General Engineering Division.
3. G. M. Watson and G. W. Keilholtz, Fuels and Materials Development Program Quart. Progr. Rept. March 31, 1970, ORNL-4560, pp. 235-236.

23. JOINING RESEARCH ON NUCLEAR MATERIALS

J. R. Weir, Jr. G. M. Slaughter

The purpose of this program is to gather the fundamental and applied data needed to understand the weldability of materials that are either being considered or are currently used for nuclear applications. Fundamental studies are concerned with the effects of minor constituents on the behavior of weldments. We are especially interested in the austenitic stainless steels and the alloys that are rich in Ni, such as Incoloy 800 and Inconel 600. In addition, a modest program concerned with the influence of weld defects will provide reference results in this much-talked-about but little-investigated field.

As a result of this broad-based program, we plan to suggest modifications in both alloy composition and procedures needed to improve the quality of weldments used in the various activities of the Commission.

The Effect of Minor Variations in Chemical Composition on Weldability

Our continuing investigation of the effect of minor variations in those elements usually present in structural material has included Inconel 600, Incoloy 800, and stainless steel.

Weldability of Incoloy 800 (D. A. Canonico, W. J. Werner)

The welds made in 1/8-in. commercial Incoloy 800 sheet using experimental heats of Incoloy 800 as the filler metal were tensile tested at 650°C. The welding conditions and tensile properties at room temperature were discussed previously.[1,2] The results of these tests at 650°C are given in Table 23.1, and the data for the tests at room temperature are also included. Welds were also made from an electroslag-remelted heat of commercial Incoloy 800 and Inconel 82T, a commercially available filler metal recommended for joining Incoloy 800.

All of the tensile failures, except for the weld made with Inconel 82T, failed in the weld metal at strength levels considerably

Table 23.1. Results of Tensile Tests on Incoloy 800 Welds Made with Experimental and Commercial Filler Metals

Weld Identity	Nominal Chemical Analysis of Filler Metal, wt %			Tensile Strength, psi				Elongation in 3 in., %	
				Yield		Ultimate			
	Al	Ti	Other	Room Temperature	650°C	Room Temperature	650°C	Room Temperature	650°C
				× 10^3	× 10^3	× 10^3	× 10^3		
143	0.38	0.15		27.1	26.0	70.2	44.9	23.7	13.5
144	0.38	0.60		35.2	26.3	73.5	46.3	25.5	14.7
145	0.15	0.38		21.9	25.7	72.1	42.9	24.8	11.9
146	0.60	0.38		27.5	25.7	70.7	41.8	24.1	8.8
175	0.15	0.15		21.4	25.3	72.3	45.7	23.7	14.9
176	0.38	0.38		25.7	24.8	71.5	44.4	26.5	15.3
177	0.60	0.60		20.0	23.8	71.6	47.2	28.5	17.5
187	0.38	0.38	0.010 P	30.2	25.1	73.3	44	25.4	13.9
189	0.38	0.38	0.02 P	38.2	24.2	70.6	47.6	23.9	17.0
191	0.38	0.38	0.015 P 0.015 S	25.6	25.3	66	43.6	17.4	13.8
Electroslag-remelted Incoloy 800				23.8	25.7	77.2	49.6	35.9	23.3
Inconel 82T				31.4	24.0	79.5	49.2	44.5	32.9

below those obtained at room temperature. The strength advantage of Inconel 82T at room temperature was not evident at 650°C. At the elevated temperature, the ultimate strength of the electroslag-remelted Incoloy 800 was similar to that of Inconel 82T. Further, the alloys with high Ti content, alloys 144 and 177, and the alloy that nominally contained 0.02% P, alloy 189, had ultimate strengths that approached that of the higher strength weld metals.

The yield strengths of all the welds were nearly identical; they ranged from 23,800 to 26,300 psi. These results of tests at 650°C in many instances were similar to those of tests at room temperature. However, some alloys – particularly alloys 144, 187, 189, and Inconel 82T – noticeably lost yield strength.

The ductility of the experimental alloys was low at 650°C. This tem-temperature corresponds closely with the minimum-ductility temperature reported by Werner.[3] The Inconel 82T alloy and the electroslag-remelted Incoloy 800 had the best ductility. The next best ductility was recorded for alloy 189, the alloy that nominally contained 0.02% P.

The specimens from this study are being prepared for metallographic examination.

Effect of Certain Minor Elements on the Ductility of Inconel 600 at Intermediate Temperatures (W. J. Werner, D. A. Canonico)

We are beginning to obtain data on the ductility of Inconel 600 at intermediate temperatures.[2] Our tensile tests are being run on an Instron Universal Testing Machine at a strain rate of 0.002 min^{-1} in Ar. The nominal compositions of the alloys for which we have tensile data are shown in Table 23.2. The ductility data that we have measured to date on these alloys are shown in Fig. 23.1.

Although there are not yet enough data available for an analysis of these alloys, a few general remarks are pertinent. First, it is evident that these alloys exhibit a minimum in ductility at intermediate temperatures. The ternary alloy (without minor alloying additions) behaves similarly to the Incoloy 800 ternary alloy;[3] that is, it does not recover ductility at elevated temperatures. This appears also to be the case of alloy CVO-148, which nominally contains the minor elements, except

Table 23.2. Composition of Inconel 600 Alloys Tested to Date

Alloy	Composition, wt %							
	Fe	Cr	C	Cu	Mn	Si	S	Ni
CVO-147	8	15.5						Bal
CVO-148	8	15.5	0.03	0.04	0.2	0.2		Bal
CVO-149	8	15.5	0.03	0.04	0.2	0.2	0.005	Bal
CVO-150	8	15.5	0.03	0.04	0.2	0.2	0.010	Bal

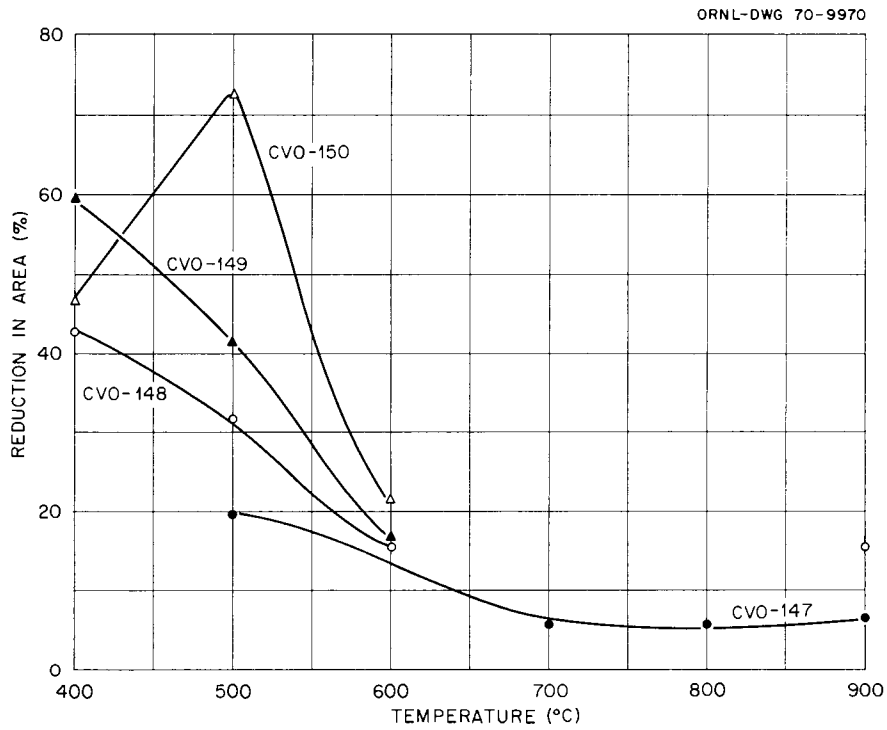

Fig. 23.1. Effect of Temperature on Ductility of Special Inconel 600 Alloys.

for S and P, present in commercial material. The other two alloys also exhibit poor ductility at intermediate temperatures. Whether they recover their ductility at elevated temperatures remains to be seen. The initial increase in ductility with increasing test temperature exhibited by alloy CVO-150 may very well be attributable to effects of strain aging.

Weldability of Stainless Steels (A. J. Moorhead, D. A. Canonico)

We continued our study of the effect of chemical composition on the quantity, morphology, and composition of secondary phases that may be present in primarily austenitic stainless steels. The interest in this program is primarily in the body-centered cubic second phase (ferrite) that has empirically been shown to be beneficial in reducing the tendency toward hot-cracking in austenitic weld metals. However, the mechanism of this beneficial effect has never been determined, and this determination is one of the goals of this program. Another second phase of interest is the body-centered tetragonal or martensitic phase. The transformation kinetics of these two phases are entirely different. However, there may be an important interaction between the two, and the mechanical properties of a welded structure may also depend on the presence (or absence) of martensite.

Previously,[4] we listed the nominal compositions of the initial alloys under study and presented some Magne-gage data for the as-cast and homogenized coupons. We also presented photomicrographs of homogenized specimens that were etched with Murakami's reagent to reveal ferrite and described a partitioning phenomenon that was observed during electron-beam microprobe analysis.[5]

Using the quantitative television microscope, we measured the ferrite content of specimens from the homogenized drop-cast bars. These data, the ferrite content predicted on the basis of the Schaeffler diagram, and the Magne-gage number for the same specimen are tabulated in Table 23.3. The quantitative television microscope measurements were taken on a representative 500× photomicrograph. Note, however, that ferrite content varies greatly in a given metallographic field and that the Schaeffler diagram is intended for predicting ferrite content in weld metal and should only be used as a rough guide for homogenized microstructures.

We produced the martensitic second phase by cold rolling 0.365-in.-thick cast-and-homogenized bars at room temperature to 0.250 in. thick (31.5% reduction) by a series of about 20 passes. No precautions were

Table 23.3. Indications of Ferrite Content of Experimental Stainless Steels in Homogenized Condition

Heat	Ferrite Content, %		Magne-Gage Number[c]
	Predicted[a]	Measured[b]	
5408	1	0.74	159[d]
5409	0	2.73	157
5410	7.5	2.72	157
5415	7	8.60	124
5416	8	1.43	157
5419	10	9.7	120
5420	6	4.7	153

[a]Predicted from Schaeffler diagram.

[b]Measurements taken on micrographs by means of quantitative television microscope.

[c]All readings were made with a No. 4 magnet at each of four locations on the side of the bar. The higher the number, the lower the magnetic strength and ferrite content.

[d]The magnet would not adhere to this specimen since its magnetic strength was so low.

taken to allow the bars to return to room temperature between passes. The Magne-gage was then used to indicate the quantity of martensite induced by stress in each bar. These data, along with corresponding data for hardness, are given in Table 23.4. An interesting feature of the hardness data is the softness of the bars after homogenization. Apparently, due to the relatively high purity of these alloys, the bars had an average Rockwell B hardness of 55. Similarly, heat-treated commercial alloys in the same composition range had Rockwell B hardnesses of about 80.

After the rolled bars were homogenized at 1150°C for 60 min in vacuum, they were cold rolled at a starting temperature of 0°C to 50% reduction in thickness. The bars were held in an ice bath between passes until their temperature stabilized. Chromel-P vs Constantan

Table 23.4. Magne-Gage and Hardness Data for Stainless Steel Bars Cold Rolled[a] at Room Temperature

Casting Heat	Magne-Gage Number[b]		Rockwell Hardness Number[c]	
	After Rolling	After Homogenization[d]	After Rolling (C Scale)	After Homogenization (B Scale)
5408	126	159[e]	28.4	46.9
5409	153	159[e]	25.4	48.2
5410	0[f]	159[e]	31.3	60.7
5411	159[e]	159[e]	26.6	48.5
5412	159[e]	159[e]	25.6	51.2
5415	99	143	29.5	63.4
5416	153	159[e]	28.0	51.3
5417	159[e]	159[e]	25.5	51.1
5418	159[e]	159[e]	25.6	52.8
5419	98	126	29.0	67.6
5420	143	152	27.2	59.2
5421	159[e]	159[e]	25.1	56.2
5422	159[e]	159[e]	23.8	56.6

[a] To 31.5% reduction in thickness in about 20 passes.

[b] All readings were made with the No. 4 magnet; the higher the number, the lower the content of magnetic phase.

[c] Each value is the average of four measurements.

[d] Homogenized 1 hr in vacuum at 1150°C after 31.5% reduction.

[e] Would not adhere.

[f] Would not pull away.

thermocouples (0.020 in. in diameter) capacitor-discharge welded to an edge of four of the bars were used to monitor the temperature rise during rolling. These couples were connected through an ice-bath reference junction to an oscillograph recorder. The temperature rise caused by working was measured during the first, middle, and last rolling passes. Magne-gage readings and metallographic specimens were taken after

25 and 50% reduction. The Magne-gage and peak temperature data are presented in Table 23.5. Note that these Magne-gage readings (Tables 23.4 and 23.5) are influenced not only by the ferrite present, as in Table 23.3, but also by the presence of martensite induced by stress in the cold-worked microstructures.

We began an investigation into the identification of the martensitic second phase by microscopic techniques. We found it difficult to distinguish between the martensite, the slip lines, and the mechanical

Table 23.5. Magne-Gage Readings and Peak-Temperature Data for Stainless Steel Bars Cold Rolled at 0°C

Heat	Magne-Gage Number[a]		Peak Temperature, °C		
	After 25% Cold Work	After 50% Cold Work	First Pass	After 25% Cold Work	After 50% Cold Work
5408	−3	−10[b]			
5409	144	118	c	16.8	24.0
5410	−10[b]	−10[b]			
5411	d	148			
5412	d	d			
5415	90	−10[b]			
5416	d	154	10.0	14.0	27.0
5417	d	d			
5418	d	d			
5419	108	103			
5420	146	144	3.6	18.3	22.0
5421	d	d	4.8	11.6	25.0
5422	d	d			

[a]All readings were made with a No. 4 magnet.

[b]Magnet would not pull away from bar.

[c]Thermocouple caught in rolls.

[d]Magnet would not adhere to bar.

twins by bright-field optical microscopy at magnifications up to 500×, as shown in Figs. 23.2 and 23.3. Therefore, we tried other techniques such as bright-field oil-immersion and phase-contrast microscopy at magnifications up to 1500×. These techniques enabled us to get a clearer picture of the morphology of these microstructures, as shown in Figs. 23.4 and 23.5. We are now investigating a magnetic-particle etching technique that may help improve our interpretation of these specimens.

Electron-beam and gas W-arc bead-on-plate welds were made on both annealed and 50% cold-worked coupons of the drop-cast heats 5408 to 5422 to produce specimens for a comparison of the ferrite content and morphology of welds in base metals both with and without martensite. The welding parameters used produced penetration of about 0.015 in. in the arc welds and about 0.030 in. in the electron-beam welds.

We received 16 additional 1-lb drop-cast bars that have nominal compositions (Table 23.6) similar to those of our initial heats 5409, 5410, 5411, 5420, and 5422 with intentional additions of varying percentages of S or C. Each bar was homogenized at 1150°C for 60 min in vacuum and cold rolled 31.5% at room temperature. These bars will be processed similarly to the 13 original bars to determine the effect of S and C on the formation of ferrite and martensite and on the weldability of these relatively pure alloys.

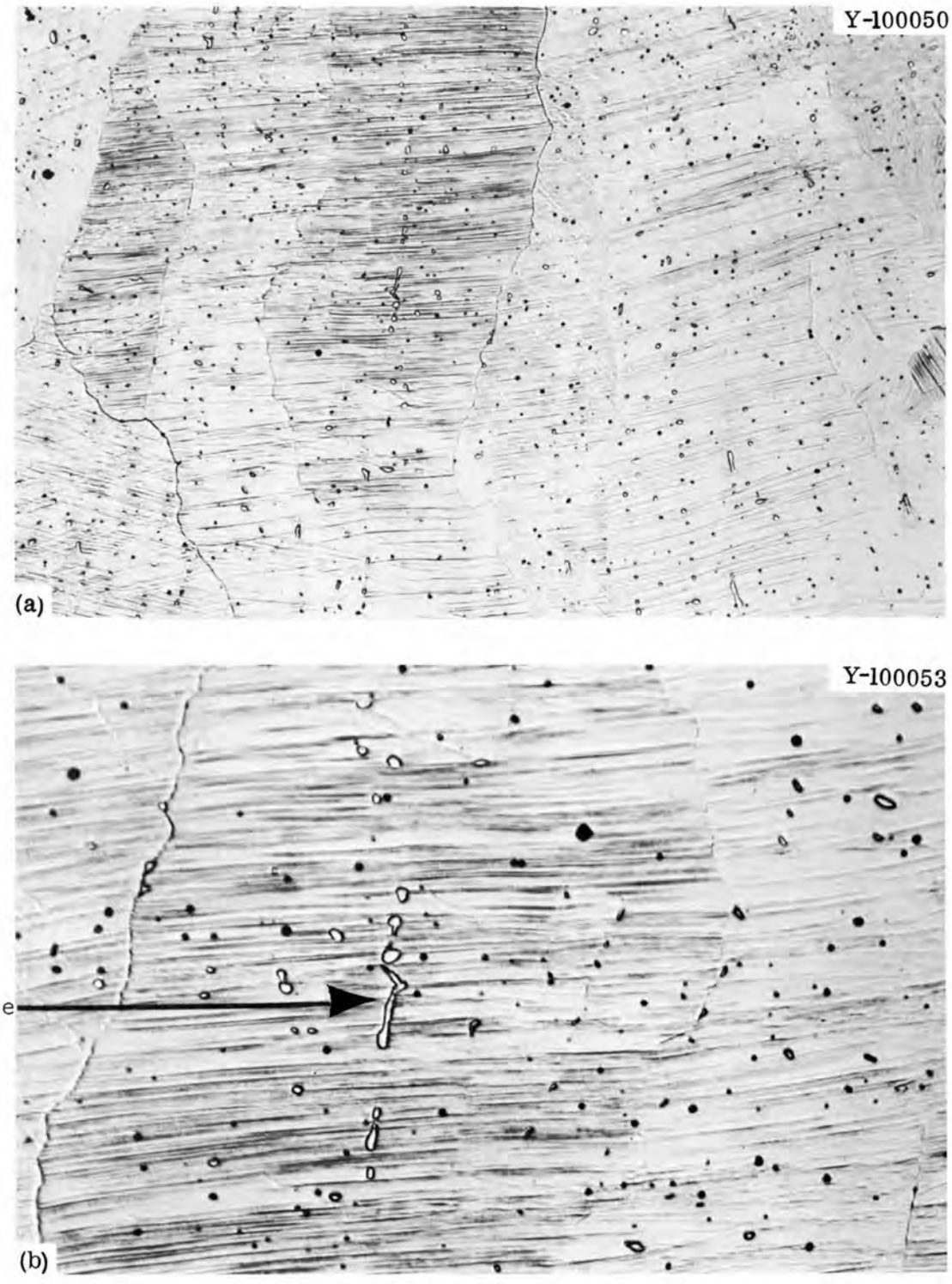

Fig. 23.2. Heat 5409 (Fe–11.9% Ni–18.9% Cr–4.8% Mn) after 31.5% Cold Work at Room Temperature. (a) Bright field, near side of bar in contact with rolls. 200×. (b) Bright field, near center of cross section. 500×.

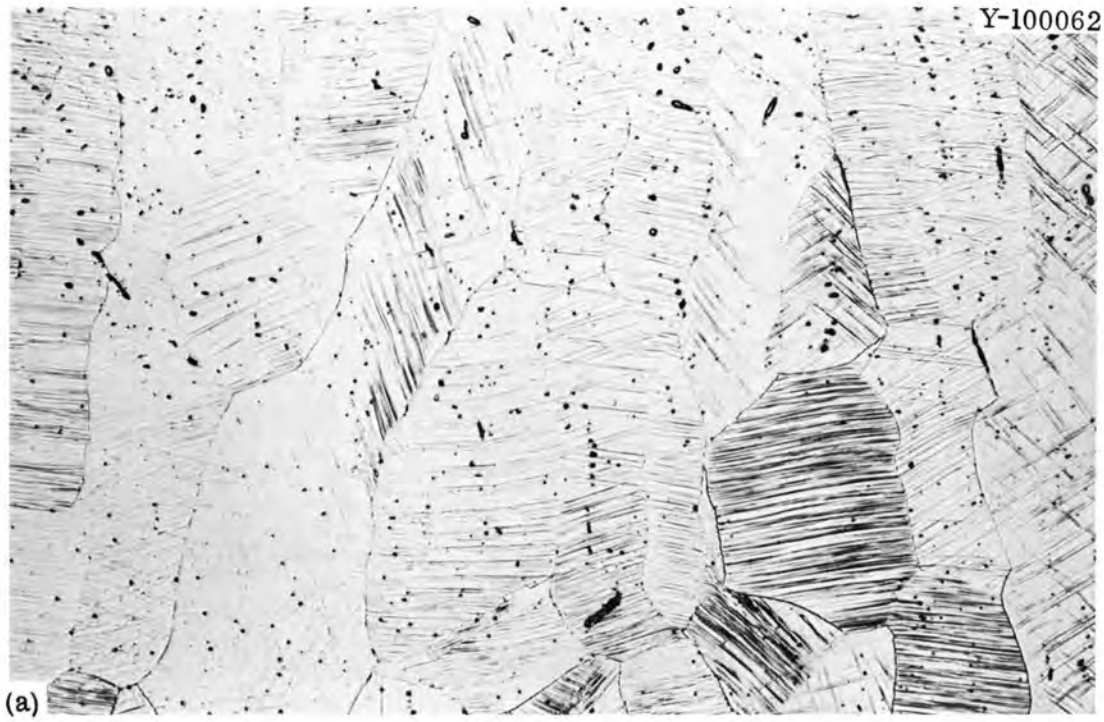

Fig. 23.3. Heat 5420 (Fe–15.3% Ni–23.3% Cr) after 31.5% Cold Work at Room Temperature. (a) Bright field, near side. 200×. (b) Bright field, near center. 500×.

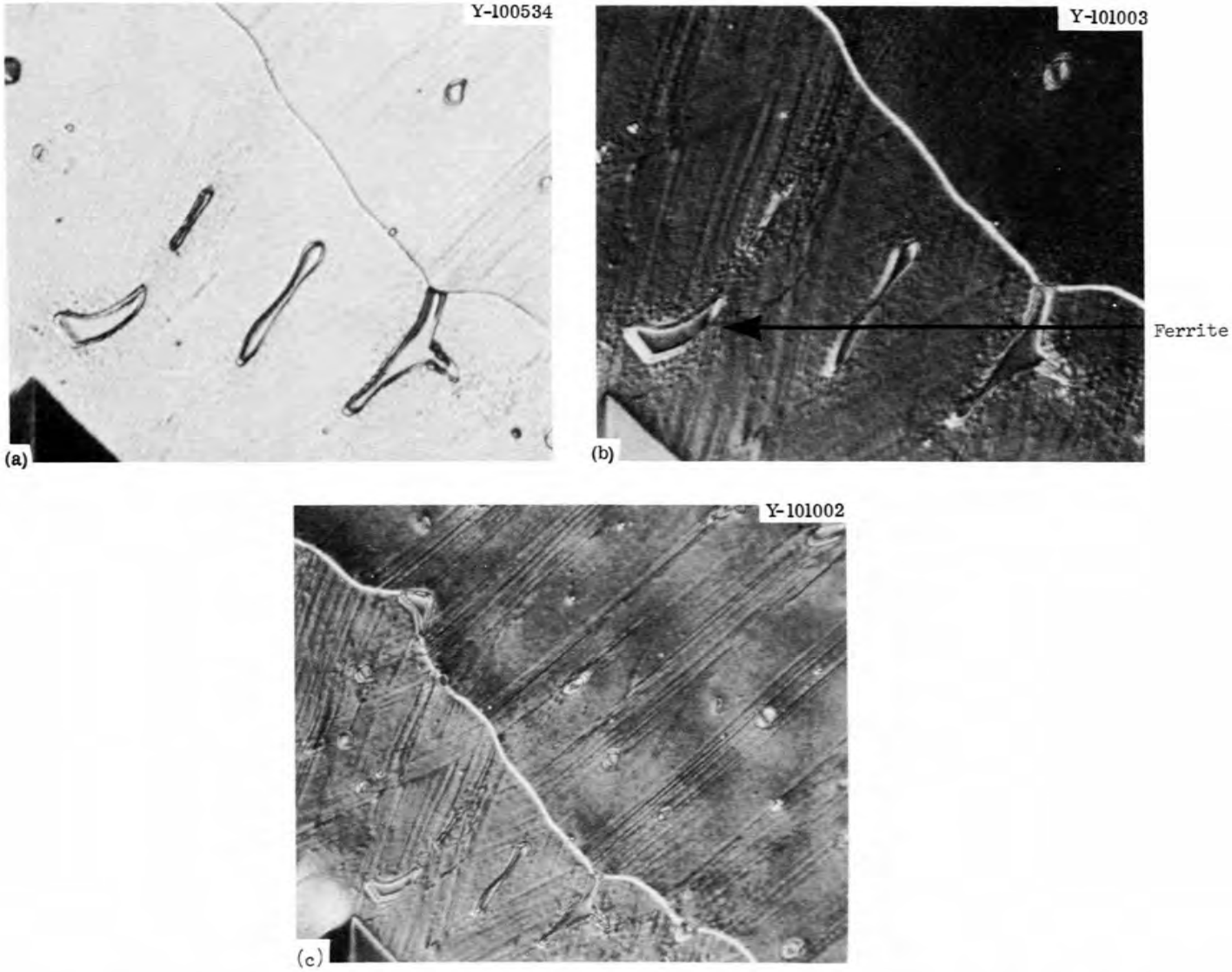

Fig. 23.4. Heat 5409 (Fe–11.9% Ni–18.3% Cr–4.8% Mn) after 31.5% Cold Work at Room Temperature. (a) Bright field. 1500×. (b) Phase contrast. 1500×. (c) Phase contrast. 750×.

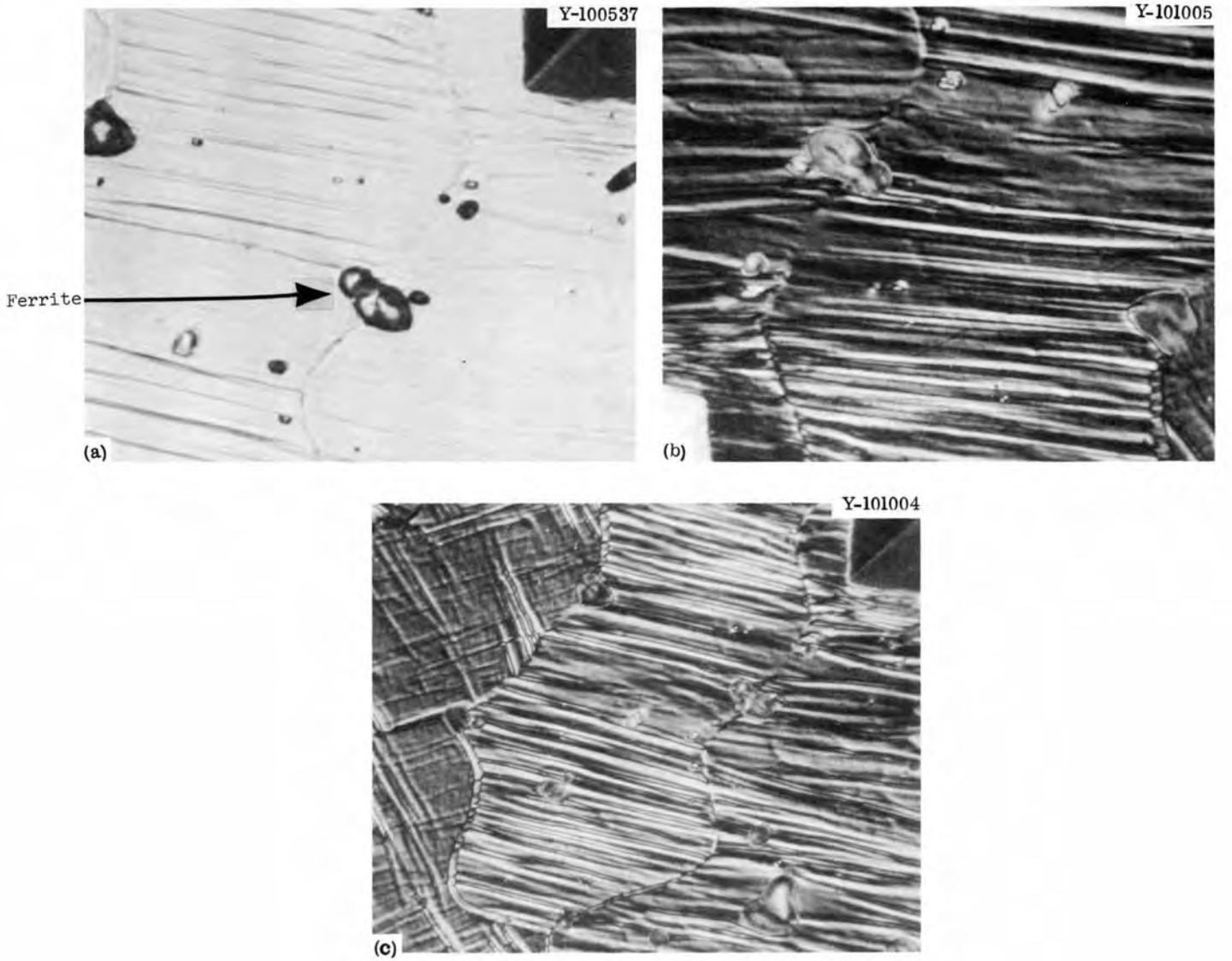

Fig. 23.5. Heat 5420 (Fe–15.3% Ni–23.3% Cr) after 31.5% Cold Work at Room Temperature. (a) Bright field. 1500×. (b) Phase contrast. 1500×. (c) Phase contrast. 750×.

Table 23.6. Nominal Compositions of Drop Castings

Heat	Composition,[a] wt %		
	Ni	Cr	S
5502[b]	10	19	
5534[c]	12	19	0.025
5535[c]	12	19	0.10
5536	10	19	0.025
5537	10	19	0.10
5538	10	19	0.30
5539	14	19	0.025
5540	14	19	0.10
5541	14	24	0.025
5542	14	24	0.10
5543	14	24	0.30
5544	16	24	0.025
5545	16	24	0.10
5546	16	24	0.30
5547	20	24	0.025
5548	20	24	0.10

[a]For all heats, the balance is Fe.

[b]Plus 0.04% C.

[c]Plus 5% Mn.

Notes

1. D. A. Canonico and W. J. Werner, Fuels and Materials Development Program Quart. Progr. Rept. Dec. 31, 1969, ORNL-4520, pp. 298–300.

2. D. A. Canonico and W. J. Werner, Fuels and Materials Development Program Quart. Progr. Rept. March 31, 1970, ORNL-4560, pp. 239–241.

3. W. J. Werner, An Investigation of the Effect of Certain Minor Elements on the Elevated Temperature Ductility of Incoloy 800, ORNL-4504 (March 1970). M.S. Thesis, the University of Tennessee, December 1968.

4. D. A. Canonico, A. J. Moorhead, and W. J. Werner, Fuels and Materials Development Program Quart. Progr. Rept. Dec. 31, 1969, ORNL-4520, pp. 300–303.

5. W. J. Werner and D. A. Canonico, Fuels and Materials Development Program Quart. Progr. Rept. March 31, 1970, ORNL-4560, pp. 243–244.

24. NONDESTRUCTIVE TESTING

W. O. Harms R. W. McClung

Our task is to develop new and improved methods of nondestructively testing reactor materials and components. We are studying various physical phenomena, developing instruments and other equipment, devising techniques, and designing and fabricating reference standards. Among the methods being studied for both normal and remote inspection are electromagnetics (with major emphasis on eddy currents), ultrasonics, penetrating radiation, and holography.

Electromagnetic Inspection Methods (Eddy Currents)

Solutions for Electromagnetic Induction Problems (C. V. Dodd, W. A. Simpson, C. C. Cheng,[1] W. E. Deeds[2])

We solved the problem of a coil above, below, or between an arbitrary number of conducting planes by means of a matrix method for finding the Green's functions of multiplane boundary-value problems. The matrix equations enable us to simplify the calculation of the unknown coefficients in a boundary-value problem. The explicit forms of the general Green's functions are obtained for axially symmetrical configurations of coil and conductor. We also made some calculations for those physical quantities of interest in eddy-current theory. Heat-flow solutions can also be readily obtained using the same technique. We are preparing a paper that describes in detail these advances and are working on computer programs that will calculate coil impedance, induced voltage, and the effect of defects for a coil near an arbitrary number of planes by means of the matrix method.

We used our computer programs to design a 1/2-in.-diam coil for operation with the phase-sensitive eddy-current instrument that will measure electrical conductivity to within ±0.05% for a lift-off variation of 0 to 0.020 in. We are obtaining materials with a low temperature coefficient of resistivity to use as standards for measurement of conductivity.

Ultrasonic Inspection Methods

Ultrasonic Frequency Analysis (H. L. Whaley, Jr., K. V. Cook, Laszlo Adler[2])

We are studying the spectral variations in a broadbanded ultrasonic pulse as a function of the nature of the acoustical discontinuity with which it has interacted. Such a study can lead to improvements in the characterization of hidden flaws in materials by ultrasonic inspection. Spectral analysis of ultrasonic pulses returned from reflectors of various types and orientations revealed systematic variations as a function of the size, shape, orientation, and position of the reflector. Analytical expressions that we derived successfully account theoretically for these variations.

General Case (Two Angles). — Previous experiments and analysis considered only a single angle (in a horizontal plane) to describe the relative orientation of transducer and reflector. This was possible because the design of the apparatus with which the experiments were performed allowed the axes of the transducer and reflector to be kept in the same horizontal plane. Should either axis not lie in this plane, an additional angle would be required to define the relative orientation. In general, a real flaw in a material would possess not one, but two, such angular components to describe its orientation with respect to the surface of the material. Therefore, it was necessary to generalize the technique in order to allow its application to randomly oriented flaws. A detailed analysis of the situation predicted that the size of the flat reflector, d, should be given by

$$d = \frac{v}{(2 \sin\theta + \frac{a}{D})\ \Delta f}\ , \qquad (24.1)$$

where v is the velocity of ultrasound in the material, D is the distance between the source and reflector, a is proportional to the radius of the source, Δf is the separation between adjacent interference peaks in the analyzed spectrum, and θ is the angle between the axis of the source and that of the reflector. This equation has exactly the same form as that

for the case of a single angle except that θ is now a composite angle that may be expressed in terms of a component θ_1 in the horizontal plane and a component θ_2 in a vertical plane by the expression

$$\theta = \sin^{-1} [\sin^2\theta_2 + \cos^2\theta_2 \sin^2\theta_1]^{\frac{1}{2}} . \qquad (24.2)$$

We thus have

$$d = \frac{v}{\{2[\sin^2\theta_2 + \cos^2\theta_2 \sin^2\theta_1]^{\frac{1}{2}} + \frac{a}{D}\} \Delta f} . \qquad (24.3)$$

Equation (24.3) was tested with data collected at various combinations of angles θ_1 and θ_2 at a 6-in. water path for an 0.281-in.-diam reflector. As can be seen in Table 24.1, the calculated diameter obtained from Eq. (24.3) agrees well with the true value in each case.

Procedure for Characterization of Flaws. — For a flaw of random orientation in a material, d, θ_1, and θ_2 would all be unknown quantities. Therefore, it would be necessary to have three separate equations to determine all of them. A conceptual scheme to do this was devised and is reported in detail elsewhere.[3] This approach is based upon making known changes in angle to achieve new separations between adjacent interference peaks in the analyzed spectrum.

Use of Higher Frequencies. — Some tests were performed in a higher frequency range (10 MHz) than that (1 to 4 MHz) used for all the previously mentioned results. The results at these higher frequencies are explained by the same general approach. Working in higher frequency ranges will offer new capabilities (e.g., sensitivity to smaller flaws).

Penetrating Radiation and Holographic Inspection Methods

Radiation Scattering[4] (B. E. Foster, S. D. Snyder)

We continued our studies of the use of scattered and fluorescent radiation for measuring the thickness of coatings or claddings on reactor components. The most recent measurements were on the fluorescent x rays emitted from the L shell of U energized by the 38-keV x rays emitted

Table 24.1. Experimental Data and Calculated Results for the General Case (Two Angles)

Incident Angles, deg		Calculated Angle, Θ, Between Source and Reflector (deg)	Average Frequency Interval (MHz)	Diameter of Reflector, in.	
θ_1	θ_2			Actual	Calculated
8.4	0	8.4	0.62	0.281	0.280
11.4	0	11.4	0.50	0.281	0.267
14.7	0	14.7	0.40	0.281	0.265
8.4	5	10.5	0.53	0.281	0.272
11.4	5	12.5	0.44	0.281	0.278
14.7	5	16.2	0.37	0.281	0.272
8.4	10	13.5	0.42	0.281	0.274
11.4	10	15.0	0.37	0.281	0.281
14.7	10	18.2	0.32	0.281	0.275

from our ^{147}Pm source. We monitored the relative decrease in intensity as different thicknesses of Al were placed on the U substrate. Good sensitivity was shown for Al from about 0.003 to 0.042 in. thick.

Closed-Circuit Television for Radiographic Evaluation (B. E. Foster, S. D. Snyder)

We are experimenting with the use of a closed-circuit television system as a rapid densitometer for reading radiographs. The preliminary setup consists of a film viewer as a source of illumination, a Radio Corporation of America 525-line closed-circuit television system with a scan rate of 9,623 in./sec, and an oscilloscope to delay and view any one of the 525 active scan lines of the picture. Presently, we are using a zoom lens with a 20- to 80-mm focal length on the camera. The video and synchronizing sections of the television chassis were modified to allow the injection of a "pip" pulse (a white dot on the screen) from the oscilloscope and to obtain proper synchronizing signals for the oscilloscope. This pip pulse is used to identify the particular line being viewed.

When we view a standard radiographic density step wedge with step increments of 0.2 density units, we observe a 5-V change in video signal per step over a density range of 0.4 to 1.4. We have not extended the density range (e.g., from 1.4 to 2.4) by increasing the intensity of illumination, but would expect a change of video signal per step comparable to that observed in the range 0.4 to 1.4.

Notes

1. Consultant from Northwestern College, Orange City, Iowa.
2. Consultant from the University of Tennessee.
3. H. L. Whaley and Laszlo Adler, A New Technique for Ultrasonic Flaw Determination, ORNL-TM-3056. In press.
4. This work is jointly supported by the Development of Fuel Element Fabrication Program and is also discussed in Chapter 20, p. 235, this report.

25. IMPROVEMENT OF HASTELLOY N AND RELATED COMPOSITIONS

J. R. Weir, Jr. H. E. McCoy, Jr.

This program is aimed at defining and understanding the metallurgical variables that affect the engineering performance of Ni-based structural alloys in reactor environments. Such alloys have been shown to have reduced stress-rupture properties and greatly reduced fracture strain after exposure to thermal-neutron fluences. Our work has concentrated on Hastelloy N. We have found that small additions of Ti, Zr, Hf, and Nb effectively reduce the deterioration of properties caused by irradiation. The end products sought by this program are a better understanding of the factors important in controlling irradiation damage in Ni-based alloys and development of a modified Hastelloy N with improved resistance to irradiation damage.

Mechanical Properties of Hastelloy N and Related Compositions

Effect of Composition on the Mechanical Properties of Modified Hastelloy N After Irradiation (C. E. Sessions)

We continued creep-rupture testing of various modified Hastelloy N alloys after irradiation in order to assess the influence of composition on the irradiation damage at high temperatures. We measured the creep properties of about 35 different alloys at 650°C after irradiation at 760°C to a thermal fluence of 3×10^{20} neutrons/cm^2. All alloys were annealed 1 hr at 1177°C before irradiation. The creep properties at 650°C after irradiation at 760°C are shown in Fig. 25.1 for alloys that contain various amounts of Ti. For tests at the relatively high stress of 47,000 psi, the rupture life varied from 0 to 1500 hr with Ti concentrations of 0 to 3%. This increased rupture life resulted from a drastic decrease in the creep rate. Unfortunately, the superior creep resistance at the higher Ti concentrations is offset by low ductility, which we attribute either to precipitation of intermetallic compounds or carbides. Compositions with about 2% Ti seem to offer the best combination of strength and ductility under these test conditions.

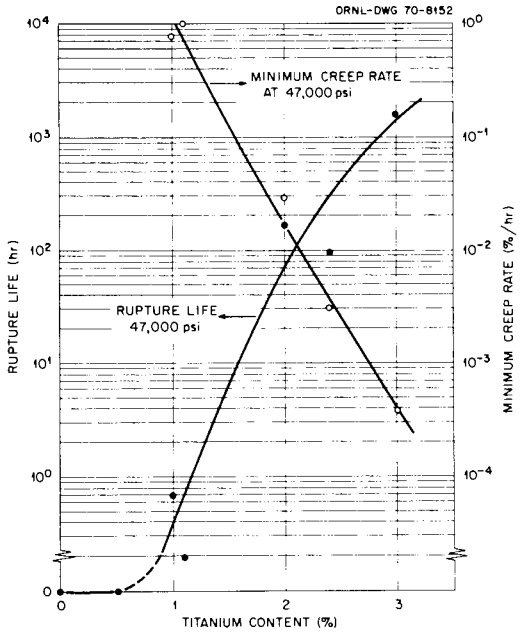

Fig. 25.1. Effect of Titanium Content in Hastelloy N on the Post-irradiation Creep-Rupture Properties at 650°C and 47,000 psi Stress. Samples solution annealed 1 hr at 1177°C and irradiated at 760°C to a thermal fluence of 3×10^{20} neutrons/cm^2.

The influence of other alloying additions on the creep-rupture behavior of Hastelloy N after irradiation is shown in Fig. 25.2. The curves plotted in each case correspond to the maximum effect attributable to either single or multiple additions of the elements Ti, Nb, and Hf to a nominal Ni–12% Mo–7% Cr–0.06% C base. Figure 25.2(a) compares the maximum rupture life achieved for alloys with additions of either Ti, Nb, or Hf. We investigated additions of 0 to 3.0% Ti, 0.5 to 1.5% Hf, and 0 to 2.0% Nb. It is clear that 3% Ti produced greater creep-rupture lives after irradiation than either 1.2% Hf or 2% Nb. The alloy with 1.2% Hf was superior to the alloy with 2% Nb and, in fact, was comparable in rupture strength to an alloy with 2% Ti, which is not plotted here. Thus, for independent additions of either Ti or Nb, the maximum rupture life corresponds to the highest alloy content. For Hf additions the longest rupture life occurred for the heat with 1.2% Hf rather than for that with the highest Hf content, 1.5%.

Combined effects of the additions of Ti and Hf, Ti and Nb, and Ti and Hf and Nb to the Ni–12% Mo–7% Cr–0.06% C base are compared in Fig. 25.2(b). The four curves represent the maximum rupture lives obtained for various alloy classes, each of which contained multiple

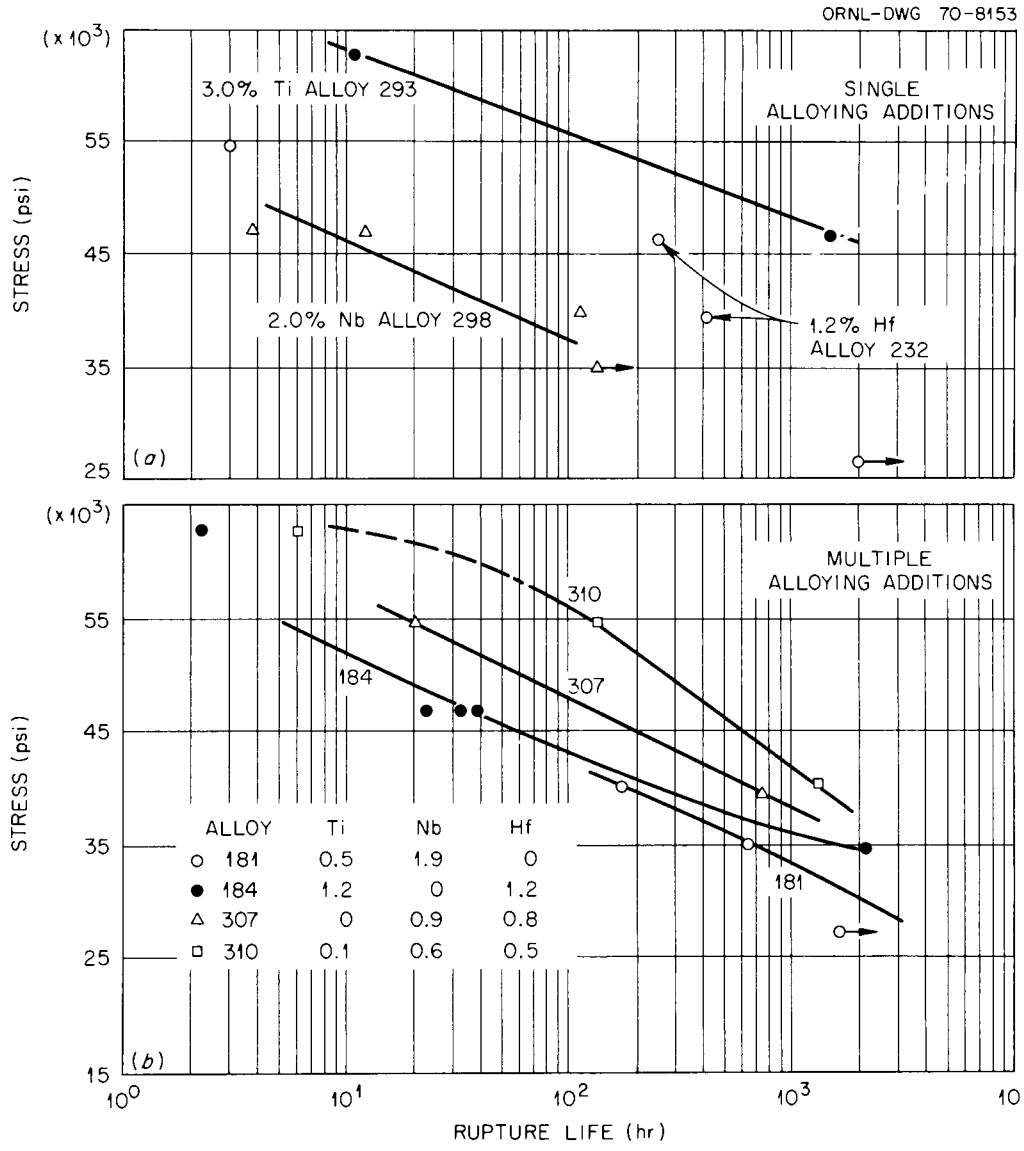

Fig. 25.2. Postirradiation Creep-Rupture Properties of Several Modified Hastelloy N Compositions at 650°C. Samples annealed 1 hr at 1177°C, irradiated at 760°C to 3×10^{20} neutrons/cm^2, and tested at 650°C. Alloys had a basic composition of Ni–12% Mo–7% Cr–0.067% C. (a) Properties achieved with single additions of either Ti, Nb, or Hf, and (b) properties achieved with combined additions of Ti, Nb, and Hf.

additions of Ti, Nb, or Hf. The greatest rupture life obtained at 650°C after irradiation at 760°C was for alloy 310, which contained additions of Nb, Ti, and Hf. Several other alloys containing multiple additions of Ti, Hf, and Nb also had good properties. Alloys such as alloy 307, which contained Nb and Hf, had properties inferior to those of the

Ti-Hf-Nb alloys but superior to those of the Ti-Hf and Ti-Nb alloys over the range of compositions investigated.

The creep rates of these alloys after irradiation are shown in Fig. 25.3. For the singular additions of Ti, Nb, or Hf [Fig. 25.3(a)] the lowest creep rate was obtained for the alloy that contained 3.0% Ti.

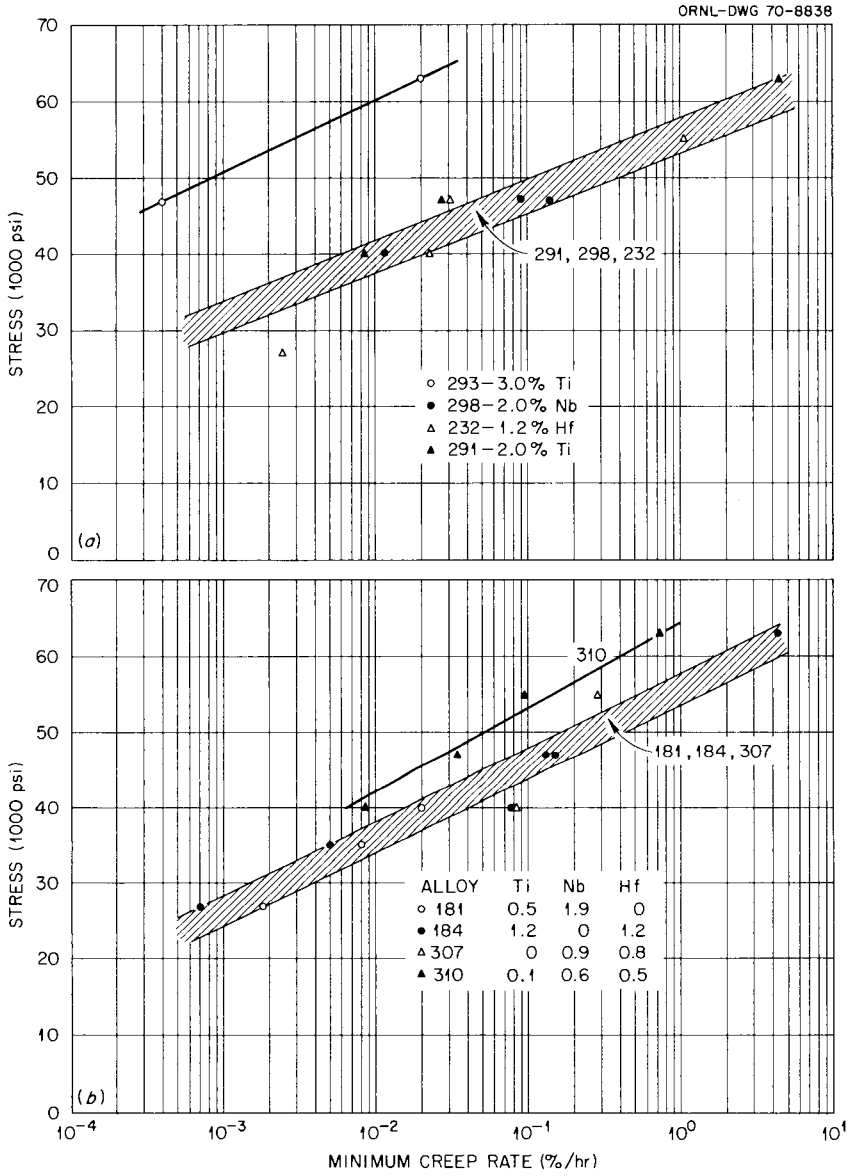

Fig. 25.3. Effect of Alloy Content on Postirradiation Creep Rate at 650°C. Samples annealed 1 hr at 1177°C, irradiated at 760°C to a thermal fluence of 3×10^{20} neutrons/cm^2, and tested at 650°C. (a) Single additions of Ti, Nb, or Hf, and (b) multiple additions of Ti, Nb, and Hf.

Alloys that contained 2.0% Ti, 2.0% Nb, or 1.2% Hf had creep rates that were about equivalent. Of the alloys that contained multiple additions [Fig. 25.3(b)], alloy 310 had the lowest creep rate, and the other three alloys had very similar creep strengths. The scatter bands shown in Fig. 25.3(a) and (b) are almost equivalent and indicate that the creep strength is not strongly affected by small additions of Ti, Nb, and Hf.

The fracture strains for these alloys after irradiation are shown in Fig. 25.4. The strains shown for short rupture times are lower than actually occurred because of the experimental procedure used. The samples were stressed before we began measuring the strain. Since the stresses involved in the tests that failed in short times were above the yield

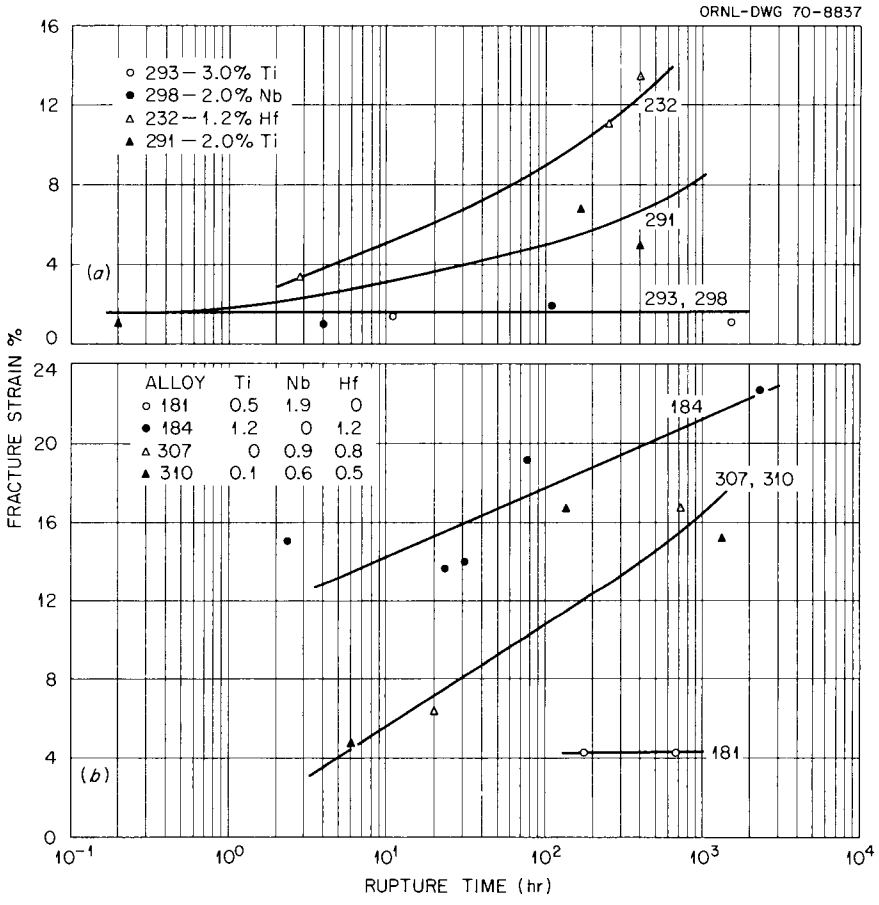

Fig. 25.4. Effect of Alloy Content on the Postirradiation Creep Ductility of Modified Hastelloy N at 650°C. Samples annealed 1 hr at 1177°C, irradiated at 760°C to a thermal fluence of 3×10^{20} neutrons/cm^2, and tested at 650°C. (a) Single additions of either Ti, Nb, or Hf, and (b) multiple additions of Ti, Nb, and Hf.

stress, some strain occurred on loading. Thus, the strains shown in Fig. 25.4 for short rupture times may be too low by as much as 6%. However, the results in Fig. 25.4(a) show the relative effects of additions of Nb, Ti, or Hf. The fracture strains after irradiation were quite low for alloy 293, which contained 3.0% Ti. However, alloy 291, with 2.0% Ti, had higher fracture strains. Alloy 298, which contained 2.0% Nb, had low fracture strains. Alloy 232, with 1.2% Hf, had the highest strains. The properties shown in Fig. 25.4(b) for the alloys with multiple additions show that various fracture strains were obtained after irradiation. Alloy 184, with 1.2% Ti and 1.2% Hf, had the highest fracture strains. Although alloy 181, with 1.9% Nb and 0.5% Ti, had the lowest fracture strain, the strains were higher than were those of standard Hastelloy N. Generally, the alloys with the higher fracture strains contained some Hf.

Electron Microscopy of Modified Hastelloy N Alloys (R. E. Gehlbach)

Our studies of modified Hastelloy alloys by electron microscope and phase analysis were concentrated on characterizing the microstructures of several commercial alloys and their relation to laboratory heats that contain the same modifying elements. As reported previously,[1,2] additions of Ti, Nb, and Hf change the precipitates from the M_2C (where M is the metallic component) to the MC type of carbides, provided appropriate quantities of these elements are used. Metallics in the MC type carbides consist of Mo, Cr, and one or more of the modifying elements. The result is a wide range of lattice constants of the face-centered cubic MC type of carbides found in the modified alloys.

The lattice constants of the MC type of carbides formed on aging at elevated temperatures can generally be grouped according to the alloying addition used; a carbide with the constant indicated below will always be present, but others may also be present:

Alloying Addition	Lattice Constant (A)
Ti	4.21–4.29
Ti + Nb	4.35–4.40
Hf Hf + Ti Hf + Ti + Nb	4.50–4.60

Two or three different carbides of the MC type are usually found in the alloys when Ti is used in combination with Nb or Hf, and an MC with a lattice constant of 4.27 to 4.29 A is often present. The M_2C type of carbide is stable in addition to the MC types when the Hf concentration is below about 0.8%.

The microstructures of commercial heats of Hastelloy N modified with Ti closely resemble those of the higher purity laboratory melts after the same thermal treatments. When 1% Ti is added, precipitation on stacking faults is observed along grain boundaries and in the matrix. For concentrations of about 2% Ti, the stacking fault morphology is absent, but the MC type of carbides are precipitated in and along grain boundaries and in the matrix.

The microstructures of several commercial alloys are shown in Fig. 25.5 with the compositions listed in Table 25.1. The major difference between laboratory and commercial alloys occurs in heats that contain Hf as an alloying addition. Particles or platelets about 0.2 μm in diameter had been precipitated in the matrix and grain boundaries of all laboratory melts that contained Hf examined to date.[1,2] This characteristic microstructure is shown in Fig. 25.6. These alloys contain 0.4 to 1.2% Hf either as the sole modifying element or in combination with various amounts of Ti, Nb, or both. However, none of the commercial alloys that contained Hf (0.4 to 1%) formed this morphology of the MC type of carbide after aging at temperatures in the range under consideration, 650 to 760°C. In the commercial alloys that contained about 1% Ti, the microstructure characteristic of Ti additions appears to predominate with little differences noticeable when Nb, Hf, or both are added. We have not determined any reasons for this difference in carbide morphology between laboratory and commercial alloys. We have no basis for suspecting that the large amount of precipitate in the grain boundaries, along the boundaries, and extending into the matrix would necessarily lead to poor properties after irradiation. This structure is generated during aging at both 650 and 760°C, unlike that observed in several other alloys that had similar precipitate distributions at 650°C but much coarser particles after aging at 760°C. The coarser precipitate at 760°C correlated with deteriorating mechanical properties after irradiation at higher temperatures.

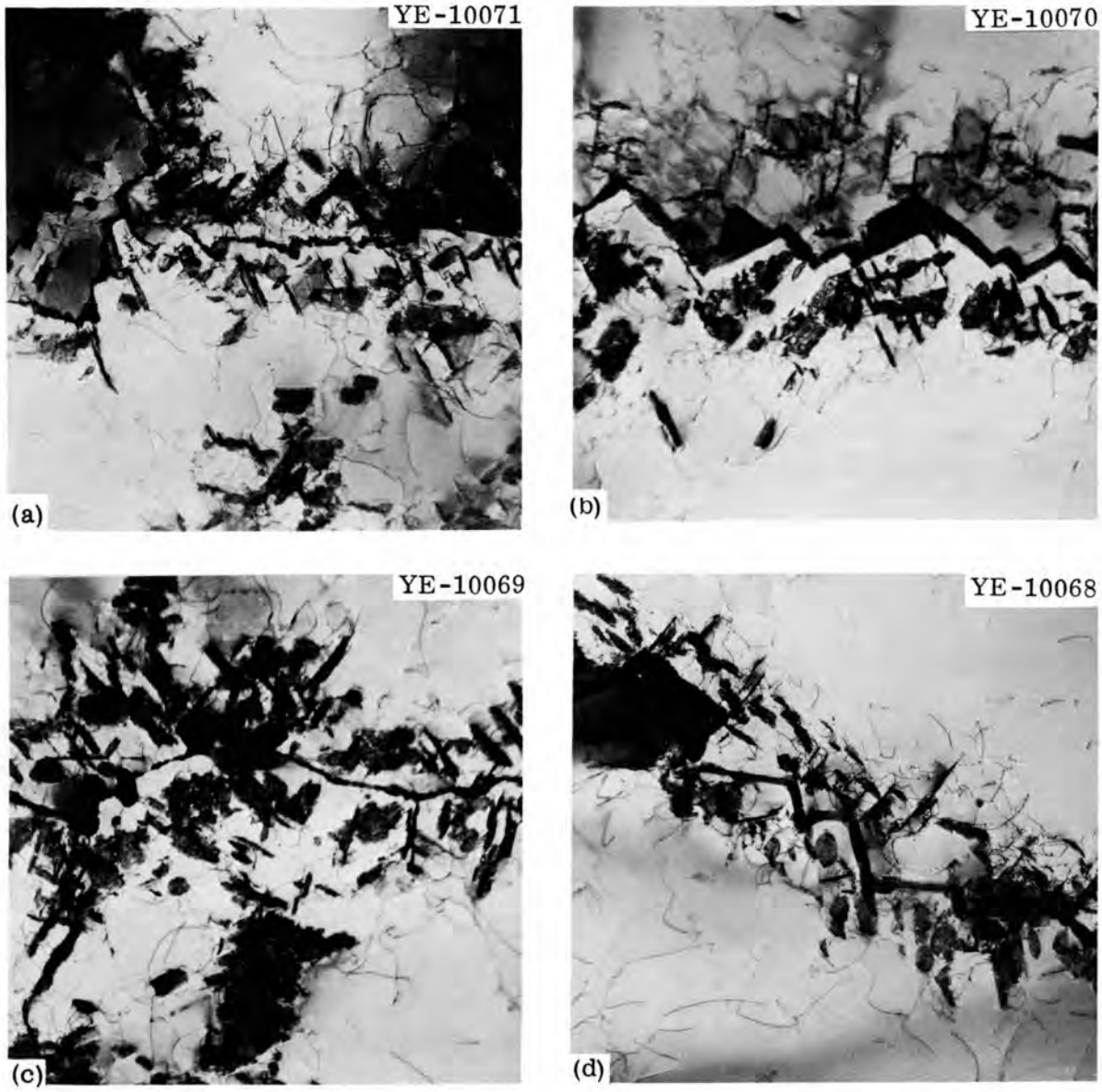

Fig. 25.5. Microstructures of Several Commercial Modified Hastelloy N Alloys that Contain the MC Type of Carbides after Annealing 1 hr at 1177°C and Aging 500 hr at 760°C. (a) 1.1% Ti, 0.1% Nb (70-785), (b) 0.8% Ti, 0.6% Nb (70-786), (c) 0.9% Ti, 0.1% Nb, 0.8% Hf (70-787), and (d) 1.4% Ti, 0.7% Nb, 0.3% Hf (70-788). 10,000×.

Table 25.1. Composition of Commercial Modified Hastelloy N Alloys[a]

Alloy Number	Alloying Additions, %			
	Ti	Nb	Hf	Si
67-548	1.2			
70-785	1.1	0.1		
70-727	2.1			
69-344	0.8	1.7		0.3
69-648	0.9	1.95		
70-786	0.8	0.6		
69-345	1.0		0.9	0.25
69-641	0.8		0.75	
70-787	0.9	0.1	0.8	
70-788	1.4	0.7	0.3	

[a]Compositions not given were < 0.1%.

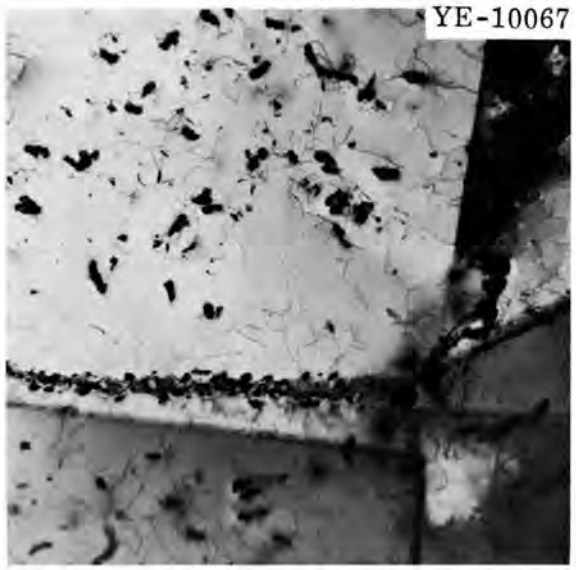

Fig. 25.6. Characteristic Morphology and Distribution of the MC Type of Carbides in Laboratory Heats of Hastelloy N that Contain Hafnium. This alloy (heat 310) contained 0.5% Hf, 0.1% Ti, and 0.6% Nb. It was annealed 1 hr at 1177°C and aged 200 hr at 760°C. 5000×.

The effect of Si on microstructure is consistent with all earlier observations in Hastelloy N. Although all of the alloys listed in Table 25.1 that contained no Si contained only the MC type of carbides, the addition of several tenths of a percent Si resulted in coarse, stable precipitates of the M_6C type of carbide in the matrix and grain boundaries, as shown in Fig. 25.7. This structure is characteristic of the standard air-melted Hastelloy N. A very small amount of the MC type of carbide does exist, however, and any significant improvement in mechanical properties after irradiation for these two heats (69-344 and 69-345) would probably be due to B being tied up in the MC type of carbides rather than to the effects of the morphology and distribution of the precipitate.

In summary, the effect of Hf on the morphology and distribution of the precipitates in commercial alloys that contain Ti differs from that in small laboratory heats; the "Ti structure" prevails rather than the "Hf structure" that is observed in the purer materials. The microstructure of the commercial alloys, however, may well be quite resistant to irradiation damage.

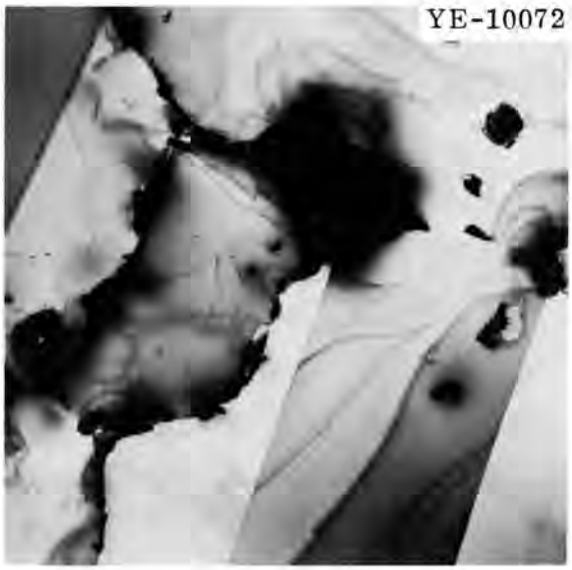

Fig. 25.7. Microstructure of Hastelloy N that Contains the M_6C Type of Precipitate. Alloy 69-345 contains 0.25% Si, 1.0% Ti, and 0.9% Hf. It was annealed 1 hr at 1177°C and aged 500 hr at 760°C. 5000×.

Notes

1. R. E. Gehlbach and C. E. Sessions, Fuels and Materials Development Program Quart. Progr. Rept. Sept. 30, 1969, ORNL-4480, pp. 291–295.

2. R. E. Gehlbach, Fuels and Materials Development Program Quart. Progr. Rept. March 31, 1970, ORNL-4560, pp. 267–274.

26. ADVANCED MATERIALS FOR STEAM GENERATORS

P. Patriarca G. M. Slaughter

The purpose of this program is to determine the corrosion resistance of welds in several high-temperature alloys being considered for use in steam generators for advanced high-temperature reactors. We need to know how well these weldments will resist both general and preferential corrosion in steam at 595 to 760°C.

The program currently includes two areas of investigation: (1) general corrosion (formation of a uniform scale) at 595 and 650°C, including an evaluation of the general weldability of various combinations of base and filler metals, and (2) preferential corrosion (e.g., oxidation at the fusion line, pitting, and stress cracking).

General Corrosion at 595 and 650°C

Studies of Weldments Between Similar and Dissimilar Metals (J. P. Hammond)

We determined the amounts of corrosion of the weldments of alloys for steam generators for a total accumulated steam exposure of 12,000 hr at 595 and 650°C and added averaged corrosion values to the corrosion curves based on weight gains. These data were the first determined since those recorded after 8000 hr. All of the curves continued to show an approximately linear relationship between corrosion and time. The few deviations from linearity were very slight and almost invariably in the negative direction, suggesting that the protective nature of the scales improved with time.

The calculated amounts of corrosion in terms of metal penetrated in 20 years for Inconel 625, Hastelloy X, and IN 102 welded with themselves was less than 0.0005 in. after exposure at 595 and 650°C. Weldments of these alloys joined to Incoloy 800 with themselves and with Inconel 82 as filler metal were about as good at 595°C and only moderately inferior at 650°C. The calculated penetration after 20 years for Inconel 600, which showed the highest amount of corrosion of the high-Ni alloys, was 0.002 in. at 595°C and 0.003 in. at 650°C.

The corrosion of these weldments was usually substantially less than that reported for these same materials in the wrought form.[1,2] Wozaldo and Pearl[1] investigated the isothermal corrosion of the base metals of our program (except for IN 102) in superheated steam at 565 and 620°C. A comparison of our data for 650°C with their data for 620°C showed that, in spite of the temperature difference, our weldments between similar metals after 8000 hr exposure corroded only 1/2 to 2/3 as much as their wrought samples, except for type 304 stainless steel, which corroded less than 1/9 as much. Although Wozaldo and Pearl's steam contained 20 ppm O and 2.5 ppm H, compared to undetectable levels in our work, the reason for less corrosion of our specimens is probably associated with a difference in the surface conditions of the specimens. Our specimens were ground on a 100-mesh Carborundum belt to achieve an economical standard finish, whereas their specimens were pickled and probably had little cold work in their surfaces.

To determine how large an effect surface condition has on corrosion of materials for steam generators, we exposed three alloys to superheated steam at 595 and 650°C. The 100-mesh ground finish was retained on one set of specimens and removed by electropolishing 0.003 in. of material from the surfaces of a second, identical set. The results for exposure times to 8000 hr are given in Table 26.1. For type 304 stainless steel and Incoloy 800, the amounts of corrosion were one to two orders of magnitude higher for the electropolished surface than for the ground surface. On the other hand, surface condition had only a minor influence for the Ni-base alloy Inconel 625. The electropolished surface was corroded slightly less than the ground surface. Note that for Incoloy 800 the difference between the amounts of corrosion for the ground and electropolished surfaces is not attributable entirely to differences in the early, parabolic stage of corrosion. The linear rate of corrosion for the electropolished condition also appears to be significantly higher, even for periods considered after 4000 and 6000 hr. This consideration is important from the point of view of the extrapolated long-term corrosion represented.

Table 26.1. Effect of Surface Finish on Corrosion of Three Alloys by Steam

Alloy	Surface Condition	Weight Gained[a] After Indicated Exposure, mg/cm^2				
		1000 hr	2000 hr	4000 hr	6000 hr	8000 hr
	Test Temperature 595°C					
Type 304 Stainless Steel	Ground	0.07	0.10	0.14	0.22	0.29
	Electropolished	5.19	6.87	b		
Incoloy 800	Ground	0.055	0.095	0.100	0.120	0.140
	Electropolished	3.97	4.66	5.24	5.45	5.61
Inconel 625	Ground	0.050	0.065	0.070	0.075	0.085
	Electropolished	0.050	0.055	0.055	0.070	0.080
	Test Temperature 650°C					
Type 304 Stainless Steel	Ground	0.11	1.20	1.21[c]		
	Electropolished	6.33	b			
Incoloy 800	Ground	0.215	0.310	0.415	0.475	0.535
	Electropolished	5.32	5.57	5.79	5.90	5.99
Inconel 625	Ground	0.115	0.130	0.150	0.185	0.205
	Electropolished	0.065	0.055	0.060	0.080	0.085

[a]Values listed are usually an average of three determinations.

[b]Spalled badly during weighing; test discontinued.

[c]Apparently had flaked substantially during exposure and weighing; test discontinued.

Studies on Simulated Root-Pass Compositions (J. P. Hammond)

The total accumulated exposure of a set of corrosion specimens specially synthesized to simulate the root passes of weldments in both composition and structure now have reached 4000 hr. The root-passes are receiving a special investigation because they generally are more highly alloyed (from base-metal dilution) than subsequent passes, and it is the root-pass that is actually exposed to steam in service. These synthetic root-pass compositions were designed to match the compositions corresponding to the 50% dilution factor that we obtained for welds in the studies of general corrosion.

After establishing the surprisingly large effect of surface finish on corrosion resistance, we increased the number of root-pass compositions

and surface conditions selected for investigation. The alloys to be examined and the status of the samples are listed in Table 26.2. All are being studied in the as-welded, electropolished, sandblasted, and belt-ground conditions; in addition, some have been belt ground and annealed. At the extremes, examinations to date have shown the corrosion rates of type 304 stainless steel welded with type 308 stainless steel and Incoloy 800 welded with Inconel 82 with the as-welded finish to be two orders of magnitude higher than those of Hastelloy X joined to Incoloy 800 with Inconel 82 with any of the four surface finishes.

Preferential Corrosion

Preparations for Tests with High-Pressure Steam Corrosion Loop
(J. P. Hammond)

The construction of the Incoloy 800 steam-corrosion loop with provision for injecting chloride and O_2 contaminants to investigate stress-corrosion cracking of weldments was completed. This unit operated successfully in a trial run designed to test its functional units and to provide a stress-relieving thermal exposure to critical portions of the loop.

We are preparing specimens and holding fixtures for U-bend tests for the first two test runs, which will probably begin in late July. These runs will be conducted under conditions that will produce low rates of corrosion and will be designed primarily to determine whether chloride-induced stress-corrosion cracking can occur in "dry" steam and under what thermal conditions. Subsequent tests will investigate cycling below the steam saturation temperature (to introduce moisture) and introduction of chloride and O_2 contaminants at higher levels (2 to about 8 ppm each).

Specimens with and without purposely introduced welding flaws (to act as corrosion crevices) are being prepared in all of the weldment combinations used for the general corrosion study. Additionally, specimens are being made of similar-metal weldments in types 316 and 410 stainless steel, in an 18% Cr–18% Ni–2% Si stainless steel especially marketed for stress-corrosion use by United States Steel Corporation, and in Inconel 601.

Table 26.2. Composition and Status of Simulated Root-Pass Specimens

Code	Composition	Status
A12	50% Inconel 82 25% Inconel 625 25% Incoloy 800	As-welded and electropolished specimens exposed 4000 hr; other specimens prepared
A13	75% Inconel 625 25% Incoloy 800	Specimens being prepared
A7	50% Inconel 82 25% Hastelloy X 25% Incoloy 800	As-welded and electropolished specimens exposed 4000 hr; other specimens prepared
A6	75% Hastelloy X 25% Incoloy 800	Specimens being prepared
A20	50% Inconel 82 25% IN 102 25% Incoloy 800	Specimens being prepared
A19	75% IN 102 25% Incoloy 800	Specimens being prepared
A2	50% Inconel 82 50% Incoloy 800	As-welded and electropolished specimens exposed 4000 hr; other specimens prepared
A3	50% Inconel 600 50% Inconel 82	Specimens being prepared
A4	50% Type 304 SS 50% Type 308 SS	As-welded, electropolished, and ground specimens prepared; other specimens prepared
	100% Inconel 82	Specimens being prepared

Notes

1. G. P. Wozaldo and W. L. Pearl, Corrosion 21, 355–369 (1965).

2. F. Eberle and J. H. Kitterman, "Scale Formations on Superheater Alloys Exposed to High-Temperature Steam," pp. 67–113 in Behavior of Superheater Alloys in High-Temperature, High-Pressure Steam, American Society of Mechanical Engineers, New York, 1968.

Previous reports in this series:

ORNL-4330	Period Ending June 30, 1968
ORNL-4350	Period Ending September 30, 1968
ORNL-4390	Period Ending December 31, 1968
ORNL-4420	Period Ending March 31, 1969
ORNL-4440	Period Ending June 30, 1969
ORNL-4480	Period Ending September 30, 1969
ORNL-4520	Period Ending December 31, 1969
ORNL-4560	Period Ending March 31, 1970

ORNL-4600
UC-25 — Metals, Ceramics, and Materials

INTERNAL DISTRIBUTION

1–3. Central Research Library
4. ORNL — Y-12 Technical Library
Document Reference Section
5–34. Laboratory Records Department
35. Laboratory Records, ORNL RC
36. ORNL Patent Office
37. R. E. Adams
38. G. M. Adamson, Jr.
39. S. E. Beall
40. R. J. Beaver
41. M. Bender
42. R. G. Berggren
43. D. S. Billington
44. N. C. Binkley
45. E. E. Bloom
46. A. L. Boch
47. E. S. Bomar
48. C. D. Bopp
49. B. S. Borie
50. R. A. Bradley
51. R. J. Breeding
52. R. B. Briggs
53. R. E. Brooksbank
54. D. A. Canonico
55. P. T. Carlson
56. R. W. Carpenter
57. R. M. Carroll
58. J. M. Corum
59. J. V. Cathcart
60. D. L. Clark
61. G. W. Clark
62. Nancy C. Cole
63. K. V. Cook
64. W. H. Cook
65. G. L. Copeland
66. W. B. Cottrell
67. C. M. Cox
68. F. L. Culler
69. C. W. Cunningham
70. J. E. Cunningham
71. V. A. DeCarlo
72. W. E. Deeds
73. J. P. De Luca
74. J. H. DeVan
75. J. R. DiStefano
76. C. V. Dodd
77. R. G. Donnelly
78. D. A. Dyslin
79. T. Eck
80. J. H. Erwin
81. K. Farrell
82. J. I. Federer
83. D. E. Ferguson
84. R. B. Fitts
85. B. Fleischer
86. B. E. Foster
87. A. P. Fraas
88. J. H Frye, Jr.
89. W. Fulkerson
90. L. C. Fuller
91. R. E. Gehlbach
92. T. G. Godfrey, Jr.
93. G. M. Goodwin
94. J. M. Googan (Y-12)
95. R. J. Gray
96. B. L. Greenstreet
97. W. R. Grimes
98. A. G. Grindell
99. H. D. Guberman
100. L. L. Hall
101. W. O. Harms
102. R. F. Hibbs
103–105. M. R. Hill
106. D. O. Hobson
107. H. W. Hoffman
108. F. J. Homan
109. R. W. Horton
110. W. R. Huntley
111. H. Inouye
112. D. H. Jansen
113. J. D. Jenkins
114. W. H. Jordan
115–147. P. R. Kasten
148. G. W. Keilholtz
149. R. T. King
150. R. L. Klueh
151. R. W. Knight
152. W. J. Lackey
153. C. E. Lamb
154. J. A. Lane

155. J. M. Leitnaker
156. B. C. Leslie
157. C. S. Lever
158. T. B. Lindemer
159. C. T. Liu
160. H. R. Livesey
161. B.T.M. Loh
162. E. L. Long, Jr.
163. A. L. Lotts
164. C. D. Lundin
165. J. W. Luquire
166. R. N. Lyon
167. R. E. MacPherson
168. M. M. Martin
169. W. R. Martin
170. R. S. Mateer
171. R. W. McClung
172. H. E. McCoy, Jr.
173. H. C. McCurdy
174. R. E. McDonald
175. W. T. McDuffee
176. D. L. McElroy
177. C. J. McHargue
178. A. J. Miller
179. E. C. Miller
180. J. P. Moore
181. R. E. Moore
182. A. J. Moorhead
183. C. S. Morgan
184. J. G. Morgan
185. F. H. Neill
186. T. A. Nolan (K-25)
187. K. Notz
188. A. R. Olsen
189. M. F. Osborne
190. P. Patriarca
191. W. H. Pechin
192. R. B. Perez
193. A. M. Perry
194. S. Peterson
195. L. E. Poteat
196. R. A. Potter
197. M. K. Preston
198. W. W. Proaps
199. C. E. Pugh
200. R. E. Reed
201. G. A. Reimann
202. A. E. Richt
203. P. L. Rittenhouse
204. H. E. Robertson
205. M. W. Rosenthal
206. D. J. Rucker
207. C. F. Sanders
208. G. Samuels
209. A. W. Savolainen
210. J. E. Savolainen
211. A. C. Schaffhauser
212. J. L. Scott
213. J. D. Sease
214. C. E. Sessions
215. W. A. Simpson
216. O. Sisman
217. G. M. Slaughter
218. S. D. Snyder
219. I. Spiewak
220. J. E. Spruiell
221. W. J. Stelzman
222. R. L. Stephenson
223. J. O. Stiegler
224. D. A. Sundberg
225. R. W. Swindeman
226. V. J. Tennery
227. K. R. Thoms
228. D. B. Trauger
229. T. N. Washburn
230. G. M. Watson
231. S. C. Weaver
232. M. S. Weschler
233. A. M. Weinberg
234. J. R. Weir, Jr.
235. W. J. Werner
236. H. L. Whaley, Jr.
237. G. D. Whitman
238. F. W. Wiffen
239. J. M. Williams
240. L. C. Williams
241. R. K. Williams
242. R. O. Williams
243. J. C. Wilson
244. R. G. Wymer, Jr.
245. F. W. Young, Jr.
246. C. S. Yust
247. C. M. Adams, Jr. (Consultant)
248. Leo Brewer (Consultant)
249. L. S. Darken (Consultant)
250. Walter Kohn (Consultant)

EXTERNAL DISTRIBUTION

AIR FORCE MATERIALS LABORATORY, Wright-Patterson Air Force Base

251. C. H. Armbruster
252. H. M. Burte
253. G. Glenn
254. Technical Director

AIR FORCE WEAPONS LABORATORY, Kirtland Air Force Base

255. D. Brooks

ARGONNE NATIONAL LABORATORY

256. L. Baker
257. J. H. Kittel
258. M. V. Nevitt
259. P. G. Shewmon
260. R. C. Vogel

LMFBR PROGRAM OFFICE, Argonne National Laboratory

261. A. Amorosi
262. L. Burris
263. L. Kelman
264. J. M. McKee

AEC-RDT SITE REPRESENTATIVES

265. M. E. Jackson, Argonne National Laboratory
266. D. J. Wille, Atomic Power Development Associates
267. R. L. Morgan, Atomics International
268. J. V. Levy, General Electric, Sunnyvale
269. R. H. Ball, Gulf General Atomic
270. D. A. Moss, Idaho
271. D. F. Cope, Oak Ridge National Laboratory
272. C. L. Matthews, Oak Ridge National Laboratory
273. P. G. Holsted, WADCO
274. J. Sako, WADCO
275. Theodore Iltis, Westinghouse Advanced Reactor Division
276. Atomic Energy Commission Library, Washington

DIVISION OF NAVAL REACTORS, AEC, Washington

277. R. H. Steele

DIVISION OF REACTOR DEVELOPMENT AND TECHNOLOGY, AEC, Washington

278. J. C. Crawford, Jr.
279. G. W. Cunningham
280. A. Giambusso
281. H. G. Hembree
282. K. E. Horton
283. J. R. Hunter
284. E. E. Kintner
285. W. H. Layman
286. W. H. McVey
287. J. J. Morabito
288. R. E. Pahler
289. A. J. Pressesky
290. M. A. Rosen
291. J. M. Simmons
292. E. E. Sinclair
293. B. Singer
294. A. Taboada
295. A. N. Tardiff
296. A. Van Echo
297. C. E. Weber
298. M. J. Whitman

DIVISION OF RESEARCH, AEC, Washington

299. P. W. McDaniel
300. D. K. Stevens

DIVISION OF SPACE NUCLEAR SYSTEMS, AEC, Washington

301. R. E. Anderson
302. D. Beard
303. J. F. Griffo
304. C. E. Johnson
305. A. P. Litman
306. J. A. Powers
307. F. C. Schwenk

OAK RIDGE OPERATIONS OFFICE

308. Laboratory and University Division
309. Patent Office

ATOMIC POWER DEVELOPMENT ASSOCIATES

310. E. C. Kovacic
311. A. A. Shoudy

ATOMICS INTERNATIONAL

312. T. A. Moss
313. H. Pearlman
314. J. G. Asquith

BABCOCK AND WILCOX COMPANY, Lynchburg, Virginia 24505

315. C. Baroch
316. S. P. Grant
317. C. Johnson
318. L. Weissert

BATTELLE MEMORIAL INSTITUTE, Columbus, Ohio

319. W. Berry
320. D. Keller
321. S. J. Paprocki
322. Defense Materials Information Center

WADCO, P.O. Box 1970, Richland, Washington 99352

323. A. L. Bement
324. J. J. Cadwell
325. T. T. Claudson
326. D. L. Condotta
327. E. Evans
328. J. E. Hanson
329. B. R. Hayward
330. B. M. Johnson
331. W. E. Roake
332. D. W. Shannon
333. W. F. Sheely
334. J. C. Tobin
335. R. G. Wheeler
336. Technical Information File

FAST FLUX TEST FACILITY, WADCO, P.O. Box 1970, Richland, Washington 99352

337. E. R. Astley

BROOKHAVEN NATIONAL LABORATORY

338. D. H. Gurinsky
339. C. Klamut

BUREAU OF MINES

340. Haruo Kato, Albany Metallurgy Research Center, P.O. Box 70, Albany, Oregon 97321
341. T. Sullivan, Bureau of Mines, Boulder City, Nevada 89005

COMBUSTION ENGINEERING

342. W. P. Chernock
343. S. S. Christopher

GENERAL ELECTRIC, Cincinnati

344. D. H. Ahmann
345. H. C. Brassfield
346. V. P. Calkins
347. E. Hoffman
348. J. McGurty

GENERAL ELECTRIC, Nuclear Systems Programs, Cincinnati

349. E. E. Hoffman

GENERAL ELECTRIC, San Jose

350. R. Duncan
351. H. Klepfer

GENERAL ELECTRIC, Pleasanton

352. H. W. Alter

GENERAL ELECTRIC, Sunnyvale

353. K. P. Cohen
354. F. Comprelli
355. R. Skavdahl
356. C. Spalaris
357. E. L. Zebroski

GULF GENERAL ATOMIC

358. D. B. Coburn
359. A. J. Goodjohn
360. J. P. Howe
361. S. Jaye
362. J. F. Watson

IDAHO NUCLEAR CORPORATION

363. W. C. Francis
364. William Yuill

ILLINOIS INSTITUTE OF TECHNOLOGY RESEARCH INSTITUTE

365. D. J. McPherson

KNOLLS ATOMIC POWER LABORATORY

366. R. F. Wojciescak
367. Document Library

LOS ALAMOS SCIENTIFIC LABORATORY

368. R. D. Baker
369. J. A. Leary
370. Reports Library

MOUND LABORATORY

371. R. G. Grove

NASA HEADQUARTERS

372. J. J. Lynch

NASA, LEWIS RESEARCH CENTER

373. M. Ault
374. J.W.R. Creagh
375. J. J. Lombardo
376. T. P. Moffitt
377. F. E. Rom
378. L. Rosenblum
379. N. D. Sanders
380. N. Saunders
381. C. M. Scheuermann
382. H. Schwartz

NAVAL RESEARCH LABORATORY

383. J. R. Hawthorne
384. C. Serpan
385. L. E. Steele

NORTH CAROLINA UNIVERSITY, Raleigh, North Carolina 27607

386. J. Beeler
387. R. E. Dahl

NUCLEAR MATERIALS AND EQUIPMENT CORPORATION

388. C. Caldwell
389. K. Puechl

OHIO STATE UNIVERSITY, Columbus, Ohio 43212

390. M. G. Fontana
391. R. W. Staehle

RENSSELAER POLYTECHNIC INSTITUTE

392. W. Dickinson
393. W. F. Savage
394. C. B. Willingham, Jr.

SANDIA CORPORATION

395. J. Read Holland
396. J. Jacobs
397. D. R. Johnson

SAVANNAH RIVER LABORATORY

398. P. H. Permar
399. S. P. Rideout

TRW SYSTEMS (NASA), Redondo Beach, California 90278

400. H. Lurie

UNION CARBIDE CORPORATION, New York

401. J. A. Swartout

UNION CARBIDE CORPORATION, Materials Systems Division, Indianapolis

402. C. F. Leitten, Jr.

UNITED NUCLEAR CORPORATION

403. A. Strasser

UNIVERSITY OF CALIFORNIA, Lawrence Radiation Laboratory, Livermore

404. W. R. Holman
405. J. S. Kane
406. L. W. Roberts
407. A. J. Rothman
408. B. Rubin

U.S. NAVAL AIR SYSTEM COMMAND (AIR-52031B)

409. T. Kearns
410. I. Machlin

USAEC Scientific Representative, American Embassy, Box 40 FPO, N.Y. 09510

411. W.L.R. Rice

WESTINGHOUSE, Advanced Reactor Division, Waltz Mill Site

412. E. C. Bishop
413. A. Boltax
414. J.C.R. Kelly
415. P. J. Levine
416. P. Murray
417. W. E. Ray
418. G. A. Whitlow

WESTINGHOUSE, Astronuclear Laboratory

419. R. T. Begley
420. D. C. Goldberg

WESTINGHOUSE, Atomic Power Division

421. T. Stern

WESTINGHOUSE, Bettis

422. R. H. Fillnow
423. P. N. Gustafson
424. Westinghouse Bettis Laboratory Library

425–623. Given distribution as shown in TID-4500 under Metals, Ceramics, and Materials category (25 copies – NTIS)